A Thesis Submitted for the Degree of PhD at the University of Warwick

http://go.warwick.ac.uk/wrap/58643

THE UNIVERSITY OF WARWICK

`AUTHOR:` **Andrew Richard Clough** `DEGREE:` **Ph.D.**

`TITLE:` **A study on the near-field interactions of ultrasonic surface waves with surface-breaking defects.**

`DATE OF DEPOSIT:` ....

I **agree** that this thesis shall be available in accordance with the regulations governing the University of Warwick theses.

I **agree** that the summary of this thesis may be submitted for publication.

I **agree** that the thesis may be photocopied (single copies for study purposes only).

Theses with no restriction on photocopying will also be made available to the British Library for microfilming. The British Library may supply copies to individuals or libraries. subject to a statement from them that the copy is supplied for non-publishing purposes. All copies supplied by the British Library will carry the following statement:

> "Attention is drawn to the fact that the copyright of this thesis rests with its author. This copy of the thesis has been supplied on the condition that anyone who consults it is understood to recognise that its copyright rests with its author and that no quotation from the thesis and no information derived from it may be published without the author's written consent."

`AUTHOR'S SIGNATURE:` ....

USER'S DECLARATION

1. I undertake not to quote or make use of any information from this thesis without making acknowledgment to the author.
2. I further undertake to allow no-one else to use this thesis while it is in my care.

DATE SIGNATURE ADDRESS

....

....

....

....

....

A study on the near-field interactions of ultrasonic surface waves with surface-breaking defects.

by

Andrew Richard Clough

Thesis

Submitted to the University of Warwick

for the degree of

Doctor of Philosophy

Department of Physics

September 2013

THE UNIVERSITY OF
WARWICK

Contents

List of Tables

List of Figures

Acknowledgments

First and foremost I would like to thank my supervisor Dr. Rachel Edwards for the excellent guidance, support and advice that she has given me throughout this project. I would also like to thank Dr. Benjamin Dutton and Dr. Fransisco Hernandez-Valle without whom the work on Rayleigh waves and real defects would have taken a lot longer! I would also like to thank the rest of my colleagues in the Warwick Ultrasound group and my original office for their friendship and 'witty' banter that have helped to make the whole PhD experience enjoyable.

A big thank-you to my fiancé Madison for standing by me each day (even the exceptionally long ones!) and helping to inspire me to keep going everyday, your love and support have helped immensely. I would also like to say how glad I am for the support and faith that my family have kept in me, and how lucky they were to be spared a read-through of the thesis for spelling mistakes! I would also like to thank the University of Warwick canoe polo squad for the great fun we've had together over the years and for the opportunity to vent my pent-up energies generated by long hours in the lab. Thanks finally to any who I have not mentioned by name, there are so many that it would require an extra chapter to mention them all.

Lastly, I would like to acknowledge the funding provided by the European Reasearch Council (ERC) which made this work possible.

Declarations

The research presented in this thesis is my original work, and was produced under the supervision of Dr. Rachel Edwards in the Department of Physics at the University of Warwick, UK between October 2009 and September 2013. Every effort has been made to accredit all contributions to those who have aided me during my research, and all consulted literature has been referenced.

No part of this work has been previously submitted to the University of Warwick, nor to any other academic institution for the purposes of obtaining a higher degree. Some parts of the work have been published as journal submissions, and a complete list can be found in the list of publications section.

List of publications

1. A. R. Clough and R. S. Edwards. Scanning laser source Lamb wave enhancements for defect characterisation. Under Review. 2013
2. F. Hernandez-Valle, A. R. Clough and R. S. Edwards. Stress corrosion cracking detection using laser/laser and laser/EMAT techniques. Under Review. 2013
3. A. R. Clough and R. S. Edwards. Detection of open and partially closed surface defects in plates using ultrasonic enhancement. In: AIP Conference Proceedings, Review of Progress in Quantitative Nondestructive Evaluation. **32A**:pp. 367-374. July 2012.
4. F. Hernandez-Valle, R. S. Edwards, A. R. Clough, M. Rosli and B. Dutton. Laser generation and detection for surface wave interaction with different defect geometries. In: AIP Conference Proceedings, Review of Progress in Quantitative Nondestructive Evaluation. **32A**:pp. 324-329. July 2012.
5. A. R. Clough and R. S. Edwards. Lamb wave near field enhancements for surface breaking defects in plates. Journal of Applied Physics. **111**.p.104906, 2012. DOI: 10.1063/1.4719983
6. R. S. Edwards, B. Dutton and A. R. Clough. Interaction of laser generated ultrasonic waves with wedge-shaped samples. Applied Physics Letters. **100**:p.184102, 2012. DOI: 10.1063/1.4711021

7. R. S. Edwards, R. Perry, D. Cleanthous, D. J. Backhouse, I. J. Moore, A. R. Clough and D. I. Stone. Measuring elastic constants using non-contact ultrasonic transducers. In: AIP Conference Proceedings, International Congress on Ultrasonics. **1433**:pp. 511-514, 2012.

8. R. S. Edwards, A. R. Clough and M. H. Rosli. Detection and characterisation of surface cracking using scanning laser techniques. In: AIP Conference Proceedings, International Congress on Ultrasonics. **1433**:pp. 563-566, 2012.

9. R. S. Edwards, B. Dutton, A. R. Clough. Scanning laser source and scanning laser detection techniques for different surface crack geometries. In: AIP Conference Proceedings, Review of Progress in Quantitative Nondestructive Evaluation. **1430**:pp. 251-258, 2012.

10. R. S. Edwards, B. Dutton and A. R. Clough. Enhancement of ultrasonic surface waves at wedge tips and angled defects. Applied Physics Letters. **99**:p. 249901, 2011. DOI: 10.1063/1.3629772

11. B. Dutton, A. R. Clough, M. H. Rosli and R. S. Edwards. Non-contact ultrasonic detection of angled surface defects. NDT & E International. **44**:pp. 353-360, 2011. DOI: 10.1016/j.ndteint.2011.02.001

12. B. Dutton, A. R. Clough and R. S. Edwards. Near field enhancements from angled surface defects: A comparison of scanning laser source and scanning laser detection techniques. Journal of Nondestructive Evaluation. **30**. June 2011. DOI: 10.1007/s10921-011-0091-y

13. A. R. Clough, B. Dutton and R. S. Edwards. Ultrasonic Rayleigh wave enhancements in aluminium. In: AIP Conference Proceedings, Review of Progress in Quantitative Nondestructive Evaluation. **30A**:pp. 137-144. 2011.

14. R. S. Edwards, B. Dutton, M. H. Rosli and A. R. Clough. Non-contact ultrasonic characterisation of angled surface defects. In: AIP Conference Proceedings, Review of Progress in Quantitative Nondestructive Evaluation. **30A**:pp. 257-264. 2011.

Abstract

This thesis is concerned with the detection of surface-breaking defects, such as stress corrosion cracking, using an ultrasonic scanning approach in which a laser source and detector are scanned over the near-field of a defect. Large increases in the amplitude and frequency content of an incident ultrasonic wave are present when either the source or the detector is very close to the defect, leading to a phenomenon known as ultrasonic near-field enhancement. The extent of the ultrasonic enhancement varies with defect characteristics such as defect depth and angle to the surface.

Ultrasonic enhancement is observed in both experiment and finite element simulations using Rayleigh waves for both scanning laser detection and scanning laser source methods. The near-field enhancement is shown to vary as a function of the angle of the defect to the horizontal for Rayleigh wave enhancements, allowing the positioning and characterisation of artificial angled defects that are similar to rolling contact fatigue defects in railtrack. The mechanisms behind the near-field enhancement of Rayleigh waves at angled defects are identified, and this aids in the understanding of the behaviour of ultrasound as it interacts with surface-breaking defects.

Ultrasonic enhancements are also reported to be present in individual Lamb wave modes for interactions with artificial open-mouthed defects in thin plates, which are similar to the open end of stress corrosion defects. The mechanisms behind both the scanning laser detection and scanning laser source enhancements are identified and used to explain the variation in the enhancement as a function of increasing defect severity. Positioning of these defects is also achieved by identification of the enhancement location.

Finally, the scanning laser technique is applied to real stress-driven defects, and both scanning approaches are shown to be capable of detecting partially-closed defects in a variety of sample geometries. The position, geometric alignment and an estimate of the defect depth are obtained for real defects in thin plates, pipework sections and in irregularly shaped engine components.

Chapter 1

Introduction

This thesis is concerned with the development of a dual laser scanning system that can be used to identify and characterise surface-breaking cracks, with a focus towards partially-closed defects, in a variety of materials, through the use of ultrasonic surface waves. Both Rayleigh and Lamb surface ultrasonic waves are used in this work and interesting phenomena are identified when either the detection or the generation laser is passed directly over a defect. An understanding of the physical processes behind these phenomena is developed and used to identify important features of defects, such as their depth, position and geometric alignment. The detection of surface-breaking cracks in such a nondestructive manner allows damaged components to be identified and replaced, preventing costly material failure. The techniques presented here offer an alternative to traditional methods of detecting defects by visual inspection, which may struggle to identify certain types of partially-closed defects.

1.1 Nondestructive testing

For any industry the shutdown of operations is a costly and time consuming process, however, in many areas maintainance strategies involve removal or replacement of components without in-situ testing[1]. One such approach is the reactive replacement of components, i.e. replacement of parts after failure has occurred, with an alternative strategy being the regular replacement of components to a pre-defined schedule of maintainance[2,3]. The disadvantages of the former technique are obvious in that delaying repairs until actual component failure can lead to issues such as an entire plant shutdown, chemical leakage and the potential for damage to be spread between components[4,5]. The latter method also has disadvantages in that regular maintanance may lead to the replacement of perfectly healthy components, thereby increasing the plant running costs. To avoid these issues many industries take a nondestructive testing approach in which the health of components can be regularly monitored, with replacements only made when necessary[6,7].

Nondestructive testing (NDT) involves the inspection of a component or series of components without altering the physical condition of the component. In certain cases this means that testing can be carried out in-situ without the need for removing a component, leaving no adverse side effects for the system[8,9]. Nondestructive testing can be applied at many different points in the engineering process, from component production[10] to the maintainance of components in use[11]. There are many different nondestructive testing techniques avaliable, all of which aim to give an assessment of a component to determine whether it is still fit for purpose.

The following sections outline some of the various nondestructive testing methods avaliable and provide a brief overview of their applications and merits. There is no ‘magic bullet’ in nondestructive testing and methods are suited to the detection of specific types of defects, such that there are advantages and disadvantages to all the techniques presented here.

1.2 Nondestructive testing as a tool for research and industry

Early detection of defects is vital to many industrial applications to prevent costly economic and environmental damage arising from component failure[12,13]. Many components or systems operate in high stress environments which can precipitate defect growth from the material surface, meaning that detection of millimetre scale partially-closed defects, such as the stress corrosion cracks detailed in section 1.4.2, is essential[14]. Stress corrosion cracking defects are particularly prevalent in the petrochemical and nuclear industries, but have been reported in many other industries[15,16]. Nondestructive identification and characterisation of these defects allows damaged components to be replaced and minimises plant downtime, allowing smoother and more efficient repairs to take place[17].

Nondestructive techniques have been sucessfully used to monitor many different component health issues, including the monitoring of corrosion damage and its resulting wall thickness changes[18,19], monitoring the integrity of welds and joints[20], and the identification of surface and subsurface defects on a structure[21,22].

Some of the inspection techniques require direct contact with the sample, which can be challenging for a moving surface or a scanned transducer[23] or in the presence of elevated temperatures[24], and some require surface preparation (for example polishing of the surface or removal of cladding layers) which leads to an extended plant shutdown.

This thesis concentrates on the detection and characterisation of surface-breaking defects, with the eventual aim of detecting small, partially-closed defects without the need for surface polishing. Many different techniques have been applied to surface defect detection, involving both contact techniques, such as ultrasound generated using piezoelectric transducers[25,26] (section 2.2.1), and non-contact approaches, such as laser ultrasonics[27] (section 2.2.4), electromagnetic acoustic transducers (EMATs)[28] (section 2.2.3), thermography[29] (section 1.3.7) and eddy current techniques[30] (section 1.3.10), with many more availiable. The ever expanding range of NDT applications means that research into new techniques is essential to meet the demand for reliable defect detection techniques in industry.

1.3 Overview of nondestructive testing techniques

The following section provides an overview of some of the various nondestructive techniques employed for the detection of defects. Some of the advantages and disadvantages of each technique are given and help to illustrate the need for continuing research in this area in order to improve the inspection process.

1.3.1 Visual inspection

Visual inspection of a component is the oldest form of nondestructive testing, and in its simplest form involves an experienced tester performing a visual check of a component, usually as a precurser to the application of more rigorous inspection methods. Such inspection is often assisted by magnifying optics but it is still a lengthy, time consuming method, and is sensitive only to large defect sizes[6,7,31]. This form of inspection is usually employed as a means to identify a region of possible component failure in order to reduce the area over which a more detailed inspection is to take place.

Direct visual inspection by eye is often limited by restricted access to the components of interest and often requires the removal of a component or a cladding layer, thereby increasing the plant downtime and duration of the inspection. The probability of the detection of closed cracks by this method is very low[32].

In addition to simple visual surface inspection there exist several methods of optical inspection, one of which is the use of optical-fibre endoscopes to investigate internal structures or components with access issues[6,7]. The flexible endoscope provides direct imaging of difficult to reach parts of a system without the need for the removal of external casings, and is used in applications such as the inspection of power plants, in which the removal of external cladding would result in a temporary plant shutdown[33]. This inspection method has also been used for the inspection of parts within structures, such as turbine blades, without the need to dismantle the entire assembly, however, it still relies on an experienced operator identifying defects visually. Visual inspection is commonly used to detect defects with sizes of the order of millimetres.

1.3.2 Fibre optic inspection

Changes in the light transmitted through an optical fibre forms the basis of the fibre optic inspection technique. Fibre optics are either positioned on the sample surface or embedded within the structure, and variations in the phase, intensity, polarisation and arrival time of the light transmitted along these fibres are monitored. These variations are caused by movement of the material under test, such as that generated by a propagating ultrasonic wave, and allow the measurement of many material variables, such as material strain and pressure variations[34]. This inspection method is popular in civil engineering where sensors require long term placement within a structure, and as fibre optics are highly resistant to corrosion they are the perfect candidate for long term monitoring of civil engineering structures, such as bridges and buildings[35].

At each inspection an ultrasonic wave is propagated into the material and the resulting variations in the propagation of the light in the fibre optic are measured, and recorded as a reference for when no defect is present. Changes in the behaviour of the fibre optic variations are detected when a defect is present in the structure[36]. An example of the experimental setup for a fibre optic inspection is shown in figure 1.1. The fibre optic approach has also been utilised in the monitoring of multi-layered composites due to the ease in which the fibres can be introduced into the layered structure during construction[36,37]. Due to the small size and weight of the fibre optics this contact method introduces little impact on the structural behaviour of the material under test, allowing the natural behaviour of the system to be observed[34]. Fibre optic inspection is commonly used to detect defects with sizes of

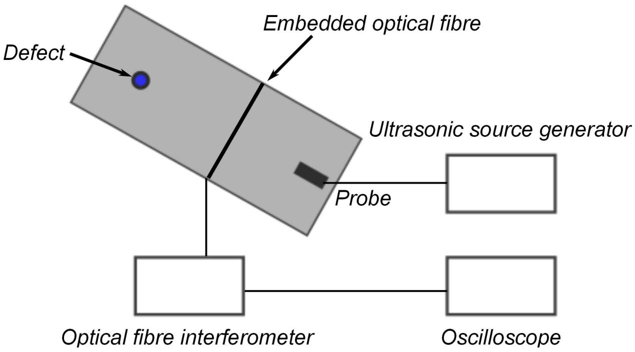

Figure 1.1: Schematic diagram of a typical experimental setup for optical fibre inspection.

the order of millimetres.

1.3.3 Dye penetrant inspection

Liquid penetrant inspection utilises the propensity for fluids to accumulate around surface discontinuities to identify surface-breaking defects[31,38]. The liquid penetrant will accumulate through capilliary action in a higher concentration at the position of a surface-breaking crack, and this location is easily identifiable if the concentration gradient with respect to the non-damaged surface is sufficiently high[31].

The penetrant, usually a brightly coloured or fluorescent liquid, is applied to the material under test and after a short delay any excess liquid that is not drawn into a defect is removed. A secondary liquid known as a developer is then applied, allowing the location of the residual penetrant to be clearly identified, usually with a change of colour[7].

The success of penetrant testing depends on the test material and the penetrant chosen, and variations in porosity or surface condition can produce erroneous results[39]. The liquid needs to be fully removed in order to prevent contamination or corrosion of the system after testing is complete. The advantages of penetrant inspection lie in the fact that it is cheap, portable, requires little time to apply, and gives reliable defect locations, with some degree of information about the size and shape of the defects.

No knowledge of the defect depth is obtained, however, and the effectiveness of penetrant inspection on rough surfaces or those with complicated geometry is limited. An example of a pipework section investigated by dye penetrant inspection is shown in figure 1.2, in which the dye can be seen to have gathered at the rough

Figure 1.2: Pipework section that has undergone dye penetrant inspection; note the collections of penetrant around areas of rough surface which are liable to give a false defect indication.

surface region in the middle of the image. Penetrant testing is limited to components at moderate temperatures and in most cases will involve the removal of cladding, or a surface layer such as paint. Penetrant testing has been used in many areas of industry, including quality control of nuclear power plants, in which large inspection areas need to be covered quickly[40]. Issues with liquid penetrant inspection often occur during the cleaning process prior to inspection as cleaning liquid can enter the surface defects in the same manner as the penetrant, making it hard for the dye to be retained and giving false inspection results[32]. Dye penetrant inspection is capable to resolving defects with sizes of a few millimetres, and a good overview of penetrant techniques can be found in[7,31,38]. Dye penetrant inspection is commonly used to detect defects with sizes of the order of millimetres.

1.3.4 Magnetic flux leakage inspection methods

Magnetic particle inspection is a technique that is specific to ferromagnetic materials and exploits the magnetic flux leakage that occurs in the vicinity of a surface-breaking defect or discontinuity[41]. A uniform magnetic field is applied across the sample, and the presence of a surface discontinuity acts to distort the lines of magnetic flux. A fine powder of ferromagnetic particles is applied to the sample surface and are magnetised by the leakage field and held in place at the defect, as shown in figure 1.3.

The particles captured by the flux leakage field at the defect are then observed visually in a similar fashion to liquid dye penetrant testing, however, with an understanding of the relation between the concentration of the magnetic particles and the degree of magnetic flux leakage, some determination of the defect depth and

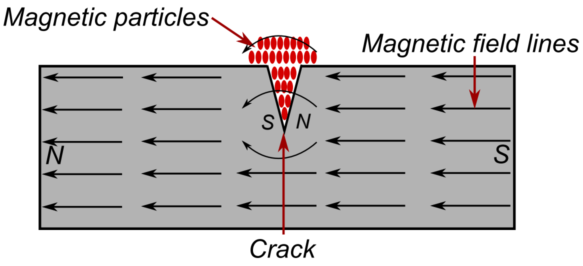

Figure 1.3: Schematic diagram of a defect under magnetic particle inspection with magnetic particles attracted to the flux leakage that occurs at a defect site.

geometry is possible[42].

Magnetic particle inspection on small tightly closed defects is challenging and they are often overlooked in testing[32]. However, magnetic particle inspection has been sucessfully used, with both dry ferromagnetic powder and as a liquid suspension, for the testing of welds[43], particularly those on offshore structures where underwater access makes other methods challenging[44].

Magnetic flux leakage inspection can also be carried out by scanning a probe over the material to detect the flux leakage field[45]. The leakage of magnetic flux from a magnetised material is commonly employed as a means of detecting defects in pipelines, rail tracks and other metal components[6,19,45–47]. This method has the advantage of being noncontact and does not require any surface preparation. However, the method can only be applied to inspect ferromagnetic and magnetically permeable materials and therefore its application is limited for industrial applications[45,48,49]. Magnetic flux techniques are commonly used to detect defects with sizes of the order of hundreds of micrometres.

1.3.5 Electromagnetic radiography

Electromagnetic radiography is a technique that utilises the penetrating nature of electromagnetic radiation to detect internal flaws in materials, with both x-ray and gamma ray radiography in use[50]. Standard radiographic inspection operates through the generation of electromagnetic radiation on one side of the sample under test; the radiation penetrates into the material and the intensity of the radiation is evaluated on the far side of the material[6]. The intensity of the transmitted radiation is dictated by the density of the material through which it has passed, with more dense material, like lead and iron, causing a higher degree of attenuation[7].

A defect or similar imperfection in the material will be apparent when there is a sufficient difference between the radiation intensity that has passed through

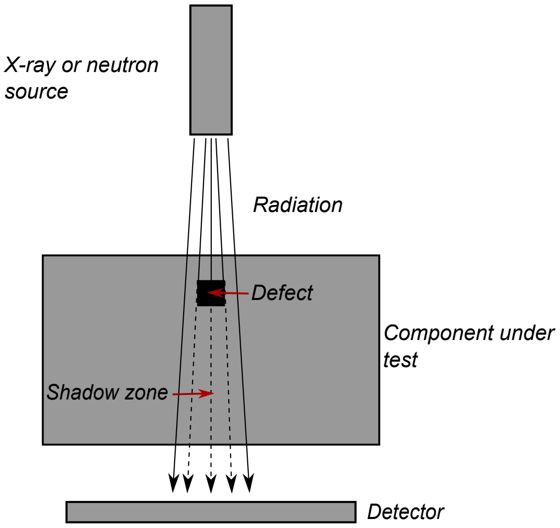

Figure 1.4: An example of an experimental setup that could be implemented for electromagnetic or neutron inspection by through-transmission monitoring.

the defect compared to the radiation that has travelled through the undamaged sample[7], as shown in figure 1.4. Electromagnetic radiography is an effective tool for detecting open cracks, inclusions of foreign material and voids within the structure. Techniques that examine the Compton scattered radiation that is directed back towards the x-ray source have also be used to obtain information about near surface defects, with the advantage that access is only required to a single side of the component[51,52].

One of the strengths of radiography is the ability to build up 3D images of complicated sample structures through the use of computed tomography (CT), in which many scans from different angles are combined to produce a full image[53,54]. However, the use of ionising radiation means that there are safety considerations limiting the exposure of testing personnel. Due to the high costs, both in terms of the x-ray source equipment and in computational time spent producing a CT image, this technique is limited to applications in which the detection of small defects outweighs the cost of the inspection process.

Radiographic methods can also use gamma radiation, with this approach chosen when the object under test has a large amount of material between it and the source (for example underground pipelines) or for particularly dense structures; here gamma rays are employed for their longer penetration depth[55]. Electromagnetic radiography is commonly used to detect defects with sizes of the order of micrometres.

1.3.6 Neutron radiography

Neutron radiography uses beams of neutrons that penetrate into the material to perform nondestructive testing in a manner similar to electromagnetic radiography. Changes in the transmission of a neutron beam or in the extent of the backscattering experienced by the neutrons are used to determine different material characteristics, such as the differences between the test material and a void, in order to identify defects[7,56]. Contrast is provided by the difference in the degree of interaction between the neutrons and the material atoms, which is dictated by the neutron cross-section, the value of which is not a simple measure of density or atomic number, and the higher the neutron cross section the more attenuation the beam will undergo[7].

The image produced by neutron radiography is a 2D shadow pattern, which shows areas of greater or lesser interaction with the neutron beam as it passes through the material under test[56], as outlined in figure 1.4. This makes it ideal for investigating materials in which a highly interacting material is covered by different layers, with for example a metal jacket (low neutron cross section) over hydrogen rich material (high neutron cross section)[57].

The most readily avaliable source of neutrons is from a nuclear reactor, placing limits on testing capabilities and ensuring that a component has to be removed completely in order to be tested[57]. Neutron radiography has been used to detect surface cracks through the addition of a contrast agent with a large neutron cross section[58] and is also used for the measurement of residual stresses within materials, particularly in single crystal turbine blades[59]. Neutron radiography is often used to complement x-ray radiography as neutrons do not interact with orbiting electrons, thereby giving a low attenuation for heavier elements, such as lead, which are conventionally sensitive to x-rays, allowing both methods to look at different aspects of a component[7]. Neutron radiography is commonly used to detect defects with sizes of the order of micrometres.

1.3.7 Thermographic inspection

Thermal inspection methods use heat sensing devices to measure the heat distribution across a sample, looking for the presence of thermal gradients or atypical temperatures in samples as they are heated or cooled[6]. Thermographic methods can either be passive, in which the natural heat distribution is studied in a structure, or active, in which the surface is heated and the resulting distribution of the

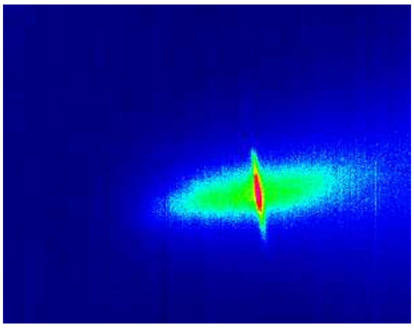

Figure 1.5: Surface-breaking defect imaged by an infra-red camera following the scanning of a continuous wave laser over the defect. This is a cumulative image formed from summation of the images from a video sequence, courtesy of Dr. Sue Burrows.

heat studied using an infra-red imaging camera[29]. Conventionally this is achieved through illuminating the sample with high powered flash lamps to heat the surface. An infrared image is produced of the sample after heating, and variations in the thermal properties of voids, cracks and delaminations with respect to the undamaged material are used to identify material damage[60,61]. Thermography has the advantage of being a noncontact inspection method that is capable of investigating large areas rapidly, however, it can struggle to determine the presence of closed defects that provide little impedance to heat flow[62].

Recent work has looked at combining thermography with other nondestructive methods, in particular with laser irradiation (see section 2.2.4) to produce a technique that is sensitive to closed defects and that can be targeted at specific regions of a sample instead of causing widespread heating, such as that achieved with flash lamps[63]. The thermal behaviour, as observed with an infra-red camera, of the sample under pulsed laser heating has been shown to differ dramatically between regions with no surface damage and those with surface-breaking defects present, due to changes in the boundary conditions at the damaged sample surface[64]. This scanning approach allows the defect position and geometry to be determined reliably without widespread heating of the sample, which may produce damage to heat sensitive coatings, with an example of a thermographically examined defect shown in figure 1.5.

Another crossover between nondestructive techniques can be found in the field of thermosonics, in which thermographic detection is combined with ultrasonic (section 1.3.11) excitation of a defect. In thermosonics experiments, thermographic detectors are used to detect the presence of local temperature increases in the sample arising from friction between defect edges that have been forced to rub together

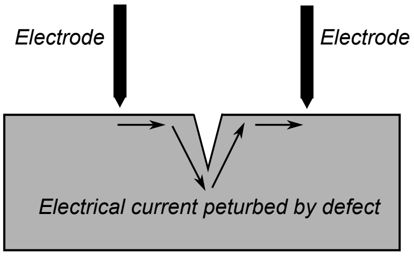

Figure 1.6: Schematic diagram of the process by which an induced electrical current is perturbed by the presence of a surface-breaking defect in ACPD and ACFM.

by the presence of an ultrasonic wave, thereby enabling the detection of closed defects[62,65]. The ultrasonic excitation can be performed in a noncontact manner so as to maintain the remote nature of thermographic inspection, and remove any possibility of damage to heat-sensitive components[62]. Tradiational thermography is commonly used to detect defects with sizes of the order of milimetres, however techniques such as thermosonics can detect smaller defects of the order of micrometres.

1.3.8 Alternating current potential difference (ACPD) method

ACPD is an electromagnetic crack depth sizing technique that utilises the disruption caused by a crack on the flow of current in the surface of a material to give a measure of the defect depth[66,67]. A current is induced between two electrodes that are placed onto the material under test, such that the current flows within the sample parallel to the sample surface. For a region without a defect, the voltage detected between these two points is constant, however, if a defect is present the current is forced to flow around and under the defect, introducing an extra path length for the current to flow along to reach the second electrode. The resulting change in the detected voltage from this extra path length is used to estimate the defect depth[68]. This method is highly accurate and the use of alternating current avoids extreme heating of the sample, however, it requires direct contact with the material[66], as shown in figure 1.6, and the voltage changes observed are dependent upon the test material such that the probes have to be calibrated to the material before each test. ACPD techniques are commonly used to detect defects with sizes of the order of hundreds of micrometres.

1.3.9 Alternating current field measurement (ACFM) method

Alternating current field measurements (ACFM) are used for the noncontact detection and sizing of surface-breaking defects, with measurement possible through several millimetres of surface coating[67]. ACFM measurements are similar in concept to the ACPD method (section 1.3.8) with an ACFM probe inducing an alternating current into the test material, which in turn induces a uniform magnetic field above the surface. The presence of a defect causes the electric current to flow around and underneath the discontinuity and disrupts the uniformity of the induced field and the change in the field is used to obtain information about the defect position and severity. This method has many applications, from high speed inspection of conducting materials, e.g. rail lines[69], to the inspection of stress cracking in storage containers[70]. Like the ACPD technique the ACFM method requires calibration to the component material before testing can take place as the changes in the current flow are dependent upon the material under test. ACPD techniques are commonly used to detect defects with sizes of the order of hundreds of micrometres.

1.3.10 Eddy current testing

Eddy current testing is an electromagnetic inspection method that is used for its high sensitivity to small surface cracks in electrically conductive materials[71,72]. In conventional eddy current testing a wire carrying an alternating electric current of a single frequency is held near to the test sample, generating an alternating magnetic field within the skin depth of the sample, the depth of which is dictated by the chosen frequency[73,74]. The varying magnetic field induces eddy currents within

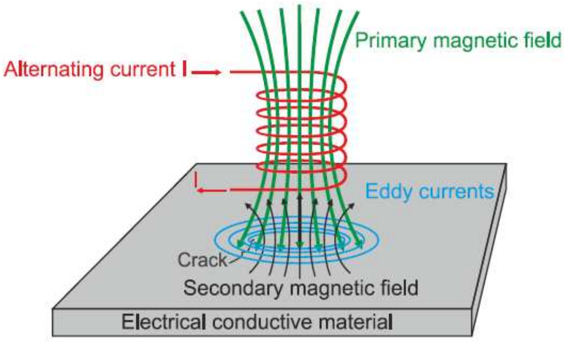

Figure 1.7: Schematic diagram of the process by which eddy currents are generated within a sample. Image taken from[71].

the skin depth of the material, and these in turn produce their own magnetic field, the influence of which is observed through changes in the impedence of a second detector coil or by variations in the impedence of the original coil, as shown in figure 1.7[71]. The presence of defects in the material surface act to alter the phase and amplitude of the measured current, thereby providing a measure of the surface condition[72,75,76].

Whilst conventional eddy current testing is highly effective at detecting small defects, the single frequency character, and the subsequent fixed skin depth, makes determination of defect depths difficult. To achieve depth sensitivity a non-contact technique known as pulsed eddy current testing was developed in which a broadband chirp signal is used instead of a single frequency[71]. This broadband pulse acts to induce eddy currents at a range of skin depths, with each depth being associated with a frequency component in the excitation signal, allowing the changes in the induced eddy currents to be observed as a function of depth, thereby giving depth sensitivity to the technique[71].

Although highly sensitive, both conventional eddy current and pulsed eddy current testing are restricted to the skin depth of a conducting material and hence are only sensitive to surface defects or near-surface defects. Despite this they find many applications in NDT, particularly in aircraft inspection where large areas of conducting materials require inspection[77,78]. Eddy current techniques are commonly used to detect defects with sizes of the order of hundreds of micrometres.

1.3.11 Ultrasound

Inspection of a material through the study of the changes in the propagation of ultrasonic sound waves (waves with frequency $\geq$ 20kHz) is a common nondestructive testing method[20,21,79–83]. Ultrasonic inspection is the method of nondestructive testing that is utilised in the work presented in this thesis, and an in-depth discussion of ultrasonic methods, experimental techniques and a mathematical treatment of ultrasonic propagation can be found in chapter 2. Many different methods exist for generating and detecting ultrasound within a material, with examples ranging from conventional contact piezoelectric methods[26,84] (section 2.2.1) to non-contact methods such as laser ultrasonics[22,27,85] (section 2.2.4) and electromagnetic acoustic transducers[28,86] (section 2.2.3).

Ultrasonic techniques have been sucessfully used in a variety of NDT applications including surface and sub-surface defect detection[21,22,80,87], corrosion detection[81,82], thickness measurement[83] and in the inspection of the integrity of welds[20], to name but a few. These inspections are carried out using many different ultrasonic wave types, including longitudinal and transverse bulk waves[26,87,88], Rayleigh surface waves[89,90] and Lamb surface waves[89,91], the details of a selection of which are found in section 2.1. A passive ultrasonic method known as acoustic emission in which transient acoustic waves are generated by the localised release of stresses in a material has also been used in several successful applications[92,93].

As a consequence of the wide array of experimental methods and ultrasonic wave probes avaliable there is a large variety of different inspection techniques in use. Ultrasonic testing methods include time of flight methods, such as the pulse-echo and time of flight diffraction (TOFD) techniques, which measure variations in the arrival time of ultrasonic waves due to the presence of material defects (section 2.3)[87,94]. Other techniques utilise changes in the wave amplitude that arise from the interaction with a defect in the far-field regime[90] and in the near-field[22,95] of the defect (section 2.3.1).

Ultrasonic inspection is the main focus of the work presented here, with a focus on laser generated and detected surface waves, with a detailed explanation of the propagation of ultrasound found in section 2.1. A discussion of the previous research that has been performed with ultrasound is found in section 2.2.

1.4 Defects in industrial applications

The work contained within this thesis focuses on the detection and characterisation of macroscopic surface-breaking defects, which are common in many areas of industry. Of particular interest are defects in the rail[96], nuclear[97] and petrochemical[12] industries, the early detection of which acts to forestall economic and environmental costs from component failures. Real defects can form complicated branched structures, with defects able to propagate to different depths and grow in a direction that is not perpendicular to the sample surface, however, new detection techniques are generally tested on perpendicular notch defects. Two such examples of real defects are rolling contact fatigue defects in rail tracks[96] and stress corrosion cracking defects, which can grown in many different industrial materials[17].

1.4.1 Rolling contact fatigue

A common issue in the rail transportation industry is rolling contact fatigue (RCF) defects, which initiate on the top surface of the rail but are not associated

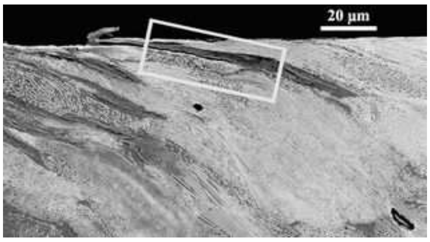

Figure 1.8: Micrograph of RCF defect propagating at an angle of approximately 25 ° from the rail head. Image courtesy of Birmingham University.

with any specific material faults or imperfections[96]. RCF defects are caused by a combination of the high normal and tangential stresses between the train wheel and the rail, causing severe shearing of the surface layer of the rail and fatigue of the material. Following the nucleation of a defect on the top surface the crack propagates through the heavily deformed top surface of the rail head at a shallow angle of approximately 25 °, giving a defect that can grown to several millimetres deep[98,99]. Defect growth is driven by the action of water trapped in the defect, which is put under large amounts of pressure whilst a train moves over the damaged region; the large forces involved help to drive the crack growth into the material[98]. In some cases the crack will propagate back towards the top surface, shearing off a small section of the rail top layer (known as spalling[99]) but in more severe instances the sloped defect will propagate downwards in the rail until failure occurs, as shown in figure 1.8, making early detection of these angled defects essential for preventing rail failure.

To simulate these types of defect, artificial angled surface-breaking defects were produced using laser micro-machining, a process which is described in section 1.4.3, with the calibration defects themselves presented in section 4. These artificial angled defects act as a good approximation of the early stages (angled defect growth) of RCF cracking and allow a method for early defect detection and characterisation to be developed.

Previous work towards detecting and charcterising RCF defects has utilised longitudinal waves[100] and guided waves[101–103] with changes in the signal amplitude and time of flight when a defect is present being used to detect and characterise the RCF. For inspection with longitudinal waves that are generated at a chosen angle of propagation into the rail, the presence of a direct reflected wave generated by the defect is used to position and size the RCF defect[100]. Recent research has begun to look at near-field enhancement effects that arise when surface acoustic waves interact with surface-breaking defects[104] to characterise the position and severity

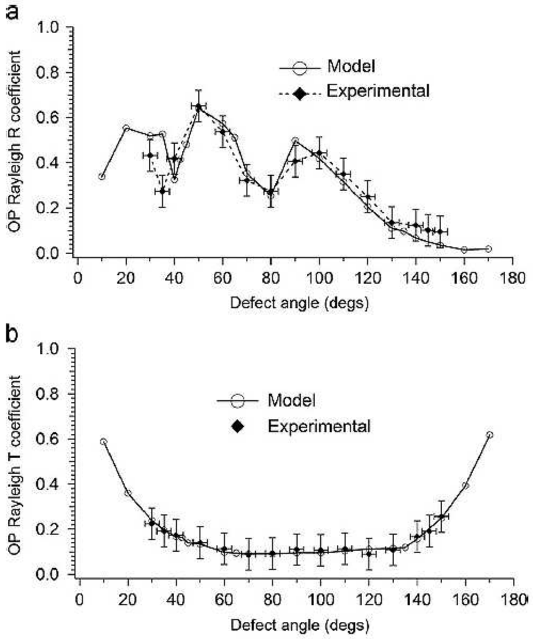

Figure 1.9: Variation in the reflection (a) and transmission (b) coefficients of the out-of-plane Rayleigh wave component for a defect of varying angle. Image taken from[107].

of defects similar to those found in RCF[105].

The main focus of this previous research has been on defects that propagate perpendicular to the sample surface, however, previous work has also shown that defects that are inclined to the horizontal, for example RCF defects, have different reflection and transmission characteristics to perpendicular defects, as shown in figure 1.9[106,107]. Therefore, the work presented in chapter 4 uses the near-field enhancement technique (section 2.3.1) to characterise not only the position of a defect, but also its angle to the sample surface, which is of benefit to the successful characterisation of defects such as RCF[95,107].

1.4.2 Stress corrosion cracking

Stress corrosion cracking (SCC) is prevalent in many different industrial applications, producing a significant loss of mechanical strength with only a small loss of material with defects forming complicated partially-closed branched defects, making it very difficult to detect on casual inspection[17]. The nucleation of a SCC defect can lead to fast fracture failure, with a very swift defect growth rate, or fatigue cracking which is a slower process in which the defect size increases at a slower rate due to the action of cyclic stresses on a component and is therefore detectable prior to component failure[17]. Defects from either mechanism have devastating consequences if they occur in sensitive components, such as in pipelines[108] and nuclear reactors[109].

SCC requires three factors; a susceptible material, a corrosive agent appropriate for the specific material and sufficient tensile stress[17]. There are three different mechanisms by which SCC can occur; active path dissolution, hydrogen embrittlement and film-induced cleavage[17]. All of the SCC mechanisms involve the action of a corrosive agent on the material of the structure, producing a position of weakness within the structure, usually located at a grain boundary or a pre-existing surface imperfection[17].

Active path dissolution occurs along a path of higher corrosion susceptibility, such as a grain boundary, at which corrosive agents can gather, meaning it is easier for corrosion to occur at these positions when compared to the rest of the structure. The action of stress on this form of corrosion acts to open the defect, exposing the internal part of the defect to the corrosive agent, thereby accelerating the corrosion growth[17].

Hydrogen embrittlement is caused by the dissolution of hydrogen atoms into the metal, which is possible as they are far smaller than the atoms of the metal. The hydrogen atoms are drawn to regions of higher stress, such as crack nucleation sites, and the presence of hydrogen impurities at the crack tip acts to embrittle the metal, making cleavage easier and accelerating crack growth[17].

The final mechanism, film-induced cleavage, is common in structures in which a metal is coated with a brittle film, such as a painted pipeline, where a crack that originates in the film layer can continue to propagate into the metal underneath. If the original defect in the film was caused by corrosion then the corrosive process will continue within the metal[17].

The corrosion process can only take place if the correct corrosive agent for the chosen material is present. This can be as simple as the accidental transport of aerated water (introducing CO and CO_2) in a carbon steel pipeline that is only designed to transport pure water. The defect grows from the corrosion site when the material is placed under tensile stress, which can be caused by something as mundane as the vibrations caused by the passage of a fluid through a pipe. This leads to rapid crack growth and component failure, unless the defect can be located early and the part monitored or replaced[17], an example of this is the rapid growth of defects in steam generator tubes carry pressurised steam at high temperatures in pressurised water nuclear reactors[109].

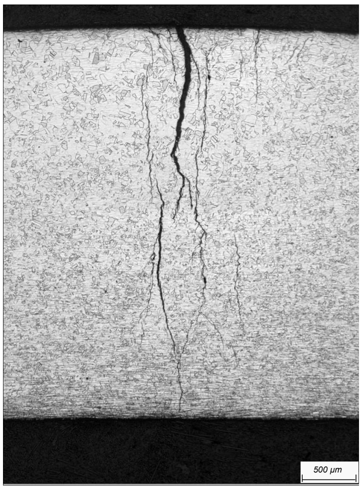

Figure 1.10: Micrograph of SCC defect showing complicated branching nature. Image courtesy of BP.

The methods commonly used to detect SCC defects include acoustic emission (in which a transient ultrasonic wave is locally generated on cracking and can be used to identify the cracking event)[110], eddy current testing (which is only sensitive to near surface defects in conductors)[76], dye penetrant testing (with resulting plant shutdown)[111], radiographic testing (with its associated cost)[51] and ultrasonic testing[112]. Currently the ultrasonic techniques are limited to recording the time of flight diffraction that occurs at the defect[112], however, this is relatively insensitive to defects on the sample surface, driving the need to develop a more reliable ultrasonic technique such as the near-field technique presented in this thesis.

SCC defects form complicated defect structures with many branches of different depths and orientations to the surface, as shown in figure 1.10, which makes the interaction of ultrasound with the defect difficult to interpret. SCC defects have a complicated reflection and transmission character due to the partially-closed nature of the defect and ultrasound will be transmitted through sections of the defect that are closed and reflected by those that are open, this makes it difficult to reliably determine the variation of either coefficient with defect depth, making it challenging to characterise the defect by conventional means[113,114].

With the aim of this thesis being to develop a defect characterisation method using near-field signal enhancements in materials, such as steel and aluminium, that are susceptable to SCC, for applications such as pipelines and storage containers[15,16], it was decided that the interactions should first be studied in the simplest sample geometry, that of a thin plate. Open mouthed v-shaped defects of different depths were machined into thin sheets (thickness between 0.5 mm and 1.5 mm) so as to simulate an open SCC defect in a storage container (see chapters 5 and 6). Artifical calibration defects have been sucessfully used in many applications as a means of understanding the physics of a simplified system prior to testing it on real defects[22,95,104,107,115,116]. The artificial defects used here enabled an understanding of the near-field interactions to be developed, which was then validated for a variety of real defects (chapter 7), using the understanding obtained from the artificial defects.

1.4.3 Laser micromachining for artificial defect manufacture

As a starting point for developing an understanding of the near-field effects, simplified artificial defects were studied without the complicated partially-closed branching structure of real defects. Artificial defect manufacture by laser micromachining uses a high powered laser to produce a narrow, highly accurate cut into the sample material[117,118]. It has the benefit of being a non-contact machining process, and the high laser power acts to vaporise the removed material, giving a smooth clean cut. An automated laser machining system was used to produce the angled v-shaped defects in aluminium bars used in the work presented in chapter 4 and also the v-shaped defects in aluminium sheets used in chapters 5 and 6, by removing sucessive layers of the material until the chosen depth was achieved. The depth of the defect was carefully controlled, so as to produce accurate v-shaped defects that represent the opening mouth of SCC defects of various depths.

Chapter 2

Ultrasonic Inspection

One of the most popular methods of non-destructive testing involves the use of ultrasound, which can be exploited in many different ways to provide a large amount of information about a material, both on the microscopic and macroscopic scale. Many fundamental characteristics of a material can be determined through the study of the propagation of ultrasound through the sample, allowing for measurement of quantities such as the elastic constants of the material[119], the dislocation density within the material[120], the average grain structure[121,122] and even the presence of material phase changes[123,124].

For the purposes of non-destructive testing, knowledge of these microscopic quantities can provide valuable insights into why materials undergo deformation and eventual structural failure. An understanding of the microscopic behaviour lends itself to an explanation of macroscopic failure, with changes at the microscopic level often acting as precursors to failure at a larger scale[119,121,125].

Many macroscopic features are also identifiable through the use of ultrasound, and most measurements are achieved through detecting a deviation from the normal propagation behaviour of ultrasound through a material. A few examples of the defects that can be identified through ultrasonic testing include the detection of corrosion damage and wall thickness changes[81,82,126,127], surface and subsurface defects (some examples of which were given in section 1.4)[114,128–130], the loss of the integrity of welded structures[20,131] and the integrity of multi-layered structures[132,133]. An overview of how ultrasound can be used to detect these defects is given in section 2.3. The focus of the work presented here is the detection and characterisation of surface-breaking defects, with the aim of using the changes in ultrasonic propagation to provide information about the defects.

Sound waves are mechanical vibrations that propagate within solids, liquids and gases, and are caused when the constituent particles of the material are forced to vibrate about their equilibrium positions by some external mechanism or force[25,26,79]. When these particles are displaced there arises an internal restoring force that acts to return the displaced particle to its equilibrium position, giving rise to an oscilliatory motion of the material[25]. The particle motion is transmitted from place to place by the deformation of the material and the resulting disturbance is described as a wave that propagates through the material[6,25,26,134].

The wave motion will experience resistance to its propagation in the form of the resistance of the material to deformation, the internal restoring force, and in the form of the resistance to motion from the inertia of the atoms, both of which must be overcome by the wave for a successful propagation[134]. The wave transfers energy, in the form of kinetic and potential energy, through the material as the motion is passed between adjacent particles, and is not a motion of the entire medium itself.

The deformable nature of the material prevents a localised force from acting on the entire material at once, which would act to give a net force to all atoms in the material, and in fact allows for the influence of the force to propagate through the material at a given speed. This gives the ultrasonic wave velocity which is not instananeous, as the resistance to motion away from the equilibrium point due to the inertia of the atoms prevents the wave from travelling instantaneously from the point of disturbance to the furthest point in the material[134]. Whilst these phenomena act to propagate the wave whilst the external stimulus is applied, once it is removed they act to reduce the propagation of the wave until the particles again regain a position of equilibrium, at which point the sound wave will no longer propagate. For a wave propagating through a material, the co-ordinated motion of the particles is such that a frequency and wavelength can be associated with the disturbance.

The term ultrasound describes sound waves with frequencies above the level of human hearing, which is the range above 20 kHz[26]. There are many different forms of ultrasonic wave that can propagate through a material, each with different particle motions, wave velocities and propagation characteristics. The propagation of a given wave is influenced by the generation method and the nature of the material through which the wave is propagating.

2.1 Waves in elastic media

The following section introduces several different types of bulk and surface ultrasonic waves that are used in the work presented in this thesis. A description of the mathematics that drive each wave is given for longitudinal and shear bulk waves, and Rayleigh and Lamb surface waves, as these are the most relevant to this work[25,26,89,134,135].

2.1.1 Elastic behaviour of materials

To produce a mathematical framework for the understanding of the time-variant oscillations within the material, a relationship between the material deformation and the restoring forces that act to return the material to equilibrium is required, and this allows the definition of what is meant by an elastic material. This provides an understanding of how the material will react under the deformative action of an external force.

For the case of three dimensional elastic solids (a description that is adequate for all of the test materials studied in this work) the deformation of a material is described through the material strain, $\underline{\underline{\epsilon}}$, and the restoring forces are described by the stress, $\underline{\underline{\sigma}}$, which are both tensor quantities. When using rectangular cartesian co-ordinates (x, y, z) these tensors are[25,134],

$$\underline{\underline{\epsilon}} = \begin{pmatrix} \epsilon_{xx} & \epsilon_{xy} & \epsilon_{xz} \\ \epsilon_{yx} & \epsilon_{yy} & \epsilon_{yz} \\ \epsilon_{zx} & \epsilon_{zy} & \epsilon_{zz} \end{pmatrix} , \tag{2.1}$$

$$\underline{\underline{\sigma}} = \begin{pmatrix} \sigma_{xx} & \sigma_{xy} & \sigma_{xz} \\ \sigma_{yx} & \sigma_{yy} & \sigma_{yz} \\ \sigma_{zx} & \sigma_{zy} & \sigma_{zz} \end{pmatrix} . \tag{2.2}$$

The first index of the stress tensor components in equation 2.2 indicates the direction in which the stressing force acts, and the second describes the direction of the normal to the surface on which the force acts[26]. So, for example, the component σ_{zx} represents a force in the z direction that acts normal to the zy plane.

The stress is a measure of the force that is applied to a face of the material, and this can be applied either normally to the surface to produce a compressional stress or tangentially to produce a shear stress[26,134]. For a chosen component of the stress tensor, e.g. $\sigma_{xx} = \frac{F_x}{A_x}$, F_x is the force applied in the x direction onto the yz plane that is perpendicular to F_x, with area A_x. This applied stress introduces a localised displacement of the material, giving the material strain $\underline{\underline{\epsilon}}$, which produces a small particle displacement, u, in a given direction that moves the particle away from its equilibrium position. This is the equivalent of a small extension of the original material dimension, so that $\epsilon_{xx} = \frac{du_x}{dx}$. For small strains this displacement is linear and an example of a off-diagonal component of the strain tensor is $\epsilon_{xz} = \frac{1}{2}(\frac{\partial u_x}{\partial x_z} + \frac{\partial u_z}{\partial x_x})$, where u_x is a displacement in the x direction. The complete stress tensor provides all of the information necessary to describe the internal forces acting within the material, and the strain tensor provides a similarly complete set of information on the possible changes of the internal dimensions of the material[26,134].

To preserve the static equilibrium of the material, the tensile stresses along any axis must balance, as must the shear stresses, so as to avoid acceleration and rotation of the body respectively[25]. This makes the stress tensor symmetric, leading to only three diagonal and three off-diagonal stresses, allowing the stress tensor in equation 2.2 to be rewritten in terms of six independent components. The same argument is applied to the strain tensor in equation 2.1, again giving only six independent components. The symmetry of the tensors further enables the use of a single subscript rather than the original two, and this reduced notation is given in table 2.1[25]. The reduced notation allows the equations to be rewritten in the following form, in which the factors of 1/2 are introduced to simplify later equations,

$$\underline{\underline{\epsilon}} = \begin{pmatrix} \epsilon_{xx} & \epsilon_{xy} & \epsilon_{xz} \\ \epsilon_{yx} & \epsilon_{yy} & \epsilon_{yz} \\ \epsilon_{zx} & \epsilon_{zy} & \epsilon_{zz} \end{pmatrix} = \begin{pmatrix} \epsilon_1 & \frac{1}{2}\epsilon_6 & \frac{1}{2}\epsilon_5 \\ \frac{1}{2}\epsilon_6 & \epsilon_2 & \frac{1}{2}\epsilon_4 \\ \frac{1}{2}\epsilon_5 & \frac{1}{2}\epsilon_4 & \epsilon_3 \end{pmatrix} \quad , \tag{2.3}$$

$$\underline{\underline{\sigma}} = \begin{pmatrix} \sigma_{xx} & \sigma_{xy} & \sigma_{xz} \\ \sigma_{yx} & \sigma_{yy} & \sigma_{yz} \\ \sigma_{zx} & \sigma_{zy} & \sigma_{zz} \end{pmatrix} = \begin{pmatrix} \sigma_1 & \frac{1}{2}\sigma_6 & \frac{1}{2}\sigma_5 \\ \frac{1}{2}\sigma_6 & \sigma_2 & \frac{1}{2}\sigma_4 \\ \frac{1}{2}\sigma_5 & \frac{1}{2}\sigma_4 & \sigma_3 \end{pmatrix} \quad . \tag{2.4}$$

The simplification of these tensors makes the calculation of subsequent quantities easier and allows for a more compact set of equations. For small deformations that are below the elastic limit, caused by the stress forces, Hooke's law can be used[25,89,134]. This states that the stress is linearly proportional to the strain in the material, and therefore each component of the stress can be written as a general linear function of all of the strain components[25], giving a general relationship as:

$$\sigma_{ij} = c_{ijkl}\epsilon_{kl} \quad , \tag{2.5}$$

where $i, j, k, l = x, y, z$, and a summation is taken over repeated subscripts using standard reduced notation[25]. The term c_{ijkl} is a component of a 4^{th} rank tensor, whose components are the elastic constants of the material[25]. The elastic constants are the microscopic analogy of the macroscopic spring constants usually considered in Hooke's law, and describe the relationship between the applied stress and the resulting strain on a material[25].

Table 2.1: A table showing the abbreviated subscript notation for simplifying tensors.

Reduced notation (I)	Long-hand notation (ij)
1	xx
2	yy
3	zz
4	yz, zy
5	xz, zx
6	xy, yx

Each elastic constant gives a measure of the stiffness of the structure; i.e. its resistance to deformation, and simplifications of the full tensor can be achieved for certain material conditions[26]. The elastic coefficients have small values for easily deformed materials or material directions, and large values for rigid structures or directions in which it is difficult to deform the material[25]. It is not necessary to find each of the 81 possible elastic constants to fully understand a material as they are not all independent, and it can be shown that the elastic constants can be represented by at most 36 independent coefficients[25].

The symmetry of the stress tensor components ($\sigma_{ij} = \sigma_{ji}$) means that some of the terms linking the strain and the elastic constants are equivalent, such as $c_{xyxy}\epsilon_{xy} = c_{yxxy}\epsilon_{xy}$ and similarly $c_{xyxy}\epsilon_{xy} = c_{xyyx}\epsilon_{yx}$[25], thereby giving the conditions $c_{ijkl} = c_{jikl}$ and $c_{ijkl} = c_{ijlk}$. This enables the use of the reduced notation that was given in table 2.1, allowing the elastic constants for a general case to be written as[25,26];

$$\underline{\underline{c}} = \begin{pmatrix} c_{11} & c_{12} & c_{13} & c_{14} & c_{15} & c_{16} \\ c_{21} & c_{22} & c_{23} & c_{24} & c_{25} & c_{26} \\ c_{31} & c_{32} & c_{33} & c_{34} & c_{35} & c_{36} \\ c_{41} & c_{42} & c_{43} & c_{44} & c_{45} & c_{46} \\ c_{51} & c_{52} & c_{53} & c_{54} & c_{55} & c_{56} \\ c_{61} & c_{62} & c_{63} & c_{64} & c_{65} & c_{66} \end{pmatrix} . \tag{2.6}$$

The elastic constants tensor is further reducible depending on additional restrictions imposed by the microstructure of the material in question, with many of the components being equal to zero in an isotropic material[25,26,134]. In an isotropic medium, such as a metal, the three co-ordinate axes (x, y, z) are equivalent, and the planes xy, xz and yz are equivalent. Therefore, the response of the material to any compressive stress must be the same if it is applied along any axis, therefore, $\epsilon_{11} = \epsilon_{22} = \epsilon_{33}$, and $\epsilon_{12} = \epsilon_{13} = \epsilon_{23}$, and similarly the response to any shear stress is the same for all planes, as $\epsilon_{44} = \epsilon_{55} = \epsilon_{66}$[25].

If a compressive stress σ_1 is applied along the x axis to produce a shear strain, ϵ_6, in the xy plane of an isotropic material, it is equivalent to the same stress applied to the material after it is rotated by 180° about the x axis (but with the sign of ϵ_6 reversed), otherwise the material would be forced to rotate about this axis. For this to hold true, $\epsilon_{16} = 0$, which in turn means that, $\epsilon_{14} = \epsilon_{15} = \epsilon_{16} = \epsilon_{24} = \epsilon_{25} = \epsilon_{26} = \epsilon_{34} = \epsilon_{35} = \epsilon_{36} = 0$, by the same argument so that no rotation of the material occurs due to a shear stress about any plane. This is also true for stresses applied to planes to give $\epsilon_{45} = \epsilon_{46} = \epsilon_{56} = 0$. In addition, the fulfilment of the elastic isotropic condition for an arbitrary rotation of the stiffness matrix about the z and y axis,

$$c_{12} = c_{11} - 2c_{44} \quad , \tag{2.7}$$

makes the stiffness matrix invariant with respect to this rotation[25]. These conditions give a simplified set of nonzero elastic coefficients for an isotropic elastic medium of:

$$\underline{\underline{c}} = \begin{pmatrix} c_{11} & c_{12} & c_{12} & 0 & 0 & 0 \\ c_{12} & c_{11} & c_{12} & 0 & 0 & 0 \\ c_{12} & c_{12} & c_{11} & 0 & 0 & 0 \\ 0 & 0 & 0 & c_{44} & 0 & 0 \\ 0 & 0 & 0 & 0 & c_{44} & 0 \\ 0 & 0 & 0 & 0 & 0 & c_{44} \end{pmatrix} \quad . \tag{2.8}$$

The elastic isotropic condition (equation 2.7) shows that the elastic behaviour of an isotropic material can in fact be described through only two elastic constants, which are the Lamé parameters $\lambda = c_{12}$ and $\mu = c_{44}$, which can be shown to be directly related to the velocities of longitudinal and shear bulk waves.

2.1.2 Propagation of ultrasonic bulk waves

To derive the characteristic velocities of longitudinal and shear bulk waves the equation of motion for waves propagating in a solid medium must first be defined[25,26,89,134–137]. In three dimensions the wave equation can be derived by combining equation 2.5 with the following expression of Newton's second law (in which ρ is the material density) that links the stress, σ_{ij}, to the particle displacement, u_i[136,137];

$$\sum_j \frac{\partial \sigma_{ij}}{\partial x_j} = \rho \frac{\partial^2 u_i}{\partial t^2} \quad . \tag{2.9}$$

From the elastic relations given in section 2.1.1, equation 2.5 can be rewritten in terms of the relevant elastic constants and the particle displacements, giving the following equation, where $\epsilon = \epsilon_{11} = \frac{\partial u_x}{\partial x}$ and δ_{ij} is the Kronecker delta[26];

$$\sigma_{ij} = (c_{11} - 2c_{44})\, \epsilon\, \delta_{ij} + 2c_{44}\, \epsilon_{ij} \quad , \tag{2.10}$$

where the indicies of the elastic constants are expressed in reduced notation. The expression $\epsilon_{ij} = \frac{1}{2}(\frac{\partial u_i}{\partial x_j} + \frac{\partial u_j}{\partial x_i})$ given previously is also required, where the necessity of the factor of 1/2 is now evident. Equation 2.10 can be substituted into equation 2.9 to give an equation of motion of[26,137],

$$\rho \frac{\partial^2 u_i}{\partial t^2} = \frac{\partial}{\partial x_i}[(c_{11} - 2c_{44})\frac{\partial u_i}{\partial x_i}] + c_{44}\frac{\partial^2 u_i}{\partial x_i^2} + c_{44}\frac{\partial}{\partial x_i}(\frac{\partial u_i}{\partial x_j}) \quad . \tag{2.11}$$

For convenience the equation of motion can be rewritten in vector form, in which the divergence operator is $\vec{\nabla} = (\frac{\partial}{\partial x_i}, \frac{\partial}{\partial x_j}, \frac{\partial}{\partial x_k})$ and the laplace operator is given by $\nabla^2 = (\frac{\partial^2}{\partial x_i^2} + \frac{\partial^2}{\partial x_j^2} + \frac{\partial^2}{\partial x_k^2})$, thereby giving[25,26,89,137],

$$\rho \frac{\partial^2 \vec{u}}{\partial t^2} = (c_{11} - c_{44})\vec{\nabla}(\vec{\nabla} \cdot \vec{u}) + c_{44}\nabla^2 \vec{u} \quad . \tag{2.12}$$

Any vector field, such as the particle displacement, can be written in terms of the gradient of a scalar potential $\vec{\phi}$ and the curl of a vector potential ψ, allowing the particle displacement to be represented by,

$$\vec{u} = \vec{\nabla}\phi + \vec{\nabla} \times \vec{\psi} \quad . \tag{2.13}$$

This can be used to transform equation 2.12 into a form with two separate terms, the first of which is purely a scalar quantity and the second is purely a vector quantity. Separation of this equation shows that, therefore, both parts of the equation must be equal to zero[25,26,89] as equation 2.12 becomes

$$\vec{\nabla}(\rho\frac{\partial^2\phi}{\partial t^2} - c_{11}\nabla^2\phi) + \vec{\nabla}\times(\rho\frac{\partial^2\vec{\psi}}{\partial t^2} - c_{44}\nabla^2\vec{\psi}) = 0 \quad . \tag{2.14}$$

This is the wave equation for waves moving in solid isotropic media, and allows direct identification of two distinct modes. Each part of equation 2.14 describes a different wave type, with the first part describing longitudinal waves, where displacement is in the same direction as the propagation, and the second part describing transverse waves[25,26,89], where displacement is perpendicular to the direction of propagation (described in section 2.1.3). The solution for the wave equation is assumed to be a plane wave, which is described by[25,26,89,137]

$$\vec{u} \;=\; A\;\exp i(\vec{k}.x \;-\; \omega t) \quad , \tag{2.15}$$

where A is a constant, $\vec{k}$ is the unit wave number vector and ω the angular frequency. This solution can be substituted into the wave equation, and an expression that describes the propagation of a plane wave in a freely vibrating medium without a vibrational source present is given (after some manipulation) by[26,89],

$$k^2\Gamma_{ij}u_j - \rho\omega^2 u_i = 0 \quad . \tag{2.16}$$

This equation is the Christoffel equation[25,89], in which Γ_{ij} is known as the Christoffel matrix, which has elements that are functions of the propagation direction of the wave and the elastic constants of the material[25]. This matrix differs between isotropic and anisotropic materials and hence provides information about the propagation of planar waves in different materials. The full form of the Christoffel equation for an isotropic material can be calculated by substituting equations 2.7 and 2.8 into the Christoffel matrix, to give:

$$k^2\begin{pmatrix} c_{44} & 0 & 0 \\ 0 & c_{44} & 0 \\ 0 & 0 & c_{11} \end{pmatrix}\begin{pmatrix} u_i \\ u_j \\ u_k \end{pmatrix} = \rho\omega^2\begin{pmatrix} u_i \\ u_j \\ u_k \end{pmatrix} \quad . \tag{2.17}$$

This formulation defines wave solutions that are dependent on the wave propagation and polarisation directions, allowing for the development of equations to describe shear and longitudinal waves[25]. These are waves that propagate through the bulk of a material and will contribute to the phenomena described in chapter 4.

2.1.3 Shear and longitudinal bulk waves in materials

Both shear and longitudinal waves propagate through the bulk of a solid, with particle displacements relative to the propagation direction that are unique to the wave types. A longitudinal wave has a particle motion in the same direction as the propagation direction of the wave, while shear waves have particle motion perpendicular to the propagation direction of the wave, giving them the freedom to be polarised horizontally, vertically or radially[26]. A description of both of these wave types can be obtained from equation 2.17 for isotropic materials by separating the equation into the three independent equations[25]:

$$k^2 c_{44} u_i = \rho\omega^2 u_i \quad , \tag{2.18}$$

$$k^2 c_{44} u_j = \rho\omega^2 u_j \quad , \tag{2.19}$$

$$k^2 c_{11} u_k = \rho\omega^2 u_k \quad . \tag{2.20}$$

As before, the directions i, j, k correspond to x, y, z respectively in cartesian co-ordinates. Cartesian geometry will be used from this point on so as to aid in the intuitive understanding of wave propagation directions. The first two equations correspond to shear wave modes, which are degenerate, such that they can be combined to produce different wave polarisations, whilst the third equation corresponds to a longitudinal wave mode[25]. From this the phase velocity, which is defined as $v_p{=}\omega/k$, for each wave type is given by:

$$v_L = \sqrt{\frac{c_{11}}{\rho}} \quad , \tag{2.21}$$

$$v_S = \sqrt{\frac{c_{44}}{\rho}} \quad , \tag{2.22}$$

where L corresponds to longitudinal waves and S corresponds to shear waves.

Bulk waves are used in many non-destructive testing applications[25,89], however, for the work presented here they are produced as a by-product of the generation mechanism and are not directly used for characterisation of the defects described in section 1.4. The detection of surface-breaking defects, whilst it has been achieved with bulk waves[80,94,138–140], is improved by the use of a wave mode that is sensitive to changes in the surface conditions of the test material, such as Rayleigh or Lamb surface waves[89].

2.1.4 Surface acoustic waves

Surface acoustic waves propagate along the material surface and must fulfill specific boundary conditions at the surface of the material, whilst also satisfying the wave equation[89]. The work reported in this thesis utilises several different surface acoustic waves, depending on the sample geometry; the Rayleigh wave, the Lamb wave and circumferential waves constrained to the surface of a hollow cylinder[89].

2.1.4.1 Rayleigh waves

Rayleigh waves can be used as a probe of surface-breaking defects on samples where the material thickness is much larger than the ultrasonic wavelength, λ. First identified by Lord Rayleigh in 1885, the Rayleigh wave propagates along the sample surface, with the majority of the energy of the wave confined within a depth of one wavelength from the surface[26,89]. Rayleigh waves are described as free waves on the surface of a semi-infinite half space[89]. The particulate motion is a combination of the motion described for both the longitudinal and shear waves, giving rise to an elliptical particle motion[89]. The boundary conditions for the propagation of a Rayleigh wave in a semi-infinite solid stipulate that the boundary must be traction-free (i.e. there are zero tangential stress components at the material surface) and that the waves must decay with depth[89]. The argument presented by Rose is used here to derive the Rayleigh wave equations[89].

In order to achieve the elliptical surface displacement, the displacements of the Rayleigh wave are purely in the x (parallel to the direction of propagation along the surface) and z (out of the plane of the direction of propagation and of the surface) directions. As was done for bulk waves in equation 2.13, the displacement vector can be split into a scalar (ϕ) and a vector ($\vec{\psi}$) potential using equation 2.13, which represent longitudinal and shear wave components respectively[25,89,135]. This produces Rayleigh wave equations of,

$$\nabla^2\phi - \frac{1}{v_L^2}\frac{d^2\phi}{dt^2} = 0 \quad , \tag{2.23}$$

$$\nabla^2\psi - \frac{1}{v_S^2}\frac{d^2\psi}{dt^2} = 0 \quad . \tag{2.24}$$

As with bulk waves, the proposed solution is a plane wave that propagates with a given wavenumber k and frequency ω[25,26,89]. For the chosen 2D plane wave the displacement in the y direction is zero, and the displacement vector is simply $\vec{u} = (u_x, 0, u_z)$, which in turn gives the functions $\phi = \phi(u_x, u_z, t)$ and $\psi = \psi(u_x, u_z, t)$. This gives the relevant components of the displacement vector as,

$$u_x = \frac{\partial \phi}{\partial x} + \frac{\partial \psi}{\partial z} \quad , \tag{2.25}$$

$$u_z = \frac{\partial \phi}{\partial z} - \frac{\partial \psi}{\partial x} \quad . \tag{2.26}$$

The plane wave solutions have the general format of $\phi = F_1(z) \exp\ i(k\,x - \omega\,t)$ and $\psi = F_2(z) \exp\ i(k\,x - \omega\,t)$, where $F_1(z)$ and $F_2(z)$ are amplitude functions that decay with increasing depth into the sample z. If the general solutions are substituted into equations 2.23 and 2.24, the following solutions are obtained[25,89],

$$\phi = A_1\ \exp\ (-kqz) \exp\ ik(x - vt) \quad , \tag{2.27}$$

$$\psi = B_1\ \exp\ (-ksz) \exp\ ik(x - vt) \quad , \tag{2.28}$$

where $v = \frac{\omega}{k}$, $q = \sqrt{1 - (\frac{v}{v_L})^2}$, $s = \sqrt{1 - (\frac{v}{v_S})^2}$, A_1 and B_1 are arbitrary amplitude constants and v is the velocity of the wave that is being derived[89]. These solutions are substitued into the equations for the displacement components given in equations 2.25 and 2.26 to give the following expressions for the displacements,

$$u_x = k\ (iA_1 \exp(-kqz) - sB_1 \exp(-ksz)) \exp(ik(x - vt)) \quad , \tag{2.29}$$

$$u_z = -\,k(qA_1 \exp(-kqz) - iB_1 \exp(-ksz)) \exp(ik(x - vt)) \quad . \tag{2.30}$$

Expressions can be derived for the tangential and normal stresses from equation 2.10 by using the expressions for material strain in terms of particle displacements, e.g. $\epsilon_{zz} = \frac{\partial u_z}{\partial z}$ and $\epsilon_{xz} = \frac{1}{2}(\frac{\partial u_x}{\partial x_z} + \frac{\partial u_z}{\partial x_x})$, and the particle displacements in equations 2.29 and 2.30. The boundary conditions of the problem state that these stresses must be zero at the material surface ($\sigma_{zz} = \sigma_{xz} = 0$ at $z = 0$), giving,

$$\sigma_{zz} = k^2 G(rA_1 \exp(-kqz) + 2isB_1 \exp(-ksz)) \exp(ik(x - vt)) = 0 \quad , \tag{2.31}$$

$$\sigma_{xz} = k^2 G(-2iqA_1 \exp(-kqz) + rB_1 \exp(-ksz)) \exp(ik(x - vt)) = 0 \quad , \tag{2.32}$$

where $r = 2 - (\frac{v}{v_S})^2$ and G is an arbitrary constant that contains details of the relevant elastic constants. From the boundary conditions it can be seen that $rA_1 + 2isB_1 = 0$ and $-2iqA_1 + rB_1 = 0$. From these equations the two constants can be found to be $A_1 = \frac{-ir}{2q}$ and $B_1 = \frac{-2is}{r}$. A characteristic equation for the propagation of Rayleigh waves can then be obtained as,

$$r^2 \; - \; 4sq \; = \; 0 \quad , \tag{2.33}$$

where r, s and q are all functions of the unknown wave velocity v and this equation can be rearranged to give an expresssion for the Rayleigh wave velocity equation as[89],

$$(\frac{v}{v_S})^6 \; - \; 8(\frac{v}{v_S})^4 \; + \; 8(\frac{v}{v_S})^2(3 \; - \; 2(\frac{v_S}{v_L})^2) \; + \; 16((\frac{v_S}{v_L})^2 \; - \; 1) \; = \; 0 \quad . \tag{2.34}$$

The velocity v here is the Rayleigh surface wave velocity, $v \; = \; v_R$, and from the approximate solution given by Viktorov ($\frac{v}{v_S} \; = \; \frac{(0.87+1.12\nu)}{1+\nu}$ where ν is the Poisson's ratio) for aluminium $v_R \; = \; 2940$ ms^{-1}[89,135,141]. The Rayleigh wave travels at a constant speed and propagates along the material surface, with an amplitude that decreases with increasing depth into the material. The study of the interactions of this particular surface wave with surface-breaking defects is the focus of chapter 4.

2.1.4.2 Lamb waves

Rayleigh waves are waves that are guided along the surface of materials with thicknesses that are much larger than the ultrasonic wavelength, but for thinner plates a different type of surface wave must be considered, where propagation calculations take into account both surfaces of the plate. The rigorous derivation of Lamb waves is an involved process which is well documented[26], and here the approach used by Rose is employed[89].

The governing wave equations for Lamb waves are the same as for the Rayleigh wave, equations 2.23 and 2.24, that describe longitudinal and shear motion. As with Rayleigh waves, the displacement vector is $\vec{u} \; = \; (u_x, 0, u_z)$, and the same boundary conditions for the tangential and normal stresses hold true ($\sigma_{zz} \; = \; \sigma_{xz} \; = \; 0$ at $z \; = \; \pm \; h$). However, now these boundary conditions must be applied at both the top and bottom surfaces of a material of thickness $2h$, where the midpoint of the plate is at $z \; = \; 0$[25,26,89]. This gives the relevent displacements and stresses, as with the Rayleigh wave example in equations 2.25, 2.26, 2.31 and 2.32.

Plane wave solutions are again assumed, taking the form $\phi \; = \; \Phi(z) \exp \; i(k\,x - \omega\,t)$ and $\psi \; = \; \Psi(z) \exp \; i(k\,x - \omega\,t)$, where the functions that depend on the z coordinate describe how the wave changes with depth through the material and must be determined in order to solve the wave equations[89]. The time dependent portion of the plane wave solution, ($\exp \; i(k\,x - \omega\,t)$), which describes the wave travelling in the x direction, is omitted from the following working for simplicity, where the assumed solutions have been substituted into the wave equations for Lamb waves to give expressions for the z-dependent functions of,

$$\Phi(z) \;=\; A_1 \sin(pz) \;+\; A_2 \cos(pz) \quad , \tag{2.35}$$

$$\Psi(z) \;=\; B_1 \sin(gz) \;+\; B_2 \cos(gz) \quad , \tag{2.36}$$

where $p^2 \;=\; \frac{\omega^2}{v_L^2} \;-\; k^2$ and $g^2 \;=\; \frac{\omega^2}{v_S^2} \;-\; k^2$.

The split of the functions into sine and cosine terms, which are odd and even functions about $z = 0$, allows for the wave modes to be split into symmetric and antisymmetic waves, which refer to the wave motion with respect to the mid plane of the plate. If equations 2.35 and 2.36 are substituted into the expressions for the material displacement given in equations 2.29 and 2.30, the following is obtained:

$$u_x = [ik\Phi + \frac{d\Psi}{dz}] \quad , \tag{2.37}$$

$$u_z = [\frac{d\Phi}{dz} - ik\Psi] \quad . \tag{2.38}$$

As the field variables Φ and Ψ contain sine and cosine terms, which are odd and even functions about zero respectively, the displacements can be expressed in terms of functions that are either both even or both odd about the mid plane of the plate.

Symmetric motion about the mid plane of the plate is described for u_x displacements when u_x contains cosine terms, and antisymmtric motion when u_x contains sine terms[89], with the reverse being true for the u_z components. This split is possible due to the symmtery of the plate problem and gives rise to two families of Lamb modes. The displacements of the Lamb waves are therefore given by:

$$u_x = ikA_2 \cos(pz) + qB_1 \cos(gz) \quad , \tag{2.39}$$

$$u_z = -pA_2 \sin(pz) - ikB_1 \sin(gz) \quad , \tag{2.40}$$

for the symmetric waves, and,

$$u_x = ikA_1 \sin(pz) - qB_2 \sin(gz) \quad , \tag{2.41}$$

$$u_z = pA_1 \cos(pz) - ikB_2 \cos(gz) \quad , \tag{2.42}$$

for the antisymmetric waves, where the constants A_1, A_2, B_1 and B_2 are obtained from the solution of the Lamb wave dispersion relation. As for Rayleigh waves the stresses that are zero at the material surfaces, σ_{xz} and σ_{zz}, can be found by substitution of the particle displacements into equation 2.10 to give,

$$\sigma_{xz} = \mu(-2ikpA_2 \sin(pz) + (k^2 - g^2)B_1 \sin(gz)) \quad , \tag{2.43}$$

$$\sigma_{zz} = -\lambda(k^2 + p^2)A_2 \cos(pz) - 2\mu[p^2 A_2 \cos(pz) + ikgB_1 \cos(gz)] \quad , \tag{2.44}$$

for symmetric modes, and,

$$\sigma_{xz} = \mu[2ikpA_1 \cos(pz) + (k^2 - g^2)B_2 \cos(gz)] \quad , \tag{2.45}$$

$$\sigma_{zz} = \lambda(k^2 + p^2)A_1 \sin(pz) - 2\mu[p^2 A_1 \sin(pz) - ikgB_2 \sin(gz)] \quad , \tag{2.46}$$

for antisymmetric modes. The boundary conditions give these stresses as zero at ±h, and as the boundary conditions must be satisfied at both the top and bottom surfaces the Lamb modes are described as standing waves in the transverse direction[89]. This gives for each wave type (symmetric and antisymmetric) a pair of equations both of which have components that are related to two constants, i.e. A_2 and B_1 for the symmetric, and A_1 and B_2 for the antisymmetric[135]. Each system, i.e. symmetric and antisymmetric, only has a nontrivial solution when the determinant of a matrix formed from the components of each constant, i.e.,

$$\begin{bmatrix} -2\mu ikp \sin(ph) & \mu(k^2 - g^2)\sin(gh)) \\ -\lambda(k^2 + p^2)\cos(ph) - 2\mu p^2 \cos(ph) & 2\mu ikgB_1 \cos(gh) \end{bmatrix} \begin{bmatrix} A_2 \\ B_1 \end{bmatrix} = \begin{bmatrix} 0 \\ 0 \end{bmatrix} \tag{2.47}$$

for the symmetric mode, is equal to zero. For the symmetric case this gives a characteristic equation of,

$$-4k^2 pq\mu \sin(ph)\cos(gh) + (k^2 - g^2)(\lambda k^2 + \lambda p^2 + 2\mu p^2)\sin(gh)\cos(gh) = 0 \quad , \tag{2.48}$$

from which, after some manipulation, the following expression for symmetric waves is obtained,

$$\frac{\tan(gh)}{\tan(ph)} = \frac{4k^2 pg\mu}{(\lambda k^2 + \lambda p^2 + 2\mu p^2)(k^2 - g^2)} \quad . \tag{2.49}$$

The denominator can be simplified using the definitions of the longitudinal and shear velocities (equation 2.21), the definition of the Lamé parameters, λ and μ and the elastic isotropic condition (equation 2.7)[89]. This enables the dispersion relation for each mode type to be given as,

$$\frac{\tan(gh)}{\tan(ph)} = -\frac{4k^2pg}{(g^2 - k^2)^2} \quad , \tag{2.50}$$

for symmetric waves[89,135]. The same process can be followed to form a characteristic equation for the antisymmetric waves, and a subsequent manipulation gives a dispersion relation for antisymmetric waves of,

$$\frac{\tan(gh)}{\tan(ph)} = -\frac{(g^2 - k^2)^2}{4k^2pg} \quad . \tag{2.51}$$

The dispersion relations describe the relationships between the frequencies and velocities of the different Lamb modes, but solutions for the actual velocities can only be found numerically[89]. It has been shown for any given frequency that there are an infinite number of wavenumbers that will satisfy equations 2.50 and 2.51, and these can be real, imaginary, or complex, which gives three different possible wavenumber regimes[89]. If the time-harmonic part of the dispersion equation, which was omitted from the calculations above, is considered with a complex wavenumber, $k = k_r + ik_{im}$ then the time harmonic part can be rewritten as,

$$\exp[i(kx - \omega t)] = \exp[i(k_r x - \omega t)]\exp[-k_{im}x] \quad , \tag{2.52}$$

which gives three wavenumber regimes of $k_{im} < 0$, $k_{im} = 0$ and $k_{im} > 0$[89].

The three regimes of k_{im} describe different types of Lamb waves, with the region $k_{im} > 0$ describing evanescent Lamb waves that exponentially decay with distance, such that they are only observed physically in the formation of the near-field region at the point of generation. Some research on experimental applications of these evanescent waves has been performed[142]. The region with $k_{im} < 0$ describes waves that would grow exponentially with distance, which have not been observed experimentally and no further consideration is given to this region. For the purposes of propagating Lamb waves, only the $k_{im} = 0$ regime describes waves that are currently useful for non-destructive testing.

The numerical solution of equations 2.50 and 2.51 for $k_{im} = 0$ is done using a simple procedure[89]. First, a frequency-thickness product and an initial estimate of the phase velocity (which in turn defines the Lamb wave number k) are chosen, and used to evaluate the signs of both sides of equations 2.50 and 2.51. There are multiple possible solutions for the dispersion relations at a given frequency-thickness, and as they are continuous functions as the phase velocity is increased, a sign change

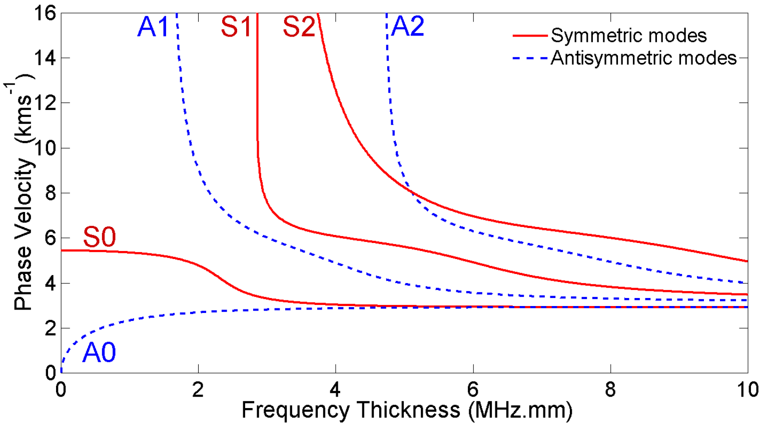

(a) Phase velocity

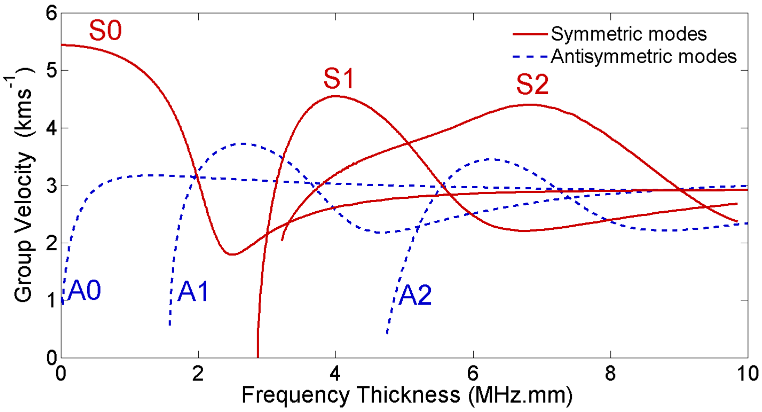

(b) Group velocity

Figure 2.1: Phase (a) and group (b) velocity dispersion curves for Lamb wave modes propagating in flat aluminium plates.

in the left hand side of either equation indicates the existance of a zero-crossing in the function, and hence a root of the equaton will lie at that point. These roots are found by varying the phase velocity away from the initial estimate for a fixed frequency-thickness until the sign change is observed, with the phase velocity here being found to a precision of 0.1 ms^{-1}. The frequency-thickness is then increased and the process repeated until a dispersion curve, such as that shown for aluminium in figure 2.1a, is produced[26,89].

Whilst the phase velocity $v_p = \frac{\omega}{k}$ describes the velocity of propagation of a wavefront of constant phase, and hence the rate at which any single frequency component of the wave moves (i.e. the crest of the wave), a second measure of velocity, the group velocity v_g, exists[25,26]. The group velocity $v_g = \frac{d\omega}{dk}$ describes the rate at which a wave packet propagates through the material, and describes how

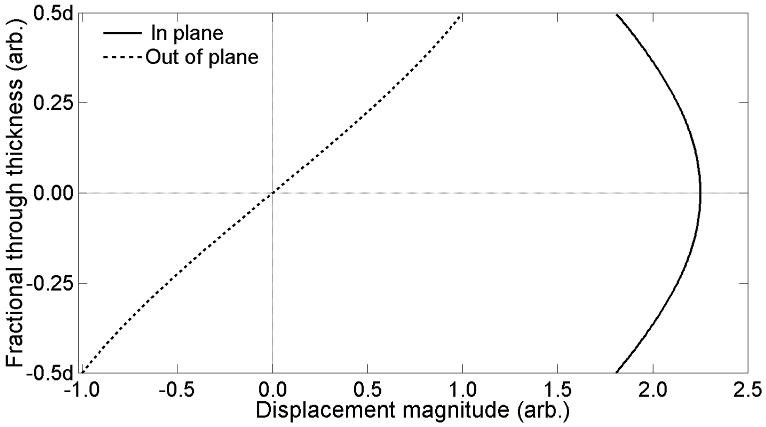

(a) S0 mode

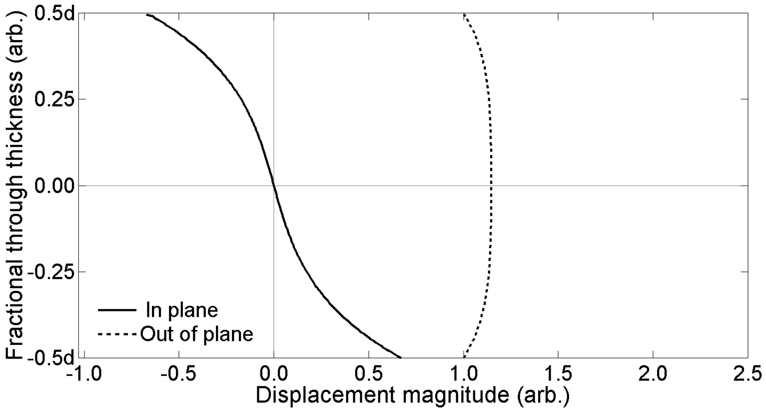

(b) A0 mode

Figure 2.2: In-plane and out-of-plane displacement profiles for the S0 (a) and A0 (b) wave modes at fractional through-thickness positions (where $z = 0$ is the midpoint of the plate) in a 0.5 mm thick aluminium plate at a frequency-thickness of 1.3 MHz.mm.

the packet moves as a whole, whilst the individual peaks that make it up will move at the phase velocity[25,26].

The group velocity of Lamb modes is found by substituting $k = \frac{\omega}{v_p}$ into the expression for $v_g = \frac{d\omega}{dk}$ and rewriting to provide an expression that describes the group velocity, v_g, in terms of the phase velocity v_p and the frequency-thickness product fd (where $d = 2h$), as,

$$v_g = v_p^2 \left[v_p - (fd)\frac{dv_p}{d(fd)} \right]^{-1} \quad . \tag{2.53}$$

The group velocity is shown in figure 2.1b as a function of the frequency-thickness for aluminium. At any given frequency-thickness, there will always exist at least two Lamb wave modes, the fundamental antisymmetric (A0) and symmetric (S0) modes, but the higher order modes will only exist above a cut-off frequency, a feature that has important consequences for the broadband generation of Lamb waves that occurs in chapter 5.

In this thesis the experimentally measured quantity is the out-of-plane surface displacement of the test material as a surface wave propagates through it (see chapter 3), and in order to interpret these results an understanding of the displacent behaviour of Lamb waves is required. The particle displacement profile for each Lamb wave mode varies as a function of position through the thickness of the plate, with the proportion of out-of-plane to in-plane displacement dependent upon the mode chosen, the frequency-thickness and the position in the plate thickness[89]. This gives a different wave structure for each wave mode, and for the detection methods described in section 2.2.6 this will determine the sensitivity of the detection method to the particular wave mode.

The displacement profiles are found from equations 2.39 and 2.40 for the symmetric modes and equations 2.41 and 2.42 for the antisymmetric modes. An example of the displacement distributions is shown in figure 2.2a for the symmetric fundamental mode and in 2.2b for the antisymmetric fundamental mode in a 0.5 mm thick aluminium plate.

2.1.5 Time frequency representations

The ultrasonic signals produced by the laser generation mechanism used for the work presented in this thesis are broadband, and, as such, many different frequencies of ultrasound are generated simultaneously within the test material (see section 2.2.4). This poses an issue for the interpretation of Lamb waves due to the simultaneous generation of several symmetric and antisymmetric wave modes within the material, many of which travel at similar speeds and hence will arrive close together in time at the detector, making it challenging to identify individual modes. In order to identify individual modes, time-frequency analysis is employed to give the arrival times of the individual frequencies[143,144]. Many different time-frequency analysis techniques exist, including the short time Fourier transform (STFT), the wavelet transform and the Hilbert transform[145,146]. The time frequency approach that is employed in this thesis is the spectrogram, which is also known as the sonogram, and it is a form of STFT[145,147].

In a STFT an A-scan, which shows the amplitude of a wave as a function of time (see the bottom panel of figure 2.3), is divided up into many smaller time segments of equal size and a Fourier transform is performed on each segment, this enables the frequency content in each time segment of the A-scan to be known. A windowing function, such as a Gaussian window, is applied to each time segment to give a weight to the data in that window, whilst making data outside of the window negligible. The time-frequency resolution of a STFT is limited by a trade-off between the time and frequency precision, which is caused by the choice of the size of the time window that was used to divide the data[147]. If the signal is divided into time segments that are too small (which would give a good resolution in time), then the Fourier transform of each segment becomes meaningless, giving an inherent trade-off between the time and frequency resolution that can be achieved with this method.

Let the unmodified A-scan signal be given by $s(\tau)$. To focus on a portion of the signal it is multiplied by a windowing function, $h(\tau - t)$, centered around the time of interest and with a chosen length in time. Data that falls outside of this window becomes negligible, giving a windowed series, $s_t(\tau)$, as;

$$s_t(\tau) = s(\tau)h(\tau - t) \quad . \tag{2.54}$$

The Gabor transform used for the work in this thesis is a type of STFT that uses a Gaussian window to ensure only the data at the time of interest is significant, and the data outside of the window becomes negligible. After a Fourier transform of the windowed section, the frequency spectrum will reflect the frequency distribution in the region around the chosen time, t, as,

$$S_t(\omega) = \frac{1}{\sqrt{2\pi}} \int e^{-i\omega t} s(\tau)h(\tau - t)d\tau \quad , \tag{2.55}$$

from which an energy density spectrum, i.e. the sonogram data, can be obtained using,

$$|S_t(\omega)|^2 = \left| \frac{1}{\sqrt{2\pi}} \int e^{-i\omega t} s(\tau)h(\tau - t)d\tau \right|^2 \quad . \tag{2.56}$$

The energy density spectrum shows how the energy in a wave form is distributed between each frequency, giving a representation of the distribution of energy between the different Lamb wave modes. A sonogram is then produced by displaying the energy density spectrum for each time interval, allowing the arrival times of individual frequency components to be resolved, with an example shown in figure 2.3 for a Lamb wave propagating in a defect free aluminium plate of 1.5 mm thickness, in which the sonogram is produced with a small overlap between each time segment to smooth the appearance of the data and ensure no discontinuities are present. The

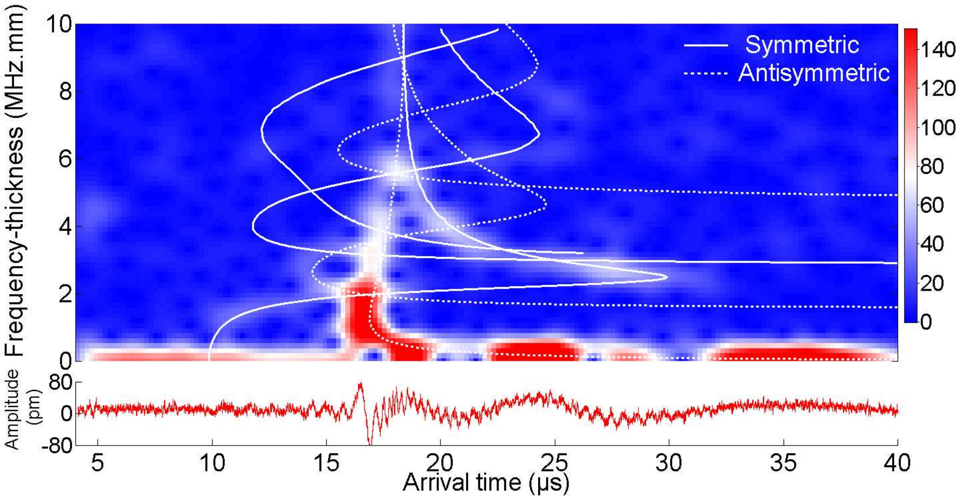

Figure 2.3: Sonogram data for laser generated Lamb waves in a 1.5 mm thick plate, with theoretical wave mode arrival times overlaid. The colour scale shows the energy density of the sonogram.

A-scan from which the sonogram is calculated is shown in the lower panel of figure 2.3 and is a good example of the complicated multimodal Lamb wave data produced by the broadband source.

The theoretical arrival times for the lower order Lamb waves, calculated from the Lamb wave group velocities from equation 2.53 for a fixed propagation distance, are also shown on the image to provide a guide to the observed frequency features. Several different wave modes are evident in figure 2.3 with the waves that possess a higher out-of-plane displacement at the material surface having a more visible presence, due to the laser detection method outlined in section 2.2.6. The ability to separate individual wave modes from a complicated time series is shown to be invaluable in chapters 5 and 6.

2.1.6 Waves in cylindrical pipes

A common industrial implementation of NDT is the detection of defects within pipework[17,108], and to this end an understanding of the ultrasonic waves that can exist within a hollow cylinder is essential. There are two different wave types that are supported within a hollow cylinder; circumferential waves and longitudinal waves, which are subdivided into longitudinal axisymmetric modes and longitudinal flexural modes[89]. Due to the circumferential scan geometry that is used to examine pipework sections in this thesis (see section 7.2), the wave modes

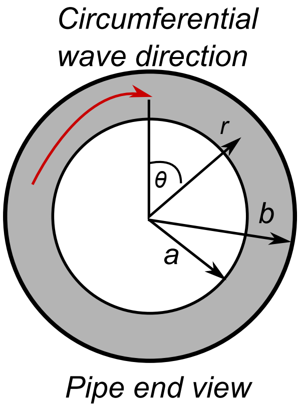

Figure 2.4: Cross-section of a cylinder with inner radius a and outer radius b, showing the direction of propagation of the circumferential wave mode. The cylindrical co-ordinate system is also shown, with the z-axis being into the page.

of interest for this work are primarily the circumferential modes, the derivation of which is outlined here[89]. The geometry of the circumferential wave problem is shown in figure 2.4.

Consider time harmonic waves that propagate in the circumferential direction, θ, of the (r,θ) plane (as shown in figure 2.4), with no dependence on the axial direction (i.e. independent of the z component). This allows the displacement components in the r and θ directions to be defined as,

$$u_r = \frac{\partial \phi}{\partial r} + \frac{1}{r}\frac{\partial \psi}{\partial \theta} \quad , \tag{2.57}$$

$$u_\theta = \frac{1}{r}\frac{\partial \phi}{\partial r} - \frac{\partial \psi}{\partial r} \quad , \tag{2.58}$$

which are obtained by eliminating the z components from the wave equations when these are written in terms of cylindrical components[89]. Both ϕ and ψ satisfy the wave equations in cylindrical co-ordinates,

$$\left(\frac{\partial^2}{\partial r^2} + \frac{1}{r}\frac{\partial}{\partial r} + \frac{1}{r^2}\frac{\partial^2}{\partial \theta^2}\right)\phi + \frac{\omega^2}{v_L^2}\phi = 0 \quad , \tag{2.59}$$

$$\left(\frac{\partial^2}{\partial r^2} + \frac{1}{r}\frac{\partial}{\partial r} + \frac{1}{r^2}\frac{\partial^2}{\partial \theta^2}\right)\psi + \frac{\omega^2}{v_S^2}\psi = 0 \quad . \tag{2.60}$$

The solution of these waves requires the use of traction-free boundary conditions on the inner $(r = a)$ and outer $(r = b)$ radii such that the stress components $\sigma_{rr} = \sigma_{r\theta} = 0$ at these positions. The solution for circumferential waves can be found by considering harmonic wave solutions of the form:

$$\phi = \Phi(r) \exp i(kr\theta - \omega t) \quad , \tag{2.61}$$

$$\psi = \Psi(r) \exp i(kr\theta - \omega t) \quad , \tag{2.62}$$

where k is an angular wavenumber and $\Phi(r)$ and $\Psi(r)$ are functions that are only dependent on the radius. These solutions are substituted into equations 2.59 and 2.60 to give a pair of general solutions of the form:

$$\Phi(r) = C_1 J_{kb}\left(\frac{\omega r}{v_L}\right) + C_2 Y_{kb}\left(\frac{\omega r}{v_L}\right) \quad , \tag{2.63}$$

$$\Psi(r) = D_1 J_{kb}\left(\frac{\omega r}{v_S}\right) + D_2 Y_{kb}\left(\frac{\omega r}{v_S}\right) \quad , \tag{2.64}$$

in which J and Y are Bessel functions of the first and second kind[148]. These equations are substituted into expressions for the stress components σ_{rr} and $\sigma_{r\theta}$, and the boundary conditions applied. This process provides a series of four linear equations; the constants C_1, C_2, D_1 and D_2, can then be found by setting the determinant of these four equations to zero[89]. From this the angular phase velocity α is found to be

$$\alpha = \frac{\omega}{kb} \quad , \tag{2.65}$$

which in turn allows for the determination of a linear phase velocity at a given radius from,

$$v_p = r\alpha = (\omega/k).(r/b) \quad . \tag{2.66}$$

This produces wave solutions, with a dispersion curve shown in figure 2.5, that are similar to those seen in figure 2.1a for flat plates. At low frequencies the dispersion curves for Lamb waves in plates and the circumferential waves differ. However, at higher frequencies, such as those used in the experiments reported in section 7.2, the lower-order circumferential waves converge to something similar to the A0 and S0 Lamb waves in a plate. This enables the same data processing approach for finding near-field enhancements to be used for both scans on pipework samples and on Lamb wave supporting plates, as shown in section 7.2.

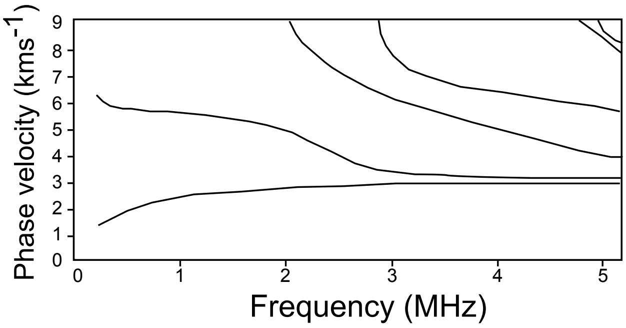

Figure 2.5: Dispersion curves for the lower-order circumferential modes in an aluminium cylinder. Image taken from[89].

2.2 Ultrasonic techniques

There are many different techniques that have been developed to generate and detect ultrasound, and these are broadly categorised into contact and non-contact methods. Contact methods, such as piezoelectric transducers[25], have the advantages that they are simple to implement, are capable of producing large wave amplitudes within a material and are often inexpensive to implement. Contact transducers require impedance matching through the use of a couplant between the transducer and the test material, which can lead to variations in the coupling efficiency. The need for couplant also makes the use of contact measurements on moving samples difficult, although it is possible with the use of wheel probes[149], and samples that are at elevated temperatures can preclude the use of liquid couplants[150].

Becoming more common in non-destructive testing is the use of non-contact ultrasonic generation and detection methods, such as laser ultrasonics, electromagnetic acoustic transducers (EMATs) and air coupled transducers, that are capable of generating and detecting ultrasound without physical contact with the material under test. Non-contact approaches offer significant advantages for many industrial applications, in particular those that are carried out at speed or in hazardous environments (such as at elevated temperatures or pressures), or in which contact with the material would cause damage to the transducer, sample or the inspector[151].

2.2.1 Piezoelectric transducers

A common contact ultrasonic technique for both generation and detection is the piezoelectric transducer, which operates by the piezoelectric effect[25–27]. In some materials, Hooke's law (as given in equation 2.5) does not fully describe the behaviour of the material under applied stress, and in piezoelectric materials the displacement of atoms by acoustic strain (following an applied stress) gives rise to electrical dipoles that combine to give a net electrical polarisation between opposite faces of the material[25]. It follows also that the presence of an externally applied electric field will produce the inverse effect and provide a piezoelectric strain within the material[25]. Examples of piezoelectric materials include quartz (SiO_2) and lead zirconate titrate (PZT). The coupling between the electrical field and the acoustic field forms the basis for generation and detection by piezoelectric materials, with full mathematical derivations avaliable in many standard texts[25,26].

The acoustic impendance of a material describes its resistance to the propagation of an acoustic wave, and large reflections of ultrasonic waves occur at interfaces with large differences in impedance. The impendence of air is very high (415 Nsm^{-3}) and the introduction of a couplant, with an impendence close to that of the material under test, between the transducer and the test material acts to avoid large losses in the ultrasound delivered into the material, such as would occur for an air gap between the transducer and the material[79]. Coupling can be achieved through water or other viscous liquids and also through dry couplants such as adhesive resins[26,79,152]. Issues can arise from poor contact between the transducer and the sample if the couplant is not evenly distributed or has poor impedance matching between the transducer and sample.

Although not all waves can be generated by piezoelectric techniques, it is possible to generate many different types of acoustic wave, including shear, longitudinal, Rayleigh waves and Lamb waves[26,79,153–155]. However, the generation of these modes may involve complicated transducer geometries with, for example, the generation of Rayleigh waves requiring the use of an angled wedge to mode convert longitudinal waves produced at the transducer into Rayleigh waves that propagate in the test material[79]. Recent developments in growing thin film piezoelectric transducers have enabled the use of small, permanently positioned transducers[150]. As the piezoelectric material itself is the active element, the spatial resolution of a transducer is dictated by the size of the piezoelectric element, and it can be challenging to achieve small spatial resolutions.

Contact piezoelectric techniques are not used in the work contained in this thesis as the scanning nature of the experiments, as described in section 3.1, precludes the use of physically attached transducers. The near-field observations performed for the work in this thesis require a high spatial resolution, on the order of 50 μm, and the manufacture of piezoelectric transducers of this size is difficult. The focus of this work therefore is on non-contact methods.

2.2.2 Air coupled transducers

One non-contact ultrasonic generation and detection method is the air coupled transducer, which uses the air itself between the transducer and the sample transfer the ultrasonic wave[26,156]. This approach is preferable to contact methods if the material is particularly absorbant to liquid couplants, for example water couplant which may damage fragile surfaces, or if the test sample is in motion. Although piezoelectric air coupled transducers have been used they are limited to low frequency operation due to the high attenuation of ultrasound in air and they are only sensitive to high amplitude waves[157]. An alternative approach known as capacitative micromachined ultrasonic transducers is preferred[26,157,158]. These devices possess an air gap sandwiched between a flexible dielectric membrane and a conducting back plate that is excited by a transient voltage applied between the membrane and the conducting backing plate. This produces a vibration of the membrane which is transferred to the air in front of the transducer, producing an ultrasonic beam that can be focussed at a test sample[157,158]. Ultrasound production in the test material follows a similar process to that used when water is the transmission medium in ultrasonic immersion testing[26,79], in which the ultrasonic vibrations are transmitted into the test material without requiring any direct contact[156,157].

Detection with an air coupled transducer involves the incident ultrasonic wave forcing the membrane into motion whilst a DC bias is applied, producing a dynamic response in the capacitative system[157]. Air coupled transducers such as these are operated at a resonance such that they achieve an acoustic impedance that is very close to that of air, helping to reduce the strong attenuation experienced in air[26]. Air coupled transducers are cheap to manufacture and can be used to generate both bulk and surface acoustic waves, and they have been used for many different non-destructive applications[91,156–159], however as with piezoelectric transducers the spatial resolution is insufficient for use in the near-field inspections carried out in this thesis.

2.2.3 Electromagnetic acoustic transducers

Electromagnetic acoustic transducers are a non-contact non-destructive inspection method that can be used to inspect materials that are electrically conductive and/or magnetic, making them ideal for inspection of metals such as steel or aluminium[6,27,28]. EMATs utilise the Lorentz force and magnetostriction phenomena to generate and detect ultrasound[28].

An EMAT probe consists of a coil of wire (which can take different configurations depending on the wave generation desired) that is brought close to the surface of the test material, with a typical lift-off of up to a few millimetres[28]. An alternating current is pulsed in the coil at an ultrasonic frequency, which in turn produces a dynamic magnetic field which can penetrate into the test material; the induction of the magnetic field is caused by the coupling between electric and magnetic fields described by Maxwell's equations[160]. The dynamic magnetic field penetrates into the sample and generates a mirror current that will flow in the surface of the test material; this current is constrained to a shallow skin depth[28,160].

In addition to the magnetic field created by the current carrying wire, a permanent magnet (or alternatively an electromagnet) may be positioned above the coil of wire, such that the static magnetic field is aligned perpendicular or parallel to the flow of the mirror current. Generation is also possible with no magnet present or with the addition of a ferrite core within the coil[28]. A moving charged particle experiences a force in the presence of a magnetic field via the Lorentz mechanism[28], and this exerts a force on the electrons of the mirror current. The moving electrons transfer this force to the nuclei of the material, and the force acts as an ultrasonic stress, allowing the propagation of an ultrasonic wave in the material[28]. The shape of the current carrying coil and of the magnet used dictates the nature of the force produced in the sample and various wave types can be produced, including shear waves, longitudinal waves and surface waves[28].

Detection of ultrasound can either be carried out by the same coil or with a dedicated detector coil. For detection a static magnetic field is applied, that exerts a Lorentz force on the electrons that orbit the atoms of the material which are oscillating due to the passage of the ultrasonic wave. This Lorentz force produces an eddy current in the local electrons which in turn induces an image current in the coil of the detection EMAT by the same process as for generation of the mirror current in the sample. The current induced in the detection coil is a measure of the particle velocity within the material[161]. The detected signal is often of relatively low strength and amplification is required for most applications. For a linear coil, changing the direction of the detector magnetic field relative to the direction of ultrasonic propagation allows EMATs to probe the in-plane (for a magnetic field perpendicular to the surface) and out-of-plane (for a magnetic field parallel to the surface) components of a wave[28].

A secondary mechanism is also present when EMATs are used on ferromagnetic materials, the magnetostrictive effect, in which the presence of an external magnetic field causes a change in the dimensions of the material as the magnetic domains within the material rotate to align with the field, with a corresponding stress field being generated[28]. Although recent research has shown the magnitude of this effect to be not as large as previously thought, its influence can still make EMAT inspection preferable to other alternatives for ferromagnetic materials[162,163].

EMATs have found a multitude of uses in many different applications, including using Rayleigh waves to gauge defect depths[164], using shear harmonic waves to detect defects in pipelines[165] and for the detection of defects in rail lines[102]. However, the limited lift-off distances and the restriction to experiments on electrically conducting and/or magnetic materials means that they are not suitable for all applications. The spatial resolution of an EMAT is dictated by the width of the coil profile on the sample surface and therefore the spatial resolution that can be achieved with a laser spot is likely to be significantly higher, making laser inspection better suited for high resolution near-field inspection of defects. It should be noted that near-field enhancements have previously been reported for scanned EMAT experiments for Rayleigh waves, however, the narrow EMATs used to achieve a good spatial resolution tend to be less efficient at generation of ultrasound and as a large amount of averaging is required the scanning process is slow[86].

2.2.4 Laser generation of ultrasound

The research presented in this thesis was carried out using optical methods to generate and detect ultrasound, using a scanning configuration that takes advantage of the high spatial resolution and non-contact nature of laser ultrasonics. The subject of laser ultrasonics has been divided into the theory of generation and detection of ultrasound, with more details on the specific experimental setups used in this work provided in chapter 3.

Generation of ultrasound by laser irradiation has many advantages over other techniques due to the remote nature of the method[166]. Laser ultrasound is a non-contact method with both generation and detection lasers able to be positioned at distances on the scale of centimetres to metres away from the test material. This is a particular advantage when access to the test material is restricted or if the material under inspection is at an elevated temperature or in a hazardous environment[10].

There is, however, a risk associated with the use of laser radiation for generation, both for the material under test and for the operator themselves. Safe operation of laser inspection equipment in a laboratory environment requires the use of protective filtered glasses of a rating appropriate to the laser wavelength and power being used, and care has to be taken to ensure that no sensitive material comes into contact with the laser beam. In an industrial setting steps must be taken to shield the general environment from the laser radiation as it may be impractical to supply eye-protection for all workers. Consideration must also be given to how the incident laser beam will interact with the material under test, as an inappropriate choice of incident power or wavelength will lead to undesirable surface damage, the effects of which can include material ablation, plastic deformation and formation of cracks[27]. The cost of laser ultrasonics is considerably higher than for other non-contact methods, such as EMATs and air coupled transducers, however, the benefits make it suitable for consideration as a scanable non-contact system.

For a low laser power the interaction with the material surface occurs in the thermoelastic regime, in which the laser impact causes rapid localised heating of the material, without the material being melted. At high laser powers the irradiated material is melted to form a plasma, damaging the surface, and this is known as the ablative energy regime. The thermoelastic regime is the power regime required for NDT[166]. The following discussion uses a model in which localised heating by the incident laser radiation gives rise to the production of thermoelastic stresses and strains within the material, producing an ultrasonic wave[27,85,166–168].

In this work laser generation of ultrasound is performed using a pulsed Nd:YAG laser, of infrared wavelength 1064 nm, with an energy per pulse of 144 mJ, a pulse width of 10 ns, and a pulse rise time of 10 ns that was fired at a rate of 2.7 Hz[95,169]. A beam of electromagnetic laser radiation illuminating a material will penetrate into the material and the photons in the incident beam will interact with the electrons in the material surface, leading to the incident energy being absorbed[27,170]. For a beam incident on a conductor some of the energy of the beam will also be reflected via scattering interactions between the photons and the electrons in the conduction band of the material, and this reduces the amount of energy that is absorbed in the material. The fraction of the incident energy absorbed is dependent upon the wavelength of the radiation and the optical reflectivity of the material surface[85]. In general more energy is absorbed by rough surfaces than shiny reflective surfaces, which direct a lot of the incident radiation away through scattering[85]. The electromagnetic absorption and the resulting temperature change is assumed not to change the thermal, elastic or electromagnetic properties of the material and the resulting mechanical deformation is assumed not to change the thermal profile of the material[167].

The absorption of the incident photons by the surface electrons in a conductor acts to screen the interior of the metal from the radiation, such that the absorption only occurs in a thin layer at the surface, the depth of which is determined by the material skin depth, δ[27]. At the skin depth the amplitude of the incident radiation falls to $1/e$ of its initial value, and the depth at which this occurs is dependent upon the frequency of the incident radiation, f, the conductivity of the metal σ and the relative permeability of the metal, μ_r, via

$$\delta = (\pi \sigma \mu_r \mu_0 f)^{-1/2} \quad , \tag{2.67}$$

where μ_0 is the permeability of free space. The choice of laser used for ultrasonic generation should take into consideration this skin depth to ensure that it is not too small, so as to ensure efficient generation of ultrasound by improving the amount of electromagnetic energy absorbed. For aluminium samples illuminated by a 1064 nm wavelength laser the skin depth is approximately 5 nm[27].

The size of the skin depth dictates the region of the material that will absorb the incident radiation, and therefore dictates the size of the region which will be heated by this absorption process[27,85,166,167]. For a laser incident on a conductor, the absorption of the photons generates heating within the skin depth, causing a localised material expansion outwards from the absorption region, as shown in figure 2.6. The expanding heated material is restrained by the surrounding cooler material, and the resulting heat gradient produces stress and strain fields within the material[27,166,167].

For incident radiation in the thermoelastic energy regime a 3D model of the thermal expansion can be produced by considering the heated absorption volume, V, which is given by the product of the area of the spatial extent of the laser spot incident on the surface and the skin depth of the absorption. The thermal gradient that is developed produces an expansion of the material, which is equivalent to the insertion of a small volume, δV, in the absorption region, which will produce localised material strains and stresses[27,167].

At the top surface of the material only the compressional stresses and strains, e.g. σ_{xx}, σ_{yy} and σ_{zz}, are present, however, within the skin depth shear stresses and strains, e.g. σ_{xy}, σ_{xz} and σ_{yz}, also exist. The thermal gradient $\delta\ T$ present in the material with thermal expansion coefficient α_T produces localised strains of,

$$\epsilon_{xx} = \epsilon_{yy} = \epsilon_{zz} = \frac{1}{3}\frac{\delta V}{V} = \alpha_T \delta T \quad , \tag{2.68}$$

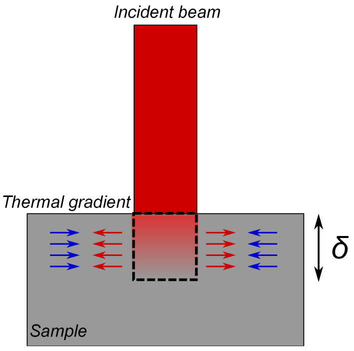

Figure 2.6: Schematic diagram illustrating the absorption of the incident laser energy within the skin depth of a sample that leads to the formation of a thermal gradient, which in turn produces ultrasonic stresses and strains.

from which the volume expansion gives localised surface stresses of,

$$\sigma_{xx} = \sigma_{yy} = \sigma_{zz} = (\lambda + \frac{2}{3}\mu)\frac{\delta V}{V} \quad , \tag{2.69}$$

where λ and μ are the Lamé constants[27]. The presence of these stresses and strains produces ultrasonic waves by the process described in section 2.1.2. A contribution to the generation of the ultrasonic stresses in the material also arises from the radiation pressure exerted on the illuminated surface by the incident electromagnetic radiation, however, this is several orders of magnitude smaller than that arising from the thermoelastic mechanism and so is negligible in this case[27,167].

To achieve a high degree of compressive stress in the heated region a Q-switched pulsed laser is used for generation. The pulsed laser allows the heat energy to be deposited into the material over a very short period of time, producing a very steep thermal gradient[27,166,167]. This model of a thermal expansion in the absorbing region is valid in the limit of no thermal diffusion[167].

As the heating is not instantaneous, with a finite laser pulse rise time, a broadband range of ultrasonic frequencies are generated simultaneously within the sample, as seen in the experimental waveform shown in figure 2.3 for Lamb wave generation. The heating profile within the material will mimic the Gaussian beam profile produced by the Nd:YAG generation laser, and variations in the pulse time and Gaussian width have been shown to affect the character of the thermal heating, and therefore the generated ultrasound, within the material[27]. The effect on the character of the ultrasound produced by variations in the spatial profile of the generation area is discussed in section 2.3.1.

Laser generation of ultrasound produces the bulk waves described in section

2.1.3, the surface acoustic waves described in section 2.1.4, and other wave modes depending on the sample geometry[171]. Laser thermoelastic generation has been shown to produce Rayleigh waves with a simple bipolar (spot source) or monopolar (line source) wave shape, making them ideal for the studies carried out in chapter 4[27,171], and in thin plate-like materials the preferentially produced surface wave becomes a Lamb wave[172].

In the higher energy ablative generation regime the energy densities involved are sufficient to vaporise the sample surface (or sometimes a sacrificial coating can be applied to the test sample if this generation mechanism is necessary), producing a plasma, and the net force of this process is downwards into the material[27]. From the momentum transfer into the material the ultrasound generated by this mechanism can be modelled as arising from a normal impulsive force applied to the surface. The ablative regime may be used if higher amplitude waves are required and the preservation of the material surface is not important[173].

2.2.5 Laser generation source geometries

Several different beam profiles have been used to generate ultrasound for the purpose of non-destructive testing, ranging from a circular spot[168,174], a line source[175,176], a ring source[177] and an array of laser sources[122,178,179]. The simplest of beam profiles is the circular spot, which is generated by passing the incident laser through a plano-convex lens. The spot source has been described in many works as approximating a point ultrasound source, with the source region being slightly bigger than the spot profile on the material[174]. This produces a radial source that is used to ensonify a sample in all directions, enabling the detection of ultrasound from many different positions relative to the source[180], as shown in figure 2.7a.

A laser line is generated by passing the incident beam through a cylindrical lens to produce a linear profile on the material surface[175]. The ultrasonic field produced by a linear source has been shown to be strongly directional, with the maximum wave generation occuring in the direction perpendicular the line axis, as shown in figure 2.7b. Although some beam spreading will occur, the highly directional nature of the line source makes it ideal for scanning laser applications and for applications on small samples, due to the reduced appearance of side wall reflections[23,95,107,128].

A ring source can be produced using a series of lenses. The incident beam is first expanded and collimated using a combination of a concave and a biconvex lens,

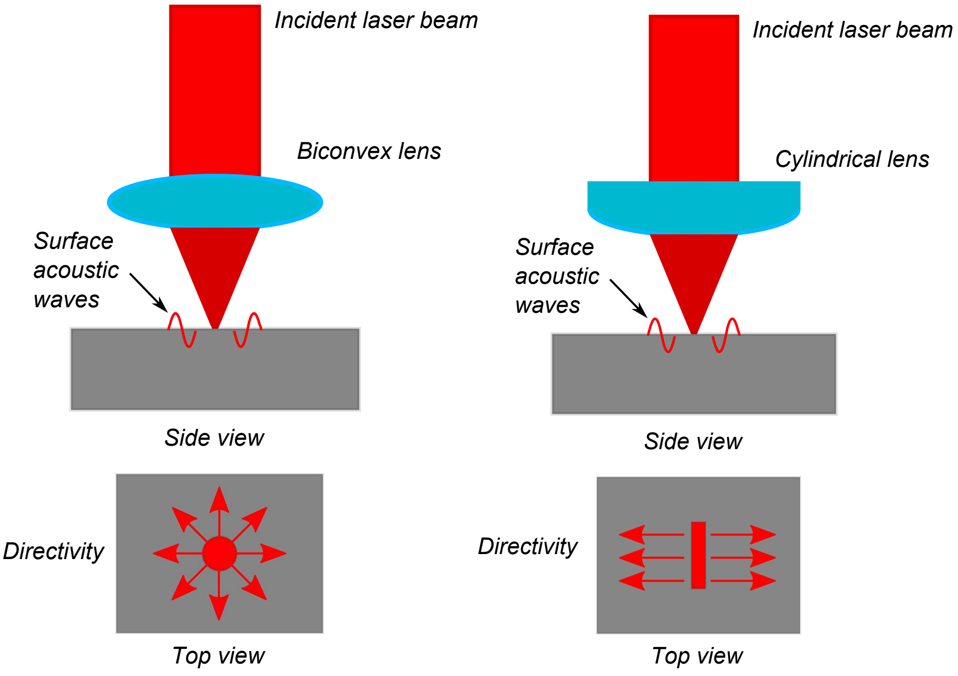

(a) Spot source (b) Line source

Figure 2.7: A schematic diagram of the laser generation optical setups for a circular spot and a line generation source with the resulting ultrasonic directivity.

before being refocussed using a convex and an axicon lens to produce a ring profile of a set radius[181]. The ring source produces two wave fronts, which propagate outwards and inwards from the ring, with the inward propagating waves capable of forming waves with much higher amplitudes due to a superposition at the ring centre[177,181,182]. This source arrangement can be used when much higher wave amplitudes are required, without the need for ablative generation, however, implementation is limited by the difficulties in producing the ring source[182].

Motivated by the desire to increase the maximum amplitude of ultrasound that can be produced without the risk of material damage there have been several laser source arrays developed. Physical arrays of lasers have been developed but have proved to be prohibitively expensive for practical applications[183], and laser source arrays are instead formed by spatially distributing a single laser source. This involves splitting a single laser source into an array of sources with a fixed separation, which can be achieved using periodic surface masks[178], lenticular arrays[184] and holographic diffraction gratings[179,185]. The series of sources interact with one another, forming a superposition of the sources, which allows the generation of a tone-burst-like acoustic source that is capable of producing narrowband acoustic waves, and this has interesting applications for techniques such as NDT of material microstructures[122]. Laser array generation also enables the frequency content of the ultrasound to be controlled, producing a narrow band ultrasonic source that can be tuned to give control over the frequency content of, for example, Rayleigh waves[179].

Narrow-band excitation of laser generated ultrasound can also be achieved through the use of a liquid crystal spatial light modulator, which allows a shaped ultrasonic source to be formed on the test material[186,187]. A computer is used to selectively excite the liquid crystal layer which is then used to selectively block the laser beam that is projected on the test material, resulting in a shaped ultrasonic source[188]. Spatial light modulators produce holograms that can be altered in real time to form a laser source with a variable spatial profile, enabling the selection of the ultrasonic frequency that is generated.

2.2.6 Laser detection of ultrasound

The non-contact nature of laser detection ensures that the material undergoes no mechanical loading which will disturb the ultrasonic field, and the lack of a permanent fixure allows for the swift scanning of the sample surface with no need to reattach transducers[189,190]. Laser detection also has a high spatial resolution, governed by the size of the beam profile on the sample, allowing for a detailed profile of the ultrasonic field to be formed (for example the detector profile in this work is 200 μm). Laser detectors possess a region in which they have a flat broadband frequency response, with the exact frequency range of this dependent upon the interferometer type[27]. A drawback of optical interferometry is the fact that the measured signal can suffer from high noise levels and averaging of data is required, thereby increasing the time required for a measurement to be taken.

Optical methods either measure variations in the intensity or the phase of radiation reflected from the material surface, with the variations caused by the passage of an ultrasonic wave in the material at the detection point. Variations in the intensity of the reflected beam, which are caused by slight changes in the reflectivity of the material that are induced by the passage of ultrasound, can be monitored directly by a photodetector and have been used in picosecond ultrasonics to measure the properties of nanostructures[191]. A second technique known as 'knife-edge' interferometery operates by focussing the probe beam into a very tight spot on the surface before blocking the central part of the reflected beam, and looking at the interference fringes that form either side of this blocked portion. The small sample surface tilt introduced by an ultrasonic wave causes the intensity of these fringes to vary periodically and gives a measure of the surface displacement, with the possibility of detecting in-plane motion[179,187,192].

Phase based optical detection techniques operate through the interference between a reference laser beam, which has undergone no interaction with the sample under test, and a probe laser beam that has been reflected from the test surface. Both beams originate from a common source, however, the interaction of the probe beam with a material surface that is vibrating due to the passage of an ultrasonic wave introduces a change in the path length travelled by the probe beam. This change in the path length introduces a phase difference between the beams, which is interpreted as a measure of the out-of-plane surface displacement that is caused by the ultrasonic wave[27,193,194].

The two types of phase sensitive interferometer used in the work in this thesis are the Michelson interferometer (section 2.2.7), and the two-wave holographic mixing interferometer (section 2.2.8). Other techniques that are commonly employed include the Fabry-Perot interferometer and Doppler vibrometers. Two classifications of detector can be made, homodyne and heterodyne; in homodyne devices the reference beam and the probe are generated from a point of common phase, such that any phase change for the probe beam is created by the material surface, whereas heterodyne devices introduce a known phase shift to the probe beam prior to interaction with the material using a Bragg cell. Both provide a measure of the ultrasound signal, but a homodyne detector, whilst it has a superior signal to noise ratio, requires mechanical stabilisation of the reference arm.

A Fabry-Perot interferometer is a device that can be used to study rough surfaces where the reflected beam has a non-specular reflection[195,196]. Reflection from a rough surface occurs at many different angles, and instead of a single clear reflection, a speckled reflection pattern is produced in which the reflections from many angles interfere with one another to produce a wave whose intensity can vary randomly[27]. In a Fabry-Perot interferometer the reflected light is collected into a cavity that has a planar or confocal mirror at each end, leading to multiple reflections of the received light between the mirrors, with only a small leakage at each reflection. The reflecting beams interfere with one another, and the transmission out of the cavity has a maximum when the two waves are in phase, and a minimum when they are out of phase, thereby enabling the phase difference (and therefore a surface displacement) to be obtained for a beam reflected from a material surface that is vibrating from a measurement of the transmission out of the cavity.

In this case the detector is referred to as self-referencing as the wave-front matched reference beam with which the probe beam interacts is a reflection of itself. A Fabry-Perot cavity has maxima in its transmitted power at frequencies that occur at multiples of the free-spectral-range, which is a function of the cavity length, and hence the sensitivity of the device is dependent on frequency. However, the cavity length must be controlled so as to ensure the frequency response of the device, and stabilisation is often needed[194–196].

Vibrometry and interferometry are very similar techniques, and Doppler vibrometry provides a measure of the target surface velocity by using the Doppler effect experienced by a probe beam incident on a surface excited by an ultrasonic vibration. Using this technique it is possible to obtain an idea of the in-plane motion of the material (employing differential doppler vibrometery with two lasers) as well as the out-of-plane motion. With a vibrometer it is possible to measure velocities caused by large surface displacements, however, signal to noise ratios drop on rough surfaces[27,197,198].

2.2.7 Michelson interferometer

The Michelson interferometer is a phase sensitive interferometric system[27,193]. In this homodyne device a source beam is divided by a beam splitting mirror, forming a probe and a reference beam, and the mirror directs the probe beam towards the sample surface under test and the reference beam to a photodetector where it is recombined with the reflected probe beam, as shown schematically in figure 2.8.

In phase sensitive interferometry the propagating ultrasonic wave causes surface displacements, which in turn introduce small variations in the pathlength of the probe beam, leading to the development of a change in the phase difference between the probe and the reference beams. The stabilised Michelson interferometer used in this thesis automatically compensates for low frequency background mechanical vibrations and thermal expansions by moving its reference mirror on a small piezoelectric controlled stage[101]. As the sample surface moves in the out-of-plane direction (for normal incidence of the probe beam) the phase difference between the beams varies between constructive interference (pathlength difference of an integer number of wavelengths, n) and destructive interference (pathlength of $n+1/2$ wavelengths), thereby giving the relationship between detector output voltage and surface displacement, z (when z is small), of:

$$V = \bar{V} + V_0 \sin(4\pi z/\lambda) \quad , \tag{2.70}$$

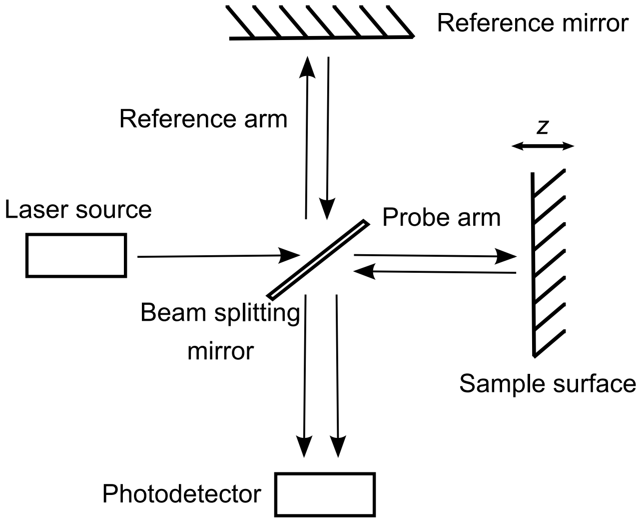

Figure 2.8: A schematic diagram of a Michelson laser interferometer, used to detect the out-of-plane surface displacement, z.

where λ is the wavelength, V is the voltage of the signal from the recombined beams at the photodetector, V_0 is the unstabilised voltage and $\bar{V}$ is a DC bias (for the interferometer at the University of Warwick, $\bar{V} = 0$)[27].

The Michelson interferometer gives a direct measurement of the absolute out-of-plane surface displacement and the system at the University of Warwick has a broadband response of up to 80 MHz a sensitivity of the order of 0.01 nm. The drawback of the Michelson interferometer lies in the fact that, in order to achieve a proper superposition between the reference and probe beams, the wave forms of both have to have the same form across their geometry[193]. Therefore, any surface roughness of the sample under test or deviation from normal incidence of the probe beam leads to a sharp decrease in the sensitivity of this method, through a loss in the recieved power of the probe beam and the low efficiency of the mixing of a non-planar probe beam with the planar reference beam[194]. The Michelson interferometer is a useful tool for the laboratory where time can be taken to produce the required highly polished samples, but is less effective when the surface of the sample is rough and cannot be altered, limiting its usefulness for in-situ industrial applications[27,194].

2.2.8 Two-wave mixing interferometry

For industrial applications of laser detection the ability to detect ultrasound on unprepared rough surfaces is important, removing the need to alter the sample properties through polishing, with a selection of rough industrial samples measured in chapter 7. This is especially important for applications in which the sample surface is at an elevated temperature, thereby making polishing challenging, or in a highly oxidising environment in which any polished area would degrade very rapidly[10,199]. There are several commercially developed systems capable of detecting ultrasound on rough surfaces, and the system used at the University of Warwick is the Intelligent Optical Systems (IOS) AIR-1550-TWM laser ultrasonic receiver[200]; the operating wavelength of the IOS is 1550 nm with an optimum lift-off distance of ≈4.5 cm, which is considerably larger than the equivalent EMAT detector described in section 2.2.3. The system has two availiable detector spot sizes of 50 μm and 200 μm, and a bandwith of 125 MHz that is sensitive from around 100 Hz, and the surface displacement sensitivity is 4x10^{-7} nm $(\mathrm{W/Hz})^{1/2}$[200].

The IOS detector is a two-wave mixing interferometer, which operates by interfering a reference and a probe beam that has been reflected from a vibrating surface, in a photorefractive crystal. The interference fringes caused by the interaction between the phase-changed probe beam and the reference beam act to alter the refractive index of the crystal, effectively producing a diffraction grating within the crystal. The diffraction grating diffracts the beams as they are transmitted through the crystal to a photodetector and variations in the phase changes between the waves are translated into variations in the voltage at the detector, giving a measure of the surface displacement.

The IOS detector uses a common source laser to produce both a probe and a pump (reference) beam; the former is directed to the surface under test and the latter is steered directly onto a photorefractive crystal at an angle to the probe beam, as shown in figure 2.9. The beams are combined using two-wave mixing, which is a dynamic holographic process in which two coherent beams interact within a photorefractive crystal, a material that, when illuminated with light, will alter its refractive index[201].

The probe beam, with a phase difference introduced by the ultrasound propagating in the illuminated sample, will interact with the pump beam to create an optical intensity variation within the photorefractive crystal[202,203]. This produces a non-uniform excitation of the electric charges in the photorefractive crystal as regions of higher light intensity undergo larger changes in refractive index. This induces a charge imbalance within the crystal that results in the creation of a refractive index grating as the material properties of the crystal develop local changes. This refractive index grating acts to diffract the interacting beams, such that the wave that is transmitted from the photorefractive crystal consists of a transmitted portion of the probe beam and a part of the pump beam that is diffracted to the same direction as the probe beam[204].

The diffracted part of the pump beam has the same wave-front structure as the transmitted portion of the probe beam, thereby ensuring perfect wavelength overlap between the two beams when they interfere with one another. This transforms the phases changes between the two beams into variations in the output voltage of the detector, which are proportional to the variations in the out-of-plane surface displacement at the sample surface. The output is only linear when the two beams are biased in quadrature (90 ° phase difference), which is achieved in this case by the application of a high voltage DC electric field to the photorefractive crystal[200,202].

The changes in the refractive index of the crystal take a small time to occur, and the photorefractive crystal can only react to changes in the incident beams that occur on a slower time scale than this characteristic time, which is largely dependent on the crystal used. This has the consequence that the diffracted portion of the pump wave is not modified by the high frequency ultrasonic changes that occur in the probe wave, giving a diffracted reference signal that is unchanged from the input signal, and therefore any observed changes from the interference are only due to changes in the probe beam. This method also compensates for ambient low frequency noise as the photorefractive crystal can adapt fast enough to compensate for these[201].

The holographic reconstruction of the diffracted pump beam from the speckled probe beam allows the interference between the two beams to be unaffected by any speckle introduced by the interaction with the sample surface. This is the case as, after diffraction, the reconstructed reference beam that is transmitted out of the photorefractive crystal has the same speckle pattern as the probe beam from which it is produced[201,205]. This approach gives no material-related upper limit on the signal bandwidth and the only limitation is the choice of photodetector, which in the IOS system gives a bandwidth of 125 MHz[200].

Although it is possible to obtain a measure of the surface displacement from a rough surface, with only a small amount of the reflected beam entering the IOS detector, the sensitivity is still improved when more of the reflected probe signal can be collected, which is achieved through the design of the IOS detector head. The detector head has a central multimode optical fibre which delivers the source signal to the sample under test, and a surrounding ring of multimode receiver optical fibres, which collect the reflected beams, as can be seen in figure 2.10. The reflected beams are recombined to provide the probe signal for input into the photorefractive crystal, thereby enabling the efficient collection of scattered light from a rough sample

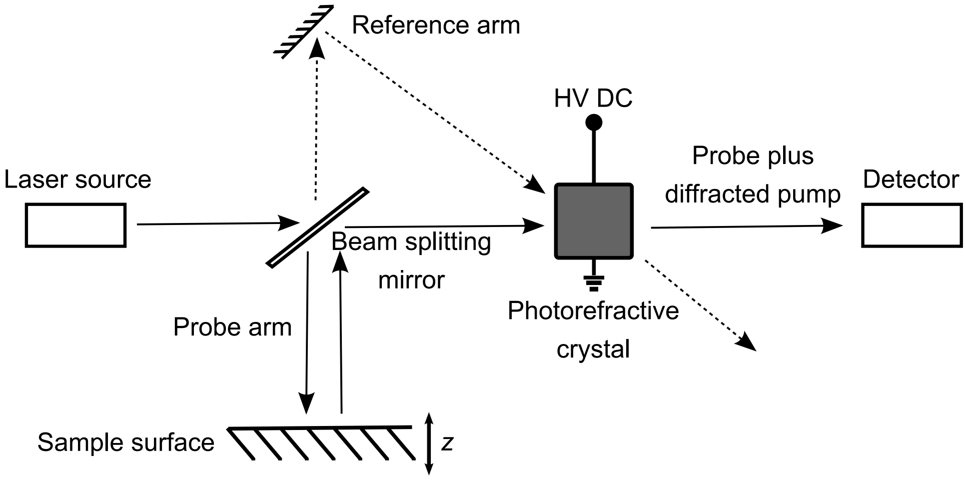

Figure 2.9: A schematic diagram of the IOS two-wave mixing interferometer, used to detect the out-of-plane surface displacement, z.

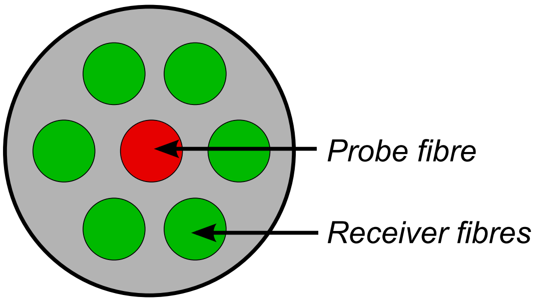

Figure 2.10: A schematic diagram of the arrangement of the fibre optics in the detector head, with a central emitting fibre surrounded by six receiver fibres.

surface. Detection is also possible on polished samples, however, the detector needs to be slightly out-of-focus so that the reflected beam enters the collection fibres and is not reflected directly back to the emitting fibre. More specific details on the use of the IOS detection system are given in chapter 3.

2.3 Overview of ultrasonic techniques

Ultrasonic techniques have been successfully employed in non-destructive testing for the detection and characterisation of many different types of defect, including the detection of microscopic changes in material grain stuctures[122,206–208], the detection of changes in material thicknesses due to corrosion damage[81–83,209,210] and the detection of internal and surface defects[31,80,94,138–140,211–219]. An overview

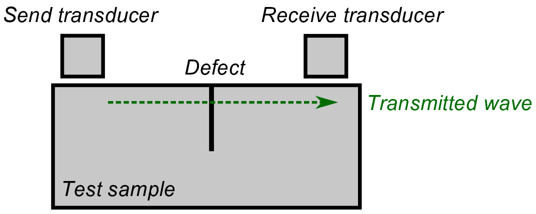

(a) Pitch-catch

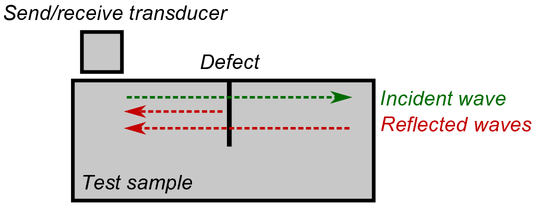

(b) Pulse-echo

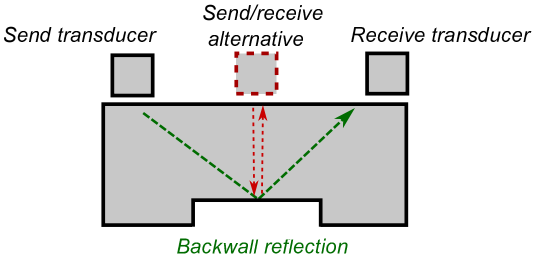

(c) Back-wall reflection

Figure 2.11: Schematic diagram of pitch-catch (a), pulse-echo (b) and back-wall reflection inspection strategies.

of the ultrasonic testing methods for the detection of each type of defect is given here, with the focus of this thesis being on the detection of surface-breaking defects.

Microscopic defects

Ultrasonics has proven adept at detecting changes in material microstructures that can be indicative of material weaknesses, which can lead rapidly to macroscopic failures[122]. Changes in the grain structure of a material are reflected in changes in the ultrasonic wave velocity, which in turn can be detected as variations in the detected wave amplitude, and can be indicative of material weaknesses or residual surface stresses. Fast inspection of material microstructure is achieved using a laser ultrasonic technique known as spatially resolved acoustic spectroscopy (SRAS)[122], in which a grating of line sources is directed onto a sample. The fringe separation contolled by the grating is swept through a range of values, which results in a peak in surface wave amplitude when the grating period is the same as the surface wave wavelength. This allows for the velocity of the surface wave to be calculated and a surface map of the material can swiftly be constructed that allows for the identification of the orientation of grain structures and identifcation of areas of local strain.

The SRAS technique provides an alternative to other methods based on arrival time differences between direct and reflected waves, that have been used to detect material grain changes[187]. Alternative techniques include the use of an acoustic microscope[220] to study the local changes in the velocity of surface skimming longitudinal[206] and Rayleigh waves[207]. Acoustic microscopy involves sending high frequency ultrasound into a small area and reconstructing a map of the structure from the arrival times of waves reflected from features, such as different material grain orientations, and although capable of detailed images it can be a time consuming process to reconstruct an entire scanned region[208].

Wall thinning measurements

Failure to detect reductions in the wall thickness of transport and storage structures and the resultant structural failures can lead to spillage of hazardous materials into the environment, resulting in costly economic and environmental impacts[15–17]. Detection of wall thinning has been achieved through the application of ultrasonic techniques that look at changes in the time of arrival of the ultrasound that propagates through a thinned section. The variations in arrival time can be caused by changes in the path length travelled (typical for through-thickness bulk wave reflection measurements)[209] or changes in the thickness-dependent ultrasonic velocity for measurements using guided waves[81,83] (see figure 2.1b). The variations of the arrival times of ultrasonic waves can be studied using several different detector configurations; through-transmission, where the source and detector are positioned either side of the inspected region, or pulse-echo where a single send/receive point is used and waves reflected by a defect or the backwall are studied, with a schematic representation of these methods shown in figure 2.11.

Pulse echo methods have been used to detect regions of wall thinning, as the time taken for the backwall reflection of the ultrasonic wave to arrive at the detector is dependent upon the amount of material travelled through (figure 2.11c). This method is reliable and only requires contact with one side of the sample, however, it can take a long time to scan an entire region point by point, and a minimum thickness exists below which the time interval between reflections is too small to resolve individual reflections[209]. As was shown in section 2.1.4.2 the velocity of a Lamb mode is dependent upon the frequency-thickness of the material in which it propagates, therefore for regions of thinner material the velocity changes lead to variations in the arrival times of Lamb waves, which can be detected with a through-transmission detector configuration, such as that in figure 2.11a (when the defect is a thinned region rather than a surface-breaking crack). This method has been shown to be effective on different material thicknesses for laser generated ultrasound, however, the thickness estimation is not as accurate as for the pulse-echo method[81,83].

Ultrasonic methods have also been used to detect the presence of corrosion damage in critical structures, such as those found in aircraft, in which failure would have devastating consequences[82,210]. The multimodal nature of laser generated Lamb wave signals can be used to detect the presence of corrosion pitting damage in through-transmission inspections. Broadband generation is used to excite the higher order S1 wave mode near to its frequency-thickness cut-off (below which it cannot propagate), such that for a scanned laser detector passed over a corrosion pit, the reduction in the thickness is evident as the S1 propagation no longer occurs[82,210]. As Lamb waves can travel large distances through a material, this far-field detection technique can be used to inspect large areas from a single generation position with a scanned detector.

Detection of internal defects

The most common implementation of ultrasonic non-destructive testing is the detection of internal defects. Detection of these usually relies on studying the interactions of longitudinal or shear bulk waves which propagate into the bulk of the material. The presence of a defect can be detected by changes in the amount of transmission recieved at a second transducer, such as in pitch-catch experiments (figure 2.11a) or, as is more common, through an examination of the reflected waves in a pulse-echo configuration (figure 2.11b).

Through-transmission requires access to both sides of the sample, and techniques such as ultrasonic tomography, in which the variations in wave velocity for different transit paths through the material are used to form detailed images of the subsurface defect[211]. Shadow based transmission techniques can indicate defects by positions of lower transmission that are caused as parts of the incident wave are scattered away by the defect, and therefore do not reach the second transducer, creating a shadowed region[212]. Whilst transmission based techniques are effective at positioning internal defects and can give an idea of the defect size, they require access to both sides of the material under test, and this may not be feasible in some applications.

Pulse-echo detection of internal defects relies on interpretation of the reflected waves that are produced by the defect, with the defect position and size being obtained by the amplitude and arrival times of the reflected waves. In a simple approach the defect depth can be obtained from the arrival time of the reflected waves (with known wave velocity) and the sizing can be performed using the 6dB drop technique, which assumes that a signal strength reduction of 6dB corresponds to a move from the defect centre to its edge[31,79]. This technique is only reliable for a straight sided defect that is perpendicular to the ultrasonic beam and positioned away from the sample walls. A more reliable technique uses variations in the arrival time of ultrasonic reflections to construct an image of the defect.

Time of flight diffraction (TOFD) locates and sizes defects within the bulk of a sample and can be used on defects that are perpendicular to the sample surface and also on tilted defects, although interpretation is more difficult[213–216]. TOFD operates by using the time of flight of a wave that has been diffracted from a crack tip (which is different to the specular reflection of waves from the sample backwall) to calculate the position of the defect[79,215,217,218]. TOFD utilises a source and detector that are scanned across a sample at a fixed separation, as shown in figure 2.12, to track the arrival time of diffracted waves, from which an ellipse of possible defect positions can be plotted from the time of flight of the defect reflection[215]. Interpretation of defect signals can be complicated, however TOFD has been sucessfully used to detect defects in such industrial applications as nuclear power plants[214,215], and can even be used to identify surface-breaking cracks by assuming that the expected reflection from the upper end of the defect sits on the surface, although the resolution of surface-breaking defects is limited to deep defects[80,94,138–140]. TOFD can be ineffective in certain sample geometries and for complex reflections defects can be difficult to resolve[215]. The inability of the TOFD technique to detect shallow defects or those with low reflectivity provides the motivation behind a drive to study the behaviour of ultrasound in the near vicinity of the defect[95,107,116,180].

Recently there has been a drive towards the implementation of arrays of ultrasonic transducers, in order to obtain as much information about a defect as possible in a single measurement[183,219,221,222]. A large material inspection volume is achieved through the use of a phased array probe, in which the probe consists of many small elements, each of which is capable of exciting ultrasound within the material. The elements are pulsed in sequence to create a single wavefront from the superposition of the waves from adjacent probe elements[219]. This produces a beam that can be steered through the sample simply by adjusting the timing between the excitation of each element of the probe[219]. Recent developments have also looked at forming wavefronts with a frequency dependent propagation angle from the simultaneous pulsing of all array elements, for the detection of defects using shear

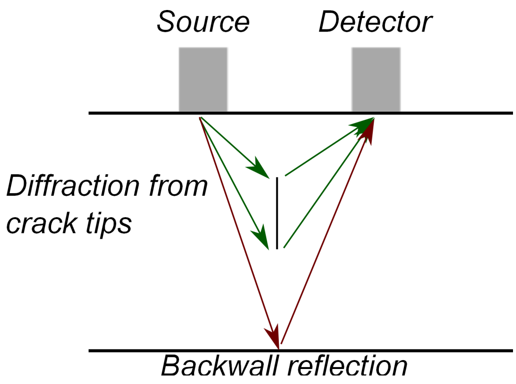

Figure 2.12: A schematic diagram showing the characterisation of a defect using the TOFD technique for waves diffracted at crack tips.

horizontal waves[223].

Recently, increases in computing power have enabled the development of full matrix capture techniques, in which every transmitter and receiver pair in an array can be pulsed simultaneously with the beam steering and interpretation being performed in post processing[222,224]. Array ultrasonics have been successful for the purposes of structural health monitoring as they allow a large area to be scanned from a single position[225], and have also enjoyed success for defect detection and characterisation from their ability to be easily steered to selected position and depths[226,227]. The phased array method allows for the swift, controllable inspection of large areas of a sample, however, due to the complicated timing sequences required the cost of such probes can be high[219].

Detection of surface-breaking defects

Recently work has also been performed into detecting surface-breaking defects, for which the most appropriate ultrasonic probe is a surface wave (section 2.1.4.2)[21,80,86,90,106,107,228–231]. Whilst the time of flight for reflected waves can be used to position a defect on the surface, issues can arise for defects that are very close to large reflectors, such as material welds, and the detection of multiple defects that are close together is very challenging if, for example, a shallow defect sits in the shadow region of a deeper defect. An alternative for defect depth estimation is to study the amplitude and frequency content of the reflected wave.

Pulse-echo techniques have been used to identify the depth of surface-breaking defects, by calculating reflection coefficients, from the amount of the incident wave that is reflected back by the defect, and these have been shown to vary with defect depth. These have been used to successfully position and size both artifical reference defects and real partially-closed cracks using Rayleigh[80,228] and Lamb surface waves[21,229–231].

Studies have also shown that there is a similar variation in the transmission behaviour of surface-breaking cracks, where transmission coefficients vary as a function of the defect depth and also the angle of the defect to the sample surface[86,90,106,107]. These methods have been shown to be successful at detecting defects in thin plates[113,114], pipework[232,233], multi-layered laminates[133] and in shaped materials, such as railway tracks[100,102]. These inspection techniques offer long range detection of defects, however, they can struggle to resolve multiple defects that are close together (as the transmission behaviour is dominated by the deepest defect in a cluster) or close to a material boundary. These methods all involve examining the ultrasound in the region far away from the defect, however, recent work has indicated that the near-field region of the defect exhibits phenomena that are useful for characterising surface-breaking defects, and research into this near-field region is the focus of this thesis.

In this thesis the terms near and far field inspection are used with respect to the near and far field of the defect, not the transducer as is more commonly used. The far field region is located at a distance of several wavelengths away from the defect, and is analogous to the Fraunhoffer region in electromagnetic waves, and in this region reflected and mode converted waves that are generated at the defect have a simple wavefront structure of maxima and minima. The near field is the region within a wavelength of the defect, analagous to the Fresnel region, in which the ultrasonic field varies greatly for a small change in position due to interference between the maxima and minima of the wavefront[26].

2.3.1 Near-field ultrasonic enhancement

Recently, interesting phenomena have been reported to occur in the region very near to a surface-breaking defect when a surface acoustic wave is incident on the defect. These near-field effects have been observed for interactions of Rayleigh waves with defects that propagate perpendicular to the sample surface when an ultrasonic source or detector directly illuminates the defect[23,128,130,234–236]. The effect is known as near-field ultrasonic enhancement and manifests as a large increase in the peak-to-peak amplitude of the Rayleigh wave as either the laser source or detector is scanned over the defect.

The enhancement is observed by time windowing the received ultrasonic signal about the arrival time of the incident Rayleigh wave for each scan position as

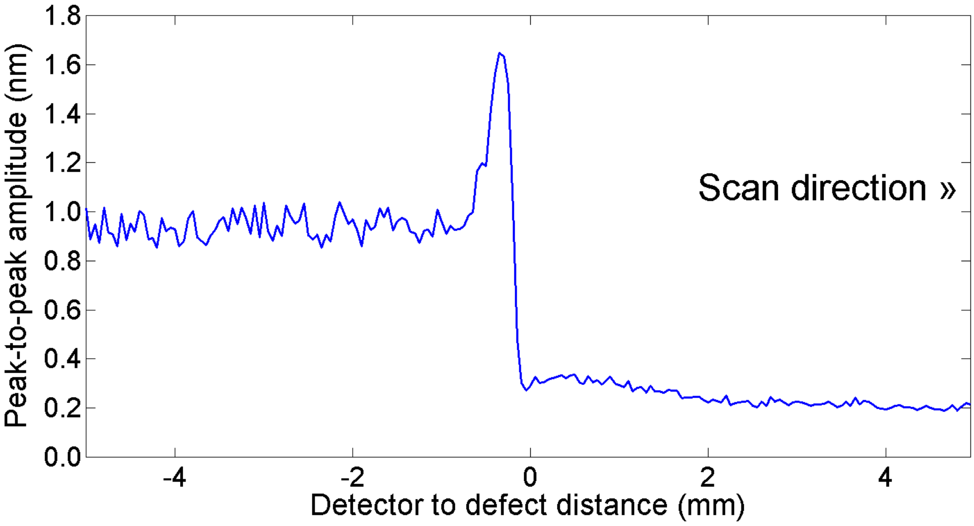

Figure 2.13: An example of near-field ultrasonic enhancement of the peak-to-peak amplitude a of Rayleigh wave as a scanned laser detector passes over a 2 mm deep normal defect.

either the source or the detector is scanned over the defective region. The peak-to-peak amplitude of the Rayleigh wave is measured at each position, and the variations in this amplitude are shown in figure 2.13 for scanning laser detection, plotted as a function of the laser detector position as it is scanned over a 2 mm deep defect propagating normal to the surface. For negative detector positions the detector and the source, which is located a fixed distance away from the detector, are on the same side, of the defect, and the peak-to-peak amplitude of the Rayleigh wave when the detector is far away from the defect is seen to have a steady value. As the detector passes over the defect a large increase in the amplitude of the Rayleigh wave is observed; this is the Rayleigh wave enhancement. As the detector continues to move, such that the defect lies between it and the source, the peak-to-peak amplitude is reduced as part of the wave energy is blocked by the defect[107].

For defects that propagate perpendicular to the material surface the increase in the peak-to-peak amplitude as the detector passes over the defect has been reported to be caused by constructive interference between the incident Rayleigh wave, the reflected Rayleigh wave and a mode converted surface skimming longitudinal wave that occurs at the defect[104,236,237]. Provided that the detector is close enough to the defect that these waves, which travel at different speeds ($v_r = 2940\ ms^{-1}$ and $v_L = 6300\ ms^{-1}$[141]) arrive within the time window that was used to monitor the peak-to-peak amplitude, a superposition of the waves occurs, which, for constuctive

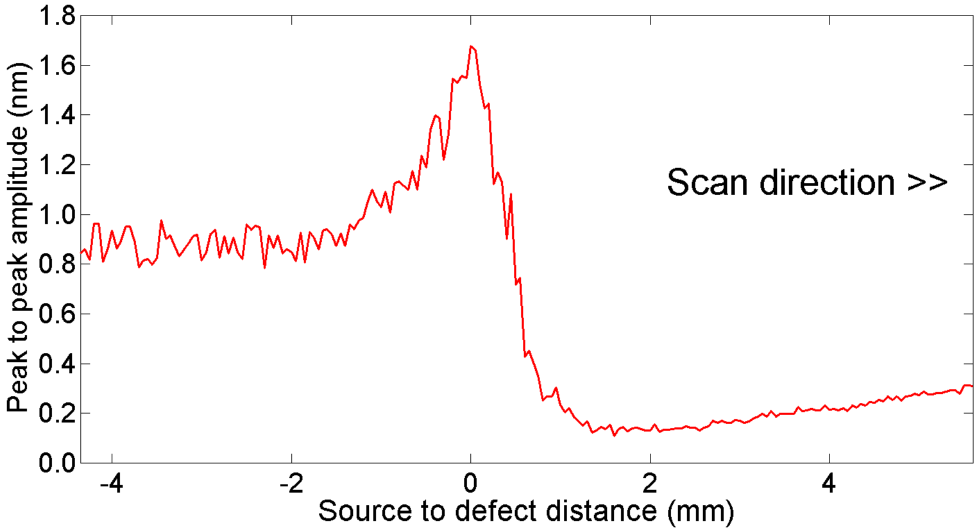

Figure 2.14: An example of near-field ultrasonic enhancement of the peak-to-peak amplitude a of Rayleigh wave as a scanned laser source passes over a 2 mm deep normal defect.

interference, produces a Rayleigh wave with increased peak-to-peak amplitude. The amplitude of the reflected and mode converted waves dictates how much they will contribute to the increased peak-to-peak amplitude, and, as the extent of the reflection and mode conversion experienced by the Rayleigh wave is dependent on the defect depth, the extent of the enhancement varies as a function of defect depth[104]. The position of the defect is also obtained to within approximately ±0.25 mm from this technique as the point of enhancement for Rayleigh waves occurs when the detector is approximately 0.25 mm from the defect[104].

A similar enhancement of the peak-to-peak amplitude of Rayleigh waves is observed when a laser source is passed over a surface-breaking defect[23,128,234,235]. The peak-to-peak amplitude of the ultrasonic signal recorded in a time window that corresponds to the incident Rayleigh wave as a laser source is scanned over a 2 mm deep defect propagating perpendicular to the material surface is shown in figure 2.14. Again, for the negative positions the laser source and the detector are on the same side of the defect, and the peak-to-peak amplitude is steady in the region in which the source is away from the defect. As the laser source passes over the defect a large increase in the peak-to-peak magnitude of the windowed Rayleigh wave is seen, which then drops off again when the defect lies between the source and the detector.

The enhancement in the peak-to-peak amplitude of a Rayleigh wave observed as the laser source passes over an artificial surface-breaking defect propagating normal to the material surface has been attributed to arise from the contributions of several mechanisms[23,235]. An increase in the magnitude of the high frequency content of the Rayleigh wave has been observed to occur simultaneously with the increase in the peak-to-peak amplitude, and this frequency enhancement has been attributed to changes in the ultrasonic generation process. The maximum frequency content f_{max} of an ultrasonic wave generated by a laser source is dependent upon the wave speed, v, and the laser spot diameter, w, from[23,185],

$$f_{max} = \sqrt{\frac{2v}{\pi w}} \quad . \tag{2.71}$$

Therefore, as the laser source passes over the lip of an artificial defect a reduction in the dimension, w, on the material surface is observed, which in turn increases f_{max}, thereby contributing to the enhancement of higher frequency components of the signal[235].

A contribution to the enhancement from changes in the boundary conditions of generation at the artificial defect has also been identified when the laser source is directly over the defect. At the defect the source no longer causes a uniform expansion of the surface material into the unheated material surroundings, and the material at the defect can expand out into the void of the defect. This alters the character of the generated ultrasound and has been shown to cause the enhancement of Rayleigh waves, although its influence is difficult to quantify[235]. A contribution to the enhancement as the source passes over an artificial defect has also been reported to arise from constructive interference between the incident Rayleigh wave and a reflected Rayleigh wave at the detector, when the source is close enough to the defect that both incident and reflected waves arrive within the time window that the peak-to-peak amplitude is studied in[235]. Surface wave enhancements have also been reported to exist for Lamb waves[22,64].

These mechanisms have been identified to contribute to the enhancement observed for artificial surface-breaking slots, however, an additional mechanism has been identified to contribute to the enhancement observed for Rayleigh waves as a laser source is passed over a real partially-closed defect. For a defect with partially contacting faces the transient heating of the defect stimulates the crack to open and close, bringing the opposing faces of the defect together. This clapping of the defect faces generates higher harmonics of the surface wave, leading to an enhancement of the Rayleigh wave for real defects[234,238].

The use of near-field enhancements to characterise defects is attractive for its ability to detect defects that are arbitrarily aligned with respect to the scan direction and for its ability to provide good estimates of defect positions. However, near-field enhancement inspection does have the limitation that the entire sample must be scanned in order to find a defect, and if the scan step is too large, the correct position required to observe the maximum enhancement may be missed.

Chapter 3

Experimental and modelling techniques

To study the near-field interactions between ultrasonic waves and surface-breaking defects the ultrasound must be studied as it propagates through the test sample. The more information obtained about the propagation of the ultrasound through the material, the easier it is to understand the interactions observed and to explain the phenomena that give rise to them. This is achieved here through an experimental scanning approach, in which the source and detector are passed over the defective area, thereby allowing the propagation of ultrasound to be monitored directly. Any changes in ultrasonic propagation caused by a defect are detected as they happen, making positioning of a defect simple, as the detector position is always known. The scanning approach allows near-field inspection by both the source and detector in a single experimental run, as well as transmission information, avoiding any issues with misalignment of the sample or setup between different experiments.

It has become common practice to validate experimental results with simulations that aim to recreate the experiment without many of the imperfections of a physical system[95,107,128,239]. To this end finite element method (FEM) simulation was used to recreate the experimental findings. Simulation allows for a drastic reduction in noise and enables certain experimental features, such as unwanted back-wall reflections, to be made negligible. Simulation also extends the range of samples that can be studied as material cost and manufacturing concerns are removed, allowing for a more complete study to be carried out. A full explanation of the FEM approach can be found in section 3.2. Although FEM simulation has been shown to provide reliable reconstructions of physical systems in many applications, differences can still arise between the simulated data and the experimental reality, and the reasons for these differences must be considered before making any decision on the validity of any conclusions drawn from simulated data.

Several different materials are used over the course of this study, including aluminium, stainless steel and titanium. The initial investigations are carried out on reference defects, with the defects being manufactured using the laser micro-machining method described in section 1.4.3. The exact reference defect geometry is described in the relevant chapter (see figures 4.1 and 5.1) but in all cases the reference defects were cut into the sample from the top surface. Artificial stress corrosion cracking defects were also produced by thermal fatigue loading in stainless steel plates, and these samples are described in chapter 7.

Experiments on real stress corrosion cracking defects were carried out on sections cut from pipework and on irregularly shaped industrial samples, with the results presented in chapter 7. In this chapter the general experimental and simulation approach is presented in which the object referred to as the test sample can be any of those described above; details specific to each sample are found in the associated chapter.

3.1 Experimental setup

For generation of ultrasound within the sample a pulsed Nd:YAG laser was used, with a wavelength of 1064 nm and a rise time of 10 ns. The generation laser was directed onto the sample under test after passing though neutral density filters, which allowed the power of the laser to be controlled to ensure thermoelastic generation conditions were enforced, as described in section 2.2.4[27,166].

Neutral density filters act to reduce the intensity of all wavelengths of radiation that pass through them within the specified range of the filter, and this is dictated by the material used and the thickness of the filter, and here a flat spectral density response exists between $400 \leq \lambda \leq 2000$ nm. The filter acts to absorb a fraction of the incident radiation intensity I_0, thereby reducing the transmitted intensity, I, with the resulting property being referred to as the optical density or absorption, $\alpha_{optical}$, of the filter, as given by,

$$\alpha_{optical} = -log_{10}\frac{I}{I_0} \quad . \tag{3.1}$$

The absorption of multiple filters is additive, such that if filters with optical density of 0.1 and 0.3 are used then a combined filter with an optical density of

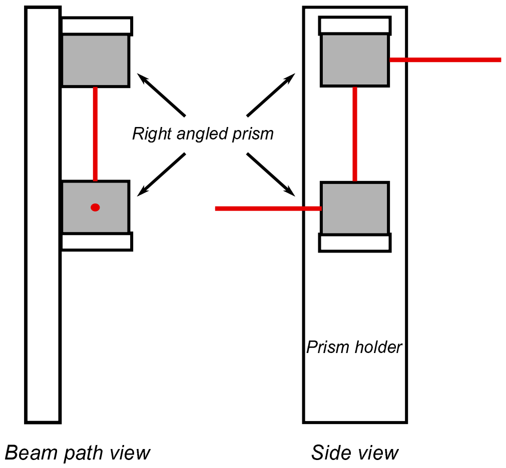

Figure 3.1: A schematic diagram of the optical periscope used to vary the height of the generation laser.

0.4 is formed. This allows the filtered intensity of the laser source to be closely controlled, and avoids any damage to the sample surface. The amount of filtering applied was varied depending on the sample to be tested so as to avoid any ablation of the surface, as described in section 2.2.4[27].

The height of the incident beam was adjusted through the use of an optical periscope, shown schematically in figure 3.1, such that when combined with a linear scan, samples could be scanned in two directions. The beam profile incident on the sample could be swapped between a circular spot, with 2 mm diameter, or a thin line source of dimensions 6 mm by 300 μm, by placing either a biconvex lens or a cylindrical lens in front of the incident beam, with these beam profiles shown in figure 2.7. Both source geometries have advantages and disadvantages, as described in section 2.2.5, and these must be considered with respect to the intended experiment.

The laser line source has been shown to provide a directional source of ultrasonic surface waves[175,176], which makes it ideal for the investigation of small samples by reducing the sidewall reflections which could obscure any useful signals from a defect[22,240]. However, the spatial dimensions of the line source are such that they produce only small changes in beam profile, as the line source passes over a surface-breaking defect, which have been shown to be responsible for signal enhancement[116,234,235], making near-field studies as the source passes over a defect more challenging with a line source than with a spot source. The narrow focal length required to form a line source also gives rise to problems with maintaining a constant focus for the line source if an object with complicated geometry is studied, such as is studied in chapter 7.

An alternative to the line source is to focus the beam to a circular spot source, which produces surface acoustic waves radially with no preferential direction[168]. The advantage of this is that it enables a large volume of the sample to be excited with ultrasound from a single generation position. However, the lack of a preferred direction means that the detected ultrasound is complicated by multiple sidewall reflections which have to be taken into consideration when interpreting results.

Laser detection was carried out through the use of a two-wave mixing laser interferometer provided by Intelligent Optical Systems (IOS), the operation of which was described in section 2.2.6[201,202]. This consists of a continuous wave laser that operates at an infra-red wavelength of 1550 nm and a detector that has a bandwith of 125 MHz, and which is sensitive to signals from around 100 Hz upwards. The detector is not sensitive to frequencies below 100 Hz and above the upper limit of the bandwidth the detector response is no longer linear. The IOS system has two signal outputs, the first of which is a DC level that represents the signal strength of the reflected probe beam at the detector. This value is directly affected by the amount of back-scattered radiation from the sample surface and must be sufficiently large enough to maintain a good signal to noise ratio on the observed signal. The second is an AC output, the voltage of which represents the out-of-plane surface displacement observed at the detector point. This is not a direct measurement of the surface displacement and requires a conversion from the received AC voltage, V_{AC}, to the actual displacement, z, using the DC signal strength, V_{DC}, and the following empirical equation,

$$z = ((V_{AC}/V_{DC} \times 100) + 5.63)/22.3 \quad , \tag{3.2}$$

which was obtained by calibrating the AC signals from the IOS detector against the measured out-of-plane surface displacements using a Michelson interferometer on a piezoelectric probe target.

The focal length of the detection beam is $\approx$ 50 mm, which relates to a stand-off of $\approx$ 46 mm from the end of the detector aperture, giving a good standoff from the test material if the system were to be used in situ. The coupling efficiency varies with detector standoff, as shown in figure 3.2, and the detector is more efficient if used at a standoff which is slightly above or below the exact value of 46 mm. This is ideal for the scanning of unprepared industrial samples, as variations in the surface texture and alignment with the detector are commonplace and so having a range of focus with a good coupling efficiency reduces the risk of the signal being

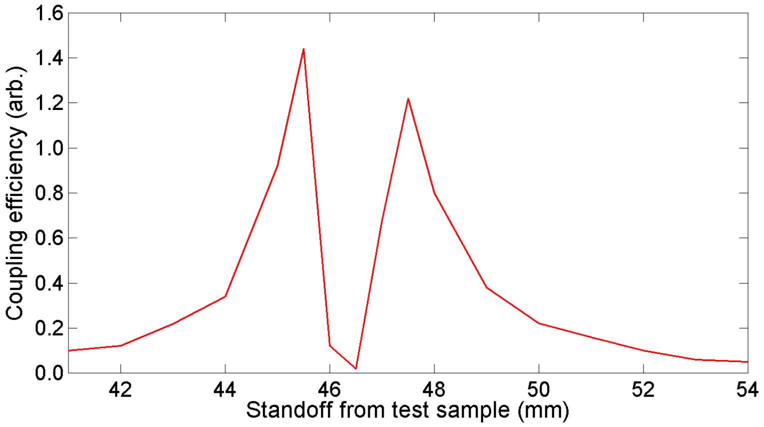

Figure 3.2: The variation in the coupling efficiency of the IOS detector as a function of the standoff from test sample.

undetectable.

The laser spot size for the detector head used was 200 μm, and the laser has a variable power up to 2 W, which is varied depending upon the surface conditions of the sample such that the received DC signal, which is a measure of the strength of the received AC signal, is kept between 0.5 V and 3 V. This range was determined from the DC voltage range for which the response of the system to the displacements described by equation 3.2 is linear.

The laser output power was chosen at the start of a scan by positioning the detector over the roughest part of the sample surface and the power was then chosen such that it sat in the middle of the DC range given above for this worst-case scenario. As the surface conditions at the detector position varied, as the sample was not prepared through any polishing prior to scanning, the reflected signal strength at the detector remained in the region for which the detector calibration was linear. The IOS detector also has an eye-safe visible laser with the same focal length as its probe laser to allow for easy positioning of the detector, and the generation laser position was identified through the use of an infra-red-sensitive target card.

Experiments were carried out by holding the generation and detection lasers at a fixed separation to one another and scanning the object under test, as shown in figure 3.3. The constant separation of the two lasers simplifies the interpretation of the wave interactions across the duration of a scan as it allows for an easy distinction between the incident waves, which will have a constant arrival time at the detector, and the reflected and mode converted waves created at the defect, which will have varying arrival times as the separation between the detector and the point of reflection changes. The second benefit of the fixed separation is that each consecutive

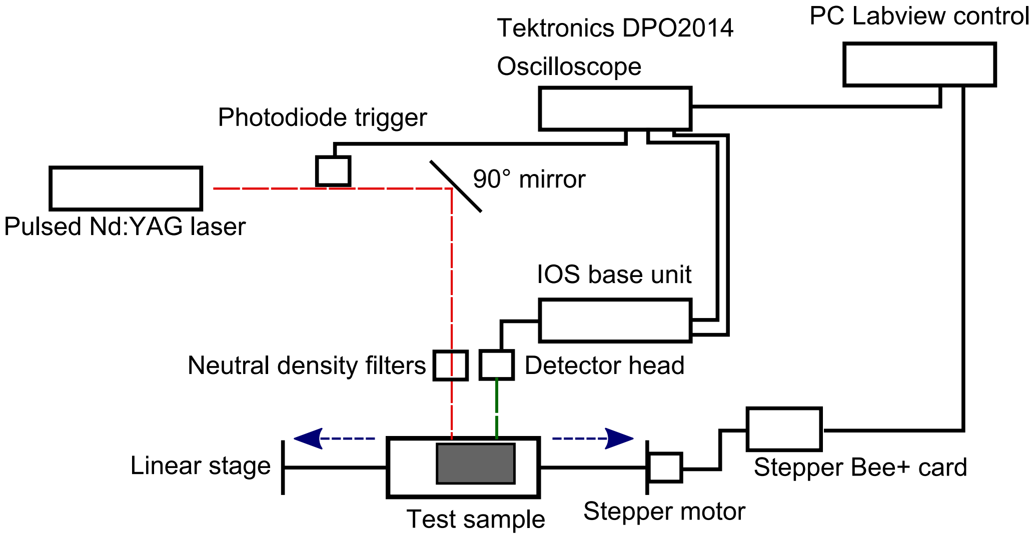

Figure 3.3: A schematic diagram showing the experimental setup for a linear scan inspection of a test sample.

scan will experience the same amount of signal loss from wave attenuation as the distance each wave has travelled is the same for each scan. In a similar fashion, the effects of wave dispersion are minimised as they will be consistent for each scan.

Both the probe AC signal and the signal strength DC signal were recorded from the IOS detector by a digital oscilloscope (Tektronix DPO 2014 Digital Phosphor Oscilloscope, 100 MHz bandwidth, 1 GS/s) for each scan position in an automated procedure controlled by LabVIEW software[241]. Data recording was controlled by a trigger from a photodiode placed near to the path of the generation laser, which provided a clear and stable trigger signal each time the source laser was fired. For the duration of the experimental investigations safety glasses were worn to avoid eye damage; these glasses were of a suitable power and wavelength rating for both lasers. An interlocked door system was used, such that if the labratory door was opened with either laser on, the laser was automatically shut down. At each scan position the detected ultrasound was averaged 64 times, to give a good signal to noise ratio.

An automated linear stage was developed during this work to allow scanning experiments to be carried out, and was controlled through the LabVIEW software package. LabVIEW is a graphical programming language which enables the easy integration and control of different electronic systems, in this case the motor control and the acquisition oscilloscope, and is a useful tool for developing control cycles of experimental equipment[241].

The linear stage was driven by a stepper motor with a minimum step dis-

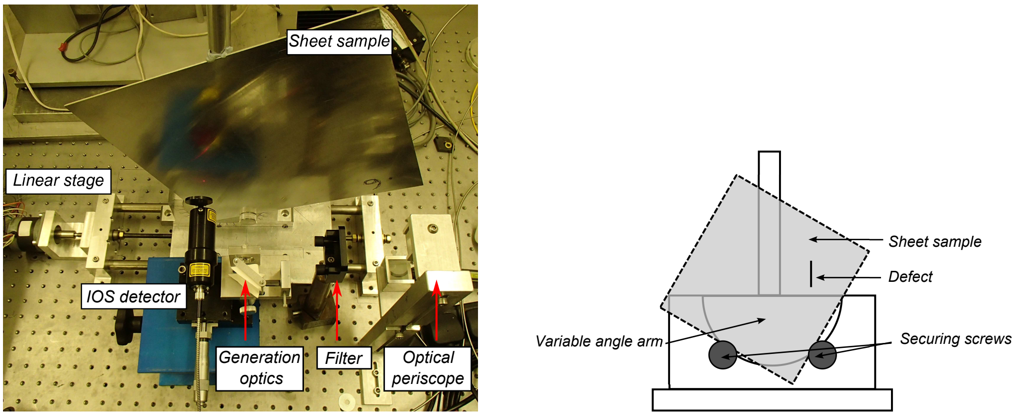

(a) Lab setup (b) Schematic diagram

Figure 3.4: Experimental setup (a) for a thin plate sample showing the IOS detector, laser source generation optics and automated linear stage. A schematic diagram for the sheet holder is also shown (b).

tance of 6.25 μm; most experiments were carried out with 8 steps between detection points, giving a travel distance of 50 μm, producing scans with a high spatial resolution. The stepper motor was controlled by a commerically avaliable Stepper Bee+ control card, provided by PC Control Ltd., which in turn was controlled through the LabVIEW software. A schematic diagram of the linear scanning setup is given in figure 3.3. The uncertainty in the position measurement for small increments, such as the 50 μm spacing used in most experiments, is negligible but for a movement of 1 cm (1600 steps) an error of ±0.1 mm was observed.

Experiments on Rayleigh wave supporting blocks (dimensions of 50 x 50 x 150 mm) were carried out with the blocks placed directly onto the linear stage and moved such that the laser generation and detection spots were scanned over the midpoint of the defect. Defects in thinner sheets (that support Lamb waves) of thickness d, with dimensions of 300 x 300 x d mm, were studied by being held in a specially designed holder. This holder allowed the defects to be angled such that the sidewall reflections at the detector were reduced, with the defects positioned such that they sat perpendicular to the laser setup. The set-up can be seen in figure 3.4. In both cases the object under test could be placed on a lab-jack on top of the linear stage such that a raster scan could be performed and enable the full defect to be examined.

For experiments carried out on pipework samples a freely rotating circular table was used with a rotational range of 360°, on which circumferential scans were taken manually every 0.5° with an uncertainty of approximately 0.25° on the position after each movement of the table. The IOS detector performs best when

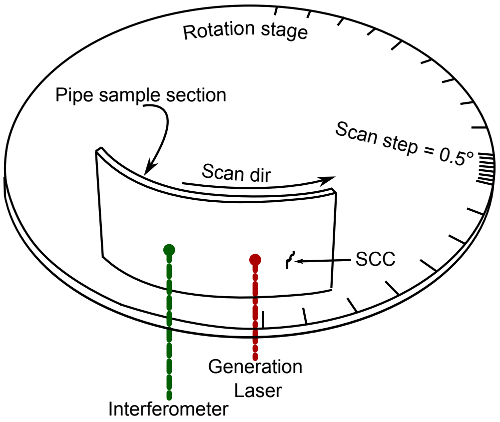

Figure 3.5: A schematic diagram showing the experimental setup for a cicumferential scan on a pipework test sample.

oriented perpendicular to the sample surface and as such the circumferential scanning system allowed a fixed arc separation to be maintained between the source and detector without the need to realign the detector to be perpendicular for each scan, as shown in figure 3.5.

The circumferential scan was preferred to a longitudinal scan as the detection laser requires realignment at each new scan position when moving vertically to ensure it is perpendicular to the sample surface, due to the curvature of the pipework samples. A misalignment can easily lead to a change in the separation, thereby introducing an extended path length into the results, which will alter the wave arrival times and make it more challenging to identify the wave modes present.

For samples with uneven or irregular geometry, such as those featured in chapter 7, the detector can be mounted on a retort stand such that it can be held perpendicular to the sample surface, and the generation laser can be targeted using a right angled prism held in a two axis holder. This enables the two laser spots to be positioned on the surface such that a constant separation is maintained. The detector was judged to be perpendicular when the received DC signal was at a maximum for a given detector standoff from the sample, indicating the position of maximum received reflected signal, as shown in figure 3.6.

3.2 Finite element method simulation

In some situations, for example on samples with complicated structures, experimental results may be insufficient on their own to validate theoretical predictions

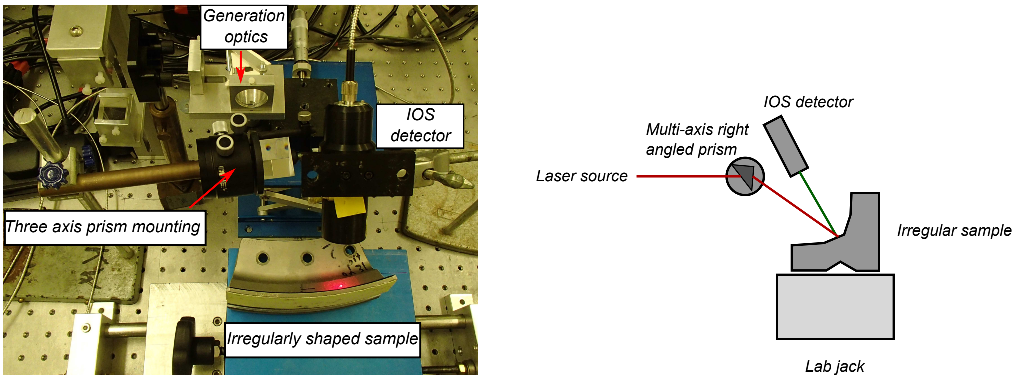

(a) Lab setup (b) Schematic diagram

Figure 3.6: Experimental setup (a) and schematic diagram (b) for an irregularly shaped test piece showing the IOS detector mounted on a retort stand and the laser source being directed onto the sample via a right-angled prism held in a three axis moveable holder.

about the interactions of ultrasound with defects. In such cases modelling of the physical system is performed, allowing aspects of the simulated system to be controlled, such as reducing the amount of backwall reflections in order to aid in the understanding of the interactions observed.

The simulation method used in this thesis is the finite element method, which splits a structure up into discrete elements, each of which represents a small part of the structure and is bordered by other similar elements[242–245], as shown schematically in figure 3.7. The method is used to solve a differential wave equation (such as equations 2.23 and 2.24) together with the boundary conditions over an object of complex shape[242]. By assuming a variation in the differential equation over an individual element, such as that caused by an ultrasonic stress/strain, once the boundary conditions on that element are considered an approximate solution of the wave equations at that element can be obtained[242]. If this solution is compatible with those for the surrounding nodes then a set of simultaneous equations can be formed and their solution will solve the wave equations at those elements, which can then be used to calculate the wave displacement, particle velocities, associated pressures and many other quantities. The FEM calculated out-of-plane surface displacement is the same measured quantity as that which is obtained from experiment but without experimental variations, such as material inhomogeneities, temperature variations, surface damage, etc, that arise in real systems. A detailed mathematical treatment of FEM simulations is found in references[243–245].

FEM models can be produced in 2D or 3D with the wave equations adjusted as appropriate, and are capable of simulating many different forms of ultrasonic

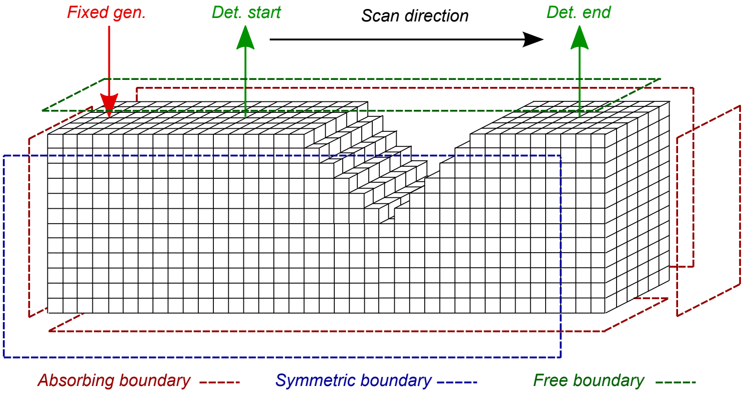

Figure 3.7: An example of a FEM simulation mesh for a Rayleigh wave incident on a v-shaped surface-breaking defect, showing the different boundary conditions applied and the scanning process. The number of nodes shown here is not representative of the true number used in a FEM simulation.

interaction depending upon the method used to excite the ultrasound within the simulation and the boundary conditions applied to the model[107]. The boundary conditions on external surfaces are described as free boundaries when they are allowed to interact in a normal fashion with any ultrasonic waves, however, this can produce lots of unwanted scattering events which lead to a complicated ultrasonic signal. To simplify this the boundaries can be made absorbing such that any ultrasonic wave that interacts with the boundary is absorbed and not propagated back into the model, reducing the complexity of recieved signals; for example in chapter 4 the interaction of a Rayleigh wave with a surface breaking defect is studied in a sample that will produce multiple unwanted sidewall reflections of the Rayleigh wave, and also bulk wave reflections from the backwall - all of which are removed if absorbing boundaries are applied.

In addition, the model can be made artificially larger by making a symmetrical boundary that mirrors the ultrasonic propagation about the boundary, thereby reducing the computational time required as only half the model volume needs to be solved. In order to avoid numerical dispersion errors, the elements defined in the simulation must be sufficiently smaller than the wavelength of the simulated ultrasound, which is largely dictated by the size of the model used and the availiable computational resources, and to maximise this the application of symmetric or absorbing boundaries is useful[243].

The implementation of this method by hand would be extremely laborious, involving solving large numbers of simultaneous equations, and therefore this form of simulation is carried out on high powered computers; even then a three dimen-

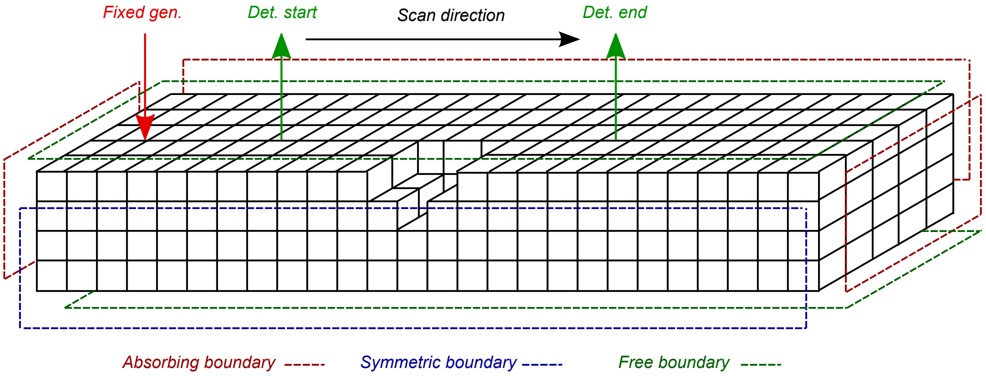

Figure 3.8: An example of a FEM simulation mesh for a Lamb wave incident on a surface-breaking defect, showing the different boundary conditions applied. In this case the defect extends only part of the width of the sample, allowing for a diffracted wave to be observed passing around the defect.

sional model may take several hours to complete. A careful balance must be struck between the number of elements used to simulate the system; too few and the model will not converge to the true value, too many and the simulation will take too long to compute.

The FEM simulations presented here were carried out using the commercial modelling package PZFlex[246]. The geometry of the FEM simulations were adapted for each experimental setup such that the overall shape was similar to that of the specimen. The FEM models were, however, scaled down in directions that were non-essential to the technique being used through the use of symmetry and by employing absorbing boundary conditions, which were applied so as to reduce the amount of sidewall scattering present. For example, for Rayleigh waves propagating in an aluminium block with a full-face width surface-breaking defect, the opposite side of the block to that with the defect and the two ends of the sample was set to be absorbing, the top surface is set to be free as it is the only surface of interest and symmetry was used about a line perpendicular to the defect, at the mid point of the defect, thus producing a situation that approximates the propagation of Rayleigh waves in a half-space,as shown in figure 3.7.

The simulations were 3D in nature as this better represents the physical systems being modelled in chapters 4, 5 and 6, however, the trade off for this is that the run-time of the simulations is dramatically increased over the 2D alternative. Simulating in three dimensions means that, for defects which do not propagate across the entire width of the sample, the diffraction of ultrasound around the defect ends can be studied. This is important for accurately replicating data for full thickness defects when the source and detector are on different sides of the defect.

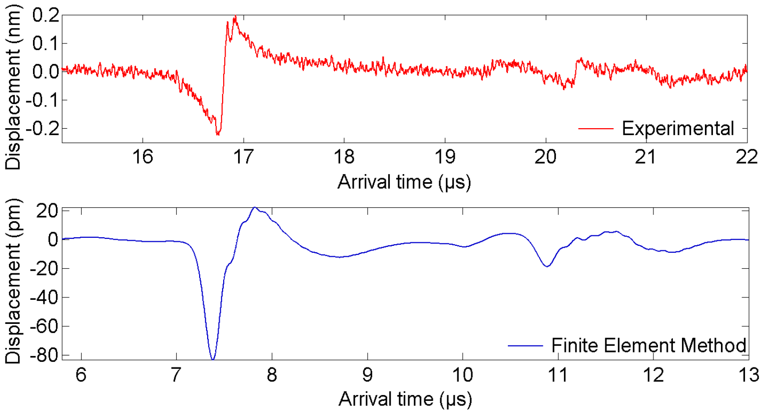

(a) A-scan

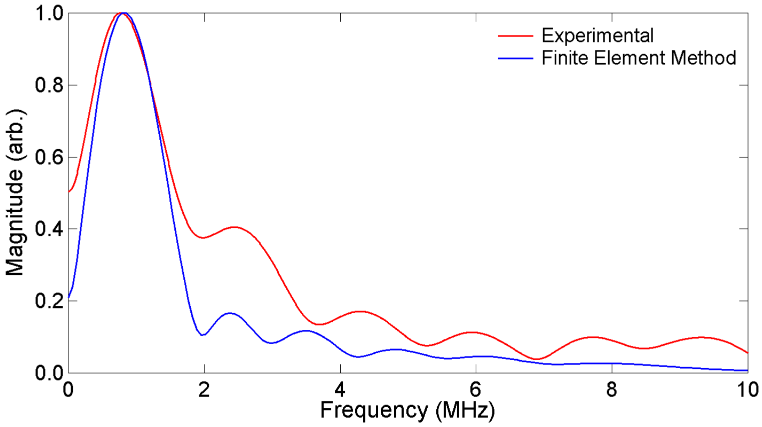

(b) Frequency content

Figure 3.9: A comparison between the wave form structure and subsequent frequency content of the experimental data and FEM data produced from a dipole force generation method for a Rayleigh wave in aluminium.

An example of a FEM simulation set-up for a defect that is not the full width of the sample is shown in figure 3.8 for a Lamb wave supporting sample. In this model both the top and bottom faces of the sample have free boundary conditions as the sample is sufficiently thin for the wave to interact with both surfaces.

For each different simulation, only the relevant simulated laser was scanned, with the other being held in a fixed position; for example in the scanning laser detection simulations the laser source was kept stationary. This acted to reduce the calculation times as there was no need to recalculate the boundary conditions of generation at each scan position.

Laser generation of ultrasound in section 4.2.1 and chapters 5 and 6 was modelled through the application of a dipole force on a series of nodes, for both Rayleigh and Lamb wave experiments. The dipole force was either applied to a

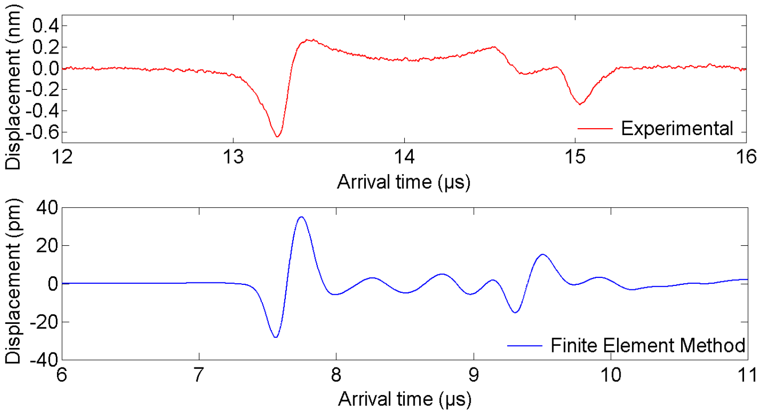

(a) A-scan

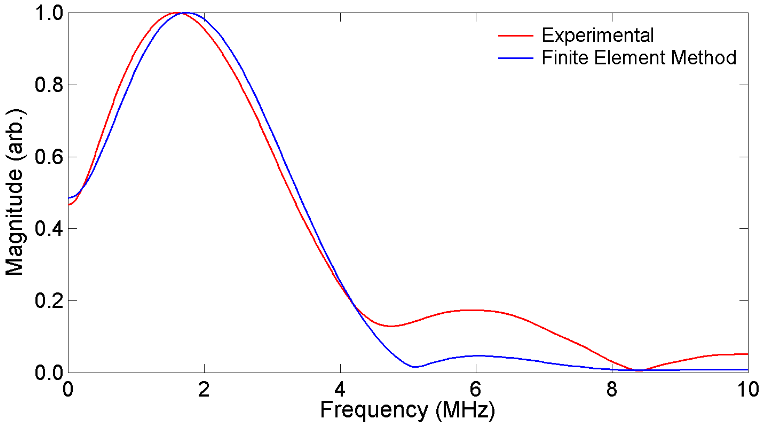

(b) Frequency content

Figure 3.10: A comparison between the wave form structure and subsequent frequency content of the experimental data and FEM data produced from a thermal generation method for a Rayleigh wave incident on a 90 ° defect.

line of nodes or a circular series of nodes depending on the generation mechanism required. This method has been shown to be reliable in replicating the ultrasonic waves observed in experimental approaches[22,95,107,128].

For simulations modelling scanning laser source experiments in section 4.4 the dipole force was replaced with a thermal generation source in order to achieve a closer agreement with the laser generation mechanism, as outlined in section 2.2.4. This generation method applies a thermal gradient, which has a gaussian distribution, to a line of nodes across the width of the line source. The heating duration and penetration depth of the heating was adjusted so that the output ultrasound of the model matched the experimentally observed form[86,95,107].

Before any correlation between the phenomena observed experimentally and those seen in the FEM simulations can be explained, the nature of the ultrasound

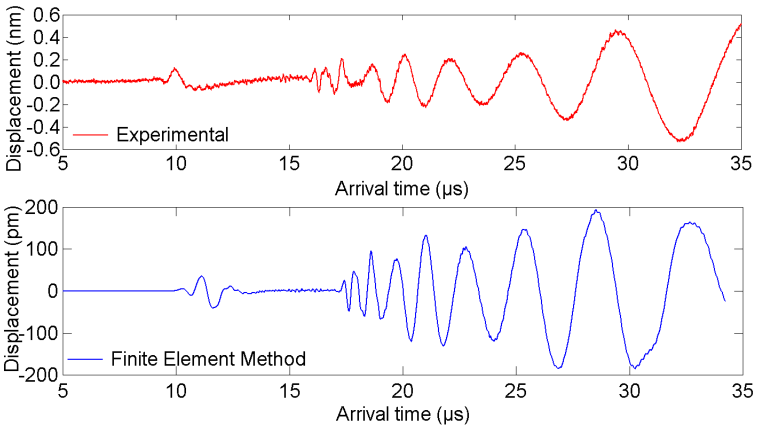

Figure 3.11: Experimental and FEM A-scans for Lamb wave propagation in 1.5 mm thick aluminium plates.

produced in the model must be compared to that seen experimentally to ensure that accurate reproduction of the waves has been achieved. This requires varying the generation conditions until the simulated waveform represents the experimental form in both shape and frequency content as closely as possible. In the case of the dipole force this requires varying the rise time and maximum value of the force applied, whereas for the thermal generation mechanism the temperature change, penetration depth and heating duration are varied to produce wave forms that closely match the experimental forms.

The wave structure and frequency content produced by simulation of a dipole force generation mechanism is compared to the equivalent experimental scanning detection approach for Rayleigh waves in figure 3.9. The arrival time for the incident Rayleigh wave differs between the experimental and simulation data due to the varying separation used in the simulations. To decrease the calculation time required for the simulations the source to detector distance is smaller than that used in the experiments, giving an earlier arrival time for the Rayleigh wave in figure 3.9.

The general structure of the wave forms between the experimental and simulation A-scans is in good agreement, with the frequency content also showing good correlation. This allows for the direct comparison between the experimental and simulated waveforms when the outcomes of scanning laser detector experiments are considered, as in chapter 4. The number of elements per wavelength ($\lambda = 3.78$ mm from peak experimental frequency) used here was 21, which has been shown to produce accurate reconstruction of experimental ultrasound in a sufficiently small calculation time[95,107].

A comparison of the structure and frequency content of the thermal gen-

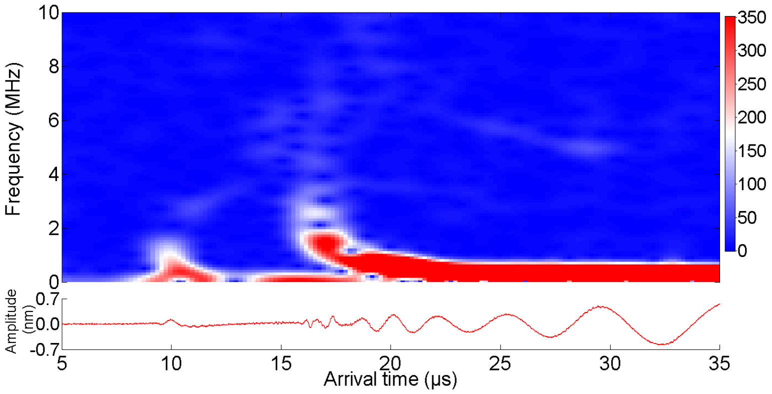

(a) Experimental Sonogram

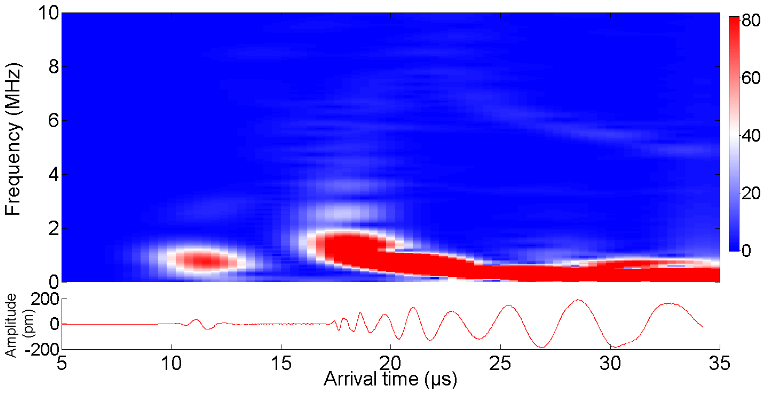

(b) FEM Sonogram

Figure 3.12: Sonograms showing the frequency content of the experimental (a) and FEM (b) data produced from a 3D dipole force generation method for a Lamb wave propagating in a thin sheet.

eration mechanism used for the Rayleigh wave simulations in section 4.4 with the experimental data is shown in figure 3.10. The wave form structure is similar between the experiment and simulation, with the exception of some higher frequency ringing of the thermoelastic model, which occurs just after the Rayleigh wave arrival. Whilst not ideal, the high frequency ringing can be dealt with through appropriate windowing of the incident Rayleigh wave, and the influence it has on the frequency content can be seen to be small, as shown in figure 3.10b.

The ringing features arrive at a constant time after the incident wave and as such will not move into the windowed region, as a reflected or mode converted wave will as the source is moved closer to a defect, as explained in section 4.4. The difference in arrival times between experiment and simulation arises due to the fact that the simulations are carried out with a varying separation between each detection point. This also means that the degree of attenuation experienced between each consecutive simulation point will vary, and this can account for some differences between the simulated and the experimental data[107]. For the thermal generation method a higher density FEM mesh is required so that the heat flow between adjacent nodes is sufficiently accurate, and in this case the number of elements per wavelength was 110.

For the simulation of Lamb waves in thin plates (chapter 5) a dipole force generation mechanism was used, with the resulting comparison between the simulation and experiment shown in figure 3.11. A 3D simulation was employed here as the defects were not the entire width of the sample, and diffraction around the tip edges was expected, which requires wave movement in a direction hitherto of only small significance in the Rayleigh wave models. To evaluate the equivalence of these simulations with the experimental data a time frequency representation (a sonogram) was employed, described in section 2.1.5. The sonograms for both experimental and simulated A-scans are shown in figure 3.12 and it can be seen that the frequency content is very similar between the two. Both have frequency content arriving at times that correspond to the arrival times of different Lamb wave modes, as explained in chapter 5. This is shown by the similar shaped frequency features that arrive at the same times relative to one another in both experimental and simulation data. Similarly to the dipole force generation for Rayleigh wave simulations, the number of elements per wavelength used was 21, which has been shown to give an accurate reconstruction[22]. The material properties for the standard materials used in all simulations were taken from Kaye and Laby[141]. Detection was modelled by extracting the out-of-plane displacements from single nodes, giving a higher spatial resolution when compared with the experimental data.

Through a combination of the experimental methods and the finite element method simulations described in this chapter the interactions of various ultrasonic surface waves with different geometry surface-breaking defects were studied, allowing the identification of several interesting near-field phenomena and the subsequent characterisation of these defects.

Chapter 4

Rayleigh wave interactions with surface-breaking defects

Material defects come in a variety of forms, from the microscale to the macroscale, and there is no single method that is appropriate for all defect types[119]. This thesis is concerned with defects that propagate downwards into the material from the sample surface, in a range of sample configurations with a variety of thicknesses and geometries. To begin, a study of the interactions between surface acoustic waves with surface-breaking defects is presented, in which the thickness of the test samples results in the dominant wave mechanism being a Rayleigh-like wave, as described in section 2.1.4.1. Of particular interest is the development of a reliable method to identify defects similar to rolling contact fatigue defects in rail tracks, as described in section 1.4.1, utilising the relatively new technique of near-field scanning laser inspection that allows for a direct study of the changes in ultrasonic propagation as they occur due to the presence of defects[23,104,234,235,237].

4.1 Detection of angled surface-breaking defects

Detection of surface-breaking defects in bulk materials can be problematic for many conventional ultrasonic techniques that rely on the reflection of bulk waves from defects[247]. The small reflected signal originating from the defect can potentially be obscured by a large backwall reflection, if the defect is very close to the wall, making defect detection challenging without significant data processing to differentiate between the two signals. It is also difficult to detect multiple defects that are close together as shallower defects are obscured in the shadow of deeper defects. It has been shown that the use of a wave that travels along the surface of the material can provide reliable defect detection and depth estimation for surface-breaking defects through the study of the influence the defect has on the reflection and transmission behaviour of the surface acoustic wave[90,164,248,249]. Time of flight investigations on surface wave reflections have been shown to give information about the defect location, and to some extent the severity of the defect, as described in section 2.3[21,228–231,250]. These techniques all examine the reflected or transmitted surface wave in the defect far-field, however, recent work has begun to examine the potential of using the near-field interactions between an incident surface wave and a surface-breaking defect to identify material damage[23,104,234,235,237].

Of particular interest to this research is the exploitation of the near-field amplitude enhancement described in section 2.3.1, with the aim of being able to position defects and obtain information about the geometry of the defect[95,107,164,235,236,239]. These near-field effects are reported here for two different experimental approaches, the first of which uses the enhancement observed when a laser source is scanned over a defect, where a combination of the change in the boundary conditions of ultrasonic generation, the truncation of the source dimensions and a superposition of incident and direct reflected waves are responsible for an increase in the amplitude and peak frequency content of a Rayleigh wave[95,235].

The second method uses a laser detector that is scanned over a defect and a superposition between the incident Rayleigh wave and several mode converted waves generated at the defect provides a similiar increase in the amplitude and peak frequency content[95,115]. These two approaches have previously been used to detect defects that propagate normal to the material surface, however, as was seen for the example of rolling contact fatigue defects in rail track in section 1.4.1, not all defects have this simple structure. Variations in the near-field behaviour as a function of defect angle show promise for the detection and characterisation of a wider range of defects[95].

Previous studies of the near-field enhancement in Rayleigh waves, as described in section 2.3.1, focused on the positioning of notched, square-based defects set perpendicular to the sample surface[23,164,235,237]. Whilst this is a good starting point for building an understanding of the near-field interactions, the case in which the defect does not propagate perpendicular to the sample surface must also be considered; many common defects, such as rolling contact fatigue on rail tracks, do not propagate normal to the sample surface, and therefore the incident wave will experience a different interaction to that which has been studied previously for perpendicular notches[96,98,99]. It has been shown that for a small separation (up to 20 cm) between ultrasonic source and detector the guided wave that propagates in rail tracks[251] exhibits Rayleigh-like behaviour[101], and so the development of an understanding of the near-field interactions between a Rayleigh wave and a surface-breaking defect is useful in understanding similar interactions between waves and defects in industrially significant structures, such as railway tracks.

The investigations carried out here were focused on developing an understanding of the near-field interactions with v-shaped defects set at various angles to the sample surface[95,104,105,107,115,252], which provide a better approximation for the opening geometry of the real defects shown in section 1.4.1. Far-field studies of angled defects have previously been performed with the aim of obtaining an estimate of the crack depth through relating the reflection and transmission coefficients to the defect depth[106,107]. From these far-field studies it was seen that the interaction of a surface acoustic wave with an angled defect was different from the interaction observed for a perpendicular defect, and the existence of a corresponding variation in the near-field behaviour for Rayleigh wave interactions with angled defects is investigated in this chapter.

4.2 Scanning laser detector enhancements from angled defects

To study the near-field enhancement behaviour of angled defects, artificial defects were created in aluminium blocks (dimensions of 50 x 50 x 150 mm) through laser micromachining (see section 1.4.3) to give a defect with a v-shaped side profile. The defects ran the full width of the sample surface and were all of length 2 mm but set at different angles to the sample surface, ranging from $20^\circ \leq \theta \leq 150^\circ$, to simulate the opening part of a real defect. The defect opening was 500 μm at the top surface, and a schematic diagram is shown in figure 4.1.

Experiments were carried out using a linear scan with the experimental setup shown in section 3.1, in which both the laser detector and the laser source, held at a fixed separation (of approximately 39 mm) to one another, were passed over the defect region. This section deals with the detector passing over the defect, with the case in which the source passes over the defect covered in section 4.4. A scan-step size of 50 μm was used in order to achieve a high spatial resolution, and a line-focused pulsed generation laser with dimensions of 6 mm by 300 μm was used as a directional ultrasound source, as described in section 3.1, in order to reduce the back and side wall reflections at the detector[95,107].

The experimental data was validated through the use of 3D FEM simulations

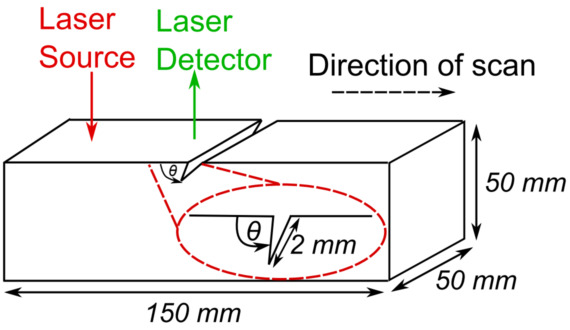

Figure 4.1: Schematic diagram of the aluminium blocks used to study angled surface-breaking defects of length 2 mm with linear scanning of the dual laser system, shown here in the scanning laser detection configuration.

using a fixed position dipole force to simulate the laser line source, as described in section 3.2. A simulated angled v-shaped defect was set into the top surface of a 3D model, with the defect extending across the width of the model, such that no diffraction around the defect ends was possible. The angle of this simulated defect was varied between $20^\circ \leq \theta \leq 170^\circ$. The ends of the model were set to have absorbing boundary conditions in order to reduce the amount of unwanted scattering and reflection.

The model top surface was set to have a free boundary condition, allowing the ultrasound to propagate. Symmetry was used about the midpoint of the defect to reduce the calculation time, and the out-of-plane displacement was recorded on a series of nodes passing over the midpoint of the defect. The dipole force used to simulate the ultrasonic source was applied to a line of nodes about the midpoint of the sample, perpendicular to the line of symmetry, as shown in figure 3.7. The modelling process presented in this chapter only was carried out by Dr. B. Dutton[95,107].

4.2.1 Scanning laser detection enhancement of Rayleigh waves

The near-field interactions between an incident Rayleigh wave and angled surface-breaking defects were studied for the case in which the laser detector was moved over the defect, with the out-of-plane surface displacement recorded at each scan position. The Rayleigh wave velocity in aluminium is well known ($v_R = 2940\ \mathrm{ms}^{-1}$), and therefore for a fixed propagation distance the arrival time of the incident Rayleigh wave is easily identified from the A-scans; see figure 4.2a. As the incident Rayleigh wave has a constant arrival time any changes the wave may undergo, such as interaction with a defect, can be observed by monitoring a time windowed section of the A-scan that corresponds to the Rayleigh wave arrival time.

A time window was selected which covered the incident Rayleigh wave, such that the peak-to-peak amplitude of the Rayleigh wave could be recorded at each detection position. The Rayleigh wave is non-dispersive in a homogeneous material (see section 2.1.4.1) and therefore the Rayleigh wave structure will not vary between scans for an undamaged specimen[89]. In addition to studying the peak-to-peak amplitude, the frequency content of the Rayleigh wave is also monitored by performing a fast Fourier transform (FFT) on the windowed wave at each detection point.

The time-windowed Rayleigh wave is shown in figure 4.2b for three scan positions, the first of which (in red) is at a position with the detector far away from the defect, the second (in blue) is when the detector is very near to the defect and the third (in black) is when the defect lies between the detector and the source. An increased peak-to-peak amplitude is evident when the detector is close to the defect; this is termed the amplitude enhancement of the surface acoustic wave. A subsequent drop in the peak-to-peak amplitude is observed when the defect lies between the source and the detector, as a portion of the incident wave is reflected and mode converted away and, as such, the wave transmitted past the defect is reduced; this variation in the transmission in the region of surface-breaking defects can be used to identify the depth of the defect[107].

A useful method for visualising the propagation of ultrasonic waves in a material is a B-scan, in which the A-scans from each adjacent scan position are stacked next to one another, producing a surface image in which each line is an A-scan. A colour scale is employed to represent positive and negative surface displacements, and this produces a pattern of light (positive displacement) and dark (negative displacement) regions from which the wave-paths of ultrasonic waves can be inferred.

The appearance of a B-scan is characteristic of the geometry of the defect that is studied[86] and B-scans for two different defect angles are shown in figure 4.3. For the work presented in this thesis the defect is located at a detector position of zero on each scan, with negative positions relating to the region in which both the detector and source are on the same side of the defect, and positive positions corresponding to the area in which the defect is between the source and the detector.

In addition to the incident Rayleigh wave (R_i), which has a constant arrival time (arriving at 13 μs), there are other waves present in figure 4.3 with varying arrival times, such as the reflected (R_r) and transmitted (R_t) Rayleigh waves. These will be shown in section 4.2.2 to be dependent upon the defect angle. The Rayleigh wave enhancement is evident when the detector position is very close to zero, with

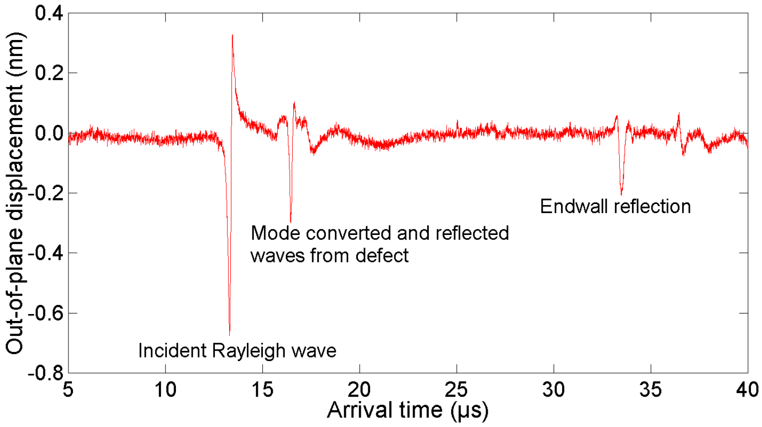

(a) Experimental A-scan

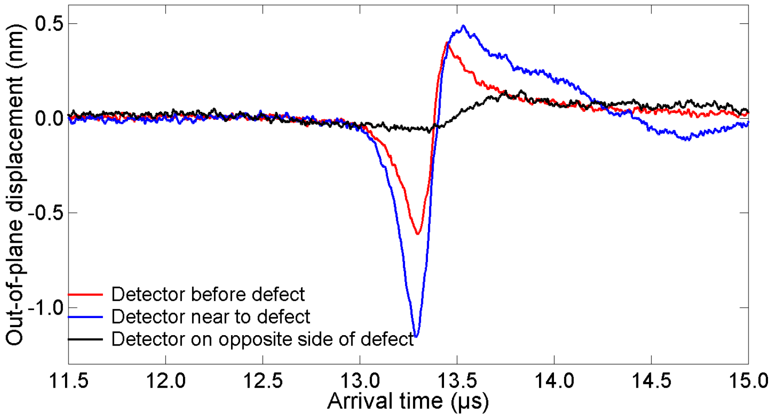

(b) Windowed Rayleigh wave

Figure 4.2: Experimental A-scan for a Rayleigh wave incident on a 90 ° defect taken at a distance of 6 mm from the defect, showing reflected and mode converted waves (a) and a time window taken over the incident Rayleigh waves at three different detector positions (b).

the large increase observed in the positive and negative displacement of the incident Rayleigh wave showing as a bright white and black pattern at this position; this is more pronounced in figure 4.3 for the 40 ° than for the 90 ° defect. It is discussed in section 4.2.2 how these characteristic images may be used to identify the defect angle and provide information about the defect.

To quantify the enhancement the peak-to-peak amplitude of the incident Rayleigh wave is measured and plotted across the duration of a scan. The variation in the peak-to-peak amplitude from experimental data is shown in figure 4.4 for two different defects, one at an angle of 40 ° to the sample surface and the other at 90 °, corresponding to the B-scans in figure 4.3.

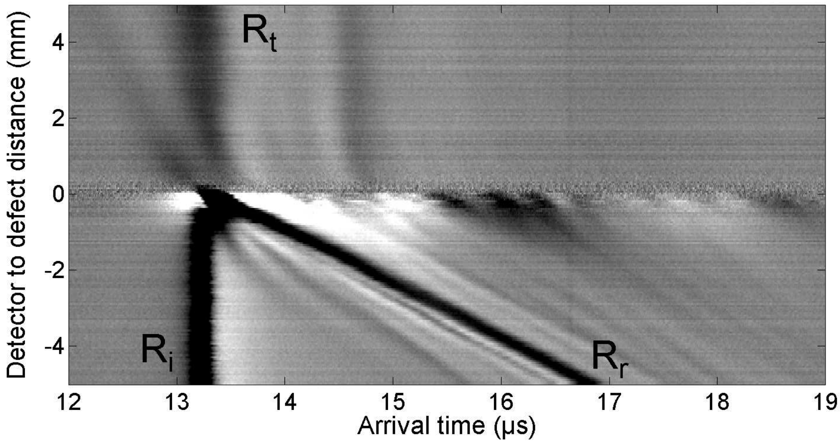

(a) 40 ° defect

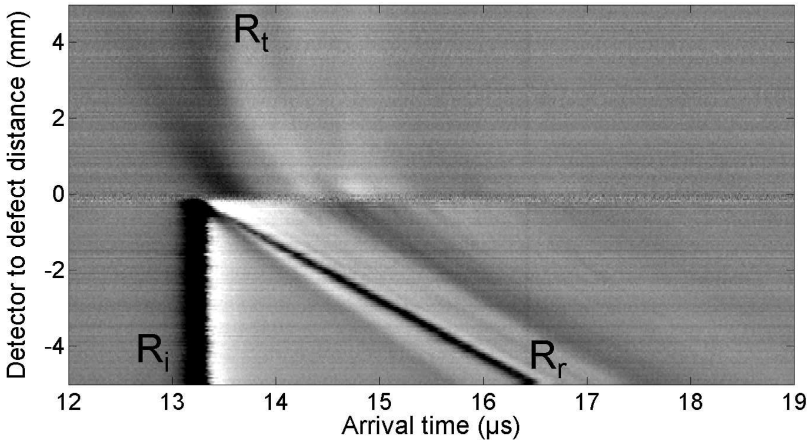

(b) 90 ° defect

Figure 4.3: B-scans for 40 ° (a) and 90 ° (b) angled defects for the case in which the detector is moved over the defect. The incident (R_i), reflected (R_r) and transmitted (R_t) Rayleigh waves are labelled.

For both defect angles a region of steady peak-to-peak amplitude is seen when the detector is away from the defect, with a large increase in the peak-to-peak amplitude when the detector is moved very close to the defect. This amplitude change is different for each defect orientation and the resulting angular dependance can be used to explain the enhancement phenomenon (section 4.3). When the defect lies between the source and the detector (positive detector positions) a drop in the peak-to-peak amplitude is observed as part of the incident Rayleigh wave is reflected or mode converted away at the defect.

The location at which this enhancement occurs, which can be seen in figure 4.4 to occur slightly prior to the defect, can be used to position the defect, as the

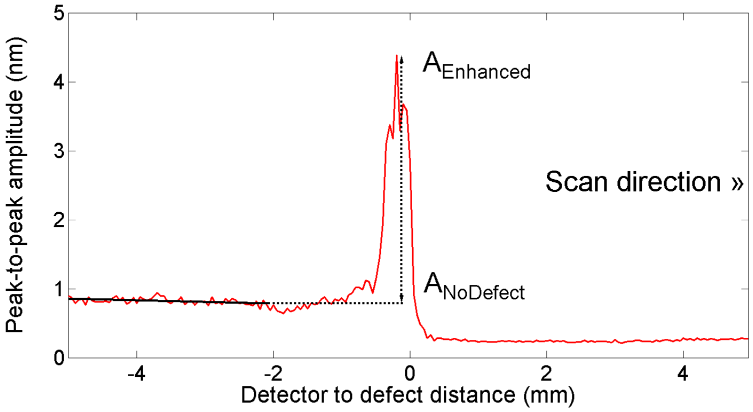

(a) 40 ° angled defect

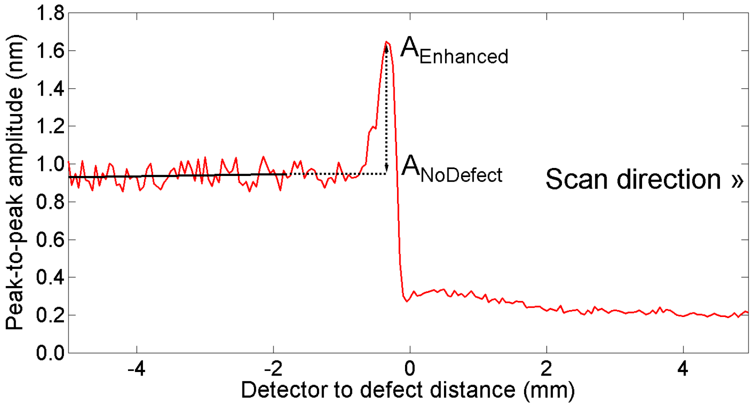

(b) 90 ° angled defect

Figure 4.4: Peak-to-peak amplitude tracking for a Rayleigh wave incident on surface-breaking defects angled at 40 ° (a) and 90 ° (b) to the sample surface for the case in which the laser detector is moved over the defect.

detector position at the point of enhancement is known. To quantify the amplitude changes in the near-field, an enhancement factor, E_{Amp}, is formed from a ratio of the maximum amplitude level, $A_{Enhanced}$, to that measured away from the defect, $A_{NoDefect}$, using the following equation,

$$E_{Amp} = \frac{A_{Enhanced}}{A_{NoDefect}} \quad . \tag{4.1}$$

The ratio was obtained from both the experiments and the FEM simulations, with the enhancements being larger in the FEM simulations due to the fact that the amplitude is recorded at an very small point, whereas the observed experimental enhancement is averaged over the 200 μm diameter spot area[95]. For a detector spot of finite area the out-of-plane displacement observed is an average over the surface

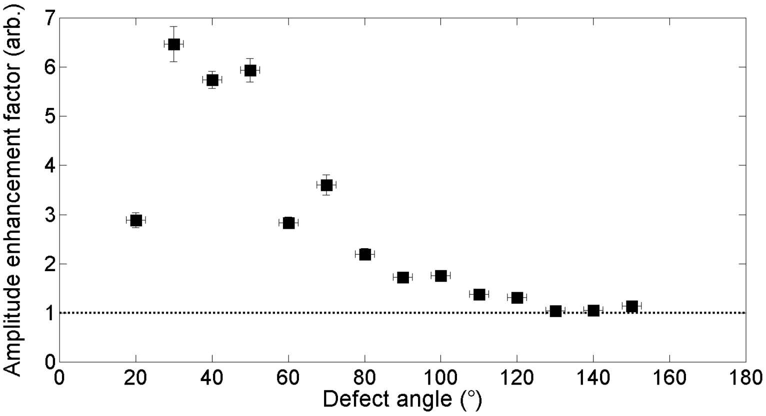

(a) Experimental enhancement factors.

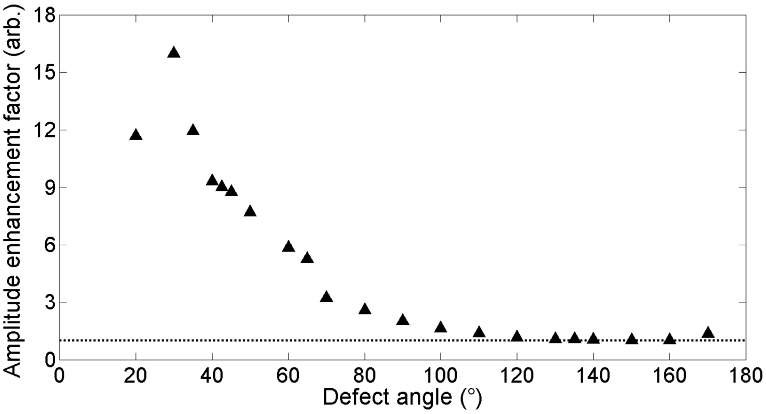

(b) Simulation enhancement factors.

Figure 4.5: Amplitude enhancment factors as a function of defect angle for the case in which the laser detector is moved over the defect for experimental (a) and FEM simulated (b) data.

that is illuminated. This means that, for the enhancement that occurs close to the defect, only part of the detector lies at the maximum enhancement position and the remainder is still on material that is not experiencing the full amplitude increase, therefore the average out-of-plane displacement is lower than the peak value in the illuminated area.

The variation of the amplitude enhancement factor E_{Amp} as a function of the defect angle to the sample surface is shown for both experimental data, figure 4.5a, and FEM simulations, figure 4.5b. In both approaches the enhancement factor varies with the defect angle, with a larger enhancement observed for smaller angles to the horizontal. The FEM simulation data covers a wider range of defect angles as it is not constrained by manufacturing concerns.

For angles between $20^\circ \leq \theta \leq 90^\circ$ the enhancement factor shows a large

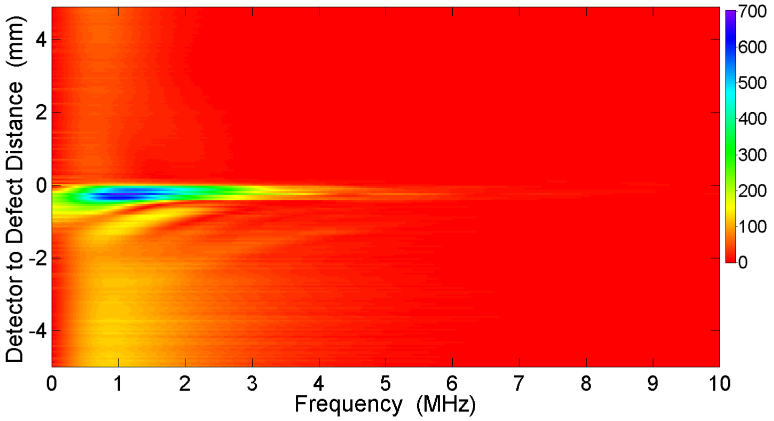

(a) 40 °

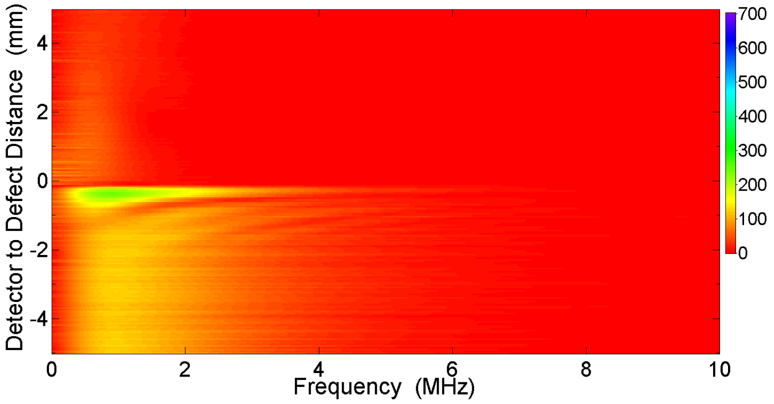

(b) 90 °

Figure 4.6: Frequency B-scans for two different defect angles, 40 ° (a) and 90 ° (b), obtained by stacking FFT data from the Rayleigh wave time window for scanning laser detector experiments.

variation and can be used as a finger-printing method to estimate the angle of the defect to the sample surface[86], however, at larger angles, $\theta \geq 120$ ° the variation in the enhancement values is small for both experimental and simulated data. This makes an estimation of the defect angle more challenging unless the scan is also performed from the other direction, effectively turning, for example, a 100 ° angle to the surface into an 80 ° angle. This increases the likelihood of a correct estimate of the angle.

The largest enhancement factors occur for defects with angles close to 30 °, which makes the technique ideally suited to the detection of critical RCF defects, which propagate at a preferential angle of approximately 25 ° to the sample surface, as the detected signals at the crack are likely to be large[98,99]. Previous work on near-field enhancement of Rayleigh waves at 90 ° defects reported signal enhance-

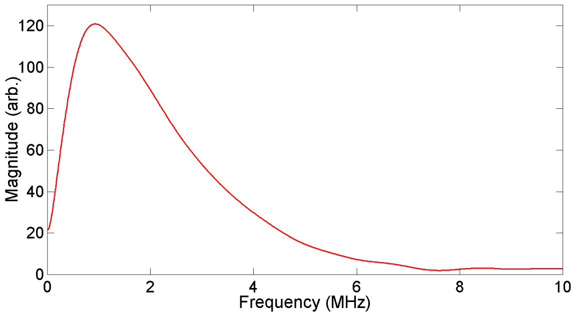

Figure 4.7: Frequency content of windowed Rayleigh wave for a defect free region.

ments at the defect that were 1.6 times the size of the signal away from the defect[104], however, the enhancements found in this work are far larger, with enhancements of up to 6.4 times the signal away from the defect measured experimentally for a 30 ° defect. This large increase at shallower angles is discussed in section 4.3.

The apparent drop in the enhancement factor for a 20 ° defect is perhaps real but could also be caused by changes in the shape of the defect arising from difficulties in the manufacturing process for very shallow defects. From visual inspection the wedge-like part of the 20 ° defect did not taper smoothly to a point, and this may cause a disruption in the mechanisms behind the enhancement described in section 4.3. Similar issues with the discretisation of the FEM mesh in the thin part of the sample may have led to a similar effect in the simulated data. Currently only one data point exhibits the drop in enhancement factor, and further careful inspection of very low angled defects is required to ascertain whether the drop in the enhancement factor at a defect angle of 20 ° is real.

At each scan position a fast Fourier transform was performed on the time window containing the incident Rayleigh wave and the frequency content of the signal at each scan position was stacked sequentially to form a frequency B-scan. Frequency B-scans are shown in figure 4.6 for two experimental scans for defect angles of 40 ° and 90 °, and an increase in the frequency content at the defect can be seen for both defect angles as a horizontal band of increased magnitude near a position of 0 mm, with the increase in the frequency content being larger for the shallower angled defect[95]. The sloping bands of frequency content near to the defect are caused by windowing effects whereby the separation of the incident and reflected Rayleigh waves leads to a second frequency component in the FFT[95].

The frequency content of the incident Rayleigh wave for a position at which the detector is far away from the detector is shown in figure 4.7. If the magnitude of a chosen frequency component within this spectrum, in this case the magnitude

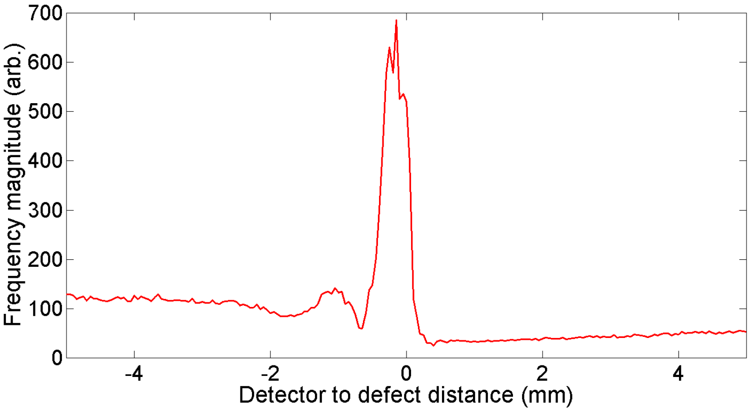

(a) Magnitude at 0.98 MHz

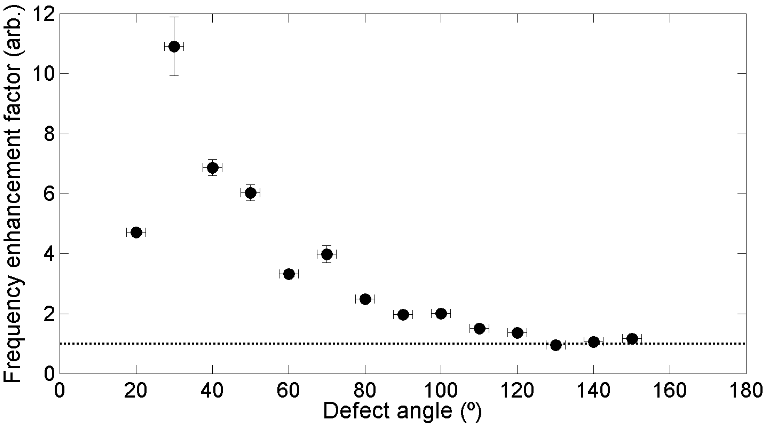

(b) Frequency enhancement factors

Figure 4.8: Magnitude of the frequency content of the time windowed Rayleigh wave at a frequency of 0.98 MHz as a function of detector position for a scanning laser detection experiment over a 40 ° angled defect (a) and the variation in frequency enhancement factor at 0.98 MHz as a function of defect angle (b).

of the peak frequency of 0.98 MHz, is studied at each detector position an enhancement that has the same form as the peak-to-peak amplitude enhancement is observed, and this analysis can be seen in figure 4.8a. The frequency enhancement varies as a function of defect angle in the same manner as the amplitude enhancement in figure 4.5, and can also be used as a finger printing technique to identfy the angle of a surface-breaking defect, as shown in figure 4.8b[95]. If the magntiude of the frequency content of the Rayleigh wave at a higher frequency, for example at 4 MHz, which has a low magnitude when the detector is far away from the defect, is tracked then an increase is also observed as the detector approaches the defect, similar to that in figure 4.8a. The increase in frequency content at a value that has a magnitude close to zero when no defect is present gives a strong indication of a surface-breaking defect. The mechanisms behind the enhancement of Rayleigh waves as the laser detector is scanned over the defect are explained in section 4.3.

4.2.2 Rayleigh wave mode conversion at a surface-breaking defect

In the B-scan images shown in figure 4.3 the incident, reflected and transmitted Rayleigh waves were identified, however, several additional waves can be observed, which have been mode converted from the incident Rayleigh wave as it interacts with the interfaces of the defect. The arrival times of these mode converted waves at the detector for a Rayleigh wave incident on a defect orientated normal to the sample surface have been calculated previously[130,228], however, the arrival times of these mode converted waves are in fact angle dependent. The angle dependence of these mode converted waves produces the unique pattern of waves observed in the B-scans in figure 4.3, and determination of the arrival times of these waves enables the angle of the defect to the surface to be found[107].

For a Rayleigh wave incident on a perpendicular defect a reflected wave is scattered back towards the source and a transmitted wave passes under the defect, however, in addition it has been observed that mode converted shear and longitudinal bulk waves and a surface skimming longitudinal wave are also created[236]. Mode conversion and reflection of waves at the defect can occur at the defect opening or at the defect tip, and the resulting travel time for waves back towards the detector is dictated by the velocity and the position at which the backward travelling wave is produced. A similar dependence is observed for the transmission of mode converted waves past the defect.

The arrival times of the angle dependent mode converted and reflected longitudinal and shear waves can be calculated via a modification of the equations previously developed for perpendicular defects[107,236]. The following equations depend upon a knowledge of the fixed separation of the source and detector, and a knowledge of the distances from these to the defect opening, which can be obtained from the position of the detector at the enhancement peak. To calculate the arrival times of mode converted waves when the detector is positioned on one side or the other of the defect, the modulus of the distance of the detector to the defect is defined as x, the propagation distance from source to defect as l, the defect length as d and the angle of the defect to the sample surface as θ, with a schematic diagram shown in figure 4.9. In the following discussion a wave marked with a subscript r is a reflected wave mode detected at position 1, while the subscript t denotes a transmitted wave, detected at position 2.

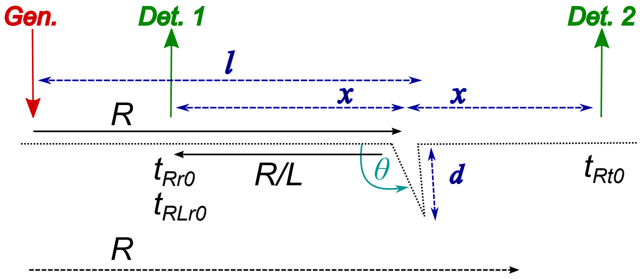

(a) Zeroth order interactions

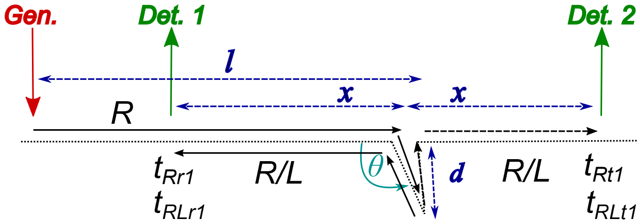

(b) kth order interactions

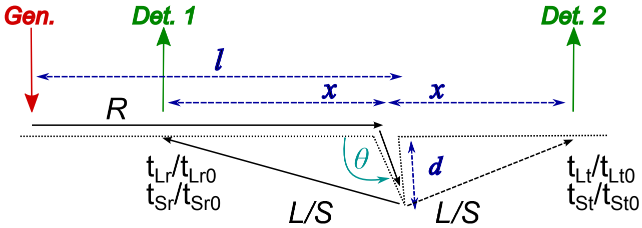

(c) Bulk wave interactions

Figure 4.9: A schematic diagram of the wave travel paths for two detector positions for the zeroth order surface waves (a), the kth order surface waves (b) and for the bulk waves generated at the defect tip (c).

First consider the direct reflection of the incident Rayleigh wave from the defect, with velocity $v_r = 2940$ ms^{-1} [141], denoted by subscript R. This is a process that can occur at the defect opening itself or at the bottom of the defect. There is the possibility for multiple reflections of the Rayleigh wave between the bottom of the defect and the opening, and the number of reflections undergone is represented by the integer k, for which a value of zero corresponds to the direct reflection from the defect opening, as shown in figure 4.9a[107,228]. The arrival time at the detector for the reflected and transmitted Rayleigh wave at a distance x before or after the defect is given by,

$$t_{Rrk} = t_{Rtk} = \frac{(l + x + 2kd)}{v_r} \quad . \tag{4.2}$$

For these transmitted and reflected Rayleigh waves, the angle of the defect has no influence on the arrival time at the detector. The length of the defect influences the arrival times for those interactions with a value of $k \geq 1$ as the Rayleigh wave can be considered to travel close to the surface of the material, such that, for the example of the $k = 1$ reflection, the wave can be traced along the top surface, down the defect and then back up again before travelling back to the detector following the path of the material surface[228]. For the Rayleigh wave interaction with $k = 0$, the transmitted wave is the low frequency part of the incident Rayleigh wave that will penetrate beneath the defect[107].

Mode conversion of the incident Rayleigh wave to a surface skimming longitudinal wave, with velocity $v_L = 6300$ ms^{-1}[141], denoted by subscript RL, also occurs at the defect opening, as shown in figures 4.9a and 4.9b[130,236,237]. This mode conversion is also independent of the defect angle as the mode converted wave again follows the sample surface. The arrival times at the detector of the transmitted and reflected longitudinal surface skimming wave are described by the following equation, in which the constant k again represents the number of transits along the length of the defect before mode conversion occurs;

$$t_{RLrk} = t_{RLtk} = (l + 2kd)/v_r + x/v_L \quad . \tag{4.3}$$

In addition to the surface waves produced from the interaction of the incident Rayleigh wave there also exist a number of mode conversions to both longitudinal and shear bulk waves that occur at the defect tip. These mode conversions have been reported for defects perpendicular to the sample surface[236], however, as they are produced at the defect tip their arrival time at the detector is dependent upon the angle of the defect to the sample surface, with this process shown schematically in figure 4.9c.

The bulk waves produced during this interaction propagate into the material and a portion of the wave will arrive at the detector at the top surface of the material. The arrival times of the longitudinal bulk waves, with velocity $v_L = 6300$ ms^{-1}, denoted by subscript L, for both the reflected and transmitted waves are described by the following equations,

$$t_{Lr} = (l + d)/v_r + \sqrt{(x^2 + d^2 - 2xdcos\theta)}/v_L \quad , \tag{4.4}$$

$$t_{Lt} = (l + d)/v_r + \sqrt{(x^2 + d^2 + 2xdcos\theta)}/v_L \quad . \tag{4.5}$$

The arrival times of the shear bulk waves, with velocity $v_S = 3110$ ms^{-1}[141] and subscript S, originating at the defect tip have a similar form as they follow the same propagation path (shown in figure 4.9c), and are described by the following equations,

$$t_{Sr} = (l + d)/v_r + \sqrt{(x^2 + d^2 - 2xdcos\theta)}/v_S \quad , \tag{4.6}$$

$$t_{St} = (l + d)/v_r + \sqrt{(x^2 + d^2 + 2xdcos\theta)}/v_S \quad . \tag{4.7}$$

There exists a final set of mode converted waves which are a series of bulk waves which are created from the interaction of the low frequency (k=0) Rayleigh wave that interacts directly with the defect tip. For both families of bulk wave mode conversions the arrival time equations tend towards those reported previously for a defect perpendicular to the sample surface when $\theta = 90^\circ$[236]. Both a longitudinal and a shear bulk wave are produced through this interaction, with arrival times that are again dependent upon the defect angle, with the following equations giving their respective arrival times,

$$t_{Lr0} = (l - dcos\theta)/v_r + \sqrt{x^2 + d^2 - 2xdcos\theta)}/v_L \quad , \tag{4.8}$$

$$t_{Lt0} = (l - dcos\theta)/v_r + \sqrt{x^2 + d^2 + 2xdcos\theta)}/v_L \quad , \tag{4.9}$$

$$t_{Sr0} = (l - dcos\theta)/v_r + \sqrt{x^2 + d^2 - 2xdcos\theta)}/v_S \quad , \tag{4.10}$$

$$t_{St0} = (l - dcos\theta)/v_r + \sqrt{x^2 + d^2 + 2xdcos\theta)}/v_S \quad . \tag{4.11}$$

The arrival times of all of the possible wave modes can be calculated and superimposed onto the B-scans, as shown in figure 4.10 for two different experimental defect angles. It can be seen that the expected arrival times correlate very well with the wave patterns shown in the B-scans. Not all of the modes can be easily observed as the experimental data only shows the out-of-plane component of the surface displacement, and is not sensitive to the in-plane components of the wave displacements, and also this does not take into account any changes due to the smaller frequency-thickness in the defect itself that is present for shallow angles (see section 4.3).

An estimate of the defect angle can be made by varying the theoretical angle, θ, used to produce the expected wave arrival times until the arrival times that are overlaid on the B-scans in figure 4.10 correlate to the light and dark patterns, however, not all of the wave modes are visible due to the detector only being sensitive to the out-of-plane motion and this method can only give a qualitative assessment of the defect angle.

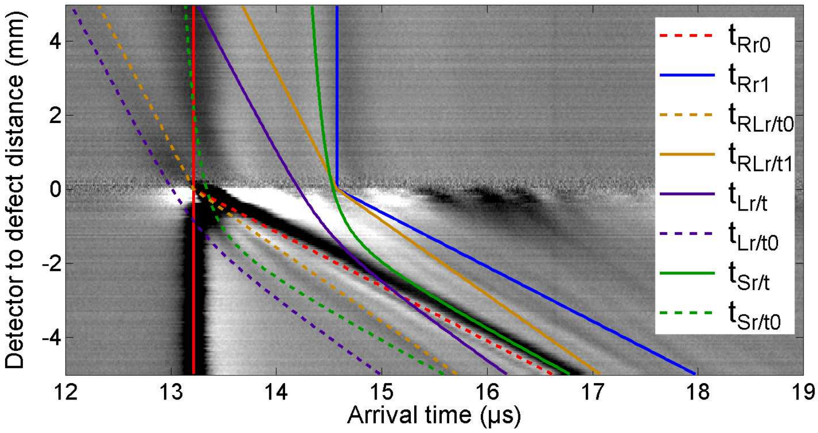

(a) 40 °

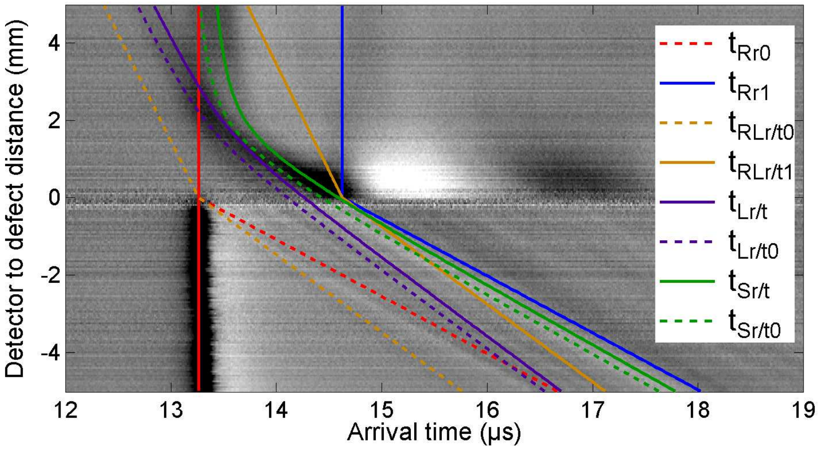

(b) 140 °

Figure 4.10: Scanning detector B-scans for two different defect angles, 40 ° (a) and 140 ° (b) with the arrival times of mode converted waves generated at the defect overlaid.

4.3 Scanning laser detection enhancement

The enhancement previously observed for a Rayleigh wave incident on a surface-breaking defect propagating normal to the surface is attributed to constructive interference between the incident wave, the reflected Rayleigh wave and the mode converted surface skimming longitudinal wave[236,237]. The amplitude of the surface skimming longitudinal wave has been shown to decrease as it travels away from the defect, becoming negliable far away from the defect[237]. For the detector located at a certain position close to the defect the arrival times of these waves at the detector coincide, forming a superposition of the waves that results in constructive interference between the waves, leading to an increase in the out-of-plane displacement on the material surface. The increase in the out-of-plane displacement is responsible for the enhanced peak-to-peak amplitude and frequency content of the time windowed Rayleigh wave.

The low frequency components of the incident Rayleigh wave penetrate further into the sample (with the majority of the wave energy contained within a depth of approximately one wavelength[26,89]) and hence some of the energy can be transmitted under the defect, and therefore the enhancement is more prominent at higher Rayleigh wave frequencies as their smaller penetration depth means that they are more likely to be affected by a defect, and so contribute to the superposition at the defect.

For defects that have an inclination that is close to 90 ° the constructive interference between the incident and reflected Rayleigh waves and the surface skimming longitudinal wave is still the dominant mechanism for forming a signal enhancement, however, in figure 4.5 the enhancement was seen to decrease as the defect angle was increased to larger angles. For the defects studied here, the length of the defect was set at 2 mm, however the vertical depth to which the defect extends will vary depending upon the angle of the defect to the surface, with, for example, a defect set at 150 ° having a vertical depth of 1 mm compared to the 2 mm of the 90 ° defect. With the smaller vertical depth, there is an increased range of Rayleigh wave frequencies that have a penetration depth that allows some energy to pass under and be transmitted past the defect. For obtuse defect angles the amount of the incident Rayleigh wave that is transmitted has also been shown to increase compared to that for a perpendicular defect, with a corresponding reduction in the amount of the wave that is reflected[106,107]. This is caused by the fact that the path that the Rayleigh wave travels as it encounters the defect only experiences a slight deviation at the defect opening, with the wave moving down the angled slope, and therefore passage of the wave to the defect tip occurs easily, allowing a large amount of the incident wave to be transmitted. The amount of the Rayleigh wave that is reflected and mode converted back towards the detector is therefore reduced, giving a corresponding reduction in the enhancement for defects that have obtuse inclinations to the surface. For shallower defects (<90 °) the change in the surface profile is much more sudden giving a the steeper change in the angle of the path travelled by the incident Rayleigh wave as it travels down the defect, and thus more of the incident wave is reflected back, increasing the contribution of the reflected wave to the superposition at the enhancement position.

Whilst the defects that have acute angles to the surface are also of reduced vertical depth compared to the 90 ° defect, the enhancement shown in figure 4.5

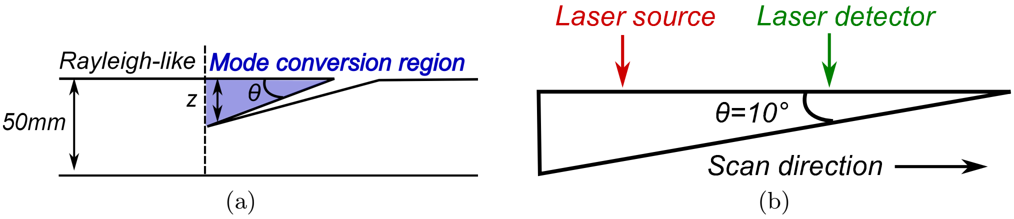

(a) (b)

Figure 4.11: A schematic diagram showing the change in material thickness at an angled defect from the full 50 mm sample thickness in the Rayleigh-like region to a position dependent thickness, z, in a region that supports mode conversion to Lamb waves (a) and a schematic diagram of a scanning laser detection inspection of a wedge sample with a 10 ° apex angle used to validate the existance of Lamb wave mode conversion (b).

sees a large increase at acute defect angles that cannot be explained using the same interference model as for the 90 ° defect. The Rayleigh wave incident on the shallow angled defects propagates into a region of the material that has a dramatically reduced thickness compared to the slight changes in the thickness of the material that the Rayleigh wave travels through for the obtuse angled defects. This change in the material thickness is demonstrated in the schematic diagram in figure 4.11, and with this reduction in the material thickness a new mode conversion mechanism is encountered, in which the incident Rayleigh wave is mode converted into Lamb-like waves[252].

The schematic diagram in figure 4.11 shows that within the defective region the material thickness through which the ultrasound travels is steadily reduced until the crack opening is reached. It was shown in section 2.1.4 that for materials that approximate a material half-space the dominant surface wave is a Rayleigh wave, however, as the thickness of the material is reduced the boundary conditions of both the top and bottom surfaces become relevant, and the dominant surface wave changes to be a Lamb wave[89]. Subsequently, as the sample thickness is reduced at the defect there exists a mode conversion in which the incident Rayleigh wave is converted to symmetric and antisymmetric Lamb wave modes[252–255]. In this reduced thickness the bulk wave reflections that were present for defects close to 90 ° are no longer considered[115], however the reflected waves will mode convert back to Rayleigh, longitudinal and shear waves when they have left the region of reduced thickness, as are observed in the far-field on the B-scans in figure 4.10.

To validate the existence of mode conversion to Lamb waves at the defect, scanning laser detector experiments were carried out on a wedge shaped sample with a 10 ° apex angle, as shown in figure 4.11b, which approximates the narrowed section of a 10 ° defect of infinite depth. The laser source was held in a fixed position close to the thickest end of the wedge and the laser detector was scanned towards the wedge tip in increments of 75 μm. At the source position the thickness of the wedge was 20 mm, which is sufficiently thick such that the generation of Rayleigh surface waves and longitudinal and shear bulk waves was observed for some of the wave frequencies[115].

For a surface wave propagating in a tapered waveguide the frequency-thickness of the sample, which was shown in section 2.1.4.2 to dictate the wave velocity, varies as a function of the position along the wedge, with the value decreasing as the wave progresses towards the wedge tip[254,255]. As can be seen from the dispersion curve in figure 2.1, as the frequency-thickness decreases the incident Rayleigh-like wave will become more Lamb-like. A split into symmetric and antisymmetric Lamb wave modes at low frequency-thickness is observed from the changes in the black and white patterns seen close to the wedge tip in the B-scan in figure 4.12, in which these features can be seen to bend due to the change in the velocity of the waves that cause them.

The arrival time, *t(f)*, of these waves at the detector as a function of frequency can be calculated by dividing the wedge into N small sections, each of width Δx, in which the wave group velocity $v_g(fd)$ differs as the frequency-thickness decreases, giving an arrival time at the detector position l of,

$$t(f) = \int_0^l \frac{1}{v_g(fd)} dx \approx \sum_0^N \frac{\Delta x}{v_g(fd)} \quad . \tag{4.12}$$

The arrival times are different for each frequency component of the broadband Rayleigh wave, and the arrival times of fundamental S0 and A0 Lamb waves at frequencies of 0.37 MHz, 0.92 MHz, 1.66 MHz and 1.9 MHz are shown overlaid onto a B-scan of the wedge data in figure 4.12. The B-scan shows an incident Rayleigh wave that splits into multiple wave modes as it approaches the wedge tip, and the theoretical arrival times of the fundamental A0 and S0 Lamb waves are seen to correlate well to the light and dark pattern in the image. Some of the mode converted S0 waves are not visible in the B-scan as the proportion of their particle displacement that is in the out-of-plane direction (section 2.1.4.2) is small, and hence the out-of-plane displacement detector is insensitive to them. The higher frequency components remain Rayleigh-like until closer to the wedge-tip than the lower frequencies[252]. Longitudinal and shear waves that have previously been observed in studies of waves in wedges are not present in the near-field at the defect tip[255,256].

Some of the features of the B-scan in figure 4.12 cannot be explained by

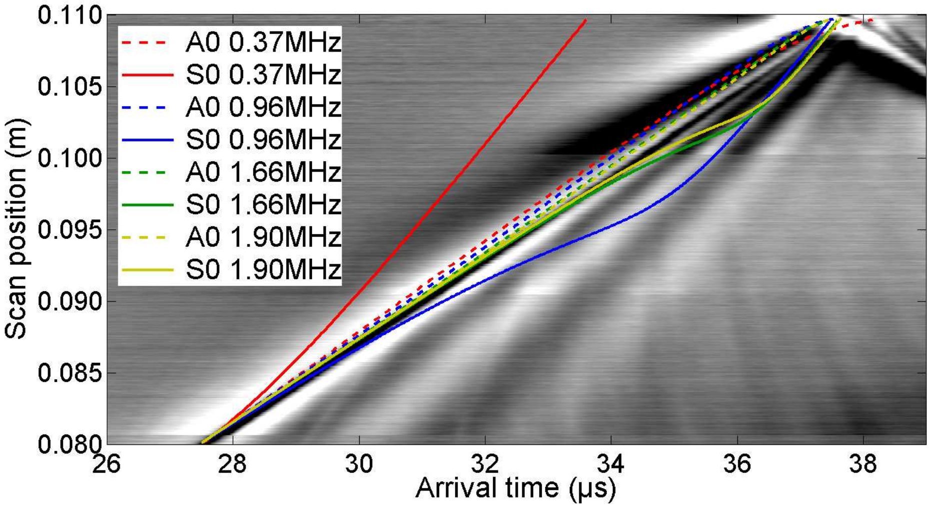

Figure 4.12: B-scan showing a Rayleigh wave incident on a wedge sample with a 10 ° apex angle. The theoretical arrival times of mode converted S0 and A0 Lamb waves at frequencies of 0.37 MHz, 0.92 MHz, 1.66 MHz and 1.9 MHz are overlaid.

the mode conversion of the Rayleigh wave to the fundamental Lamb modes, and the mode conversion of the Rayleigh wave to higher order Lamb wave modes, such as the A1 and S1 modes shown on figure 2.1b, must be considered. Here the splitting of the incident Rayleigh wave into the first order symmetric and antisymmetric waves is observed, however, both the first order wave modes are only supported in the wedge when the frequency-thickness at the detector position is above the cut-off frequency for the mode; 2.87 MHz.mm for the S1 mode and 1.58 MHz.mm for the A1 mode. As the frequency-thickness is reduced part of the wave energy of the higher order Lamb modes will be reflected but the remainder will mode converted to waves that can be supported below its cut-off frequency, with the A1 wave mode converting to A0 and a S0 modes below 1.58 MHz.mm[254]. The S1 mode could undergo several mode conversions; at 2.87 MHz.mm it will mode convert to an A0 and a S0 mode, and also to an A1 mode, which will undergo subsequent mode conversions to the fundamental modes when the frequency-thickness goes below 1.58 MHz.mm. The arrival times of the mode converted first order Lamb wave modes are shown on figure 4.13 for an incident A1 and S1 mode at a frequency of 1 MHz, and good agreement can be seen with B-scan features that do not correspond to the mode conversion of the Rayleigh wave to the fundamental A0 and S0 modes.

The mode conversion to Lamb waves which is evident in a wedge shaped sample is also present in the near-field of an acutely angled defect, and constructive interference between the different Lamb wave modes when the detector is located

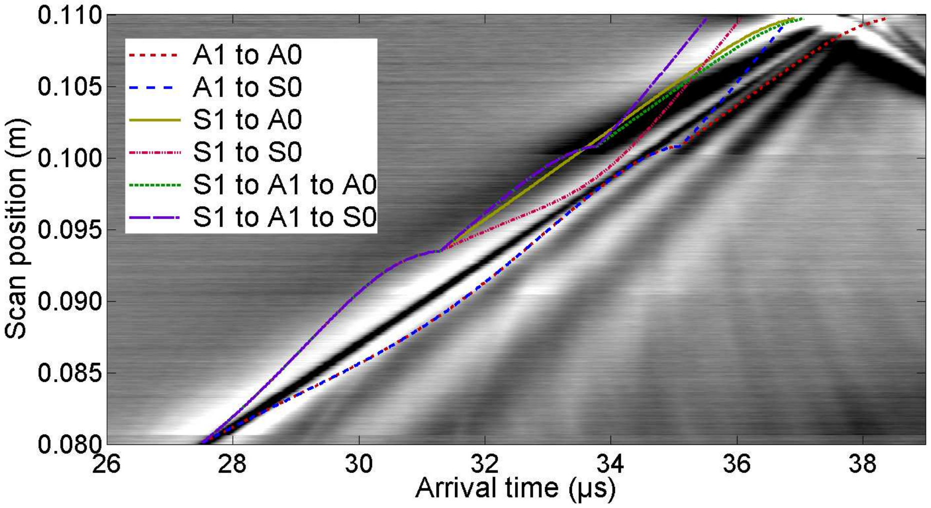

Figure 4.13: B-scan showing a Rayleigh wave incident on a wedge sample with a 10 ° apex angle. The theoretical arrival times of Lamb waves that are mode converted from A1 and S1 first order Lamb waves at a frequency of 1.0 MHz are overlaid.

in the near-field of the defect is responsible for the large enhancements seen for acute angled defects[252]. From the solution of equations 2.40 and 2.42 for the out-of-plane displacement of a Lamb wave at the material surface it can be seen that at low frequency-thicknesses the S0 mode has a small out-of-plane displacement whereas the out-of-plane displacement of the A0 mode increases at lower frequency-thickness, and therefore the superposition of the A0 modes of different frequencies will dominate the observed enhancement[89].

For acute angled defects that are close to 90 ° the angled region in which mode conversion to Lamb waves occurs is small, and when the laser detector is located over this region (see figure 4.14), it will detect the entire range of frequency-thicknesses simultaneously, with all of the mode converted Lamb modes overlapped. The out-of-plane displacement is therefore averaged over all of the different frequency-thicknesses that the detector observes. For a defect close to 90 ° this includes larger frequency-thickness values which have lower proportions of their particle displacement in the out-of-plane direction, and the average displacement observed by the detector is therefore reduced, giving a correspondingly smaller enhancement for acute angles that are close to 90 °. For a shallow defect angle, the region over which mode conversion to Lamb waves occurs is large and the detector size is such that it sees only a small range of Lamb wave frequency-thicknesses. When the detector is very close to the defect opening it sees only the smallest frequency-thickness Lamb modes, which have a higher proportion of their particle displacement in the out-of-

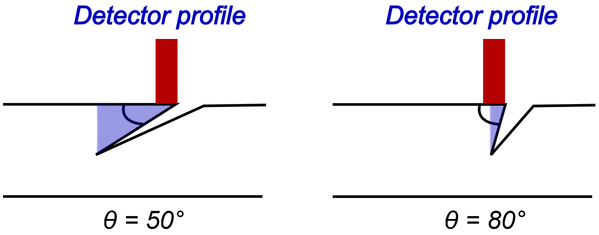

Figure 4.14: A schematic diagram illustrating the increase in the region in which mode conversion to Lamb waves occurs in angled defects, that is observed by the laser detector for a shallow angled defect and a defect that has an angle close to 90 °.

plane direction and therefore the average out-of-plane displacement at the detector is increased, leading to the increased enhancement seen in figure 4.5 at low defect angles[252].

In this section is has been shown that near-field scanning laser detection enhancements vary as a function of the defect angle to the material surface. The cause of this enhancement has been attributed to constructive interference between a superposition of different wave modes near to the defect, with defects that have angles of 90 ° and larger experiencing a superposition between the incident and reflected Rayleigh waves and a surface skimming longitudinal wave. Defects that have angles of less than 90 ° experience an enhancement arising from the superposition of mode converted Lamb waves that are generated within the wedge-like geometry of the defect. It has also been shown from a study of the arrival times in the far field of several mode converted waves generated at the defect that the mode conversion of these waves is dependent on the defect angle and that the variations in their arrival times can be used to form a qualitative estimate of the defect angle.

4.4 Scanning laser source enhancements from angled defects

Near-field enhancements of the Rayleigh wave amplitude and frequency content have also been reported to occur when a laser source is passed over a surface-breaking defect[23,128,234,235]. This phenomenon has been reported for a thermoelastic generation source, focussed into both a line[23] and a spot source[235], interacting with perpendicular surface-breaking defects. The enhancement that occurs as the laser source is passed over a perpendicular defect has been attributed to several mechanisms, including the changes in the source shape at the defect, changes in the

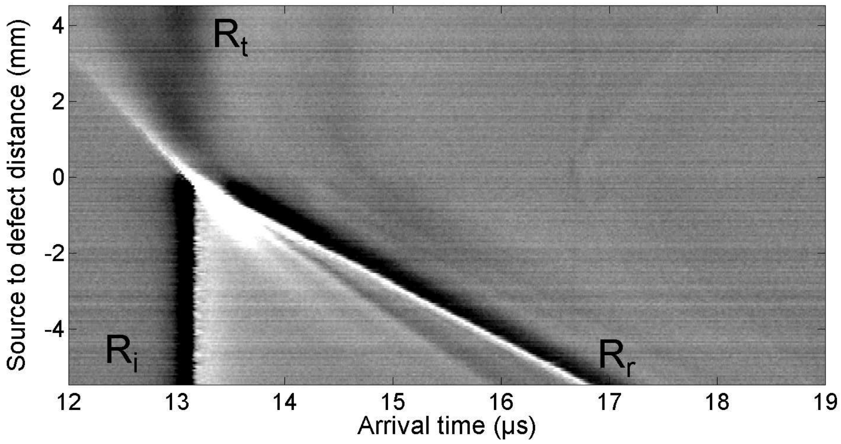

(a) 40 ° defect

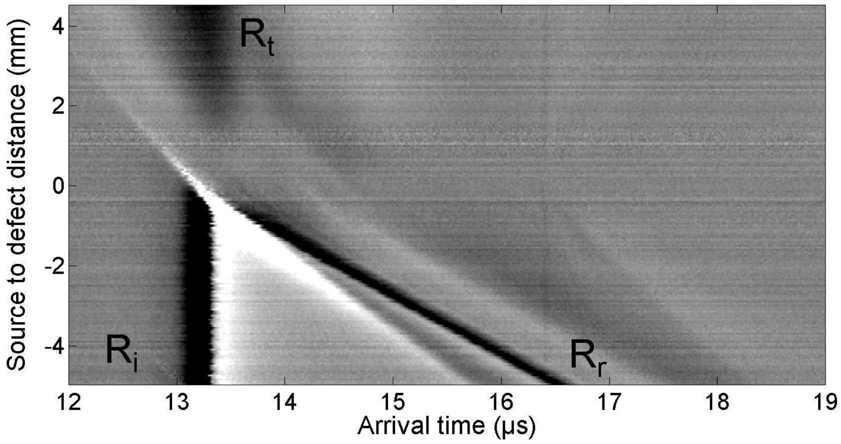

(b) 90 ° defect

Figure 4.15: B-scans for 40 ° and 90 ° angled defects for the case in which the source is moved over the defect.

boundary conditions of ultrasonic generation, and a superposition of the incident and reflected waves at the detector located in the far field[23,234,235].

As in section 4.2.1, a variation of the signal enhancement as a function of the defect angle would be useful for applications such as rolling contact fatigue crack detection in rail lines[96,98], and therefore the enhancement behaviour of angled defects is studied so as to develop an understanding of the variation of the signal enhancement as a function of the defect angle to the surface[95,107].

The same selection of angled defects as were investigated using the scanning laser detector approach in section 4.2.1 were used for the scanning laser source investigations. With the same fixed separation maintained between the source and the detector as for the scanning laser detection experiments, a laser line source was

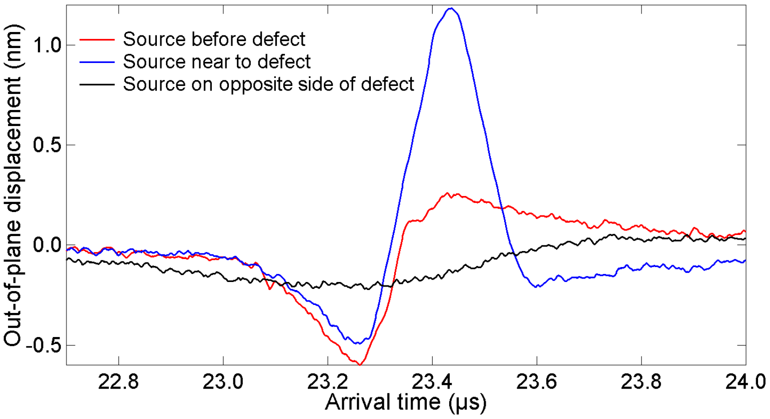

Figure 4.16: Time window taken over the arrival time of the incident Rayleigh wave for a 90 ° defect for scans taken when the laser line source and the detector are on the same side of the defect (red), when the source is passing over the defect (blue) and when the defect lies between the source and the detector (black).

scanned over the defect in increments of 50 μm, as described in section 4.2. Scans were performed by switching the positions of the source and the detector compared to the example shown in the schematic diagram of figure 4.1.

The experimental results were validated through a comparison with the results of FEM simulations (outlined in section 3.2) that used the same geometry as the experimental samples. The FEM simulations were carried out using a fixed separation between the detector and the source with the simulated source being scanned over the defect. The laser source was simulated using a dipole force model along a line of nodes, replicating the impact force from the laser line source. The boundary conditions of generation were recalculated at each scan position, making the simulation very time consuming, however they show good agreement with similar simulations performed using a simulated thermal heating source and are considered to be a good representation of the true behaviour[95]. The FEM simulations were subjected to the same data processing procedures as the experimental data.

The enhancement of the ultrasonic waves as the laser source passes over the defect can be visualised again through the use of B-scans. The B-scans again possess a pattern of light and dark regions that are unique to the defect angle, however, it is more difficult to differentiate the differences in the patterns between different defect angles by eye. These both show an increase in the intensity of these light and dark regions at the defect location, however, and this provides qualitative evidence of the near-field enhancement, and along with the presence of the reflected waves and the drop in the magnitude of the transmitted wave provides a quick visual check for the

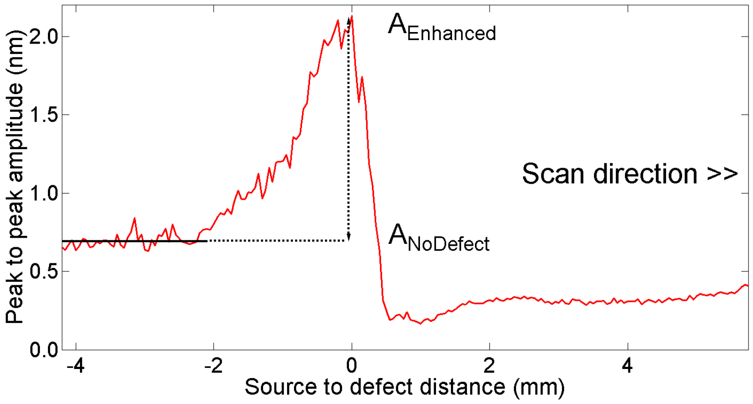

(a) 40° defect

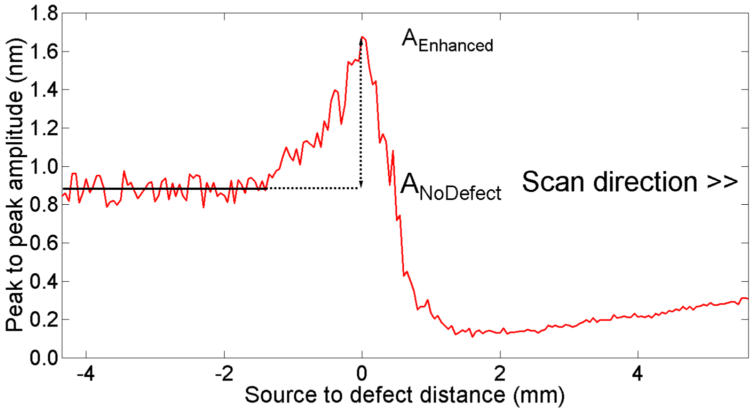

(b) 90° defect

Figure 4.17: Peak to peak amplitude tracking for a Rayleigh wave incident on surface-breaking defects angled at 40° and 90° to the sample surface for the case in which the laser source is moved over the defect.

presence of a surface-breaking defect. Experimental data B-scans for 40° and 90° defect angles are shown in figure 4.15.

A-scans taken at each scan position were windowed about the Rayleigh wave arrival time, allowing the peak-to-peak amplitude of the Rayleigh wave to be recorded as a function of the scan position, in the same manner as in section 4.2.1. As was seen for the scanning laser detector case (section 4.2.1), the peak-to-peak amplitude of the Rayleigh wave increased when the laser line source passed over the defect, with figure 4.16 showing the comparison between the windowed wave with no defect present and with the laser line source illuminating a 90° defect. As in the scanning laser detector experiments the peak-to-peak amplitude fell dramatically when the defect was positioned between the source and the detector as the defect acts to block a large portion of the incident wave. The same behaviour was observed

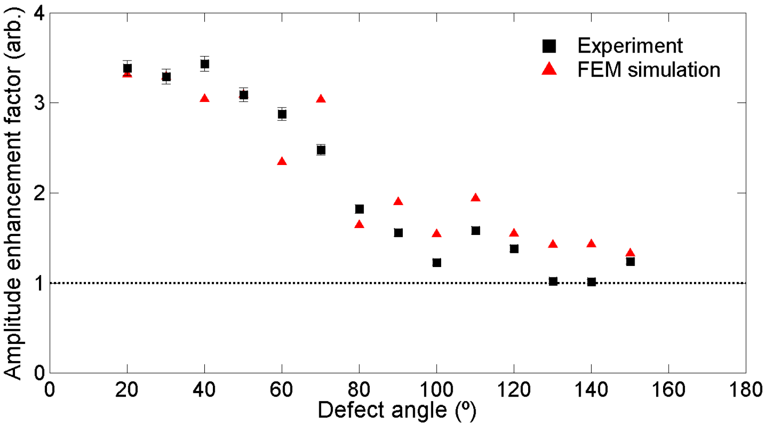

Figure 4.18: Amplitude enhancment factors as a function of defect angle for the case in which the laser source is moved over the defect for experimental and FEM simulation data.

for the FEM simulations which modelled a thermal generation process as described in section 3.2. The peak in the signal enhancement occurs at a laser line source position that is very close to the defect (located at a position of 0 mm), which allows the defect position to be determined by the location of the enhancement.

The variation in the peak-to-peak amplitude was tracked as a function of scan position, with the results shown in figure 4.17 for defects angled at 40 ° and 90 ° to the surface. As with the scanning laser detection in section 4.2.1, the amplitude varies as the defect angle to the horizontal changes, however the enhancement is less sharp than that seen for the scanning laser detection. Enhancement factors can be formed using equation 4.1 for each different defect angle, and are shown in figure 4.18.

The agreement between the experimental and simulated enhancement factors in figure 4.18 is good, with both measures showing a variation in the enhancement factor as a function of the defect angle[95]. The good agreement between experimental and simulated data highlights the legitimacy of using a simulated thermal source (as described in section 3.2) with the same line dimensions of 6 mm by 300 μm as the experimental laser line source. Both data sets show a general increase in the magnitude of the enhancement factors as the defect angle is reduced, similar to the behaviour seen for the scanning laser detector enhancements in section 4.2.1, however, the overall magnitudes of the enhancement factors are generally much smaller than those for the scanned detector. The agreement between the experimental and FEM data is better for the scanning laser source approach, this shows that the averaging effect over the area of the detector spot (described in section 4.3) is less

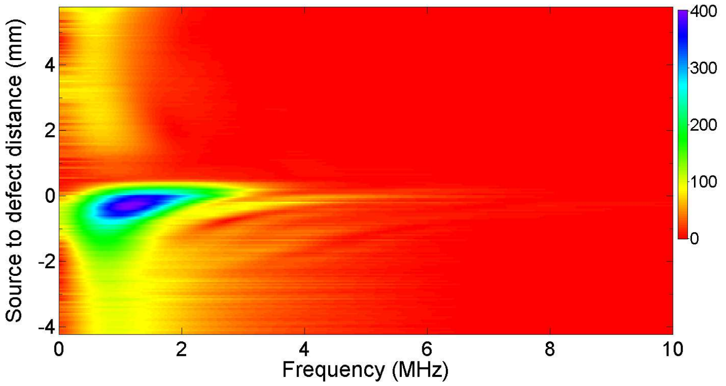

(a) 40 °

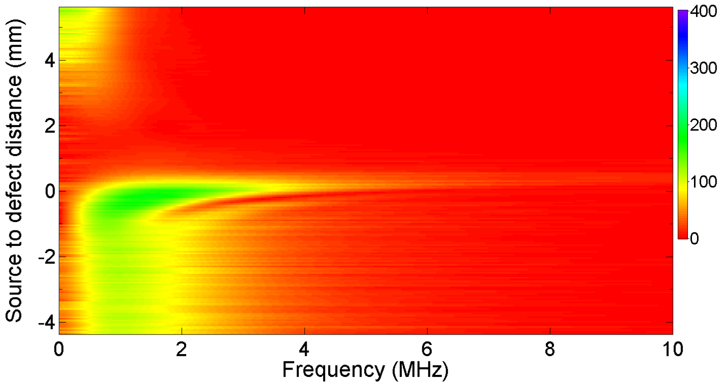

(b) 90 °

Figure 4.19: Scanning laser source frequency B-scans for two different defect angles, 40 ° (a) and 90 ° (b).

significant when the detector (for both experiment and model) is on a part of the sample that has a constant thickness.

As with the scanning laser detection enhancement factors, the scanning laser source enhancements can be used as a means of finger-printing the angle of a defect with respect to the sample surface, with more sensitivity to defects that are at an angle of less than 90 °. For defects that have an obtuse angle the variation in the enhancement factor is small, and to fully characterise the defect angle, the sample should be rotated such that the scanned angle becomes acute with respect to the direction of the scan, and would therefore have a larger enhancement factor.

The mechanisms reponsible for scanning laser source enhancements in Rayleigh waves are described in section 4.4.1. The scanning laser source enhancements have fairly large enhancement factors at around 30 °, which is again highly beneficial to the detection of rolling contact fatigue defects as it gives a good sensitivity to defects that are close to the usual propagation angle of around 25 ° for RCF defects[98,99].

As in section 4.2.1 a fast Fourier transform was taken over the windowed Rayleigh wave at each scan position, which when stacked adjacent to one another allowed the formation of frequency B-scans, such as those shown for a 40 ° and a 90 ° angled defect in figure 4.19. An increase in the frequency content at the defect is seen for both defect angles by a horizontal band of increased magnitude near a position of 0 mm, with the increase in the frequency content being larger for the shallower angled defect [95].
An enhancement is observed in the magnitude of a chosen frequency component of the Rayleigh wave as the source passes over the defect, with the enhancement at 0.98 MHz shown in figure 4.20a for a 40 ° defect. The frequency enhancement at a given frequency, for example 0.98 MHz, again varies in the same manner as the amplitude enhancements, as shown in figure 4.20b, and could be used to fingerprint a defect angle. Again, if a frequency component has a value that is close to zero with no defect present a large increase as the source is scanned over a defect gives a strong indication of the presence of a surface-breaking defect.

4.4.1 Contributory mechanisms to scanning laser source enhancement

The amplitude and frequency enhancements observed as a scanning laser source passes over a surface-breaking defect are generated by the actions of several different mechanisms, with the following section providing an outline of these mechanisms, as developed for perpendicular defects (see also section 2.3.1) [23,27,85,235]. These mechanisms are also responsible for the enhancement observed in the angled defects.

It was shown in section 2.2.4 that the frequency content of a laser ultrasonic source is dependent upon the spatial profile of the source incident on the sample surface [27,85]. It has been shown that, as the laser source passes over a surface-breaking defect, the spatial extent of the source that illuminates the sample surface is reduced, and hence w in equation 2.71 is reduced, leading to an increase in f_{max}, which is the peak frequency content of the Rayleigh wave. The subsequent rise in the frequency content of the generated ultrasound provides a contribution to the observed increase in the frequency content during the near-field enhancement [23,235]. This has previously been reported only for a laser spot incident on a perpendicular defect lip, however, for angled defects, this change in the profile may not be as sudden due to the angled change at the defect lip, thereby giving some angle dependence to the changes in the laser spot diameter and hence f_{max}. This is shown in figure 4.21

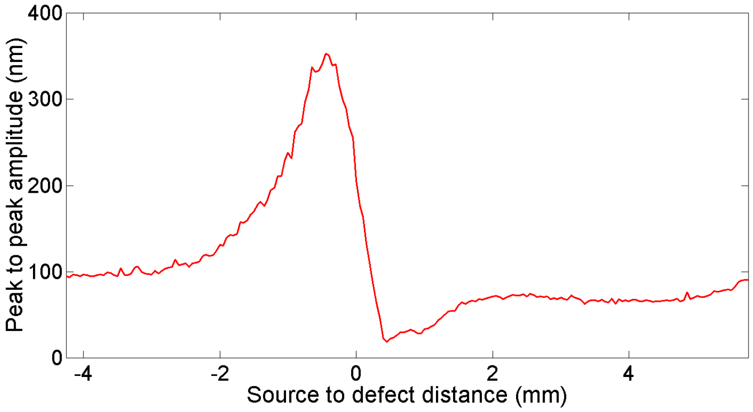

(a) Magnitude at 0.98 MHz

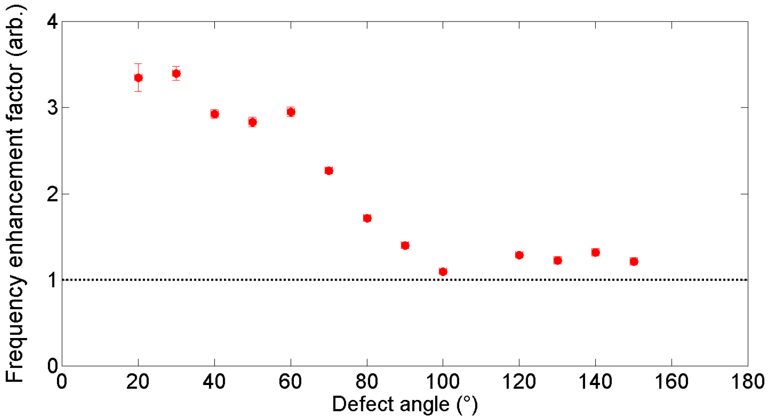

(b) Frequency enhancement factors

Figure 4.20: Magnitude of the frequency content of the time windowed Rayleigh wave at a frequency of 0.98 MHz as a function of source position for a scanning laser source experiment over a 40° angled defect (a) and the variation in frequency enhancement factor at 0.98 MHz as a function of defect angle (b).

where a laser line incident on an acute angled defect sees a sudden reduction in the irradiated area of the surface as it passes over the lip, when compared to the slow change that is experienced as the line source passes over the lip of an obtuse angled defect where generation can continue on the slope of the defect opening.

In section 4.2.1 the enhancement for scanning laser detection was attributed to a superposition of the incident Rayleigh wave with a reflected Rayleigh wave and a mode converted surface skimming lonitudinal wave for defects close to 90 °, and the superposition of mode converted Lamb waves for shallow defects[237]. For scanning laser source experiments a contribution to the enhancement from wave superposition is also expected, however, here the superposition will only occur between the incident Rayleigh wave and its direct reflection from the defect as detection occurs

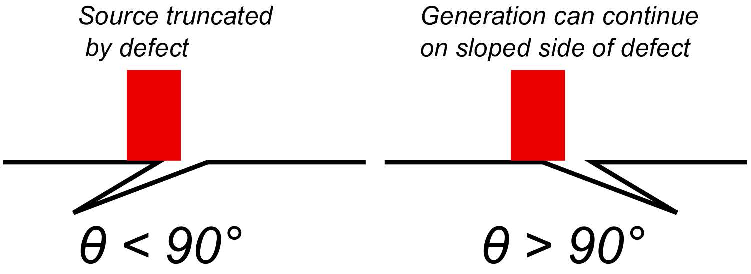

Figure 4.21: A schematic diagram showing the truncation of a laser line source as it passes over the defect lip for a sudden change in the illuminated area for an acutely angled defect (a) and the more gradual change in the illuminated area for an obtuse defect (b).

away from the defect [235]. Lamb wave modes will be generated when the source is incident on the thin part of the sample for shallow defects, and can be observed on the B-scans in figure 4.15, however, as the thickness of the sample increases the velocity of these modes rapidly converges to the Rayleigh wave velocity, giving rise to the incident and reflected Rayleigh waves that are observed at the detector. At the thinnest part of the wedge only the fundamental A0 and S0 modes are generated and will propagate at a speed that is dependent upon the frequency-thickness. The S0 mode is highly dispersive at low frequency-thicknesses (see figure 2.1b) with a large variation of the wave speed of each frequency component. Therefore, the arrival times of the Rayleigh waves that are mode converted from each frequency-thickness component of the S0 mode when the thickness of the sample increases are broadly spread out in the time window used to study the peak-to-peak amplitude. The contribution of the Rayleigh wave components that are mode converted from the S0 mode will therefore contribute little to a superposition, and hence to the enhancement. The A0 mode, however, is not very dispersive for all but the lowest frequency-thicknesses, with different frequency-thickness components possessing very similar wave velocities. This means that the Rayleigh waves that are mode converted from the A0 mode once they leave the defect will arrive almost simultaneously at the detector, therefore providing a superposition of waves that enhances the out-of-plane displacement.

No contribution will be seen from the surface skimming longitudinal wave as it travels at a speed of $v_L = 6300$ ms^{-1} [141] and so will not arrive at the detector at the same time as the Rayleigh waves. For angled defects the reflection coefficient is dependent upon the angle of the defect [90,106,107], and this gives an angle dependence to the superposition of waves that contribute to the constructive interference at the enhancement position.

The final contribution to the enhancement comes from the changes in the boundary conditions of generation of the ultrasound when the laser source moves from a continous planar material to the discontinuity of the defect[23,235]. When the source is illuminating the defect the heated region of the sample surface is free to expand into the void that is the defect, instead of being constrained by the surrounding material, therefore changing the conditions of ultrasonic generation. The change in the boundary conditions is difficult to quantify but has been identified as having a large influence on the signal enhancement[234,235,238].

4.5 Conclusion

In this chapter it has been shown that an enhancement in the amplitude and frequency content of a time windowed Rayleigh wave is observed as a laser source or a laser detector is scanned over an angled defect. The enhancement of the Rayleigh wave has been shown to vary with the defect angle such that enhancement factors could be used to estimate the angle of a defect, with shallower defect angles having higher enhancement factors, and the position at which enhancement occurs can be used to position the defect.

For scanning laser detector experiments on perpendicular defects the enhancement has previously been attributed to a superposition of the incident Rayleigh wave with a reflected Rayleigh wave and a mode converted longitudinal surface skimming wave, and it was shown here that an alternative mechanism in which the incident Rayleigh wave is mode converted into Lamb waves is responsible for the larger enhancements observed for shallow angled defects. The same enhancement mechanisms that are responsible for the scanning laser source enhancements at perpendicular defects, including a truncation of the source, wave superposition and a change in the boundary conditions of generation, were found to be responsible for enhancement at angled defects.

It was shown that the angle dependence of mode converted waves created at the defect can be utilised in the far-field for scanning laser detection experiments to estimate the defect angle by a visual comparison of the arrival times of these waves with the distinctive pattern of light and dark lines observed on B-scans. This work therefore provides a range of tools that enables the position of the defect and the defect angle to the sample surface to be estimated via a near-field scanning approach, and this could provide a new method of detecting defects found in industry, such as RCF defects, when used alongside transmission based techniques.

Acknowledgements
I would like to thank Dr. B. Dutton for his contribution to the work contained within this chapter. The majority of the FEM simulations were carried out by Dr. Dutton.

Chapter 5

Lamb wave detector enhancements for surface-breaking defects in plates

Thin plate-like structures have many applications in industry, such as in storage vessels or as panels in large structures such as boat hulls, both of which are sensitive to the development of structural defects[15,16]. Storage vessels are used to contain hazardous or valuable materials, particularly in the nuclear and petrochemical industries, and therefore the early detection of defect growth is essential to preventing costly component failure and leakage of materials[12,13]. Stress corrosion cracking defects, which were described in section 1.4.2, that develop in storage structures possess a complex defect geometry with variable defect depths and complicated branching structures. The surface-wave that is generated in the thin plate-like structures used in storage containers is the Lamb wave (section 2.1.4.2), and due to the complicated multimodal nature of the received signals the simple tracking of the variations in the peak-to-peak amplitude that was carried out for the Rayleigh waves can no longer be applied and an alternative method is required to observe the near-field interactions of Lamb waves with the defect.

Recent research has been focused at utilising long range guided waves, such as Lamb waves, to inspect the plate-like structure with some degree of success at locating regions of material damage[91,257,258]. These methods focus on the far-field interactions of the guided wave (see section 2.1.4.2) and most rely on reflection based techniques that monitor the arrival time and amplitude of reflected waves to examine the interactions of the wave a large distance away from a defect[21,229,259]. Although this far-field approach has the distinct advantage of being capable of inspecting large areas of a structure in a single measurement it also suffers from complications arising from the potentially simultaneous arrival at the detector of several different Lamb wave modes (section 2.1.4.2) and of multiple reflections from the backwall. This makes determining changes in wave amplitude or arrival time challenging, and therefore here the alternative near-field approach is investigated in which the changes in the propagation of Lamb waves in the near vicinity of a defect are examined[22]. The near-field scanning approach enables changes in the ultrasonic propagation to be observed at the point at which they occur, making defect positioning simple, and the observed near-field enhancement can provide more detailed information about the defect geometry.

In this chapter scanning laser detection experiments, similar to those carried out in section 4.2.1, were performed for Lamb waves incident on v-shaped surface-breaking defects in thin plates. Individual Lamb waves were identified from a broadband signal using time-frequency analysis and as the detector was passed over the defect an enhancement of the signal magnitude at a given frequency was observed for individual Lamb wave modes. Similar to the enhancement explained in section 4.3 for Rayleigh waves, this enhancement arises from a superposition of the incident Lamb wave with reflected and mode converted waves produced at the defect that undergo constructive interference at the detector position. This was verified through a comparison of the experimental data for v-shaped defects with theoretical enhancements based on two test models, a square based notch and an open mouthed crack. From this a method of positioning the defect, and of estimating the depth of the defect, was developed from the variation of the enhancement as a function of increasing defect depth, such that a reliable assessment of the defect could be made[22].

5.1 Experimental details

A simplified defect model of a v-shaped surface-breaking defect aligned normal to the sample surface of a plate was used to begin to develop an understanding of the interactions of Lamb waves with defects, without the added complications of the complex branching structure present in real defects. Aluminium plates, of dimensions 300 x 300 x d mm, were chosen as a test material following considerations of material costs, ease of machining and an understanding of the mechanical properties of aluminium[141]. The v-shaped defects were produced by laser micro-

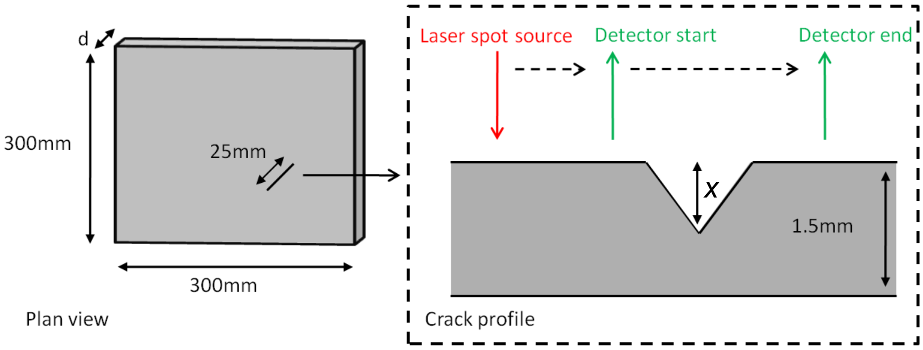

Figure 5.1: A schematic diagram showing both plan view and side profile of simple v-shaped defects, of depth x in mm, in aluminium plates. The percentage defect depth is given by $h = \frac{x}{1.5}.100\%$.

machining (see section 1.4.3), propagating normal to the sample surface to give a different defect percentage depth, h, in each plate, ranging from $15\% \leq h \leq 100\%$ of the plate through-thickness. A schematic diagram of these simplified defects is given in figure 5.1. The defects were angled with respect to the plate edges so as to reduce the sidewall reflections that were received at the detector.

Plate thicknesses covering the range $0.5 \leq d \leq 1.5$ mm, so as to cover a range of typical sheet thicknesses as may be used in industry, were used in this study. For the 0.5 mm sheets the laser micro-machining process caused large levels of localised heating, which meant that the depths of the defects could not be reliably guaranteed, and therefore these defects were produced by milling using a fine drill head. An example of a defect produced through each machining process is shown in figure 5.2 for a 50% through-thickness defect, where it can be seen that the milling process produced defects with wider openings than the laser micro-machining.

Experiments were carried out using the linear scanning experimental setup outlined in section 3.1, with the aluminium sheets held in a specially designed holder such that the defect was orientated perpendicular to the direction of the scan, as shown in figure 3.4. The sheet was scanned past the fixed laser generator and detector in increments of 50 μm such that the IOS detector passed over the midpoint of the defect, as shown on figure 5.1. At each scan position an A-scan was recorded, as shown in figure 5.3a.

The fixed separation that was maintained between the source and the detector minimises the influence of attenuation of the Lamb waves between each A-scan, as the distance travelled at each scan position is the same. This also minimises the effect of dispersion between scans, and prevents the arrival times of different Lamb modes, which travel at different speeds, at the detector from diverging between each

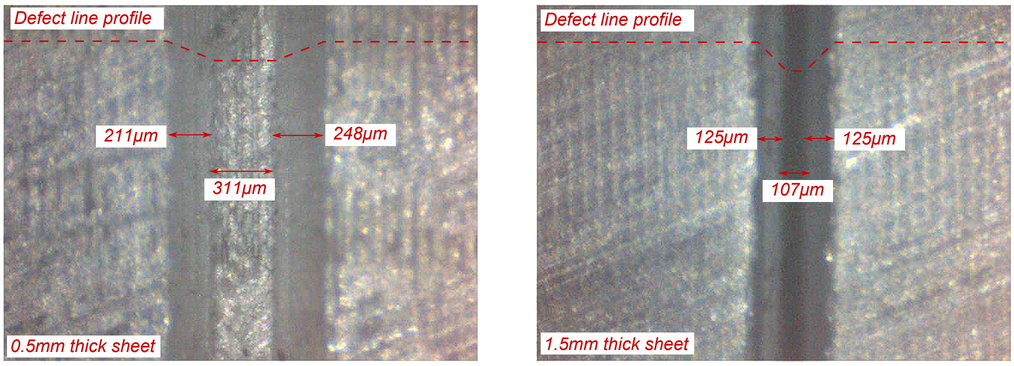

(a) 0.5 mm thickness

(b) 1.5 mm thickness

Figure 5.2: Top view of machined defects in 0.5 mm (a) and 1.5 mm (b) thickness sheets, for a 50% through-thickness defect produced by milling with a fine drill tip (a) and by laser micro-machining (b). Defect line profiles are shown as a guide for the eye.

scan.

FEM simulations using PZFlex were performed in tandem with the experiments to validate the results. An explanation of the FEM technique was provided in section 3.2. The models had reduced dimensions compared to the experimental samples and symmetry was applied about the defect midpoint, so as to reduce the computational time, as was previously used in section 4.2. All of the sheet edges were set to have absorbing boundary conditions to reduce the sidewall reflections at the detection point. The top and bottom of the sheet were given free boundary conditions, allowing the propagation of the Lamb waves. A dipole force, as described in section 3.2, was used at a fixed position to simulate the laser source and the out-of-plane displacement was obtained from a series of nodes, in a line across the mid-point of the defect, separated by 50 μm steps. A fixed generation position for the FEM process was used so as to avoid the lengthy recalculation of the boundary conditions of generation at each scan position, thereby allowing the simulations to be carried out over a reasonable time scale.

For both experimental and simulated data, the broadband laser generation mechanism (see section 2.2.4) produces multiple Lamb wave modes in the sheet, with significant frequency-thickness content up to 10 MHz.mm (see section 2.1.4.2). As can be seen in figure 5.3 for both the experiment and FEM simulation this produces complicated A-scans with some wave modes arriving simultaneously at the detector, with the arrival times of these waves dictated by the frequency-thickness dependent velocity shown in figure 2.1b. From B-scans produced during the experiments, such as that shown in figure 5.4, the appearance of reflected, mode converted and trans-

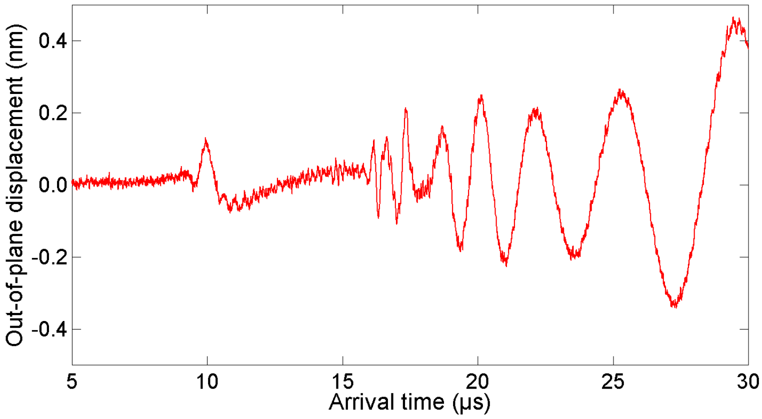

(a) Experimental

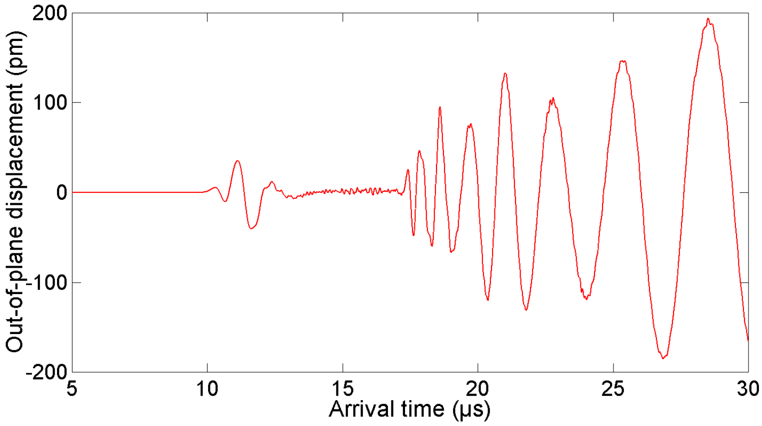

(b) FEM

Figure 5.3: Experimental (a) and FEM (b) A-scans for a defect free plate with a thickness of 1.5 mm, showing simultaneous arrival of several Lamb wave modes.

mitted Lamb waves at the defect can be seen, which will be shown to produce an enhancement in the near-field of the defect, similar to that seen for Rayleigh waves in chapter 4.

5.2 Defect position from B-scan analysis

Accurate positioning of a surface-breaking defect is an important part of identifying material damage, allowing for a more detailed inspection of the damaged region only, thereby saving time and effort for the inspector. Due to the multimodal nature of Lamb waves within plates (shown in section 2.1.4.2), it is challenging to determine the position of the defect by a simple inspection of the A-scans, an ex-

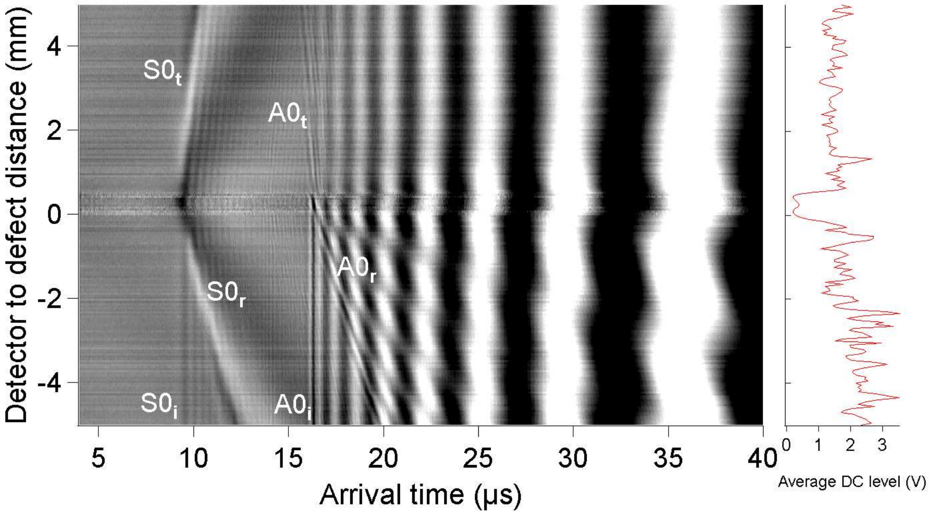

Figure 5.4: B-scan for a 75% through-thickness defect in a 0.5 mm thick sheet with incident (i), reflected (r) and transmitted (t) fundamental Lamb wave modes labelled for both symmetric (S0) and antisymmetric (A0) wave modes. The DC level at the detector is shown and can be seen to drop significantly at the defect position.

ample of which is shown in figure 5.3a, however, interpretation is made easier by stacking the A-scans sequentially in a B-scan. An example of a B-scan for a 75% through-thickness defect in a 0.5 mm thick sheet is shown in figure 5.4.

The incident wave modes are the features that are time invariant with changing detector to defect distance, due to the fixed source to detector separation, and hence appear as vertical features with constant arrival time in figure 5.4. Any non-vertical features can be identified as being the reflected and mode converted waves produced through the interaction of the incident wave with the defect, as the arrival time of these waves at the detector will vary as the detector moves closer or farther away from the defect, following the path shown on figure 5.1.

At the opening of the defect the arrival times of these mode converted and reflected waves will coincide with that of their respective incident modes, and the position of this coincidence in arrival times can be used to position the defect edge. This can be used to find both edges of the defect if the scan is reversed and the detector scanned toward the defect from the other direction, provided that the laser source is still on the same side of the defect as the detector, giving the defect opening positions.

A secondary method for determining the defect location uses the drop in the DC level recorded by the IOS detector when the laser spot encounters the defect. The DC level is a measure of the reflected signal strength received at the detector, and when the detector encounters the defect opening this is drastically reduced. It can be seen from the right hand panel of figure 5.4 that this drop in DC signal strength corresponds to the positions between the defect edges as identified from visual analysis of the B-scan.

The DC drop method is reliable on samples with a relatively consistent surface condition in the region away from the defect, however, it should be used in conjunction with visual B-scan analysis as changes in surface topology or corrosion patches can also lead to a drop in the DC value and provide a false position. The DC drop method works well for artificial open defects, however for closed or partially-closed defects the drop in the DC signal is very small and it is difficult to position the defect from this method, however it will be shown in section 5.2.1 that the presence of a frequency enhancement analogous to that observed for Rayleigh waves can also be used to position the defect.

5.2.1 Defect depth estimation using scanning laser detector near-field enhancements

In section 2.1.4.2 it was shown that there exist multiple Lamb wave modes that are supported simultaneously in a thin plate, and even below the cut-off frequencies of the higher order wave modes, there always exists two fundamental waves, the zeroth order symmetric and antisymmetric modes[89,135]. Although it is possible to produce single mode Lamb waves[260] using, for example, contact piezoelectric generation using in-phase or anti-phase pulsed signals to produce A0 or S0 waves, this does not have the benefits of the non-contact approach. The broadband generation of Lamb waves from the laser source results in multiple Lamb wave modes arriving close together at the detector, each travelling at the frequency-thickness dependent velocities shown in figure 5.5, leading to A-scans in which it is difficult to distinguish individual Lamb modes, an example of an A-scan is shown in figure 5.3a.

The arrival time of each different frequency component in the A-scan can be resolved through the use of a time-frequency representation, such as the sonogram (see section 2.1.5). When producing a sonogram there is an inverse relationship between the frequency resolution and the time resolution, and a compromise between the two was used to produce the images in figure 5.6, with a frequency resolution of 0.1 MHz and a time resolution of 0.2 μs.

The sonogram images show distinctive bands of frequency that correspond to different Lamb modes, however, in order to determine which frequency compo-

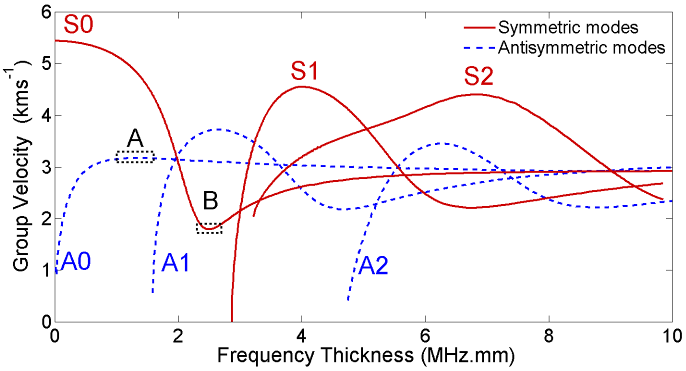

Figure 5.5: Lamb wave dispersion curve showing the frequency dependant group velocity of several Lamb wave modes. Two regions of interest for enhancement studies are highlighted, A and B, on the A0 and S0 modes respectively.

nents are associated with which wave modes the dispersion curve shown in figure 5.5 must be considered. For a known source to detector separation, the theoretical arrival times at the detector of each frequency-thickness component of each individual Lamb wave mode can be calculated, and are overlain on the sonogram images in figure 5.6. These enable the measured frequency components in the sonogram to be associated with Lamb modes, and this enables the magnitude of the frequency content of a single Lamb mode at a chosen frequency to be monitored over the duration of a scan, allowing for changes in specific Lamb modes to be identified as they occur[22].

The frequency axis of each sonogram is scaled by the sheet thickness to provide a frequency-thickness axis, which allows for direct comparison between the same wave modes in different sheet thicknesses, and a direct comparison to the waves shown in figure 5.5. Enhancement in the frequency content of several Lamb modes is observed when the detector is near to the defect, which can be seen from an increase in the magnitude of the frequency content in the region of the sonogram that corresponds to the specific wave modes, as is shown in figure 5.6b.

In chapter 4 the peak-to-peak magnitude of a time window centred around the Rayleigh wave was used to quantify the signal amplitude enhancement, however, as a time window on the A-scans in figure 5.3a would contain multiple Lamb modes this approach is no longer applicable. To quantify the enhancement in individual Lamb modes the magnitude of the frequency component that arrives in a chosen time window is used as a representative measure of the magnitude of the individual modes.

The regions that are studied for quantitative enhancement as the detector

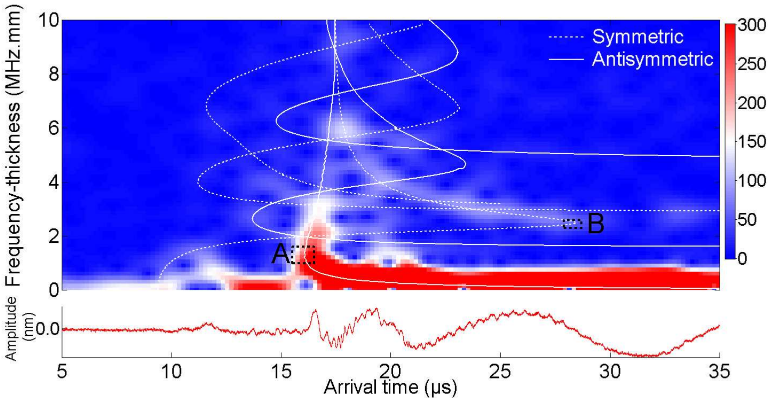

(a) No defect region

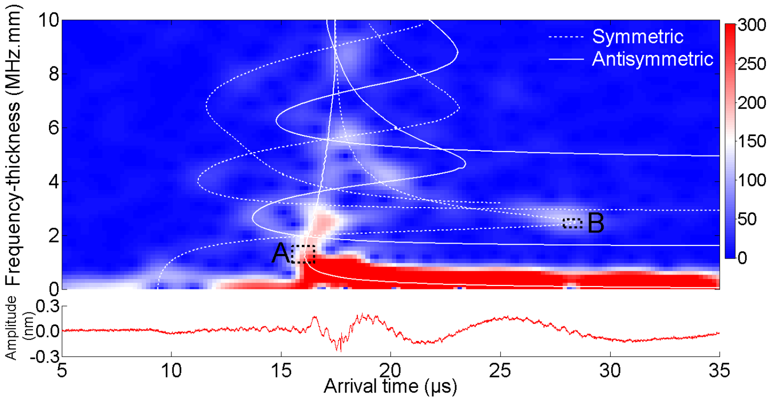

(b) Defect near-field

Figure 5.6: Sonograms with calculated Lamb wave mode arrival times overlaid for the case where the detector is far away from the defect and for when it passes over the defect for a 75% through-thickness defect in a 1.5 mm thick sheet.

passes over the defect are denoted as region A for the A0, and B for the S0, with these regions marked on figures 5.5 and 5.6. The peak value of the magnitude (also referred to as the frequency magnitude) in these two regions was measured during each scan, with the exact windows covering frequency-thicknesses between $1.0 \leq fd \leq 1.6$ MHz.mm arriving between $15.5 \leq t \leq 16.5$ μs for the fundamental antisymmetric wave mode (A0), and the region between $2.3 \leq fd \leq 2.6$ MHz.mm arriving between $27.9 \leq t \leq 28.7$ μs for the fundamental symmetric wave mode (S0). These regions were chosen as the incident fundamental wave, A0 or S0, is the only wave present in the region when the detector is located far away from the defect, giving a steady frequency magnitude when no defect is present.

The peak values of the magnitude of the frequency content in the chosen regions of the A0 and S0 waves were recorded for each scan detection point as the laser detector was moved over the defect, and these are shown in figure 5.7 for a

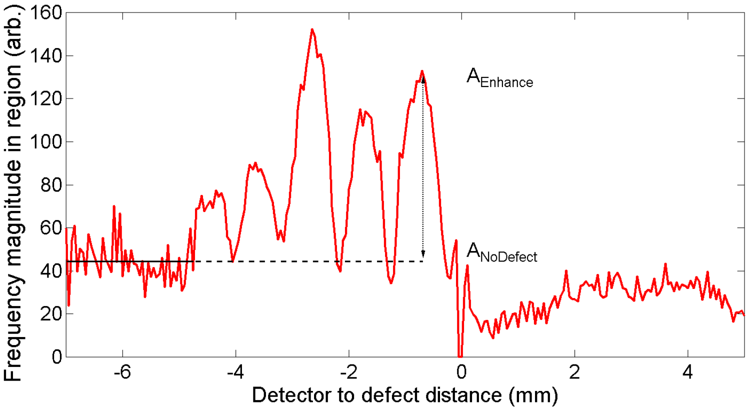

(a) S0 tracking

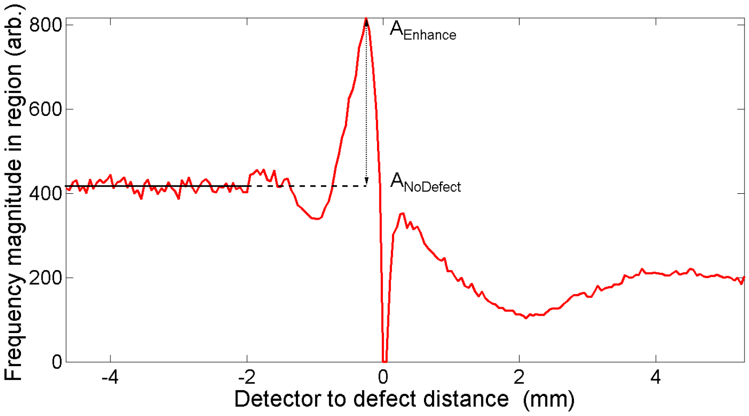

(b) A0 tracking

Figure 5.7: Experimental peak frequency magnitude tracking for the S0 (a) and A0 (b) fundamental waves as the laser detector is passed over a 75% through-thickness defect in a 1.5 mm thick sheet.

75% through-thickness defect in a 1.5 mm thick sheet with the defect located at zero on the x-axis. A large increase in the value of the peak frequency magnitude is observed near to the defect for both fundamental waves, with a single clear peak observed for the A0 wave mode and several peaks in the case of the S0 wavemode, showing clear evidence of an enhancement as the laser detector is scanned over the defect. As was seen for the variations in the peak-to-peak amplitude of Rayleigh waves, the level of the peak frequency magnitude drops when the defect is between the source and the detector, as part of the incident wave is reflected away and so is not observed at these positions. The variations in the peak structure of these enhancements is explained in section 5.4.

An enhancement factor, E_f, is formed by taking the ratio of the peak frequency magnitude at the enhanced position, $A_{Enhance}$, to that expected if there

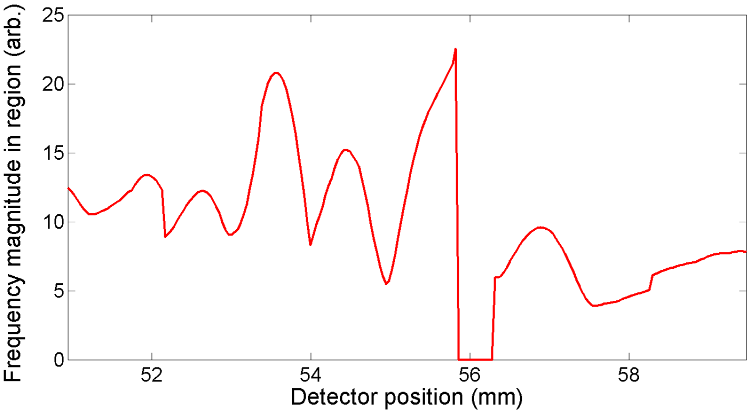

(a) S0 tracking

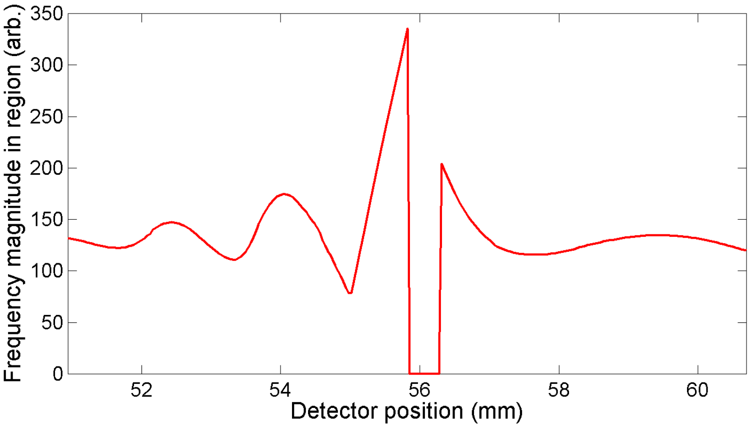

(b) A0 tracking

Figure 5.8: FEM modelling peak frequency magnitude tracking for the A0 and S0 fundamental waves as the laser detector is passed over a 75% through thickness defect in a 1.5 mm thick sheet.

were no defect present, $A_{NoDefect}$, which is defined by producing a linear fit to the region prior to the defect in which the magnitude is steady, as can be seen on figure 5.7. The enhancement factor, which is analogous to that described by equation 4.1, is given by,

$$E_f = A_{Enhance}/A_{NoDefect}. \tag{5.1}$$

For the A0 wave mode the choice of enhancement peak to use in this analysis is simple, however, for the S0 wave mode there is a choice of peak from which to obtain an enhancement. The peak closest to the point of signal drop off as the detector enters the defect is chosen to be the representative enhancement peak, which for the S0 tracking in figure 5.7a lies at the position -0.7 mm from the defect.

For the FEM simulations a similar enhancement structure is seen with a sin-

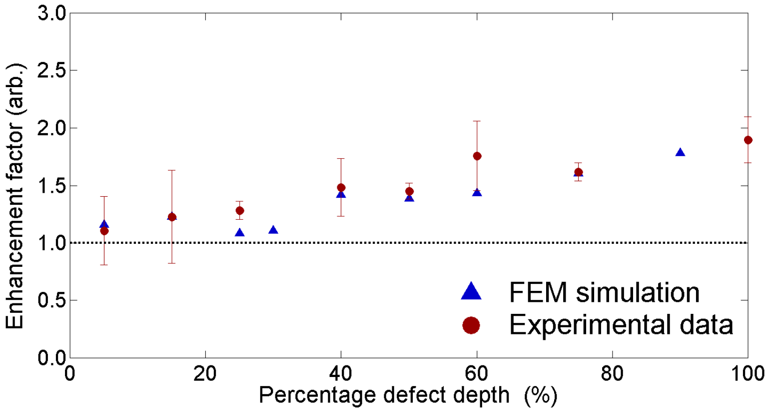

(a) 0.5mm thickness sheet

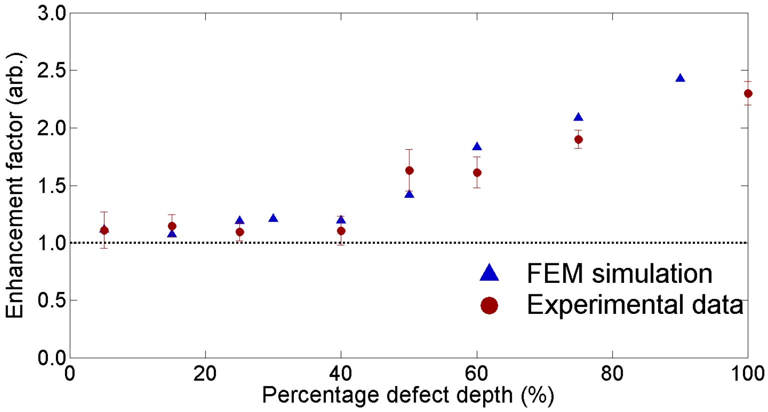

(b) 1.5mm thickness sheet

Figure 5.9: Enhancement factors as a function of defect through thickness for the A0 fundamental wave mode in 0.5 mm (a) and 1.5 mm (b) aluminium sheets.

gle enhancement peak for the A0 mode, and a multi-peaked enhancement for the S0 mode, shown in figure 5.8. The presence of small peaks in the A0 data prior to the large enhancement peak is explained in section 5.4. In spite of the varying separation necessary within the FEM simulations the agreement between the shape of the experiment and FEM data is excellent, indicating that the enhancement tracking technique could also be applied to systems with a fixed generation point and only a scanned detection laser. This may be practical for industrial applications with pre-existing ultrasonic generation systems, such as permanently installed piezoelectric transducers, as the only addition would be the scanning laser detector.

Enhancement factors were obtained for each defect depth from both experimental and FEM simulation data sets, and it can be seen from figures 5.9 and 5.10 that for both fundamental modes there is an increase in the enhancement factor with increasing defect depth, and both modes show good agreement between the

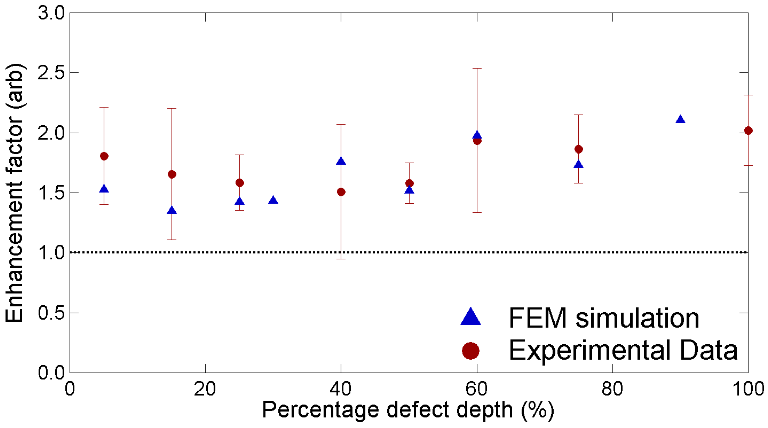

(a) 0.5mm thickness sheet

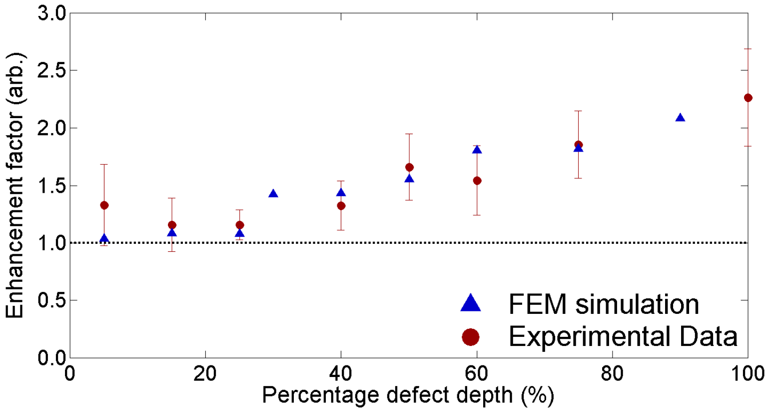

(b) 1.5mm thickness sheet

Figure 5.10: Enhancement factors as a function of defect through thickness for the S0 fundamental wave mode in 0.5 mm and 1.5 mm aluminium sheets.

experimental and FEM simulation data. This relationship offers the possibility of the use of these curves to act as a depth calibration to obtain an estimated defect depth from a measure of both fundamental enhancement factors, or to measure crack growth over time. For defect growth monitoring, even for real defects, one would expect the enhancement factors for both the A0 and S0 modes to increase as the crack grows, allowing the crack growth to be quantified and act as a guide as to the maintenance strategy for damaged components. The enhancements observed for real rough defects are presented in chapter 7.

An example of the benefit of using near-field enhancements can be seen if the case in which the detector were scanned across a defect of unknown depth in a 1.5 mm thick sheet is considered. If processing the data gave enhancement factors of 1.8 for the S0 wave mode and 1.9 for the A0 wave mode then these two values can be used together to predict a defect depth of 75% through-thickness. The identification of the defect depth from this approach is easier to achieve for a sheet thickness of 1.5 mm due to the larger spread of the enhancement factors when compared to the thinner sheet, as seen in figures 5.9 and 5.10.

The limitations of this approach can be seen in the enhancement factors for both wave modes at shallower defects, where only a small variation between enhancement factors is observed for the A0 wave in the thicker 1.5 mm sheet (5.9b) over a range of 0 - 40% through-thickness, and a small variation in the S0 wave in the thinner 0.5 mm sheet (figure 5.10a). However, a depth estimate is still possible from the enhancement of the other fundamental wave mode in both sheet thicknesses. Also, if a clear depth cannot be established from the scanning laser detection enhancements, then the enhancements from the scanning laser source experiments, shown in chapter 6, can be used to verify the defect depth.

In conjunction with the positioning techniques outlined in section 5.2, the near-field enhancement can also be used to provide information on the location of the defect. For both fundamental wave modes there is a large drop in the frequency magnitude at the defect as the strength of the received signal is reduced by the detector spot sitting in the defect. This drop in the received signal strength does not necessarily correspond to a drop in the magnitude in the region of interest but is an overall reduction in the ultrasonic signal received by the detector as it is no longer on a smooth part of the material surface. The location of this correlates with the DC drop shown in figure 5.4, thereby giving a reinforcement of the defect location.

The location of the enhancement peaks can also give clues to the defect position as they occur in a well-defined region prior to the detector passing over the defect. For a short distance after the defect a large amount of the incident wave is blocked by the defect and a drop in the frequency magnitude is observed as a result, however, this is not accompanied by a drop in the DC level and therefore can be distinguished from the initial drop at the defect itself. This drop however is only significant for defects over a depth of 50% as for shallower defects a significant transmission underneath the defect is present, and hence this method has limited applicability for defect location for shallow depths. This also highlights some of the limitations of using the far-field transmitted signal to evaluate defect depths when scanning using Lamb waves, as it is insensitive to shallow defects, and the presence of multiple defects could mean, for example, that a deeper defect could block the transmitted signal from a shallow defect, preventing it from being detected.

5.3 Mechanisms responsible for near-field enhancement

To interpret the relationship between enhancement factor and defect depth for the laser detector scanning over the defect, an understanding of the cause of the enhancement is required. It was shown in chapter 4 that for the case in which the laser detector moves over an open mouthed defect in Rayleigh wave supporting samples that the observed enhancement arises from a superposition of the incident Rayleigh wave with waves reflected and mode converted from the defect[23,95,107,236,239]. The same mechanism is shown here to be responsible for the enhancement of Lamb waves presented in this chapter, albeit with a more complex form due to the capacity for multiple Lamb wave modes to be excited simultaneously[22].

The relationship between enhancement factor and defect depth can be explained in terms of constructive interference arising from a superposition between the incident wave mode and the various possible reflected and mode converted wave modes generated through the interaction of the incident wave mode with the defect. The focus of this discussion is on the enhancement in the A0 wave mode as it is the simpler of the two interactions, owing to the fact that at the frequency-thickness studied the region is below the cut-off frequency-thickness of 1.58 MHz.mm for the higher order wave modes seen on figure 5.5[89]. This limits the mode conversions to be considered at the defect to just those taking place between the fundamental wave modes.

The interaction of a Lamb wave incident on a surface-breaking defect will produce mode conversions to other Lamb modes that can be supported at the same frequency-thickness, in addition to a reflection of the incident mode[22,113,114]. For example, it can be seen from the dispersion curve in figure 5.5 that for the A0 mode incident at a frequency-thickness of 1.3 MHz.mm, a reflected A0 mode and a mode converted S0 mode at the same frequency-thickness will be produced at the defect. As was seen on figure 5.5, these waves will propagate away from the defect at different speeds and far away from the defect they will arrive at very different times at the laser detector. However, if the laser detector is positioned sufficiently close to the defect then there will exist a position at which the incident, reflected and mode converted wave will have a coincident arrival at the detector. A superposition of the waves that arrive very close together is formed, and constructive interference between these waves can occur, producing a position with a greater out-of-plane displacement than that which would be present for the incident wave alone. The exact position of this enhancement will depend on the relative phases of the waves

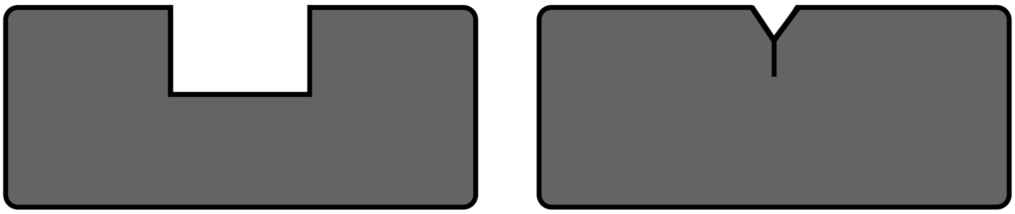
(a) Square based notch (b) Open mouthed crack

Figure 5.11: Schematic diagrams of the two test models used to approximate the interactions of Lamb waves with a defect.

as this dictates the position at which the constructive interference will occur.

The superposition of multiple Lamb modes leads to an increase in the signal detected by the out-of-plane surface displacement sensitive IOS detector, analogous to that seen for the enhancement of Rayleigh waves at low defect angles in chapter 4. For the Lamb waves this enhancement is observed as an increase in the peak value of the magnitude of the waves in certain time-frequency regions, however, the challenge lies in identifying exactly which wave modes will be present at this enhanced position and the contribution that each will make to the enhanced ultrasonic field.

To determine which backward travelling wave modes (with respect to the direction of travel of the incident wave mode) will be present at the enhancement point an understanding of the interactions at the defect is required, such as the reflection and transmission coefficients (which describe the proportion of the incident wave energy that is present in the reflected or transmitted wave) of each wave mode. As the v-shaped defects used in this study have not previously been examined in detail, the reflection and transmission coefficients from two test models, a square based notch and an open mouthed crack, which have been studied by previous authors, are used to understand the interactions of the incident wave with the defect[113,114].

Although neither test model has the same geometry as the v-shaped defects the open mouthed crack can be seen as an approximation to a shallow defect and the square based notch as an approximation to a deep defect; the geometry for both of these is shown in figure 5.11. From knowledge of the test models the mode conversions and reflections that occur when the incident mode interacts with the defect can be identified, and an estimate can be made of the proportion of the incident wave energy that these new waves will possess. An estimate of the contribution of each mode towards any superposition at the enhancement position can then be made, once the out-of-plane component of the surface displacement is known for the given Lamb mode at the chosen frequency-thickness (see figure 2.2).

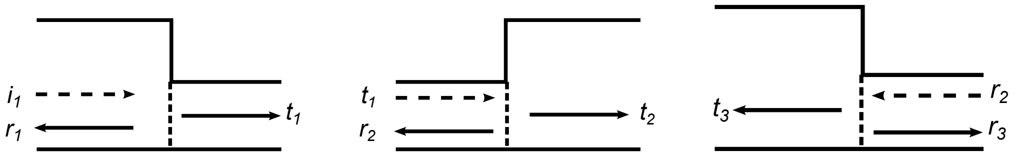

(a) Interface 1 (b) Interface 2 (c) Interface 3

Figure 5.12: Interaction interfaces for a square based notch defect showing the direction of incident, i, reflected, r, and transmitted, t, waves at each interface.

5.3.1 Wave interaction with a square based notch

The interactions between an incident Lamb wave and a square based notch were investigated by Kim and Roh by breaking down the overall scattering mechanism into individual scattering processes, such that a linear equation corresponding to the reflection and transmission coefficients could be formed[113]. The notch is separated into three boundaries, as shown in figure 5.12, with the scattering mechanism being evaluated at each interface. From this the authors produce a library of scattering interactions, in which the transmission and reflection coefficients for each interaction at each interface are recorded as a function of the defect depth. These coefficients can then be applied to any case in which the same scattering mechanism is observed.

For example the interaction involving the incidence of a A0 wave on an interface similar to interface 1 in figure 5.12a has a transmission coefficient for the mode conversion to an S0 wave of 0.225. This value can be used to predict the amount of S0 wave transmitted past this interface regardless of if it is followed by an upward notch, as in figure 5.12b, or if the material continues at this new thickness. All of the field information for the non-propagating modes that exist at the defect are described by these coefficients, removing the need for complicated calculations[113].

Each interaction at an interface is split into two components; first of which is the interaction of the Lamb wave with the interface (where the extent of the scattering is directly related to the depth of the notch) and the second is the propagation of the scattered wave into the notch where it will undergo phase shifts depending upon the length of the travel time in the notch[113,229,230]. The whole scattering process is described as a combination of these two separate processes.

When an incident Lamb wave, i_1, encounters the first defect interface, shown in figure 5.12a (dashed arrow), it will create a reflected wave, r_1, and a transmitted wave, t_1, of the same wave mode. In addition the incident wave mode will undergo a mode conversion to the other wave modes that can be supported at the chosen frequency thickness. For instance, the incident A0 wave from region A in figure 5.5

Table 5.1: Reflected and mode converted wave modes arsising from interaction of an incident A0 was at square based notch; only modes that are present at the enhancement position are shown.

Wave identifier	Interface 1	Interface 2	Interface 3	Mode at detector
A	$A0_i$-$A0_r$	-	-	A0
B	$A0_i$-$S0_r$	-	-	S0
C	$A0_i$-$A0_t$	$A0_i$-$A0_r$	$A0_i$-$A0_t$	A0
D	$A0_i$-$A0_t$	$A0_i$-$A0_r$	$A0_i$-$S0_t$	S0
E	$A0_i$-$A0_t$	$A0_i$-$S0_r$	$S0_i$-$A0_t$	A0
F	$A0_i$-$A0_t$	$A0_i$-$S0_r$	$S0_i$-$S0_t$	S0
G	$A0_i$-$S0_t$	$S0_i$-$A0_r$	$A0_i$-$A0_t$	A0
H	$A0_i$-$S0_t$	$S0_i$-$A0_r$	$A0_i$-$S0_t$	S0
I	$A0_i$-$S0_t$	$S0_i$-$S0_r$	$S0_i$-$A0_t$	A0
J	$A0_i$-$S0_t$	$S0_i$-$S0_r$	$S0_i$-$S0_t$	S0

will produce a reflected and transmitted S0 wave in addition to the reflected and transmitted A0 wave, whereas the incident S0 wave from region B in figure 5.5 is above the frequency-thickness cut-off of the higher order A1 wave, and hence will produce reflected and transmitted mode converted A0 and A1 modes. All reflected waves from interface 1 are lost from any further interactions with the defect but will contribute to the enhanced signal at the detector.

Both the transmitted wave from the incident mode and from those mode conversions that occur at the first interface will continue in the defect to undergo a similar interaction at the second interface, figure 5.12b, and at the third interface, figure 5.12c. The wave modes of interest for the enhancement calculation are those that travel back towards the source, either directly from the first interface, or after interaction with all the interfaces shown in figure 5.12. The relevant interactions are listed in table 5.1 for an incident A0 mode.

Although it is possible that all of the interactions in table 5.1 will contribute to the enhancement one must determine if they will arrive close enough in time for a superposition to occur. Take the example of a square based defect that is 50% of the sheet thickness, with a width equal to the average width of the v-shaped defects, 282 ± 16 μm, with arrival times calculated for the waves in table 5.1, considering the change in wave velocity that occurs in the thinner section of the notch. For an incident A0 wave at a frequency-thickness of 1.3 MHz.mm, this change in thickness equates to a velocity change from 3168.6 ms^{-1} to a velocity of 3048.3 ms^{-1}, and for a mode converted S0 wave at the same frequency-thickness this is a velocity change from 4862.6 ms^{-1} to 5331.4 ms^{-1}. The arrival times are shown in table 5.2, and are calculated for a detector position that is equal to five scan steps prior to the defect,

Table 5.2: Theoretical arrival times for the mode converted and reflected waves expected at the enhancement point, 0.25 mm from the defect edge.

Wave identifier	Arrival time (μs)
Incident A0	16.10
A	16.25
B	16.23
C	16.44
D	16.41
E	16.40
F	16.37
G	16.40
H	16.37
I	16.36
J	16.33

which corresponds to the position of the enhancement peak in figure 5.7b.

The time interval chosen for region A was $15.5 \leq t \leq 16.5$ μs, and, as all of the arrival times in table 5.2 are within this range, each of the interactions listed in table 5.1 can provide a contribution to the enhanced signal. Although multiple reflections within the defect are possible these are not considered here as the subsequent arrival time at the detector lies outside of the window used to examine the A0 wave enhancement.

To determine the contribution that each wave will have to the out-of-plane displacement the amount of the incident wave energy that will be present in each wave mode must be calculated. To achieve this reflection and transmission coefficients for the interactions are required, and these are listed in table 5.3 for a 50% through-thickness defect at a frequency thickness of 1.13 MHz.mm and are obtained from the work of Kim and Roh[113].

To determine the relative magnitudes of the contributing wave modes the assumption is made that energy is conserved at each interaction, such that the reflection, R, and transmission, T, coefficients follow[113],

$$R^2 + T^2 \leq 1 \quad . \tag{5.2}$$

If the energy of the incident wave mode is taken as unity then the proportion of this energy possessed by each reflection or mode conversion is represented by the relevent coefficient. For example, the direct reflection at interface one of an incident A0 wave mode, $A0_i$-$A0_r$, has a reflection coefficient of 0.262 from table 5.3 and therefore the reflected A0 possesses this proportion of the incident wave mode energy. It follows

Table 5.3: Interaction coefficients for 50% depth square based notch, at a frequency thickness of 1.13 MHz.mm[113].

Interface 1			
A0$_r$	A0$_t$	A0-S0$_r$	A0-S0$_t$
0.263	0.925	0.155	0.225
Interface 2			
A0$_r$	A0-S0$_r$	S0$_r$	S0-A0$_r$
0.325	0.175	0.300	0.163
Interface 3			
A0$_t$	A0-S0$_t$	S0$_t$	S0-A0$_t$
0.925	0.225	0.925	0.125

that the reflected A0 wave mode from interface 2, with reflection coefficient 0.325, for which the incident wave mode is the transmitted A0 wave mode from interface one (transmission coefficient 0.925), will possess 0.301 of the incident A0 wave mode energy, equal to the product of the coefficients of each interaction. The proportion of the incident A0 wave mode's energy possessed by each wave mode present at the enhancement point is calculated in this fashion to give an estimate of the relative amplitudes of each wave mode. The amount of the energy of the incident A0 mode that is present in each mode that contributes to the enhancement A_n, is given by the product of the reflection and transmission coefficients of the interactions that produced the chosen mode, C_i,

$$A_n = \prod_i C_i \quad , \tag{5.3}$$

where the relevent interactions for the A0 enhancement studied here are those given in table 5.1, with an example of the coefficients used given in table 5.3. For example the wave at the enhanced position that was generated by a transmission of the A0 wave at interface 1 ($C_i = 0.925$), followed by a reflection with no mode conversion at interface 2 ($C_i = 0.325$) and a transmission with no mode conversion at interface 3 ($C_i = 0.925$), posses a fraction of the energy of the incident A0 wave given by the product of the coefficients from each interaction, A$_n$ = 0.278.

The phase changes that the waves incident on the interaction interfaces in figure 5.12 will undergo whilst they travel through the thinner section of the plate must be considered[113], as these will describe the nature of the superposition between these waves and the incident mode, be it constructive (phase difference of 0°) or destructive (phase difference of 180°). Table 5.4 gives the phase differences between the waves present at the enhancement position to the incident wave mode

Table 5.4: Phase difference between waves at the enhancement point and the incident pure A0 wave, for a frequency-thickness of 1.3 MHz.mm, for defects with depths of 10%, 50% and 75% of the through-thickness[113].

-	-	Phase change at defect depth		
Interaction	Wave mode	10%	50%	75%
A	A0	126	83	83
B	S0	249	234	237
C	A0	114	240	297
D	S0	166	269	303
E	A0	180	211	223
F	S0	108	160	174
G	A0	269	296	317
H	S0	12	64	71
I	A0	65	52	56
J	S0	354	0	3

for the interactions, A - J, listed in table 5.1, as obtained from the work of Kim and Roh[113]. The phase differences between the reflected and mode converted waves and the incident wave vary as a function of defect depth and, therefore, different wave modes will make a different contribution to the enhanced out-of-plane displacement at different defect depths, depending on if they are more or less in phase with the incident mode.

The signal observed at the detector is the out-of-plane component of the surface displacement only, and when a superposition of wave modes occurs the resulting displacement is the cumulative ultrasonic field, with a contribution from each wave mode. To determine the contribution from each wave mode an estimate of the wave amplitude A_n is made using the method outlined above, and then a measure of what proportion of the wave energy is in the out-of-plane component of the wave displacement is required[22,89]. Although the wave motion of a Lamb wave is distributed between in-plane and out-of-plane components, the IOS detector is only sensitive to the out-of-plane motion, therefore each wave present at the enhancement point will provide a different contribution to the total out-of-plane displacement, depending on the magnitude of the out-of-plane component of that given mode. The contibution to the total out-of-plane displacement from each wave mode that is present at the enhancement point, Z_n, is calculated by solving equations 2.40 and 2.42 for the chosen wave mode and frequency-thickness, giving in-plane and out-of-plane displacements that vary with depth as in figure 2.2. An expression for the expected total displacement at the enhancement point, Z_E, is formed by considering the amplitude of each contributing mode, A_n, and the proportion of each of these in the out-of-plane direction to give (assuming constructive interference between all modes at the same position),

$$Z_E = \sum_n Z_n . A_n \quad . \tag{5.4}$$

For the incident A0 wave mode the displacement observed by the detector is obtained by choosing the energy of the incident wave to be unity and taking the proportion of the displacement in the out-of-plane direction for the A0 wave mode, at the relevant frequency-thickness, to give an out-of-plane displacement that is expected when only the incident wave is present of $\mathrm{Z}_{incident}$. This allows the formation of a theoretical enhancement factor, E_{theory}, from the theoretical displacement at the enhanced position, Z_E, and the displacement expected for the incident wave mode alone, $\mathrm{Z}_{incident}$,

$$E_{theory} = Z_E / Z_{incident} \quad . \tag{5.5}$$

The theoretical enhancement factors for the interaction of an incident A0 wave with a square based notch are shown in figure 5.14 and compared to the experimental and simulation results from section 5.2.1 and the theoretical enhancement factors from an open mouthed crack.

5.3.2 Wave interaction with open mouthed crack

A similar approach is used to form a theoretical enhancement factor for the opening mouth crack studied by Castaings et al, where the reflection and transmission coefficients for the defect were determined through the modal decomposition method[114]. In this method any acoustic field can be expressed as an expansion of the vibrational modes of the structure, so, for example, the ultrasonic field for an incident Lamb wave scattered at a defect is described by a superposition of all of the Lamb wave modes that can be supported through the plate thickness at the defect location. This includes both propagating and non-propagating waves, as were described in section 2.1.4.2, and the coexistance of these waves allows for the boundary conditions at the defect to be satisfied; these being that there are stress free crack surfaces and that the velocity and stress fields must be continuous in the plane normal to the plate[114].

The particle motions at each side of the defect are then found by restricting the infinite series of avaliable wave modes to a solvable linear system. The derivation and solution of these is not shown here but is explained in detail in reference[114], and

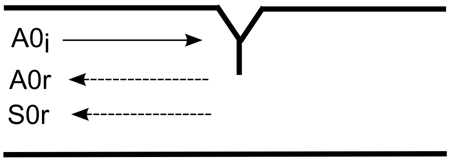

Figure 5.13: Interaction interface for a open mouthed crack defect showing the direction of incident A0 wave, A0$_i$, reflected A0 wave, A0$_r$, and mode converted S0 wave, $S0_r$.

Table 5.5: Interaction coefficients for a variety of depths of open mouthed crack defects for an incident A0 wave mode at a frequency-thickness of 1.3 MHz.mm in a 1.5 mm thick sheet.

Defect depth (%)	A0-A0$_r$	A0-S0$_r$
5	0.04	0.01
25	0.20	0.05
50	0.28	0.14
75	0.52	0.16
90	0.84	0.10

these are used to provide reflection and transmission coefficients for the propagating Lamb wave modes as a function of defect depth. The coefficients were verified by the authors against finite element method simulations, and can be used in a similar fashion to the coefficients from the square based notch, to predict which wave modes are present at the enhancement position.

For the open mouth crack only the interactions occuring at a single interface are considered, as shown in figure 5.13, which simplifies the determination of which modes will be present at the enhancement position as only the reflected and mode converted waves travelling back towards the detector need be considered. For an incident A0 wave mode at a frequency-thickness of 1.3 MHz.mm, the only interactions of interest are a reflected A0 wave mode and a mode converted S0 mode, the reflection and transmission coefficients of which are provided in table 5.5 for selected defect depths.

In a similar fashion to the approach taken for the square based notch defect the modes that will be present at the enhancement point are identified, and this knowledge is again combined with the distribution of the energy between the in-plane and out-of-plane directions to provide a theoretical expected measured signal strength using equation 5.4. A theoretical enhancement factor can then be calculated using equation 5.5.

To validate the theoretical models for the A0 enhancement they are com-

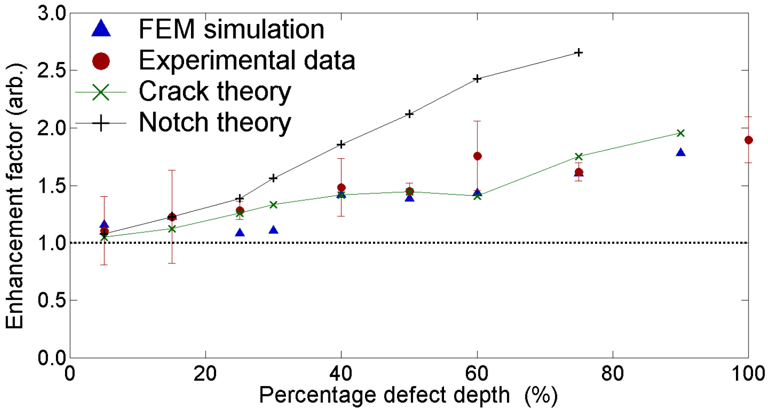

(a) 0.5 mm thickness sheet

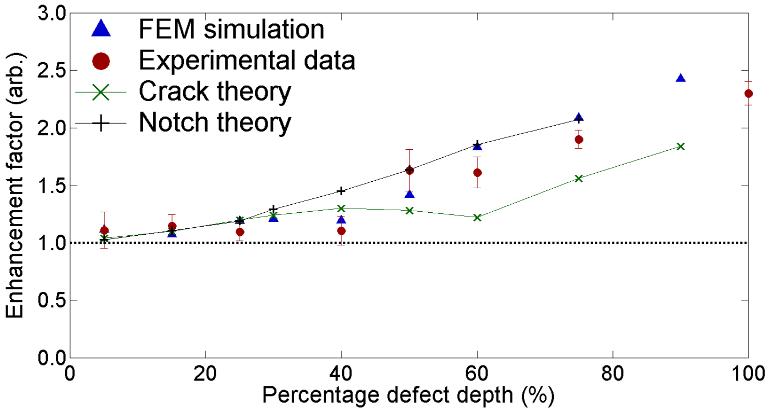

(b) 1.5 mm thickness sheet

Figure 5.14: Experimental, modelling and theoretical enhancement factors as a function of defect through-thickness for the A0 fundamental wave mode in 0.5 mm and 1.5 mm aluminium sheets.

pared to the experimental and modelling results from figures 5.9 and 5.10, and this comparison is shown in figure 5.14. It can be seen that for both sheet thicknesses the experimental and modelling results from the v-shaped defects share a good agreement with the theoretical values obtained from the test models.

For the 0.5 mm thick sheets the experimental and modelling data has a better agreement with the open mouthed crack, which can be related to the milling manufacturing process that was used to create the defects. As was seen in figure 5.2a, the milled defects have a large total width of ≈770μm, which means that the waves produced by interactions with the notch interfaces 2 and 3 in figure 5.12 have a longer distance to travel before arriving at the enhancement position. The extended path length means that the waves produced by interactions C - J in table 5.1 arrive outside of the time window used to evaluate the waves present at the enhancement point, meaning that the superposition is only possible between the incident A0 wave, a reflected A0, and a mode converted S0 produced from interface 1, and therefore as it includes modes that arrive outside of the enhancement window, the notch model will overestimate the enhancement. The open mouthed crack model predicts an enhancement arising from only these first reflections, and as such has a better agreement with the experimental enhancement factors from the wider defects in the thinner sheets.

For the 1.5 mm sheets the experimental results show a closer agreement to the values predicted by the square notch model as the smaller defect width of $\approx 357\mu$m from the laser micro-machining ensures that the mode converted waves produced within the defect width will arrive at the enhancement point within the time interval used to evaluate the enhancement, and can therefore contribute to the enhanced signal. For shallow defects in both sheet thicknesses the experimental enhancement factors shown good agreement with both of the theoretical models.

5.4 Multi-peaked enhancements

The differences between the enhancement peak structures observed in figure 5.7 for the A0 and S0 modes (where the A0 mode has a single peak and the S0 mode has multiple peaks) can be explained through an examination of the wave shapes at the chosen frequencies, beginning with the multi-peak enhancement that was seen for the S0 wave mode in figure 5.7a. Near to the defect the enhancement peak arises from a superposition of the incident S0 wave mode with a reflected S0 wave, and the mode converted A0 and A1 waves produced at the defect. The increased frequency magnitude at the enhancement position, -0.7 mm from the defect, is attributed to the constructive interference of these coincident arriving modes at the detector. The position at which this main enhancement peak occurs is dependent upon the phase change that occurs at the defect when the mode converted waves are produced, which in table 5.4 was shown to vary between interactions and to be also dependent upon the defect depth[113]. Therefore, the position of the first enhancement peak is dependent upon the defect depth, and this can be seen in figure 5.15 for several different depth defects in a 1.5 mm thick sheet.

The enhancement peaks farther away from the defect are also attributed to a superposition between the incident S0 wave mode with modes reflected from the defect, however, in this case the superposition is with reflected A0 and A1 modes. These waves are generated by the reflection and mode conversion of the faster trav-

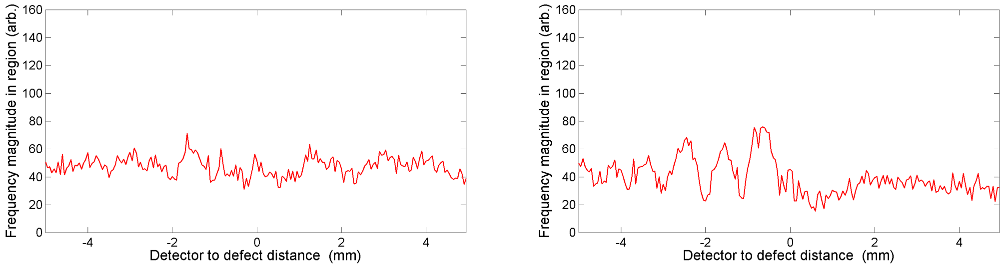

(a) 0.375 mm defect

(b) 0.75 mm defect

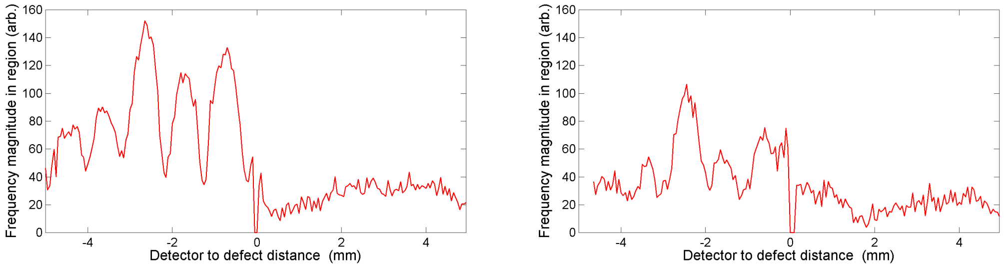

(c) 1.125 mm defect

(d) 1.5 mm defect

Figure 5.15: Multi-peaked signal enhancements for different depth defects; the enhancement peak position closest to the defect (0 mm) is dictated by the phase change upon reflection.

elling incident A0 and A1 modes that arrive at the defect before the incident S0 mode. This will occur due to the fact that each of these waves is not a simple point displacement, but has an extended wave shape in time that trails behind the wavefront, as can be seen in figure 5.16. This feature is important as if just the single value of the arrival time calculated from the known group velocity, say, of the reflected A0 mode is considered then it can be shown that it will not coincide with the time window used to examine the S0 wave mode at the enhancement position; however the trailing part of the wave form will enter the S0 time window and hence be avaliable to form a superposition.

If a time window is taken over a defect-free A-scan, starting at the arrival time of the fastest A1 wave mode at the given frequency-thickness, and extending to later than the expected arrival time of the slowest S0 wave mode, a narrow frequency filter at 1.63 MHz (middle frequency of the region of interest) can be applied to the data to reduce the interference from other frequency-thicknesses, and the wave shapes of the three supported modes, A0, S0 and A1, can be obtained. The filtered defect-free data is shown in figure 5.16, in which the most important feature is the sinusoidal shaped section that begins at 25 μs and extends to 30 μs, which encompasses the arrival times that were used to examine the enhancement in the chosen region of the S0 mode. This sinusoidal section begins before the expected

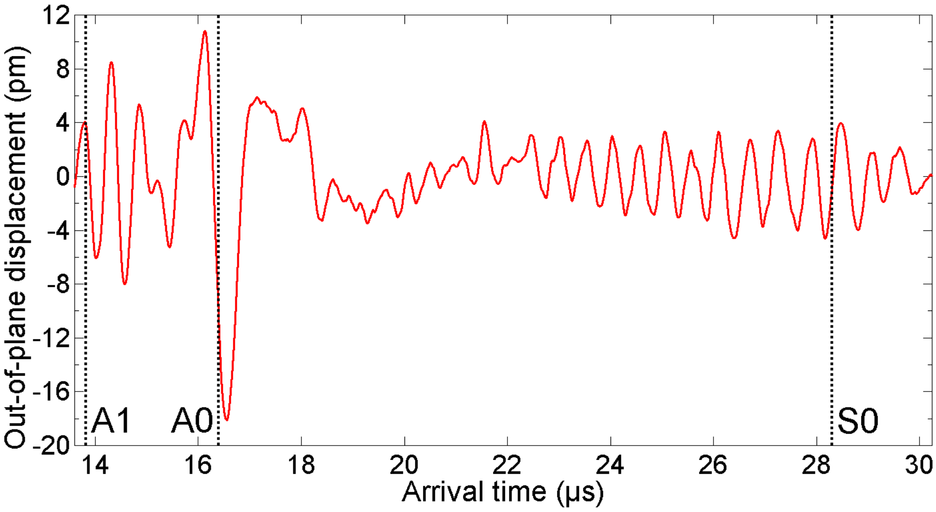

Figure 5.16: A-scan filtered at 1.63 MHz, showing the waveshapes of the incident A1, A0 and S0 wave modes in a 1.5 mm thick defect free aluminium plate.

arrival time of the S0 mode, and can be therefore seen as a trailing component of the A0 and A1 modes. Upon interaction with the defect, a phase-shifted reflected wave with a similar wave shape will be produced whose arrival time at the detector will be dependent upon the position of the detector with respect to the defect. This will produce a similar wave shape for the reflected wave to that seen for the defect free case which will arrive later in time the farther the detector is from the defect. This corresponds to a wave mode moving to the right across the image in figure 5.16 as the detector is moved farther from the defect.

As the detector moves away from the defect the sinusoidal section of the reflected wave mode will move in and out of phase with the similar section of the incident wave shape, producing a series of positions at which either constructive or destructive interference between the two is observed. This produces an alternating pattern of higher and lower wave amplitudes, corresponding to an in-phase or out-of-phase position, with a characteristic separation of $\delta = 1.0$ mm between sucessive peaks or troughs measured on figure 5.15. This separation is constant with defect depth for defects deeper than 40% of the through-thickness. For defects shallower than this, the reflectivity of the defect is insufficient to produce a meaningful reflected wave from which to produce a superposition and the pattern is not observed.

Take the example of an incident wave that is a pure sinusoid, such as that in figure 5.17a, that on reflection at a defect has a phase difference of 160° with respect to the incident wave. When these waves arrive in the same time window they form a superposition, and the resultant wave is smaller than the incident wave.

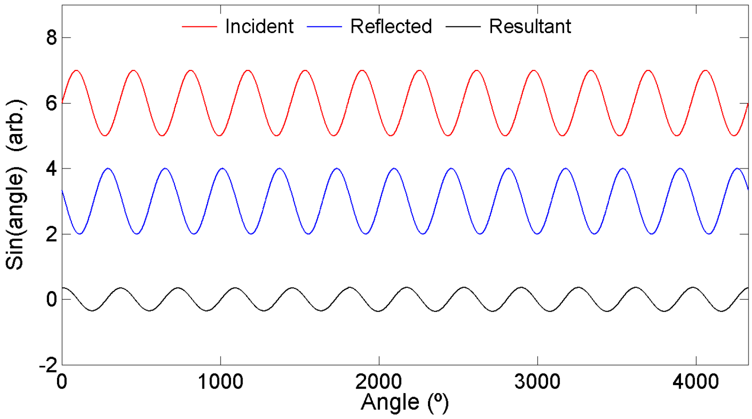

(a) Phase difference of 160 °

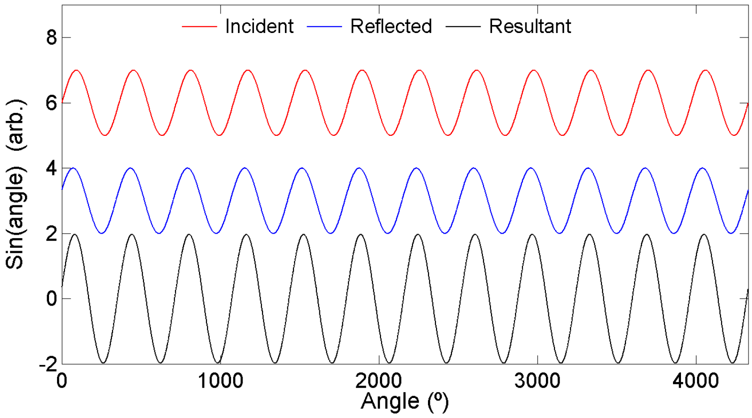

(b) Phase difference of 20 °

Figure 5.17: Resultant waves caused by interference between a simulated incident sinusoidal wave with a reflected wave for an out-of-phase reflection (a) and an in-phase reflection (b).

This is analogous to the behaviour of the S0 wave interacting with the defect when the detector is very close to the defect but not at the enhanced position, say at a position of -0.2 mm on figure 5.7a. As the detector is moved away from the defect the arrival time of the reflected wave will vary and there will come a position where the reflected and incident waves are in phase (shown here with a phase difference of 20 °), leading to a resultant wave (shown in figure 5.17b) which is larger than the incident wave. This is analogous, for example, to a detector position of -0.7 mm on figure 5.7a.

The first instance of constructive interference between the incident and reflected waves is dependent upon the distance of the detector to the defect, and on the phase of the reflected wave relative to the incident. Although the first enhancement is expected to occur at the same interval from the defect as the separation of the constructive interference peaks, it is observed to appear at less than the total separation in figure 5.15. This is due to the phase change on reflection that the wave experiences at the defect, and ensures that less than a total wavelength is required for the two waves to become in-phase. This phase change is dependent upon the defect depth, and as such the position of the first enhancement peak is correspondingly dependent upon the defect depth.

As the detector is moved away from the defect, the reflected wave must travel farther to arrive at the detector, resulting in it arriving relatively later with respect to the incident wave. At certain positions it will again achieve this in-phase relationship with the incident wave, and the separation of these positions is dependent upon the velocity differences between the wave modes that are interfering. If the difference in the velocities, Δv, is compared for each of the wave modes, which are all of the same frequency of $f = 1.63$ MHz, a characteristic length λ_{con}, can be calculated at which the waves will arrive at the detector in phase, giving rise to constructive interference, using the following;

$$\Delta v = f \cdot \lambda_{con} \quad . \tag{5.6}$$

This gives the characteristic lengths shown in table 5.6, which are very close to the peak separation observed between the enhancement peaks in figure 5.15 for various different defect depths. The calculated length values lie either side of the value of the separation between the enhancment peaks ($\delta = 1.0$ mm) and hence both modes are expected to make a contribution to the enhancement at these positions, giving the peaks at detector positions of -0.7 mm, -1.7mm, -2.7mm, -3.7mm and -4.5mm in figure 5.7a. At positions equal to δ / 2, a large drop in the observed magnitude in the window is seen, which corresponds to the positions at which the A0 and A1 modes are no longer in phase (positions separated by λ_{con} / 2) with the incident S0 mode and hence no constructive interference occurs, giving the troughs at detector positions of -1.25 mm, -2.15 mm, -3.15mm, and -4.05mm in figure 5.7a. Evidence of this interference behaviour is shown for the filtered data in figure 5.18 in which the sinusoidal part of the wave train arriving in the time window of interest is shown at various detector positions.

The small difference in the characteristic lengths for the A0 and A1 reflections leads to a spreading of the peaks farther from the defect, as can be seen in figure 5.15, and when the detector is sufficiently far away from the defect the trailing components of the A0 and A1 wave modes arrive too late at the detector to provide a contribution to the out-of-plane displacement, and a steady level is reached when

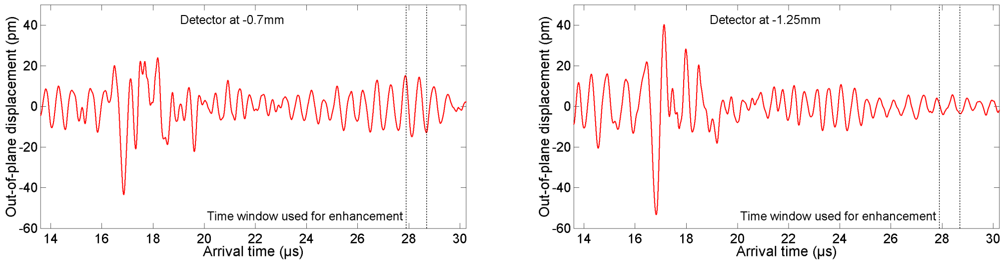

(a) Detector at -0.7 mm (b) Detector at -1.25 mm

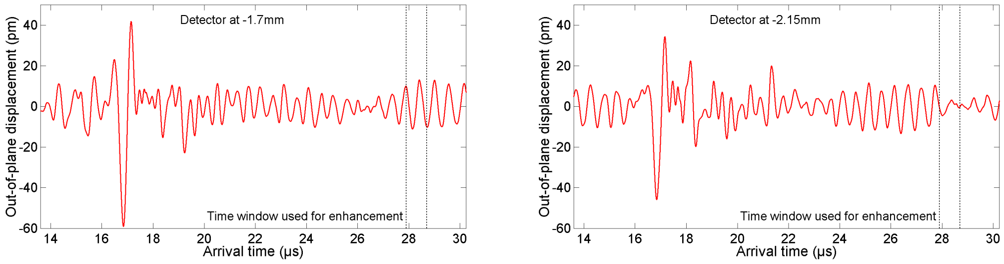

(c) Detector at -1.7 mm (d) Detector at -2.15 mm

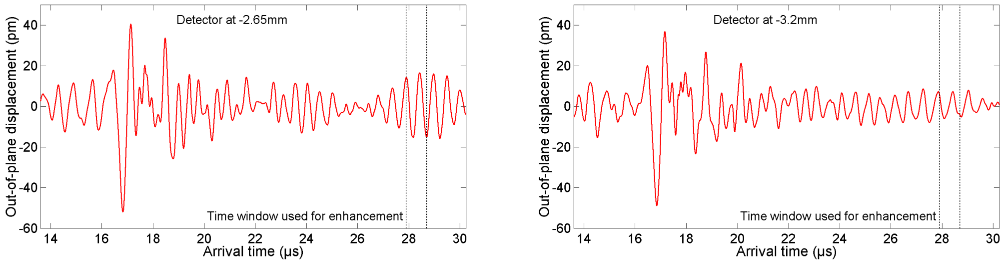

(e) Detector at -2.65 mm (f) Detector at -3.2 mm

Figure 5.18: Filtered waveshapes (at 1.63 MHz) at alternate enhanced and non-enhanced positions, illustrating a beating behaviour within the time window of interest as the detector is moved away from the defect.

the detector is away from the defect.

The peak structure of the A0 enhancement, as seen in figure 5.7b, is simplified by the smaller number of wave modes that can be supported at the chosen frequency thickness. In this case only the fundamental S0 and A0 modes need be considered, and there is a large difference in the wave velocities between the two modes. The wave shapes of these modes, filtered at 0.9 MHz, can be seen in figure 5.19, in which a large difference between the wave structures of the S0 mode, arriving at 10.6 μs, and the A0 mode, arriving at 16.1 μs is seen. Again, the point at which constructive interference is first seen is dependent upon the phase change at the defect, and the expected separation of subsequent points of constructive interference can also be calculated using the method outline above, giving a characteristic length of $\lambda_{con} = 1.8$ mm. This first enhancement is again caused by a superposition of the

Table 5.6: Calculated beat lengths for interactions between the reflected A0 and A1 waves with the incident S0, $v_g = 1802\ ms^{-1}$, wave mode.

Wave mode	v_g	v_g - v_{gs0}	λ_{beat}
A1	3689	1887	1.18 mm
A0	3109	1307	0.80 mm

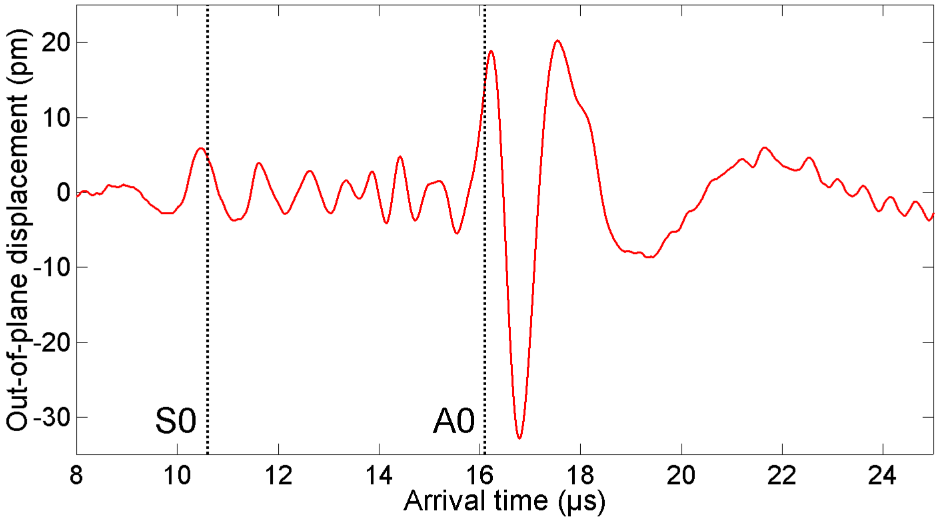

Figure 5.19: A-scan filtered at 0.9 MHz, showing the waveshapes of the incident A0 and S0 wave modes in a defect free plate.

mode converted and reflected waves produced by the interaction of incident A0 wave with the defect. The multi-peaked structure is not seen at this separation, although strong destructive interference at a separation equal to λ_{con} / 2 is observed.

The absence of subsequent positions of full constructive interference is due to the small amplitude of the S0 wave shape with respect to that of the A0 mode, meaning that as the reflected waves generated by the earlier arriving S0 wave with the defect superimpose with the incident A0 the change in the out-of-plane displacement is small. A small peak can be seen at a position away from the point of destructive interference before a steady no-defect value is established. As the detector travels further away from the defect, the S0 mode will rapidly leave the window used for the enhancement tracking, and as it does not have a long wave train, no additional enhancement positions from the trailing wave component are seen. This can be seen by examining the multipeaked nature of the A0 enhancement in the FEM simulations, shown in figure 5.8b, in which several peaks, separated by the predicted separation, are seen. As the noise associated with the FEM simulations is minimal the smaller enhancement peaks can be seen, and these are expected to still be present in the experimental data if the noise in the received signal could be sufficiently reduced.

5.5 Conclusions

In this chapter it has been shown through experimental and FEM data that near-field enhancement of Lamb waves exists when a laser detector is passed over a v-shaped surface-breaking defect. The enhancement is attributed to a superposition of the incident Lamb wave with reflected and mode converted waves generated at the defect, and this has been validated by the good agreement show between theoretical enhancements formed from two test models with the experimental data. The size of the enhancement factor can be used to estimate the defect depth for v-shaped defects in sheets and the defect position can be obtained through B-scan analysis, coupled with signal strength monitoring.

Chapter 6

Lamb wave scanning laser source enhancements for the detection of surface-breaking defects in plates

As discussed in chapter 5, thin plate-like structures are found in many essential industrial applications, and the failure of these structures can have catastrophic environmental and economic consequences[12,13,15,16]. In chapter 5 it was shown that scanning the laser detector over a surface-breaking defect gave rise to enhancements in the magnitude of the frequency content of Lamb waves that could be used to position and estimate the depth of a defect[22]. It has been reported for both Rayleigh[23,235] and Lamb waves[64,240,261] that a similar enhancement is observed when the laser source passes over the defect, however, the mechanisms responsible for the Lamb wave enhancement have yet to be studied in depth. Here, scanning laser source enhancements for Lamb waves are presented[116] in which the mechanisms responsible for the enhancement are identified, and the signal enhancements are shown to be different in structure to those presented for the scanning laser detection case (section 5.2.1).

The mechanisms that contribute to enhancements observed when a scanning laser source is passed over a defect for Rayleigh wave propagation[23,107,128,234,235] (section 4.4) are identified as also contributing to the enhancement observed for Lamb waves[116], as proposed in the work of Dixon and Burrows[64,261], with slight modifications made to accomodate the differences in defect geometry. These mechanisms include a superposition of the incident and reflected waves of the same Lamb

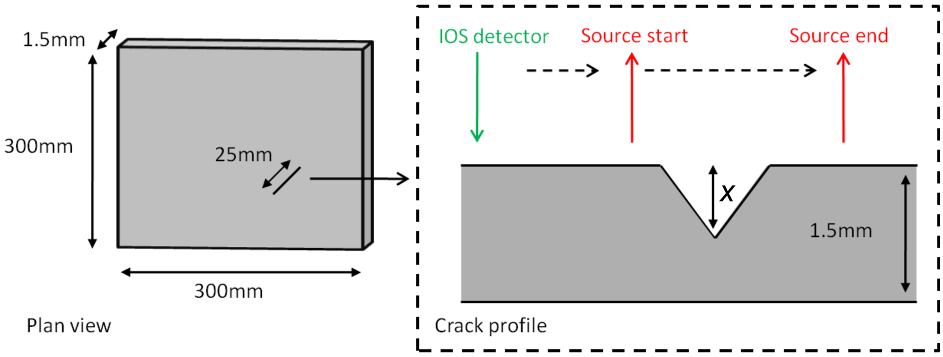

Figure 6.1: A schematic diagram showing both plan view and side profile of simple v-shaped defects, of depth x in mm, in aluminium plates for scanning laser source experiments. The percentage defect depth is given by $h = \frac{x}{1.5}.100\%$.

mode, truncation of the laser source, and a change in the boundary conditions of ultrasonic generation that occurs at the defect.

The extent of the enhancement observed at machined v-shaped surface-breaking defects is shown to be dependent upon the defect depth and an experimental procedure for characterising the defect depth and position is presented in section 6.3. A series of experiments were carried out and are presented here, with the aim of allowing a different enhancement mechanism to dominate in each experiment, thereby allowing the contribution of each mechanism to the overall enhancement to be estimated. The enhancement mechanisms and the experiments carried out into their influence on the signal enhancement are described in section 6.4.

6.1 Experimental details

With the aim of developing a means of characterising the depth and position of a surface-breaking defect, the near-field interactions of a scanning laser spot source with the crack were investigated. In order to ensure that the conclusions drawn from scanning laser source enhancements and those from scanning laser detection enhancements are complementary in a combined scanning system, experiments were carried out on the same collection of thin plate-like samples as in chapter 5.

Surface-breaking defects of different depths with a v-shaped side profile were produced by laser micromachining on aluminium sheets with dimensions of 300 x 300 x 1.5 mm. The samples were prepared in the same manner as in section 5.1 and a schematic of the experimental setup is shown in figure 6.1, in which the

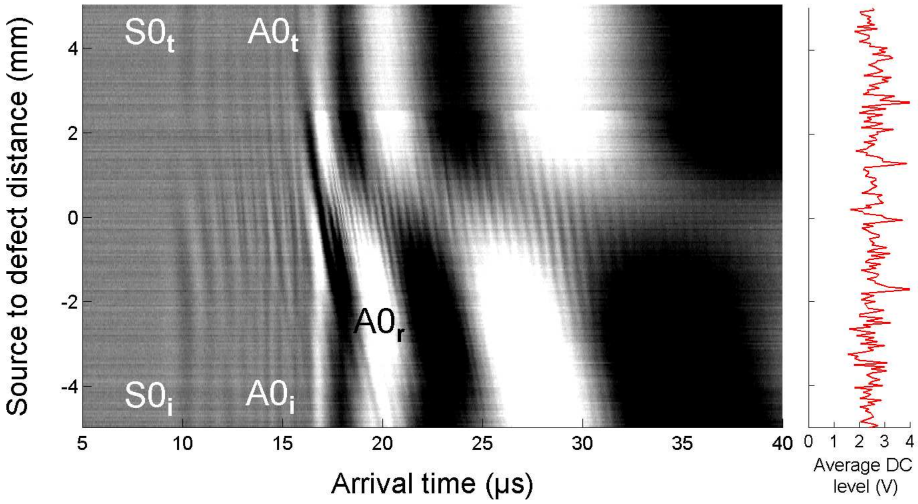

Figure 6.2: B-scan for a 75% through-thickness defect in a 1.5 mm thick sheet with incident (i), reflected (r) (only the reflected A0 wave is visible) and transmitted (t) Lamb wave modes labelled for both symmetric (S0) and antisymmetric (A0) wave modes. The DC level of the detector signal is shown in the right hand panel.

laser source was scanned over the defect in increments of 50 μm. A fixed separation was maintained between the source and detector to minimise the influence of wave dispersion and material attenuation on the results. At each position an A-scan was recorded and a sonogram produced, using the procedure outlined in section 2.1.5 and employed in chapter 5.

6.2 Defect positioning from B-scan analysis

Defect positioning can be achieved through inspection of experimental B-scans, where for a fixed separation of detector and source the incident wave modes are those with constant arrival times, and those modes reflected and mode converted at the defect have a varying arrival time with scan position. An example is shown in figure 6.2 for a 75% through-thickness defect.

The pattern of waves in the B-scan in figure 6.2 is different to that seen in the equivalent diagram for scanning laser detection (figure 5.4) in which a series of reflected waves were clearly visable, as in that case the detector was sufficiently close to their point of origin that temporal separation of these modes could occur at the defect. For the scanning source case the position at which the transmitted and reflected wave modes originate is not completely clear, making it difficult to identify the defect location using the same arguments as in section 5.2. The position of the defect can still be estimated to within ±2 mm by visual identification of the point at which the reflected modes appear in 6.2.

The second positioning technique of monitoring the DC level at the detector is also ineffective, as the detector is positioned away from the defect on an undamaged region of the sample, and so the DC level as a function of detector position is unchanged when the laser source illuminates the defect (right hand panel of figure 6.2). This makes defect positioning from the B-scan image difficult for scanning laser source experiments, however, as is shown in section 6.4, a knowledge of the enhancement mechanisms involved allows the defect position to be estimated from the structure of the enhancement peaks.

6.3 Defect depth estimation using scanning laser source near-field enhancements

Near-field enhancements for a scanning laser source have previously been reported to vary as a function of the defect depth for square based notched defects for Rayleigh wave propagation[23], however, this defect structure does not give a good representation of a true defect. The v-shaped defects studied here provide a more realistic defect structure, with an opening angle relative to the horizontal of less than $90\,^\circ$, making them more representive of the defect opening for the real open stress corrosion cracks discussed in section 1.4.2. A variation in the near-field enhancement as a function of defect depth for these defects gives a means of estimating the severity of the defect[116].

A sonogram (as described in section 2.1.5) was produced at each scan position as the laser source was moved over the defect, and the theoretical arrival times of the supported Lamb modes were overlaid onto the sonogram, so as to aid in the identification of individual modes, with examples shown for a 75% through-thickness defect in figure 6.3. A large increase in the magnitude of the frequency content of several wave modes is seen in the sonograms when the laser source is directly over the defect (figure 6.3b), and the emergence of several higher order wave modes that are not visible when the source is far away from the defect (figure 6.3a) can be seen, as has been previously reported[240]. The enhancement observed for the scanning laser source approach with Lamb waves is significantly larger than that seen for the scanning laser detection case (chapter 5), which is the opposite to the behaviour observed for the case of Rayleigh wave enhancements at angled defects (chapter 4).

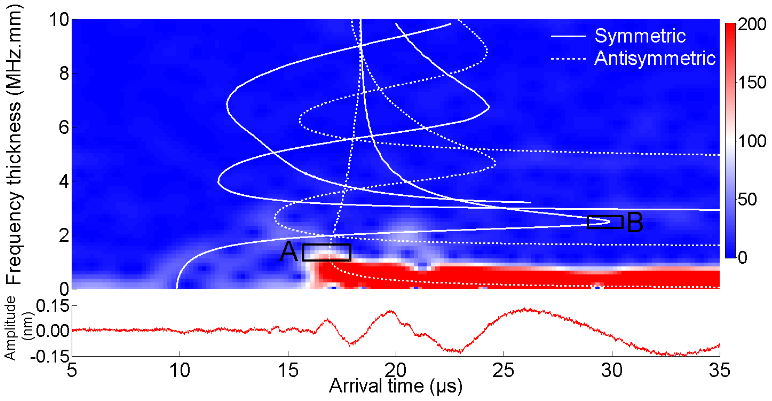

(a) No defect region

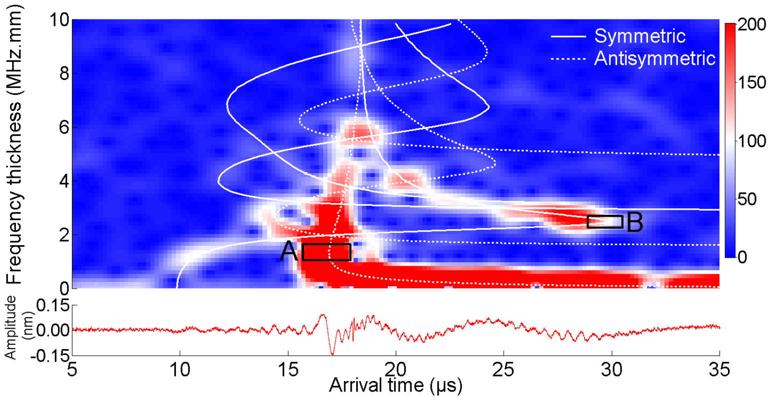

(b) Defect near-field

Figure 6.3: Sonograms with calculated Lamb wave arrival times overlaid for the case in which the laser source is far away from the defect (a), and for direct illumination of the defect (b) for a 75% through-thickness defect.

To allow for a direct comparison with the results in chapter 5 the peak magnitudes from the sonograms for the same regions of the A0 and S0 modes were investigated as a function of source position. The arrival times were adjusted slightly from the scanning laser detection experiments to account for a small difference in the source to detector distance between the two sets of experiments. The regions of interest studied were between $1.05 \leq fd \leq 1.65$ MHz.mm and $15.7 \leq t \leq 17.9$ μs for the A0 mode, and $2.25 \leq fd \leq 2.70$ MHz.mm and $28.9 \leq t \leq 30.5$ μs for the S0 mode, labelled A and B respectively on figure 6.3a.

As in chapter 5 the peak value of the magnitude from the chosen regions of the sonogram at each scan position was measured, and is referred to as the frequency magnitude. These regions were chosen for the fact that at the times and frequency-thicknesses chosen the incident wave consists of a single wave mode, thereby simplifying the interpretation of the signals.

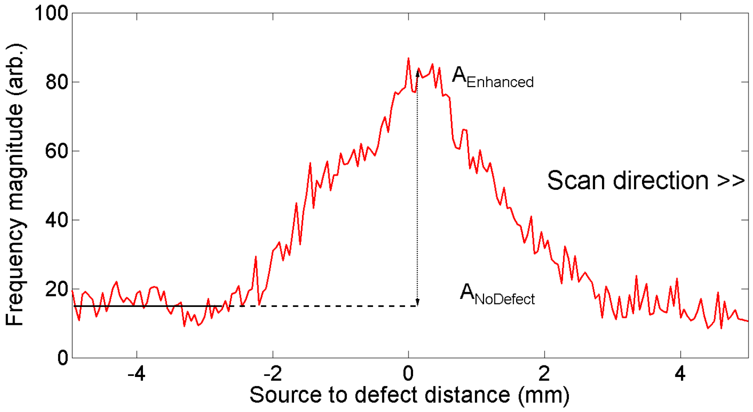

(a) S0 tracking

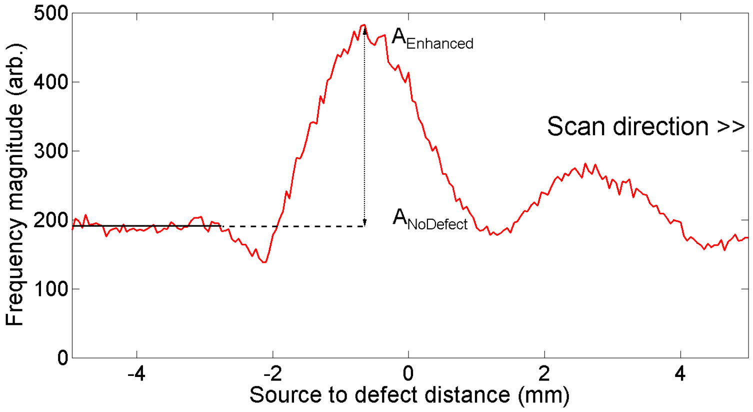

(b) A0 tracking

Figure 6.4: Experimental peak frequency magnitude tracking for the S0 (a) and A0 (b) fundamental waves as the laser spot source is passed over a 75% through-thickness defect in a 1.5 mm thick sheet.

As the laser spot source is scanned over the v-shaped defects, enhancements are observed in the sonograms. A defect free sonogram is shown in figure 6.3a, and an enhanced sonogram shown in figure 6.3b for a 75% through-thickness defect. For the enhanced position the higher order Lamb wave modes have enhanced magnitude at certain frequencies when compared to the positions at which the source is far away from the defect, with modes being generated that are not present (to any significant extent) when the laser source is a distance away from the defect[240], this can be seen in figure 6.3b. There is also an increase in the magnitude of the frequency content for the fundamental waves, such as those studied in regions A and B on figure 6.3.

An example of the variation in the peak magnitude and the subsequent enhancement is shown for a 75% through-thickness defect for both the S0 mode, figure

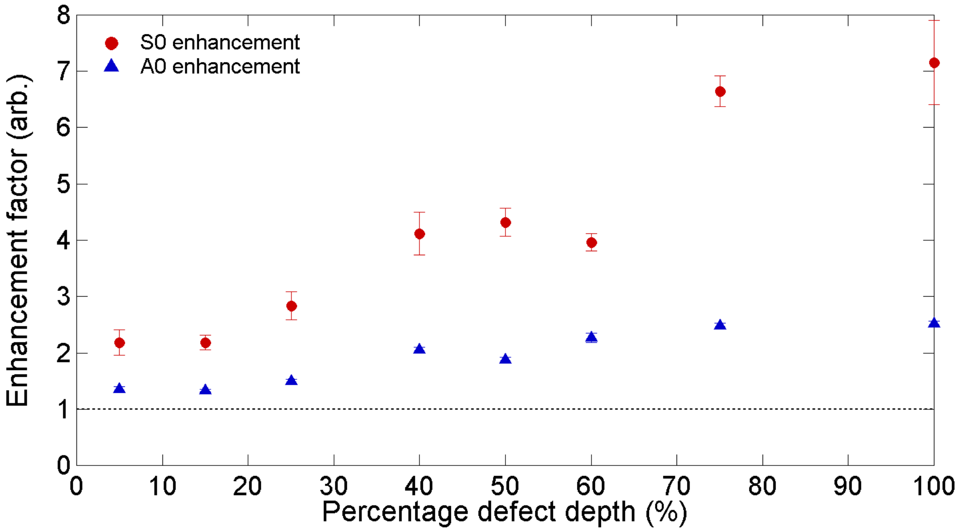

Figure 6.5: Enhancement factors as a function of defect depth for v-shaped defects in aluminium plates for the S0 and A0 wave modes.

6.4a and the A0 mode, figure 6.4b. Here the negative source positions correspond to the region of the scan in which both the laser source and detector are on the same side of the defect. Large enhancements are seen for both wave modes, with a large increase in the frequency magnitude, $A_{Enhanced}$, as the laser source passes over the defect, and a steady level when no defect is present, $A_{NoDefect}$. The enhancement factor, E_f, for this defect is obtained from equation 5.1. The peak magnitude can be seen to increase by a factor of 2.48 for the A0 mode and 6.65 for the S0 mode when the source is over the defect. These enhancements are significantly larger than those observed when the laser detector is passed over the defect, which were 1.90 for the A0 and 1.85 for the S0 mode.

The shape of the enhancement peak is again different between the two wave modes, with the S0 mode exhibiting a single enhancement peak, and the A0 mode a double-peaked structure. This suggests that the mechanisms that are responsible for the enhancement (as described in section 6.4) have a different degree of influence over the enhancement for different wave modes. The cause of the differences in the enhancement peak shapes are explained in section 6.5.

The variation in the enhancement factors in the chosen regions of the S0 and A0 wave modes as a function of the defect depth, h, is shown in figure 6.5. The overall magnitude of the enhancements is larger than the equivalent scanning laser detector enhancements for the same defect depths, shown in figures 5.9 and 5.10. This is contrary to the case for Rayleigh wave enhancements, in which the laser detector enhancements were shown in chapter 4 to be larger than those for the scanning laser source for angled surface-breaking defects[95].

For both wave modes the enhancement factors increase with increasing defect depth, with the S0 mode experiencing much larger enhancements than the A0 mode. The general increase as a function of increasing defect depth allows the enhancement factors in figure 6.5 to be used as a means to identify the depth of a defect; if the enhancement factor is found for both wave modes for a v-shaped defect of unknown depth the values obtained can be used to estimate the defect depth from figure 6.5. For example if a scan over a defect of an unknown depth yields an enhancement factor of 4.31 in the S0 region and 1.87 in the A0 region, then from figure 6.5 the defect depth can be estimated to be 50% of the through-thickness.

For defect depths between 40% and 60% of the full thickness, for both wave modes there exists a region in which the enhancement factors are very similar over a range of defect depths, introducing some ambiguity into the depth estimate. In order to reduce this uncertainty this data could be used in conjunction with scanning laser detection enhancements (chapter 5) to improve the probability that the correct defect depth is estimated.

6.4 Investigation of the contributing mechanisms to scanning laser source enhancements

In order to refine the understanding of the laser source enhancements a series of experiments were carried out to ascertain if the same mechanisms that contribute to Rayleigh wave enhancements are also responsible for enhancements in Lamb waves[23,107,128,234,235]. The enhancement observed for Rayleigh waves was found to arise from a combination of the truncation of the source as it passes over the defect, a superposition of the incident and reflected waves at the detector and the change in the boundary conditions of generation due to the presence of the defect discontinuity.

6.4.1 Truncation Mechanism

It has been shown (in section 2.2.4) that the character of the ultrasound generated by a laser spot illuminating a metal is dependent upon the incident power, and the temporal and spatial profile of the source[27]. As the laser spot passes over the lip of a defect the illuminated area is reduced by the presence of the disconti-

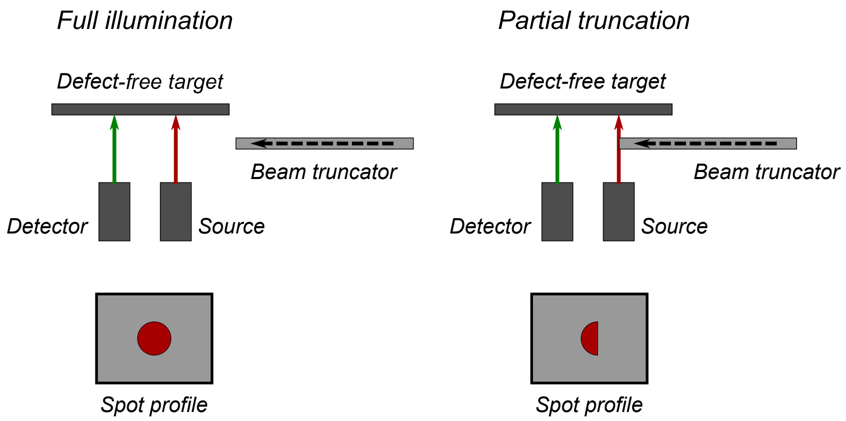

Figure 6.6: Schematic diagram showing the experimental setup used to investigate the influence of laser source truncation on Lamb wave enhancement. The beam profile incident on the sample surface is shown for free generation and partial beam obstruction.

nuity, leading to a truncation of the spatial extent of the source, whilst both the power density and pulse duration remain the same[23,27,234,235]. This truncation has been shown previously to be responsible for an increase in the frequency content of Rayleigh waves[23,166,185,235]. The presence of the defect will also affect the boundary conditions of generation and hence for this measurement a beam truncator is used.

The frequency content of the laser source is dictated by equation 2.71, and so as the source begins to pass over the defect, w is reduced, leading to an increase in f_{max}, albeit with a reduction in the wave amplitude as the illuminating area is smaller and hence less power is transferred into the test material. For Lamb wave production this will increase the energy contained in the higher order wave modes as described in section 2.1.4.2, leading to enhanced magnitudes of these waves being visible in the sonogram as the source passes over the defect.

The effect of beam truncation on the enhancement of the S0 and A0 wave modes was investigated by targeting both the detector and source onto a defect free sheet, whilst a second sheet was passed in front of the generation source in increments of 50 μm to truncate the source profile. A schematic diagram of this setup is shown in figure 6.6.

With the same data processing procedure applied to the data as described in section 6.3, the tracking of the sonogram peak magnitude for the S0 and A0 modes was obtained and can be seen in figure 6.7. For the S0 wave mode the enhancement factor is found to be $E_f = 1.35 \pm 0.25$ and for the A0 wave mode $E_f = 1.18 \pm 0.33$. These enhancements are small and they are not easy to distinguish from the unobscured signal. These enhancement factors are smaller than

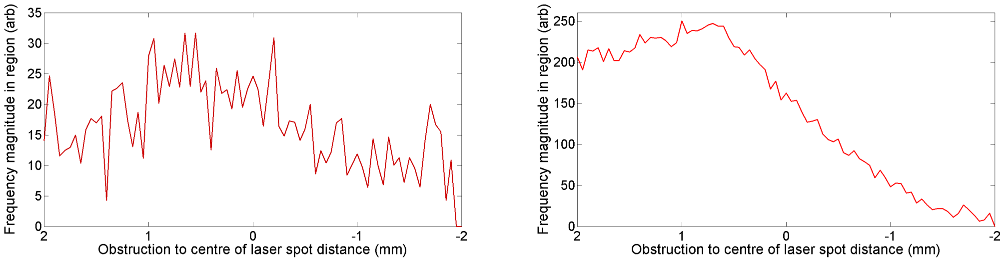

(a) S0 mode

(b) A0 mode

Figure 6.7: Frequency magnitude tracking of the S0 (a) and A0 (b) wave modes on a defect free sheet as the laser source is truncated.

those shown in figure 6.5, however, they still must be considered as contributing to the enhancement factors observed for the full v-shaped defects.

This result is consistent with previous investigations into Rayleigh waves interacting with defects propagating normal to the sample surface[235]. For the v-shaped defects here the truncation process will be more gradual as the slope of the defect opening is such that there is a possibility that generation may continue briefly on the sloped surface, meaning that the change in the boundary conditions of generation will come into play to influence the enhancement (section 6.4.3).

6.4.2 Superposition mechanism

In chapter 5 it was shown that for scanning laser detector enhancements, the increase in the observed signal is due to a superposition between the incident wave and those waves reflected and mode converted at the defect. For scanning laser detection the observation point was close enough to the defect that the arrival times of these different waves at the detector were close enough together that they increased the out-of-plane displacement in a chosen time window despite having different velocities. For the case in which the source is close to the defect the differences in wave velocities become important.

For the regions of the A0 and S0 wave modes studied here, one would still expect reflection and mode conversion to other wave modes with the same frequency-thickness on interaction of the incident wave with the defect. However, the arrival times at the detector will differ due to the different wave velocities of each mode. The arrival times of incident, reflected and mode converted waves at the detector are given in tables 6.1 and 6.2 for the A0 and S0 modes respectively, for a source positioned with its centre 0.1 mm from the defect (2 scan steps) with the detector 52 mm from the defect.

Table 6.1: Arrival times at the detector of the incident, reflected and mode converted waves when the laser detector is 52 mm away from the defect, for an incident A0 wave with frequency-thickness of 1.35 MHz.mm. Wave velocities are $v_{A0} = 3172.8\ ms^{-1}$ and $v_{S0} = 4796.9\ ms^{-1}$.

Wave at detector	Arrival time (μs)
$\text{A0}_{incident}$	16.39
$\text{A0}_{incident}$ to $\text{A0}_{reflected}$	16.45
$\text{A0}_{incident}$ to $\text{S0}_{reflected}$	10.89

Table 6.2: Arrival times at the detector of the incident, reflected and mode converted waves when the laser detector is 52 mm away from the defect, for an incident S0 wave with a frequency-thickness of 2.48 MHz.mm. Wave velocities are $v_{A0} = 3106.1\ ms^{-1}$, $v_{S0} = 1793.8\ ms^{-1}$ and $v_{A1} = 3699.5\ ms^{-1}$.

Wave at detector	Arrival time (μs)
$\text{S0}_{incident}$	28.99
$\text{S0}_{incident}$ to $\text{S0}_{reflected}$	29.10
$\text{S0}_{incident}$ to $\text{A0}_{reflected}$	16.82
$\text{S0}_{incident}$ to $\text{A1}_{reflected}$	14.14

The only waves that arrive within the time windows used for the study of the enhancements ($15.7 \leq t_{A0} \leq 17.9$ μs, and $28.9 \leq t_{S0} \leq 30.5$ μs) are the reflected wave modes of the same type as the incident mode[116]. The temporal separation of the mode converted waves means that they do not contribute to a superposition at the detector, as was seen for scanning laser detection, and the superposition that is observed is only due to the incident wave and its direct reflection.

The superposition effect is only present when the source travels close enough to the defect for the incident and reflected waves to arrive close together at the detector, as can be seen from table 6.3. As the source moves away from the defect the influence of the superposition mechanism diminishes as the arrival times of the incident and reflected waves separate, until the reflected wave arrival time leaves the time window of interest.

In order to determine the extent to which the reflected wave will contribute to the observed out-of-plane displacement at the detector, and hence how much it will contribute to the enhancement, the reflection coefficient for the relevant wave mode was found as a function of defect depth. This was achieved through the use of FEM simulations that modelled the reflection characteristics of surface-breaking v-shaped defects, similar to the simulations undertaken in section 5.1. A dipole force

Table 6.3: Arrival times of reflected waves for the A0 mode as a function of the laser source position relative to the defect. The arrival time of the direct incident wave is 16.39μs.

Source position (mm)	Reflected arrival time (μs)
0.1	16.45
0.5	16.70
1.0	17.20
1.5	17.33
2.0	17.65
2.5	17.97
3.0	18.28

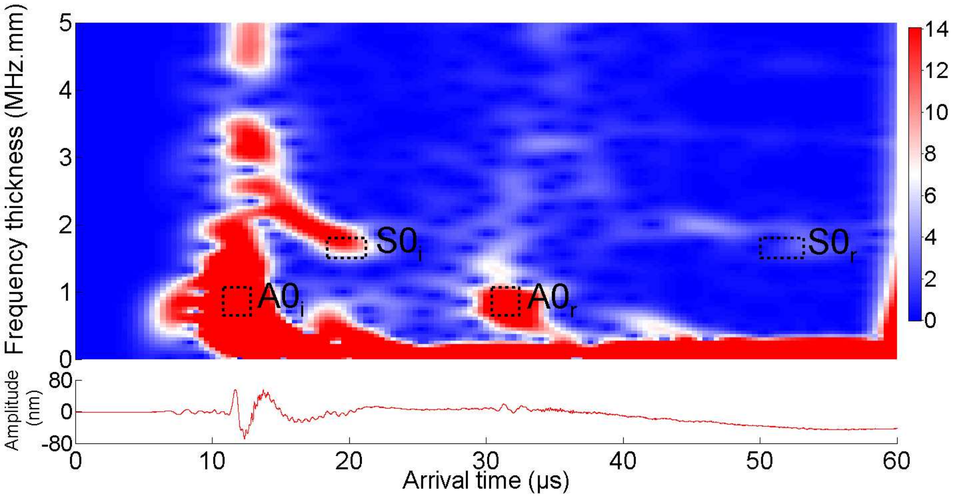

Figure 6.8: Sonogram for FEM simulated data for Lamb waves incident on a 75% through-thickness defect taken in the far-field of the defect, showing incident (subscript i) and reflected (subscript r) regions of interest.

was used to simulate an ultrasonic source located far away from the defect[107], and the ultrasound was allowed to propagate along the sample to interact with the defect, and then travel back towards the detector, located in the defect far-field. A longer path distance than was used in the experiments was employed in order to give a significant temporal separation between the incident modes and the reflected signals, allowing them to be observed separately in a sonogram, as shown in figure 6.8. This simulation setup was used because for the case in which the source is close to the defect the differences in the arrival times of the incident and reflected waves at the detector cannot be easily separated, making it difficult to determine a reflection coefficent.

From the known wave velocities and travel distances, the areas of the sonogram in figure 6.8 that correspond to the incident and reflected regions of interest are highlighted by dashed boxes. As the propagation distance is no longer constant between adjacent scans due to the setup of the model the waves will experience a spread in arrival times due to the dispersion of the waves. For the A0 wave the variation in the velocity within the chosen region is small and hence the influence of dispersion on the arrival times is correspondingly small. For the S0 wave one expects a larger spread in the arrival times due to bigger variations in the wave velocity, which are compensated for by an extension of the time window for the region of interest. The peak magnitude within these regions was used to give an estimate of the relative amplitude (as the energy is proportional to the square of the amplitude of the wave) of the reflected, $A_r(f)$, and incident waves $A_i(f)$, at the chosen frequencies for each wave mode. This allows for the calculation of a frequency dependent reflection coefficient, $R_f(f)$, using

$$R_f(f) = \frac{A_r(f)}{A_i(f)} \quad . \tag{6.1}$$

If the energy contained within the incident wave mode at the chosen frequency is set as unity, the fraction of energy that is present in the reflected wave can be estimated by the value of the reflection coefficient[113,114]. Therefore, if the enhanced signal consists of the superposition of the incident wave and the reflected wave, and the defect-free signal is caused only by the incident wave, then one can form an enhancement factor E_f as

$$E_f = \frac{(1 + R_f)}{1} \quad , \tag{6.2}$$

with the calculated values of the enhancement factors shown as a function of defect depth in figure 6.9 for both the A0 and S0 wave modes, using the values of $R_f(f)$ for each region as obtained from the FEM model.

The enhancement factors calculated from the superposition approach exhibit a general increase for both the A0 and S0 modes as the defect depth increases, in a similar fashion to the enhancements for the experimental results from the v-shaped defects in figure 6.5. The variation in the A0 enhancement factors is larger than that for the S0 mode which is contrary to the behaviour observed in figure 6.5. These enhancements are, however, much smaller in magnitude than those seen for the experimental data, as is to be expected from comparing the relative sizes of the enhancement factors seen in chapter 5 for scanning laser detector experiments, which are dominated by the superposition of wave modes, to those from the scan-

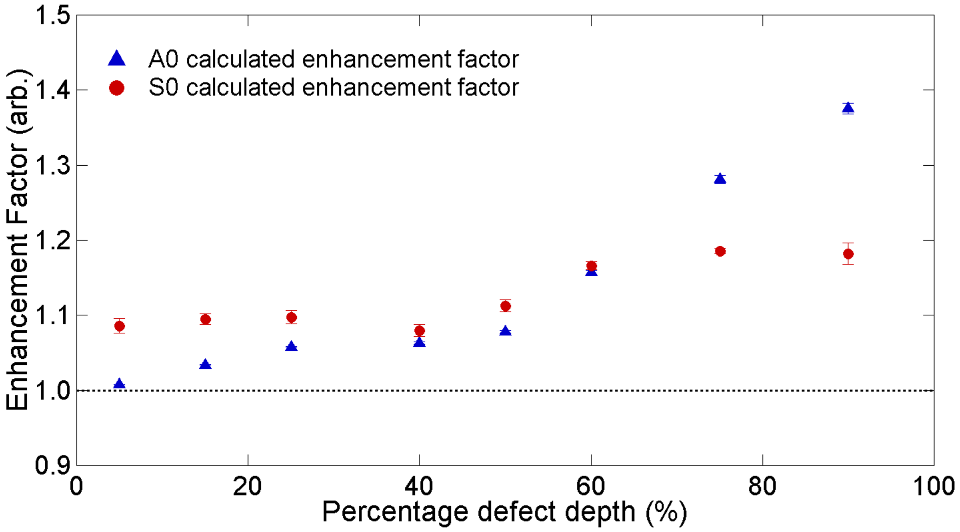

Figure 6.9: Enhancement factors as a function of defect depth calculated from a superposition of the incident and reflected waves for the A0 and S0 wave modes in FEM simulations.

ning laser source data. The enhancement due to the superposition, whilst having the correct increasing trend with increasing defect depth, is insufficient to explain the results shown in 6.5 as no consideration has been made of what happens to the generation process itself when it is carried out directly over the defect. This must be considered in tandem with the superposition data.

6.4.3 Changing boundary conditions mechanism

Changes in the boundary conditions of generation at the point of ultrasonic generation have been shown to influence the character of the generated ultrasound, as the surface on which the laser source impinges is disrupted from a smooth continuous surface by the presence of the defect discontinuity[128,235,238]. For the interaction of Rayleigh waves with defects propagating perpendicular to the sample surface this change of the boundary conditions was shown to be a major contributor to the observed enhancement, and has been modelled[23]. The change in boundary conditions at the defect will also be present for Lamb wave interactions and will contribute to the enhancement as the source passes over the defect.

At the defect lip the edge of the sample is free to expand into the void created by the defect as it is heated by the laser source, providing very different boundary conditions to the case in which the laser is generating on a smooth planar surface,

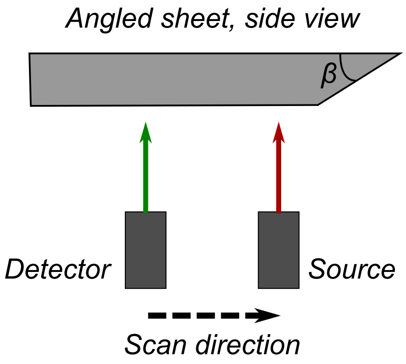

Figure 6.10: A schematic diagram showing the scanning laser set-up used to study the influence of the defect opening angle on the scanning laser source enhancement.

where the expansion is constricted equally in all directions in the plane. Ultrasonic enhancement as a consequence of these changing boundary conditions, similar to that observed for Rayleigh waves, is also present for Lamb waves. The v-shaped defects examined here introduce a gradual change in the boundary conditions compared to the sudden discontinuity introduced by perpendicular square-based defects, and therefore the enhancement factors for the two regions of interest in the A0 and S0 modes were investigated as a function of the defect opening angle. The opening angles of the v-shaped defects studied here were in the range of 70 ° to 85 °, with the shallower defects having the smaller angles. The variation in the defect opening angle is a consequence of the laser micro-machining method (section 1.4.3), and here the extent of its influence on the enhancement was studied.

This investigation was carried out by producing a series of full-thickness defects with varying opening angles, β, which act like wide 100% through-thickness defects. In these experiments the contribution from source truncation is still present, however, as the enhancement arising from beam truncation was shown to be small in section 6.4.1 its resulting contribution to the enhancements from angled defects is correspondingly small. The laser spot source was scanned over the edge of the defect, as shown in figure 6.10, and the same data processing procedure as in section 6.3 was applied in order to produce an enhancement factor for each defect angle. The variation in the ultrasonic enhancement as a function of the defect opening angle is shown in figure 6.11. The enhancement factors for both wave modes show a large variation as a function of angle (even for the restricted set of angles shown here) and the behaviour differs between the two wave modes, similar to the behaviour seen in sections 6.3 and 6.4.2.

The v-shaped defects have opening angles between 70 ° and 85 °, depending on the depth, and for the S0 mode there is an increase in the enhancement factor

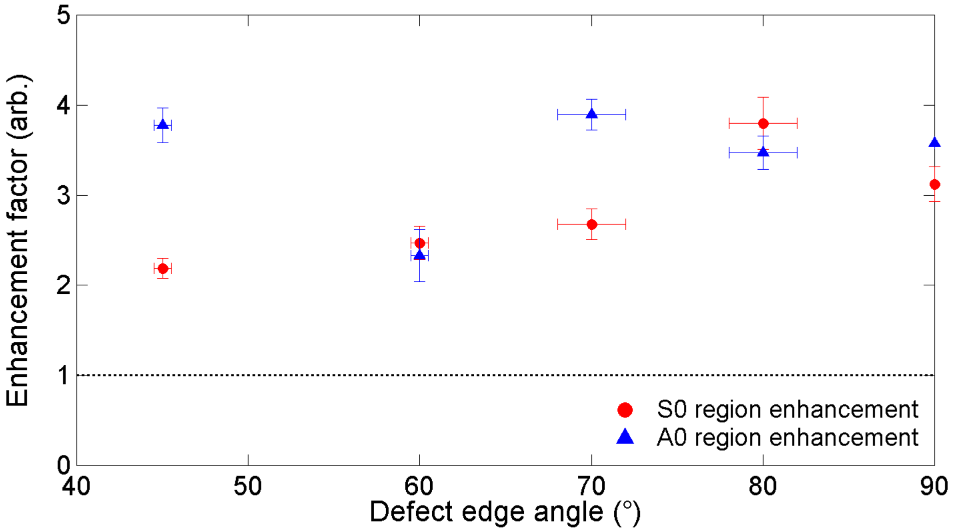

Figure 6.11: Variation in enhancement factor as a function of defect opening angle for a full-thickness defect.

between these values. As the lower defect angles correspond to the shallower defects in section 6.3, with the defect angle then increasing with increasing defect depth, the increase in enhancement factor with increasing defect angle correlates to the increase in enhancement factor with increasing defect depth seen in section 6.3. For the A0 mode the smaller reduction in the enhancement factor as the defect angle increases over the range of opening angles of the v-shaped defects, suggests that the variation in the enhancement for this mode is influenced less by the variation in the angle than that of the S0 mode.

6.5 Enhancement peak structure

It has been shown that there are several contributory mechanisms that cause the enhancement observed for open v-shaped defects (figure 6.5), including a contribution from the truncation of the generation area, one from the changing boundary conditions of generation as the source passes over the defect lip and one from a superposition of the incident wave mode with a reflection of the same mode, provided that the source is close enough to the defect[116].

The A0 and S0 wave modes are influenced to different degrees by these mechanisms, giving rise to the variation in the appearance of their enhancement peaks as a function of the scan position seen in figures 6.4a and 6.4b and an understanding of

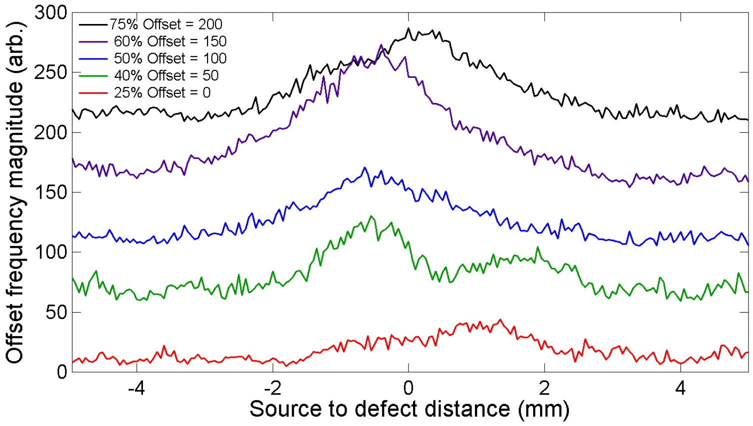

Figure 6.12: Frequency magnitude tracking of the S0 mode at a frequency-thickness of 2.70 MHz.mm for different through-thickness percentage defect depths, each trace has been offset for clarity.

these mechanisms allows the differences in peak structure to be explained. In figures 6.4a and 6.4b the tracking of the peak frequency magnitude has a different structure for the A0 and S0 modes, with the S0 mode possessing a single enhancement peak, and the A0 mode a double peak. Examples of the variation in the peak sonogram magnitude as a function of scan position is shown in figures 6.12 and 6.13 for different defect depths for both A0 and S0 wave modes. The differences between these two peak structures can be explained through identifying which of the mechanisms described in section 6.4 is dominant at the source position.

The enhancement due to the change in the boundary conditions of generation and the truncation of the source will be present whenever the laser source passes over a defect lip, and hence enhancement from these mechanisms will be observed as the source passes over each side of the defect. However, the enhancement due to a superposition of the incident and reflected wave modes is only expected when the laser source is close enough to the defect that the arrival times of the incident and reflected waves are both within the time windows of the regions of interest (A and B on figure 5.5). The superposition mechanism will therefore be dominant only when the source is very close to the defect, thus, the superposition mechanism has the largest effect in the central portion of the tracking enhancement in figures 6.4a and 6.4b.

As was seen in section 5.4 the A0 and S0 wave modes are not single point displacements and superpositions are possible between the incident wave and the trailing components of the reflected wave, as was responsible for the multi-peaked detector enhancements. In this case this leads to a smearing out of the enhancement

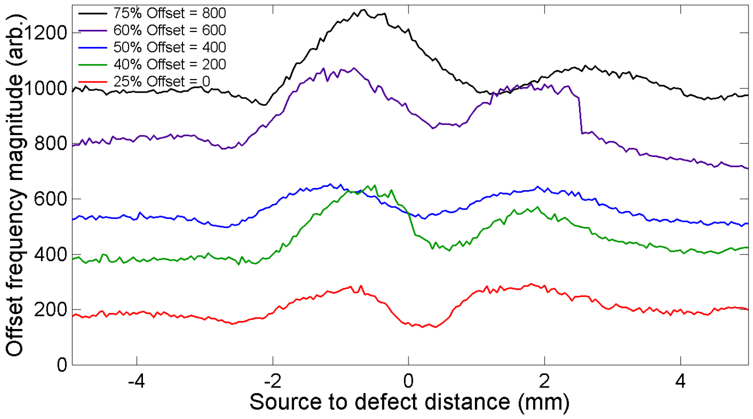

Figure 6.13: Frequency magnitude tracking of the A0 mode at a frequency-thickness of 1.65 MHz.mm for different through-thickness percentage defect depths, each trace has been offset for clarity.

peaks in figures 6.12 and 6.13.

The position at which superposition occurs and the extent to which the superposition mechanism generates constructive interference between the incident and reflected modes is dictated by the relative phase of the reflected wave with respect to the incident mode[116]. An in-phase reflection will give constructive interference over the central part of the enhancement, therefore increasing the level of the observed frequency magnitude in between the enhancement due to the changing boundary conditions, whereas destructive interference, if the reflection is out-of-phase with the incident, will see a reduction in the same region. The determination of the relative phases of the reflected and incident waves was performed using the FEM simulated data (section 6.4.2). With the simulated dipole force located far away from the defect, the time intervals corresponding to regions A and B on figure 6.8 were identified on the A-scans.

A fast Fourier transform (FFT) was performed on the time windows in each A-scan that corresponded to the arrival times of the incident and reflected waves of interest for both A0 and S0 modes. The phase of the incident, $\phi_i(f)$, and reflected waves, $\phi_r(f)$, was obtained by unwrapping the phase information from the FFT. The phase information was obtained at three different frequency-thicknesses within the regions of interest, corresponding to 1.05 MHz.mm, 1.35 MHz.mm and 1.65 MHz.mm for the A0 mode and 2.25 MHz.mm, 2.48 MHz.mm and 2.70 MHz.mm for the S0 mode, which correspond to the two upper limits and the midpoint of the frequency-thickness regions A and B. A phase difference $\Delta\phi$ between the reflected

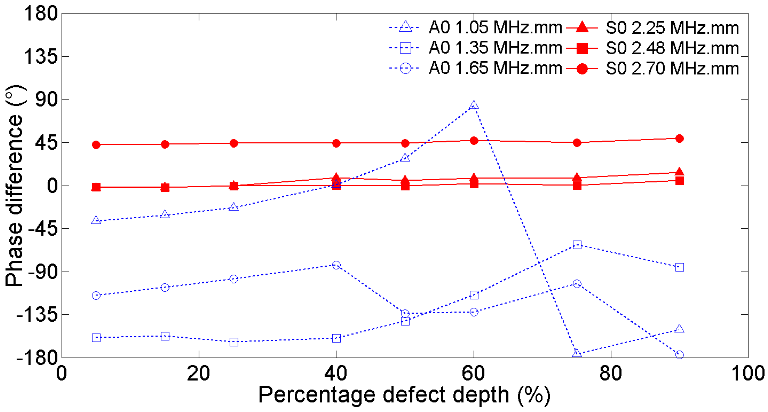

Figure 6.14: Phase differences between reflected and incident waves from FEM simulated data for three frequency-thicknesses within the A0 and S0 regions of interest as a function of the defect depth.

and incident modes was obtained from,

$$\Delta\phi = \phi_r - \phi_i \quad . \tag{6.3}$$

The variation in the phase differences between reflected and incident waves as a function of defect depth for the A0 and S0 modes is shown in figure 6.14. The phase difference is shown for three frequency-thicknesses of each mode, with full constructive interference in the central region expected for a phase difference of 0 ° and full destructive interference for a phase difference of 180 ° when the source is located right at the defect.

For the S0 mode the middle and lower frequency-thicknesses have a phase difference close to 0 ° for all defect depths, giving rise to constructive interference at the defect and a single peak structure in the enhancement from this mechanism, as shown in figure 6.12. For the higher S0 frequency-thickness the average phase difference is closer to 45 °, which means that the constructive interference at this frequency-thickness will occur slightly further away from the defect lip, giving rise to a slightly shifted enhancement peak structure at this frequency-thickness.

For the A0 mode the phase differences are much larger, with variations in the phase difference as a function of the defect depth, which is responsible for the shifts in the positions of enhancement seen between different defect depths in figure 6.13. The middle and upper frequency-thicknesses have a phase difference such that one would expect destructive interference when the source is very close to the defect, and constructive interference up to a half wavelength distance away, giving rise to a structure with a central dip and enhancement away from the defect edge, as seen in figure 6.4b. The lower frequency-thickness has a highly variable phase difference, so one would expect the position of the enhancement to be heavily dependent upon the defect depth for this frequency-thickness.

The overall structure of the enhancement peaks is therefore a combination of the influences of the mechanisms outlined in section 6.4, which have shown to have differing effects for different wave modes, and with an understanding of this the position of the defect can be estimated from the enhancement data. For analysis of the S0 mode in the specified region the defect will be located at the peak enhancement value, corresponding to the peak in the central region in figure 6.4a, whereas for the A0 mode it will be located between the two enhancement peaks. This is based on the fact that the superposition mechanism is only dominant when the source is very close to the defect position, and from knowing how the phase differences between the incident and reflected components of the two wave modes behave.

6.6 Conclusions

In this chapter it has been shown that scanning laser source enhancements exist for Lamb wave modes, and several of the mechanisms reponsible for that enhancement have been identified. From this a method of estimating the defect depth from the magnitude of the scanning laser source enhancement factors has developed to characterise surface-breaking defects. Whilst the defects studied in this chapter are only representations of real defects, the scanning laser methods described here and in chapter 5 give a method of identifying the position and approximating the severity of these defects. However, the true test of the capabilities of scanning laser inspection comes when it is applied to real defects with a complicated structure, and which can be partially-closed, as is demonstated in chapter 7.

Chapter 7

Inspection of real surface-breaking defects

It was shown in chapters 4 - 6 that ultrasonic enhancements can be used to detect and characterise surface-breaking defects, enabling the defect position and depth to be found for artificial reference defects[22,95,115,116,252]. Whilst these defects are useful for developing an understanding of the mechanisms behind the enhancements, they are only an approximation to real defects, and in order for the enhancement technique to become industrially viable it has to be able to detect real stress-driven defects, such as those described in section 1.4. In this chapter the effectiveness of the scanning laser enhancement technique is demonstrated on several examples of stress-produced defects, some of which were artificially grown while others were in samples removed from service in the petrochemical and aeronautical industries[180].

Scanning laser source and scanning laser detection enhancements are reported here for grown stress-driven cracks in flat plates, whilst scanning laser source enhancements are also shown for defects in pipework samples and in irregularly shaped engine components. These scanning laser source experiments were effective at detecting multiple small partially-closed defects that were located close together in the pipework sections. The same mechanisms as described in chapters 5 and 6 are responsible for the enhancement, with an additional contribution to the scanning laser source enhancement arising from an interaction between the partially contacting faces of the defect[234,238].

Figure 7.1: Image of artificially grown 3 mm deep defect in 10 mm thick stainless steel plate.

7.1 Artificial stress corrosion cracking defects

To determine the existence and variation with depth of ultrasonic enhancement arising from real defects, a series of artificial partially-closed defects were studied using both scanning laser source and scanning laser detection techniques. These defects were produced in stainless steel plates with dimensions of 200 x 200 x 10 mm, and were designed to mimic SCC defects in large flat structures, such as ship platings and storage vessels[12,13,15,16,64,262]. The artificial SCC defects were produced by Trueflaw[263] using controlled thermal fatigue loading, as opposed to the more traditional approach of mechanical loading, allowing the defects to grow in a similar fashion to those that occur in industrial applications[264]. An image of the opening of one of the artificial defects is shown in figure 7.1 for the 3 mm deep defect.

The thermal loading approach allows the defect growth procedure to be carried out locally at the site of crack initiation, meaning that no unnecessary stress is put on the remainder of the material. The thermal fatigue is achieved through a series of thermal loadings and water spray quenching, and loading on the material is achieved purely through thermal loading with no mechanical contribution[264].

The defect depths are determined through exhaustive destructive testing by Trueflaw on samples that have undergone the same thermal fatigue cycling, giving a depth measurement accurate to ±0.6 mm. Three different defect depths, 1.4 ± 0.6 mm, 2.3 ± 0.6 mm and 3.0 ± 0.6 mm were studied. The laser detector and source were scanned over the midpoint of the defect with a fixed separation between the two lasers, with A-scans taken at each scan position, in the same manner as for the inspection of Lamb wave interactions with artificial defects presented in chapters 5 and 6. To avoid damage to the test samples a low incident laser power was used so as to avoid any possibility of material ablation in the defect region. In addition to single scans carried out using the setup described in section 3.1, raster scanning techniques (see section 7.1.3) that enable the whole defect to be imaged were performed for both scanning methods.

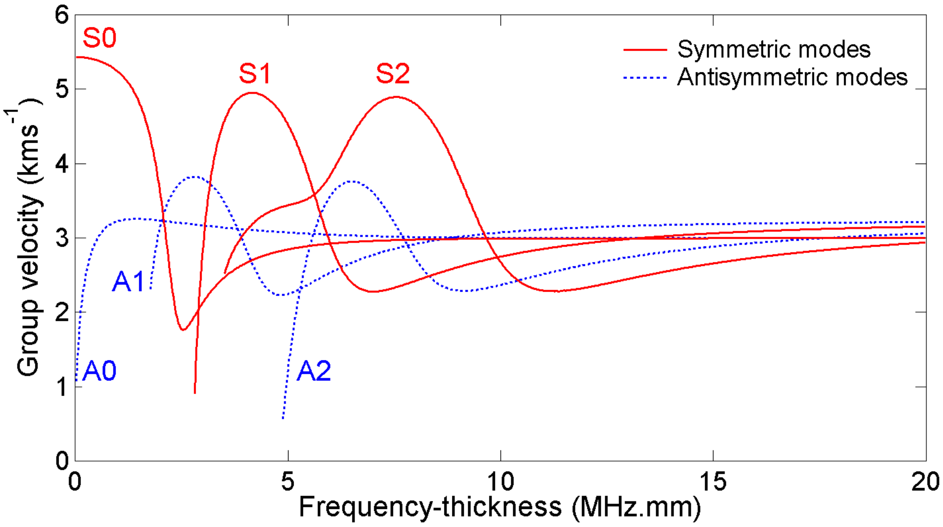

Figure 7.2: Group velocity dispersion curve for Lamb wave modes propagating in flat steel plates (v_L=5960 ms^{-1}, v_S=3235 ms^{-1}).

7.1.1 Scanning laser source enhancements

For the plate thickness of 10 mm (that is much larger than that used in chapters 5 and 6) and laser source energies used here the dominant generation mechanism is the production of Lamb waves with high frequency-thickness values (between 6 and 15 MHz.mm), producing Lamb waves that tend to Rayleigh-like behaviour as the frequency-thickness product increases (figure 7.2)[89]. Although the Lamb modes will not all propagate at exactly the same velocity at these frequency-thicknesses, the differences between their velocities is too small to be resolved with the sonogram resolution of 0.1 MHz in frequency and 0.2 μs in time used here.

A-scans taken as the laser source was scanned over the defect were examined using the same process described in chapter 6, in which sonograms were produced at each scan position. Sonograms taken when the source is far away from a 3 mm deep artificially grown defect and when it is directly illuminating the defect can be seen in figure 7.3b, with the theoretical arrival times of lower order Lamb modes overlain. As was observed for Lamb waves in chapter 6 there is an increase in the magnitude at higher frequency-thicknesses when the source is directly over the defect and higher order modes are generated. The noise on the A-scans shown in figure 7.3 is high and is caused by the low laser power that was chosen so as to avoid surface damage, however, the use of the sonogram representations allows these signals to be clearly seen when the colour scale starts at the noise level.

To quantify this enhancement, the peak frequency magnitude in the region

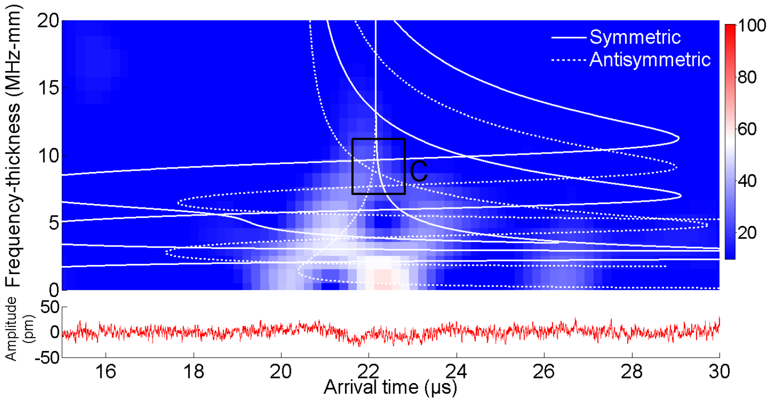

(a) No defect region

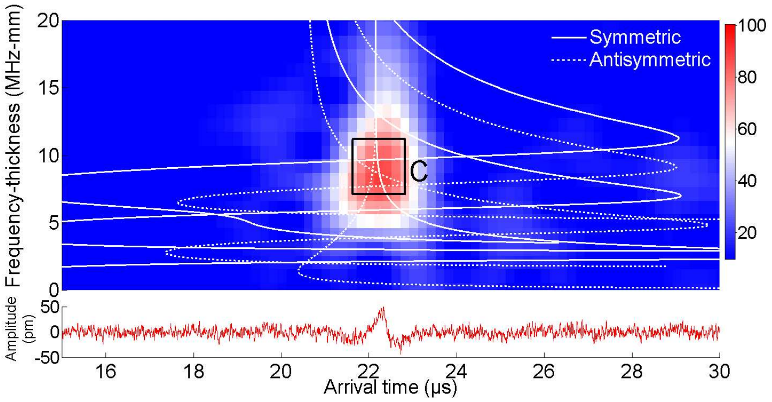

(b) Defect near-field

Figure 7.3: Sonograms produced from A-scans taken with the laser source away from the defect (a) and when the source illuminates the defect (b) for a 3 mm deep defect. The colour scale has been adjusted so that the base level is that of the background noise.

corresponding to the boxed area labelled C in figure 7.3b was tracked across the scan. Region C corresponds to a frequency-thickness region between $7.14 \leq fd \leq 11.22$ MHz.mm, arriving between $21.63 \leq t \leq 22.82$ μs. This region was chosen as it is located at a position at which many Lamb wave modes arrive simultaneously at the detector located away from the defect. The velocity of these wave modes at this frequency-thickness is very similar and hence many different contributions to a superposition of waves at the detector is expected, which was shown to be partly responsible for the enhancement in open v-shaped defects (chapter 6).

The tracking of the frequency magnitude in region C is shown in figure 7.4 for the three available defect depths. As was seen for the v-shaped crack, when the source is away from the defect the frequency magnitude remains at a steady level, but in the defect near-field a large increase is observed as the source passes

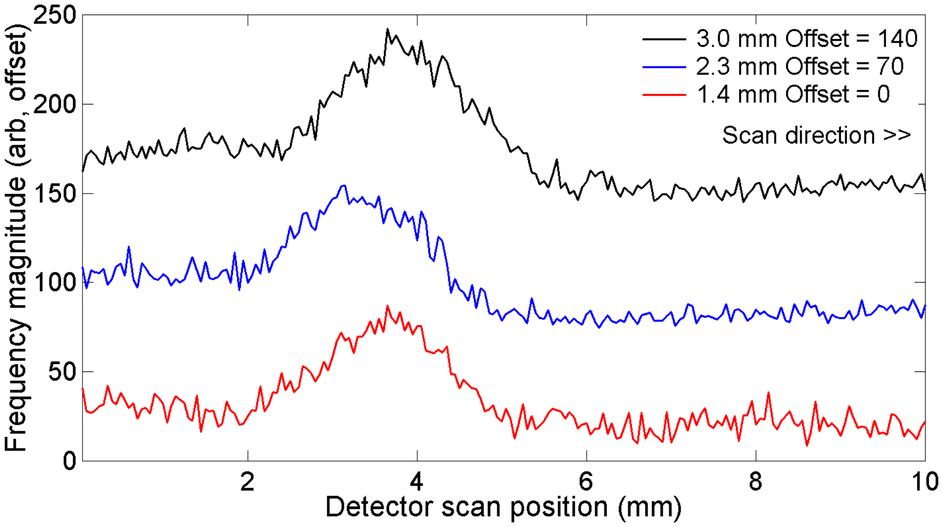

Figure 7.4: Peak magnitude tracking in region C for scanning laser source experiments for 1.4 mm, 2.3 mm and 3.0 mm deep defects. Scans have been offset to one another for comparison. On the left hand side of the scan both laser source and detector are on the same side of the defect.

over the defect. The enhancement factors, E_f, were calculated from the ratio of the enhanced frequency magnitude, $A_{Enhanced}$, to that when the source is away from the defect, $A_{NoDefect}$, using equation 5.1. These values are shown in table 7.1.

From table 7.1 the enhancement factor can be seen to increase with defect depth, as expected from the study of v-shaped defects in chapter 6, however, the limited range of defect depths avaliable precludes the extension of this observation to a greater range of defects. If the defects are considered in terms of their depth as a percentage of the material through-thickness (14%, 23% and 30% respectively), the large enhancement values observed make the scanning laser source technique very attractive for detecting a range of defect depths for real defects. The successful detection of a defect that is only 14% of the through-thickness enables a component to be removed from service before the defect reaches a size that will cause complete failure[17]. The mechanisms identified in section 6.4 will again provide contributions

Table 7.1: Scanning laser source enhancement factors for region C on figure 7.3 for artificially grown stress defects.

Defect depth (mm)	Enhancement factor
1.4±0.6	2.46±0.19
2.3±0.6	2.86±0.23
3.0±0.6	3.08±0.23

to the observed enhancement, with the laser source undergoing truncation, a change in the boundary conditions of generation, and a superposition of the incident and reflected modes as the source is over the defect [235,240,240].

The truncation of the laser profile as it passes over the discontinuity that is the defect is the same as was observed for the v-shaped defects, with the reduction in the beam width w leading to an increase in the value of f_{max} in equation 2.71. The size of the enhancement produced by this effect is expected to be small based on the investigations carried out into the effects of truncation in section 6.4.1. For the open v-shaped defects it was seen that some generation of ultrasound could continue on the sloped surface of the defect, this effect is not present for the real defects due to the narrow defect opening for the real defects, which is on average 10.4 μm compared to the value of 282 μm for the v-shaped defects.

At the location of the enhancement in figure 7.3b the theoretical arrival times of several wave modes coincide, with the A0, A1 and S0, and to a lesser extent the A2 and S2, modes having very similar velocities in this region. A superposition between these Lamb modes occurs at the detector located away from the defect as the similar wave velocities ensure that they arrive within the same time window at the detector, as compared to the spread out arrival times for different wave modes observed in the enhancement regions studied for v-shaped defects, due to the different sample thicknesses. This provides a contribution to the enhanced magnitude at these frequency-thicknesses, however, to fully quantify the extent of this enhancement an analysis of the reflection behaviour would be required for the partially closed defect. This would enable the amount of the incident energy that is reflected back in each of these wave modes could be ascertained, similar to that presented in section 6.4.2 for v-shaped defects, allowing the estimation of their contributions to a superposition of waves at the detector. The generation of the higher order wave modes at the defect occurs due to the change in the boundary conditions of generation when the source is directly over the defect and is related to the geometry of the partially-closed defects [240].

Whilst the mouth of the stress-grown defects has an opening that is on average 10.4 μm, the defect swiftly narrows as it progresses deeper into the sample, reducing the opening between the opposing faces of the defect, giving a structure that is very similar to that seen for real SCC defects in figure 1.10. As the defect faces are not smooth the tapering of the defect can lead to portions of the defect in which the two faces are in contact with one another, or are close enough that they can easily be forced into contact by a transient motion, such as that caused by the heating influence of a laser source [64,248,265,266].

The additional enhancement mechanism observed for partially-closed cracks arises from the opening and closing behaviour of the crack under heating[64], which creates a nonlinear response due to the clapping between crack faces[265]. For partially-closed defects excited by an ultrasonic wave, contact can be made between the opposing faces of the defect at certain points as the crack is forced open and closed by the vibration of the ultrasonic wave. The pertubation of the crack walls can also be caused by the heating of the incident laser source, which causes thermo-optical excitation of the defect, which has been shown to also generate nonlinear crack opening and closing behaviour[238,265]. In turn this varies the extent to which the opposing faces are in contact; this has been shown to be dependent upon the crack length and the interfacial stiffness of the defect walls[64,267]. The influence of this partial contact has been utilised in several studies aimed at determining the depth of a defect through the variations that this transient contact introduces into the reflection and transmission characteristics of real defects[248,266]. The variations in the reflection behaviour of partially contacting cracks, which has been shown to vary as a function of the frequency of an incident wave for Rayleigh waves[266], will influence the extent to which the superposition of the Lamb waves occurs at the enhanced position, as different modes will experience differing degrees of reflection. A similar effect has previously been shown for the fundamental Lamb modes at lower frequency-thicknesses[114].

The localised thermo-optical heating of the defect causes the opposing faces to clap together, modifying the interfacial stiffness of the defect, which in turn produces a non-linear ultrasonic response that excites higher-frequency components of the ultrasonic wave[238,265]. These higher-frequency components are not present in the ultrasonic signal when the laser source is away from the defect, and their existence contributes to the enhancement observed in table 7.1 for partially-closed defects only when the laser source directly illuminates the defect[180].

7.1.2 Scanning laser detection enhancements

The artificial stress grown defects were also investigated by scanning the laser detection spot (in step increments of 50 μm) over the midpoint of the defect for all three defect depths, and a sonogram was produced at each scan point, as in chapter 5. For positions at which the detector was far away from the defect the sonogram only shows a low frequency incident wave, however, as the detector nears the defect a higher frequency signal is observed with an accompanying increase in the magnitude, and this can be seen in figure 7.5b with the theoretical arrival times overlain

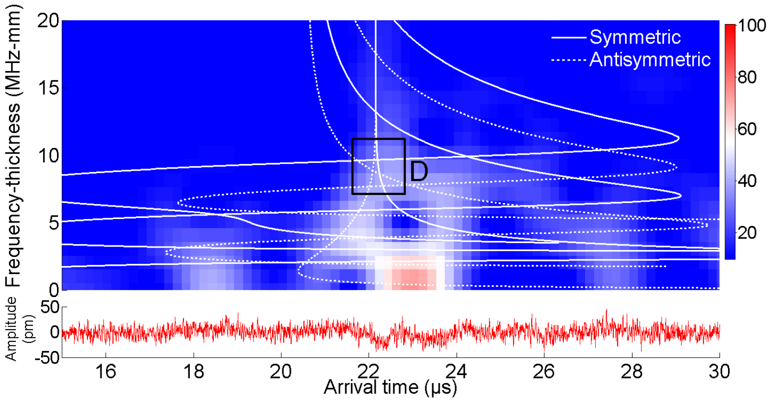

(a) No defect region

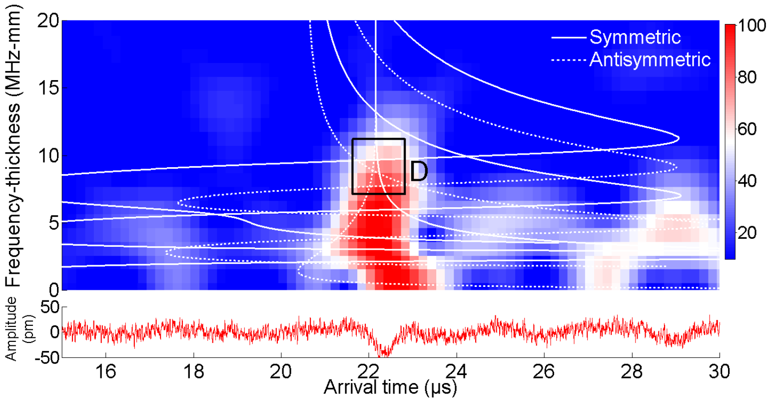

(b) Defect near-field

Figure 7.5: Sonograms produced from A-scans taken with the laser detector away from the defect (a) and when the detector is close to the defect (b) for a 3 mm deep defect. The colour scale has been adjusted so that the base level is that of the background noise.

for Lamb waves in a steel plate.

The peak frequency magnitude of the region, labelled D, with $7.14 \leq fd \leq 11.22$ MHz.mm and $21.63 \leq t \leq 22.82$ μs, was studied for evidence of signal enhancement near to the defect. The frequency-thickness range was chosen so as to provide a direct comparison to region C studied in section 7.1.1, and the resulting tracking is shown in figure 7.6.

As was seen for the case of a v-shaped crack, when the detector is away from the defect the magnitude remains at a steady level, but in the near-field a large increase is observed as the detector passes over the defect. The enhancement factors, E_f, are calculated similarly to before using equation 5.1. These values are shown in table 7.2.

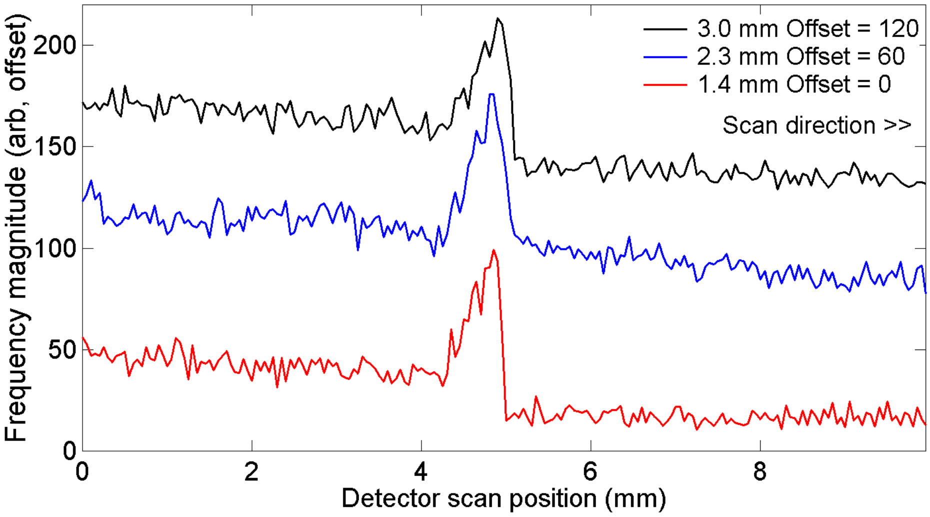

Figure 7.6: Peak magnitude tracking in region D for scanning laser detector experiments for 1.4 mm, 2.3 mm and 3.0 mm deep defects. Scans have been offset to one another for comparison. On the left hand side of the scan both laser source and detector are on the same side of the defect.

The detector enhancements in table 7.2 show a significant signal increase in the near-field of the defect, although the variation between the different depths is small. The lack of variation is to be expected if the enhancement factors are compared to the equivalent percentage through-thickness depths of 14%, 23% and 30% for the v-shaped defects shown in figures 5.9 and 5.10, for which the enhancement factors vary between 1.20 and 1.25, with large changes from these values only observed from 50% depths onwards. It should also be noted that the magnitude of the enhancement factors for the real defects is around twice that of those observed for the open v-shaped defects. The increase in the magnitude of the enhancement factors for the real defect is caused by the choice of the region used to study the enhancement, as in region D there are many more wave modes that can contribute to an enhancement than there were in the regions studied for the v-shaped defects (chapter 5).

Table 7.2: Scanning laser detector enhancement factors for region D on figure 7.5 for artificially grown stress defects .

Defect depth (mm)	Enhancement factor
1.4±0.6	2.92±0.24
2.3±0.6	2.21±0.12
3.0±0.6	2.62±0.21

The same superposition mechanism of incident and reflected waves is responsible for the enhancement of the ultrasonic signal at the real stress defects. In addition to the fact that there are more modes arriving close together in time that can contribute to a superposition, the larger magnitude of the enhancement factors suggests that the reflection coefficients for the real defects may be greater than those for an open v-shaped defect of the same depth. A similar effect has been reported previously for the interaction of Rayleigh waves with surface-breaking defects, in which the reflectivity of a partially-closed crack was shown to be greater than that of an open crack for certain conditions[268].

In the work by Pecorari the reflection coefficient of a partially-closed crack was reported to increase under a small applied load, such as that produced by the transient influence of the ultrasonic wave, when compared to that for an open crack of the same depth[268]. The variation in the reflection coefficient occurs as a function of the interfacial stiffness of the defect and the defect depth. The increase was reported for the interaction of Rayleigh waves incident on cracks that had a depth that was greater than half the Rayleigh wavelength. At the frequency-thicknesses studied in this section the behaviour of the Lamb waves is close to Rayleigh-like, and this assumption can be extended to form an estimate for a Rayleigh-like wavelength.

For a frequency-thickness of 10 MHz.mm and a sample thickness of 10 mm the Rayleigh-like wavelength can be estimated to be 2.93 mm, using the relation $\lambda = \frac{v_R}{f}$. All the crack depths studied (including the 1.4 mm defect due to the uncertainty on the depth) can be seen as being close to or deeper than $\frac{\lambda}{2}$, and hence may exhibit the increase in reflection coefficient under a small applied force. The increase in reflection coefficient will in turn increase the magnitude of the wave superposition and therefore the enhancement will increase with respect to that seen for an open defect.

As with the scanning laser source data in section 7.1.1 the range of defect depths avaliable is insufficient to form a full understanding of the variation of the observed enhancement with defect depth. However, the presence of near-field signal enhancements in both the scanning laser source and scanning laser detection data can be used to identify the position and the orientation of a surface-breaking defect, and shows promise for depth estimation. If a wider range of defect depths was studied, a ‘finger-printing’ method similar to that developed in chapters 5 and 6 could be produced, which would also enable an estimate of the defect depth to be made.

Figure 7.7: Image of the 1.4 mm deep defect used for raster scanning, showing the direction of the raster scan. The image has been rotated by 90 ° to the left, relative to the image in figure 7.8 so as to fit on the page.

7.1.3 Raster scanning of surface-breaking defects

A popular technique for the swift investigation of large regions of a test sample is a raster scan, in which a chosen area is divided into a series of linear scans, each one offset from its neighbour by a small amount, forming a two dimensional scan region that allows the surface of the material to be visualised[261]. An entire component can be raster scanned with no prior knowledge of the defect location. The defect under inspection for this measurement is shown in figure 7.7, which has been rotated by 90 ° to the left relative to the experimental set-up and scan directions for presentation purposes.

Raster scans were produced using both scanning laser source and scanning laser detection methods by performing several scans with a step size of 50 μm over the defect area, with a vertical increment of 1 mm between each scan. The experimental data for each individual scan line on the raster scan was subjected to the data processing described in sections 7.1.1 and 7.1.2. At each position on each scan a sonogram was produced and the peak magnitude within the regions C and D for scanning laser source and scanning laser detection respectively was recorded. This produces a series of scans that show the peak magnitude in the region of interest, giving images similar to those shown in figures 7.4 and 7.6; these data sets are then stacked next to one another to form a type of C-scan of the sample, showing an enhancement surface map. The enhancements caused by the defect can clearly be seen in figures 7.8b and 7.8a for a 1.4 ± 0.6 mm deep defect with a measured surface length of 4.8 ± 0.6 mm.

The small size of the defect, both in terms of depth and spatial extent, makes it difficult to detect from changes in the transmitted wave observed in the defect far-field. Although the defect acts to block the transmission of the ultrasound, resulting in the shadowed regions in both raster scans of figures 7.8b and 7.8a, the magnitude of the ultrasonic wave once the source or detector is past the defect returns to the pre-defect value within a distance of several millimeters from

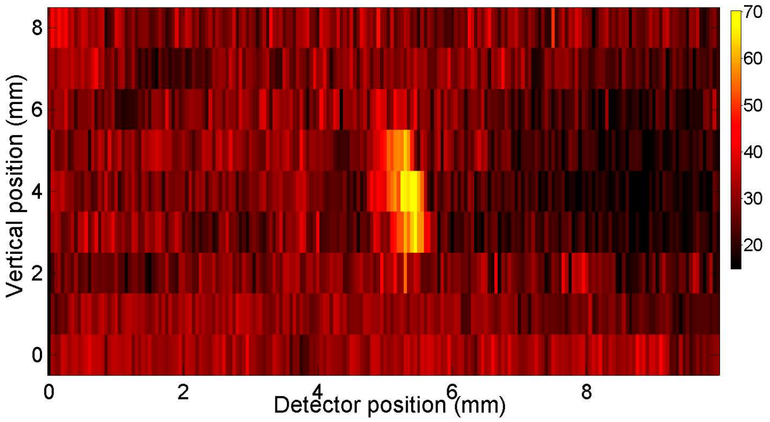

(a) Scanning laser detection

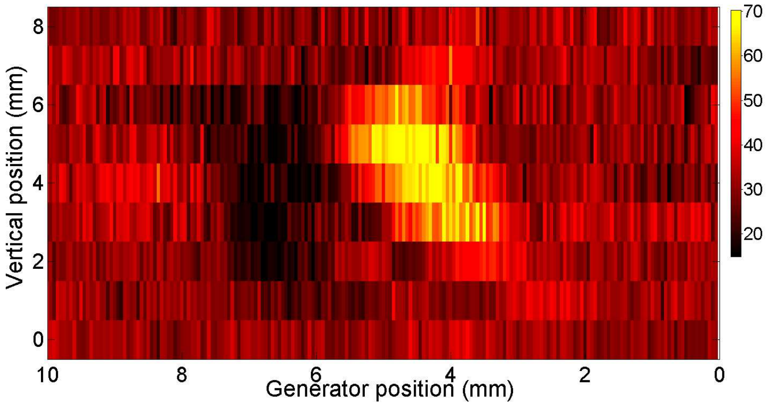

(b) Scanning laser source

Figure 7.8: Enhancement surface maps of a 1.4 mm deep defect in a stainless steel plate for scanning laser detection (a) and scanning laser source (b) experiments. The maximum of the colour scale represents the largest value of the peak frequency magnitude.

the defect, as the wave diffracts around and under the defect [269].

The enhancement as either the laser source or laser detector are moved over the defect is clear to see in figure 7.8 for both experimental approaches. Both scans were performed on the defect in a single run with the detector approaching the defect first, and so the left hand side of figure 7.8a and the right hand side of figure 7.8b correspond to regions of the scans in which both the detector and source were on the same side of the defect. The scanning source raster scan shows a defect that is approximately 4 mm long with the same approximate shape as that of the real defect, as seen in figure 7.7. The scanning detector raster scan shows a defect that is approximately 3 mm long, with a similar geometry to that obtained from the SLS data. The reduced length of the defect in the SLD approach is due to the small spot size of the detector, 200 μm, which combined with the relatively large vertical increment of 1 mm used here means that the detector may miss part of the defect. As the enhancement is only present when the detector approaches a defect along its line of scan, a smaller spatial extent is recorded. For the 2 mm diameter laser source size used here, even if part of the defect is missed, the diameter of the spot is large enough that a portion of the source will still pass over the defect, making the scanning laser source approach with this generation setup a more attractive option for detection of a defect.

The enhancement region in the scanning laser detection raster scan is narrower than for that in the scanning laser source raster scan, which is again due to the difference in the spatial extent of the detector and source. The large laser source diameter means that the enhancement behaviour is spread over the entire region in which the source can be interacting with the defect, resulting in an elongated enhancement region, which can also be seen in figure 7.4. This gives a wider enhancement region than that for the scanning laser detection case, which, as figure 7.6 shows, has a sharper enhancement. This makes scanning laser detection a more attractive choice for higher accuracy positioning of defects in flat plates, however as it is easier to miss a defect with the smaller spot size, the scanning laser source approach is also useful in finding a defect in the first instance. Unlike the enhancements observed in thin plates the magnitudes of the enhancements are very similar between the two approaches. The differences between the two surface maps highlights the benefits of using both scanning methods to fully identify a defect.

7.2 Stress corrosion cracking defects in industrial pipelines

In section 1.4.2 stress corrosion cracking (SCC) in pipelines was identified as a cause of component failure, with the material damage located either on the internal or external faces of the pipe[17]. To demonstrate the industrial applications of the laser enhancement method for SCC detection, two different pipework samples provided by the petrochemical industry were inspected for SCC damage. Prior to inspection the defect positions were approximately known from dye penetrant inspections carried out by the component contributor (see section 1.3.3). Investigations were carried out with both scanning laser detection and scanning laser source raster scanning methods. The ability of the scanning laser enhancement technique to detect multiple defects that are close together is demonstrated here[180], enabling the identification of defects that can prove difficult to achieve through conventional methods[270].

No evidence of near-field enhancement was observed for the scanning laser detection case, which was due to the low reflectivity of the defects. In chapters 5 and 6 the magnitude of the peak frequency content within a sonogram region was shown to be reduced when the defect lay between the source and the detector for both experimental set-ups as the presence of the defect acted to reflect a portion of the wave, thereby reducing the magnitude of the transmitted wave (see for example figures 5.7 and 6.4). In figure 7.10, for a scanning laser source experiment, no reduction in the level of the peak frequency magnitude is observed when the defect sits between the source and the detector, indicating that the transmission rate of the ultrasound through the defect is high. From this it follows that the resulting reflected wave, from which a wave superposition would occur for scanning laser detection experiments, is very small, and therefore, insufficient to show any evidence of enhancement for the scanning laser detector approach. For the scanning laser source approach enhancements can still be observed which are caused by the changing boundary conditions of generation at the defect and the nonlinear excitation of higher order modes when the source sits over the defect[180].

7.2.1 Pipework sample A

Sample A was a section of 3.9 mm thick 304 stainless steel pipework with an outer diameter of 168.28 mm that was removed from service after the detection of stress corrosion cracking, with two SCC defects and several instances of pitting corrosion damage identified through dye penetrant and visual investigation. The pipework sample was inspected using the experimental setup for a circumferential scan shown in figure 3.5, with a schematic image of the pipework section and the damaged region shown in figure 7.9. The circumferential scan was performed by rotating the stage in 0.5 ° increments, equating to a distance of approximately 0.67 mm between each measurement on the outer surface, such that the laser source was raster scanned over the defect region.

The A-scans taken at each source position were subjected to the same data processing as in section 7.1.1, and an example of a sonogram taken with the source far away from the defect and one at a position at which the source directly illuminates a defect are shown in figure 7.10. As was seen for the artificial stress defects in section 7.1.1, when the source is far away from the defect there exists only a low frequency signal, however, at the position at which the laser source is directly illuminating the defect a large high frequency enhancement is observed, that can be

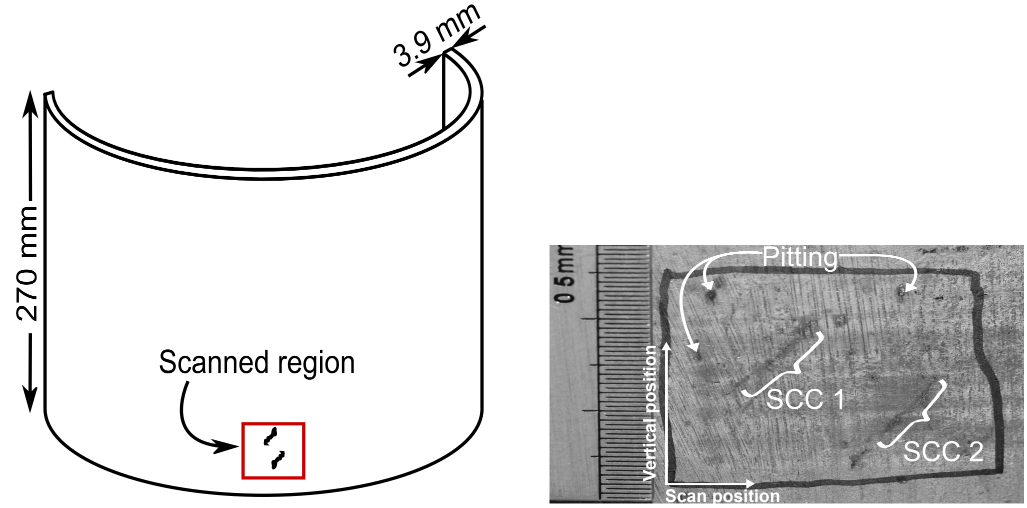

(a) Sample schematic (b) Defect close-up

Figure 7.9: A schematic diagram of pipwork sample A (a) and a close-up image of the inspection region showing two stress corrosion defects labelled SCC1 and SCC2 (b).

seen as a near-vertical line arriving at around 19 μs on the sonogram in figure 7.10b.

For the pipe thickness used here the circumferential waves that are observed exist in the frequency-thickness regions of figure 2.5, in which the fundamental circumferential wave modes exhibit behaviour that is very similar to the A0 and S0 Lamb modes in plates[89]. The magnitude of these modes is small when the source is far away from the defect, however, when the source directly illuminates the defect, the mechanisms reported to produce enhancement in section 7.1.1, such as the thermo-optical excitation of the defect and clapping between the defect faces, act to increase the generation of higher frequency-thickness waves, in a similar fashion to Lamb waves in plates.

From a consideration of the regions of the sonogram that show clear signal enhancements, two regions were chosen in which to track the peak sonogram magnitude, both of which were chosen as they correspond to frequency-thicknesses at which the two lower order circumferential modes in figure 2.5 have very similar wave velocities, and can be seen as an analogue of the A0 and S0 Lamb wave modes in plates converging to a Rayleigh-like velocity. Therefore, both regions will possess a contribution from both of the fundamental circumferential waves; the first region is between $4.0 \leq fd \leq 8.0$ MHz.mm arriving at $18.54 \leq t \leq 20.54$ μs, and the second is at a higher frequency-thickness of $8.0 \leq fd \leq 12.0$ MHz.mm also arriving at $18.54 \leq t \leq 20.54$ μs, marked E and G respectively on figure 7.10b.

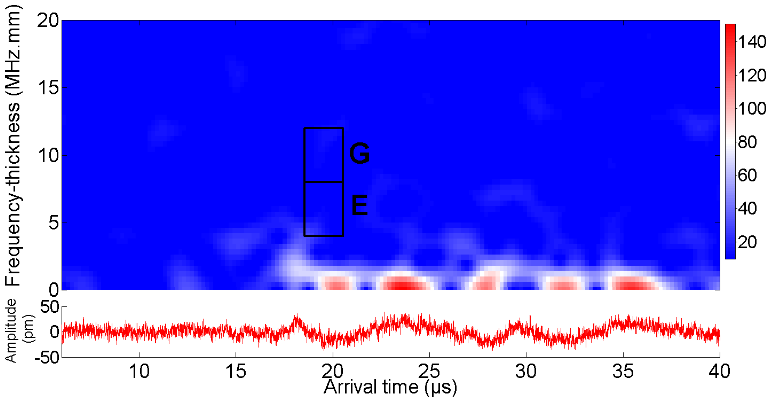

(a) No defect region

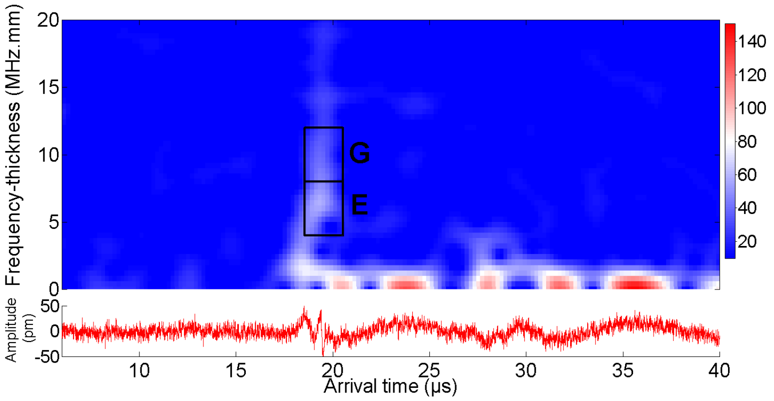

(b) Defect near-field

Figure 7.10: Sonograms produced from A-scans taken with the laser source away from the defect (a) and when the source is close to the defect (b) on pipework sample A, with the regions of interest E and G shown. The colour scale has been adjusted so that the base level is that of the background noise.

The peak magnitudes in the two regions of the sonogram, E and G, were measured during the scan, producing the images in figures 7.11a and 7.11b respectively. These images show two regions of increased magnitude, the first, smaller, increase at a position of 5 mm, and the second at a position of 16 mm, with the latter being larger than the former. The increase at 16 mm looks very much like the enhancements observed for the real defects in sheets (section 7.1.1), however, the peak at 5 mm has a slightly different shape and smaller magnitude. To improve the resolution of the smaller peak and to confirm that it is not caused by a spike in the signal noise, the product of the two scan regions was taken, and is shown in figure 7.12.

Calculating the product of the two regions has the effect of emphasising positions at which both scan regions have enhancements and smoothing any regions in

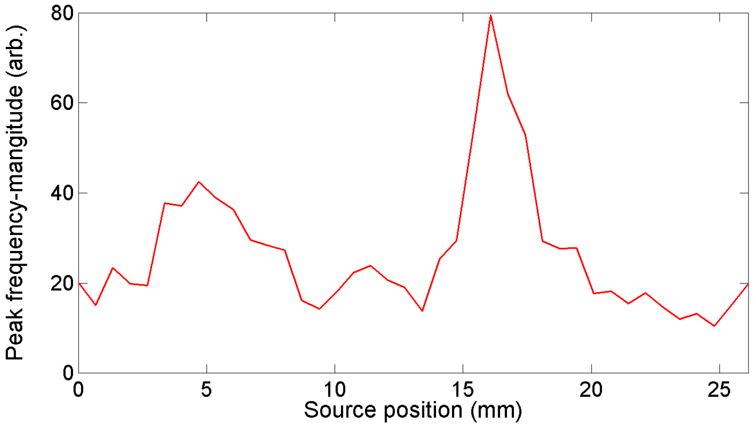

(a) Low frequency-thickness

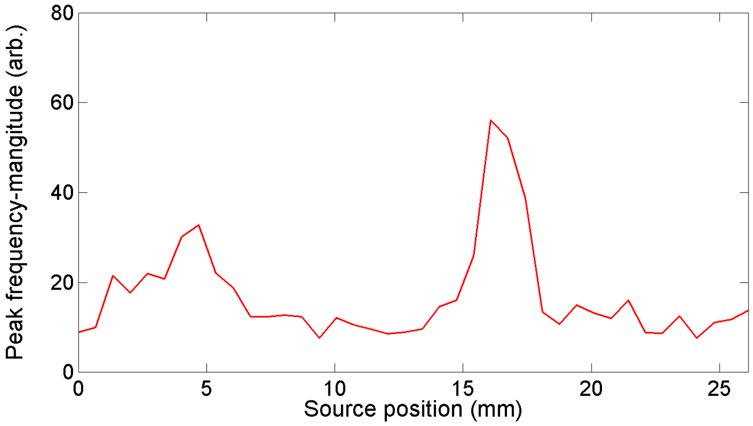

(b) High frequency-thickness

Figure 7.11: Peak frequency magnitudes within the sonogram regions for the lower frequency-thickness region E (a), and for the higher frequency-thickness region G (b) for pipework sample A.

which only one of the regions plotted has increased magnitude, therefore minimising the effects of any spikes in the noise level. The existence of two clear peaks in figure 7.12 indicates that they are both true enhancements caused by the presence of defects in both regions of interest G and E, and in this case the positions of enhancement correspond to the two SCC defects, SCC1 and SCC2 in figure 7.9b. The lower magnitude of the enhancement peak at the 5 mm position could indicate that the defect is shallower than the defect at the 16 mm position from the arguments put forward in section 7.1.1, however it was not possible to undertake destructive testing of the sample to confirm this.

The enhancement observed in figure 7.12 can be used to obtain information about the positioning and geometric alignment of any defects present in the

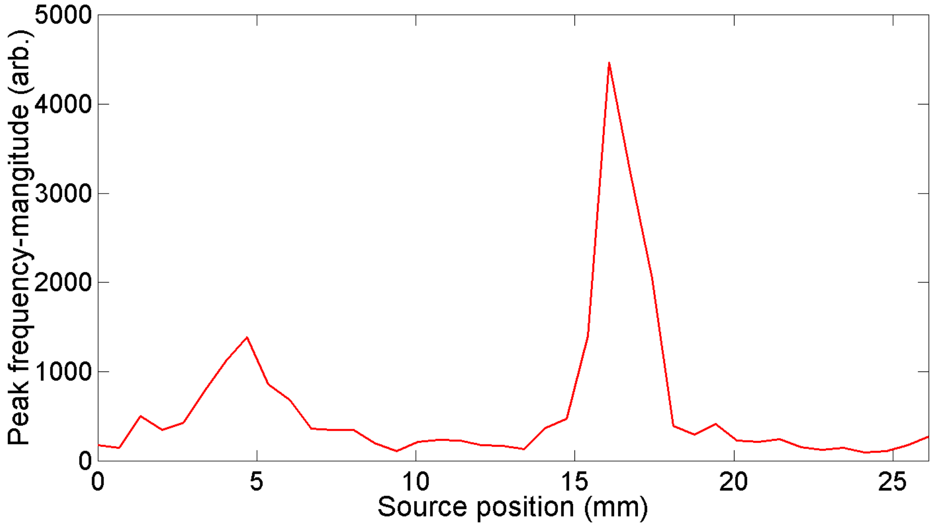

Figure 7.12: Product tracking scan formed from the product of the peak frequency magnitude tracking of the low and high frequency-thickness regions in pipework sample A.

pipework sample through the raster scanning procedure outlined in section 7.1.3. The laser spot source was raster scanned over the region shown in figure 7.9b with circumferential increments of 0.67 mm and vertical steps of 2 mm, and the data was processed to produce the enhancement surface map shown in figure 7.13.

The enhancement surface map shows two extended regions of enhancement that are attributed to the SCC defects seen in figure 7.9b, and two smaller regions that correspond to instances of pitting damage. The enhancements observed for the SCC2 defect are larger in magnitude than those for the SCC1 defect, and it is reasonable to assume that this equates to SCC2 being a deeper defect than SCC1 if the trend for the enhancement magnitude to increase as the defect deepens, observed for the artificial defects in plates, holds true for defects in pipework.

The agreement between the position and alignment of the enhancements arising from SCC1 and SCC2 in figure 7.13 and their locations on the image in figure 7.9b is excellent. Neither defect possesses a clear shadowed region such as that seen for the artificial defects, and from this it can be inferred that the transmission of ultrasound through these SCC cracks is high, which also provides an explanation as to the failure of the scanning laser detection approach to detect any significant enhancement. The clear defect signatures in figure 7.13 highlight the advantages of using the near-field enhancement method for the detection of multiple defects that are close together on a sample, allowing the resolution of the positions and alignments of both defects without either one obscuring the other.

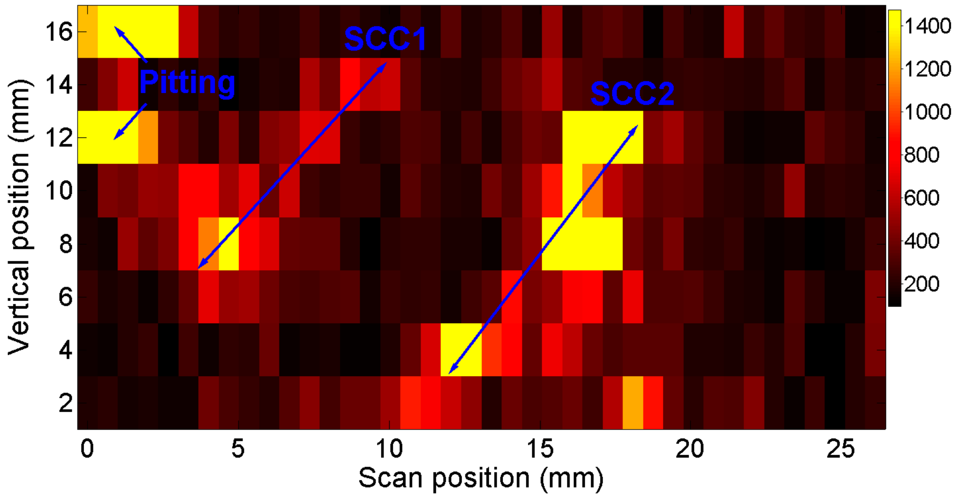

Figure 7.13: Enhancement surface map produced from a raster scan over the damaged region of pipework sample A. The colour scale has been adjusted so that the base level is that of the background noise.

7.2.2 Pipework sample B

The defects in sample A are located near the middle of the pipe section, away from the cut edges from which wave reflections could possibly obscure the defect signals, however small defects close to large reflectors can also be resolved by the near-field scanning approach. Sample B was a second section cut from 3.9 mm thick, 304 stainless steel pipework with an outer diameter of 168.28 mm, that was removed from service after the detection of stress corrosion cracking defects, which

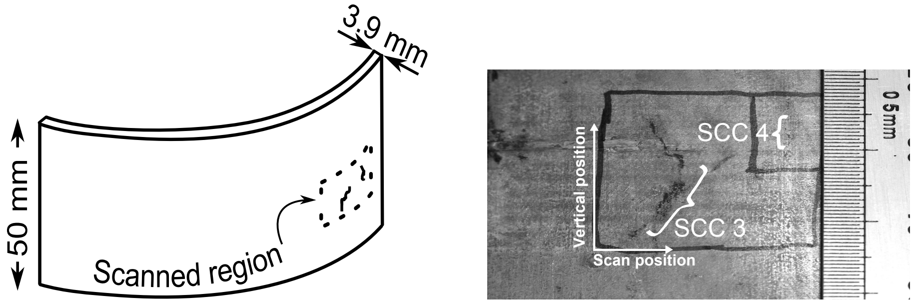

(a) Sample schematic

(b) Defect close-up

Figure 7.14: A schematic diagram of pipework sample B (a) and a close-up image of the inspection region showing two stress corrosion defects labelled SCC3 and SCC4 (b).

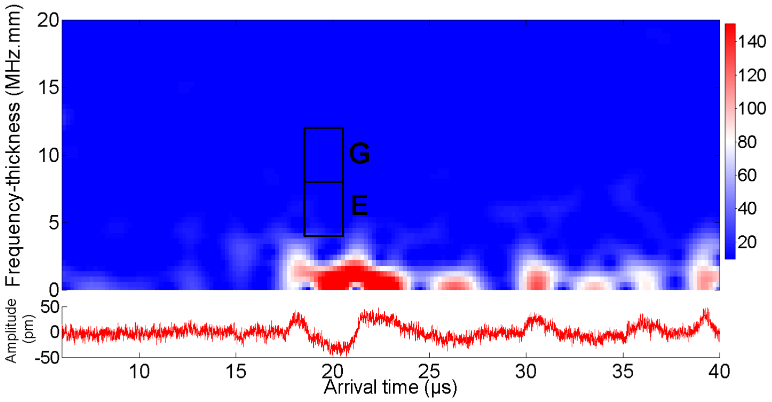

(a) No defect region

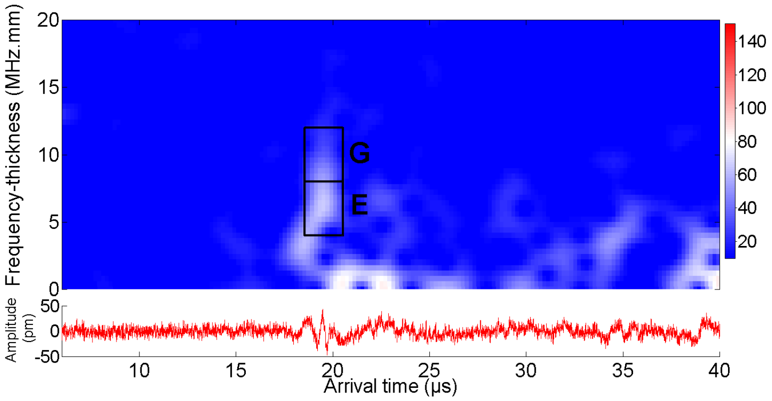

(b) Defect near-field

Figure 7.15: Sonograms produced from A-scans taken with the laser source away from the defect (a) and when the source is close to the defect (b) for a scan across the defect region on pipework sample B.

were again identified through dye penetrant inspection. A schematic image of the pipework section is shown in figure 7.14 with the photo taken prior to cleaning, and two instances of SCC are highlighted, labelled SCC3 and SCC4 respectively. The defects are very close to the sample edge, such that if a reflection based technique was applied for inspection it may be difficult to distinguish the small reflections arising from the defects from the large reflection from the sample edge. Using the same experimental setup as for pipework sample A, a circumferential scan was performed by rotating the sample in 0.5 ° increments, which equates to steps of approximately 0.67 mm on the outer surface of the section. Again, due to the lack of evidence of any signal enhancement from scanning laser detection experiments, only the laser source scans are reported here.

A-scans were taken at each scan position, and were processed in the same manner as in section 7.2.1, with an example of a sonogram taken with the source far

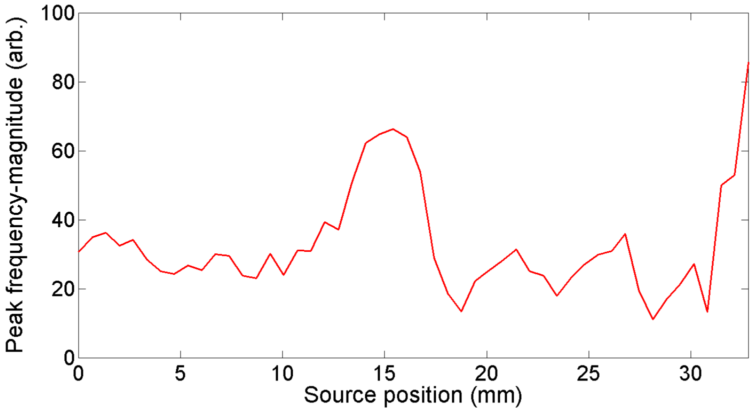

(a) Low frequency-thickness

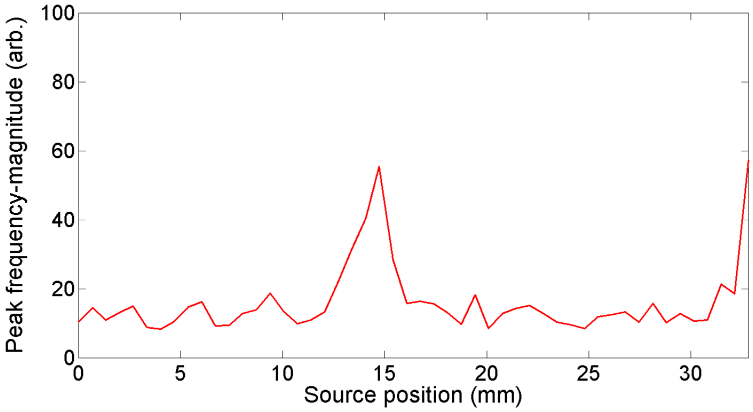

(b) High frequency-thickness

Figure 7.16: Peak frequency magnitudes within the sonogram regions for the lower frequency-thickness region (a), and for the higher frequency-thickness region (b) for pipework sample B.

away from the defect and one with the source illuminating the defect shown in figure 7.15b. As in section 7.2.1, it is seen that when the source is far away from the defect there exists only a low frequency signal, however, when the source illuminates the defect a high frequency signal is generated, with a corresponding change observed in the sonogram.

The same regions of the sonogram in which the fundamental circumferential waves have very similar velocities, chosen for the larger pipework section A sample, were also studied here. The first of these lay between $4.0 \leq fd \leq 8.0$ MHz.mm arriving at $18.54 \leq t \leq 20.54$ μs and the second lay at a higher frequency-thickness of $8.0 \leq fd \leq 12.0$ MHz.mm arriving at $18.54 \leq t \leq 20.54$ μs. These regions are labelled E and G respectively on the sonograms in figure 7.15b.

The peak magnitude within regions E and G are plotted as a function of

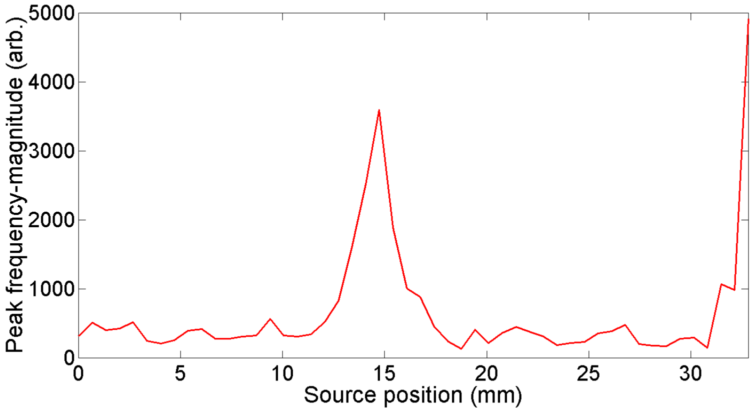

Figure 7.17: Product tracking scan formed from the product of the peak frequency magnitude tracking of the low and high frequency-thickness regions in pipework sample B.

source position in figures 7.16a and 7.16b for a scan line passing over the midpoint of the lower defect SCC3, and again the product of these two regions is plotted in figure 7.17 so as to emphasise positions at which both regions show enhancement, and hence to confirm the features in the data relating to true defects. Two clear enhancements can be observed in figure 7.17. The first is located at a source position of 15 mm and corresponds to the corrosion defect labelled SCC3 in figure 7.14b. The second sits at a source position of 35 mm and is caused by the laser spot passing over the sample edge. The enhancement caused by the sample edge is expected, as discussed in section 6.4.3 for a laser spot passing over an angled defect lip, with the sample edge acting here as a full-thickness 90 ° defect; the enhancement from the pipe edge will not be present if the sample is a complete pipe inspected in-service. Therefore, the position of the source on the sample with respect to the location of the enhancement must be considered before any decision about the presence of a defect is made.

To build a complete image of the damaged region the laser source was again raster scanned over the region in horizontal steps of 0.67 mm and vertical steps of 1 mm, to construct the surface map shown in figure 7.18. The enhancement surface map in figure 7.18 shows two regions of enhancement that correspond to the defects labelled SCC3 and SCC4 in figure 7.14b, giving their positions and allowing their alignment to be seen. The larger magnitude of the enhancement experienced by SCC3 suggests that it is a deeper defect than SCC4, as the enhancement is expected to increase with increasing defect depth, similarly to the artificial defects in plates in section 7.1.1. The detection of the SCC4 defect, which is difficult to see

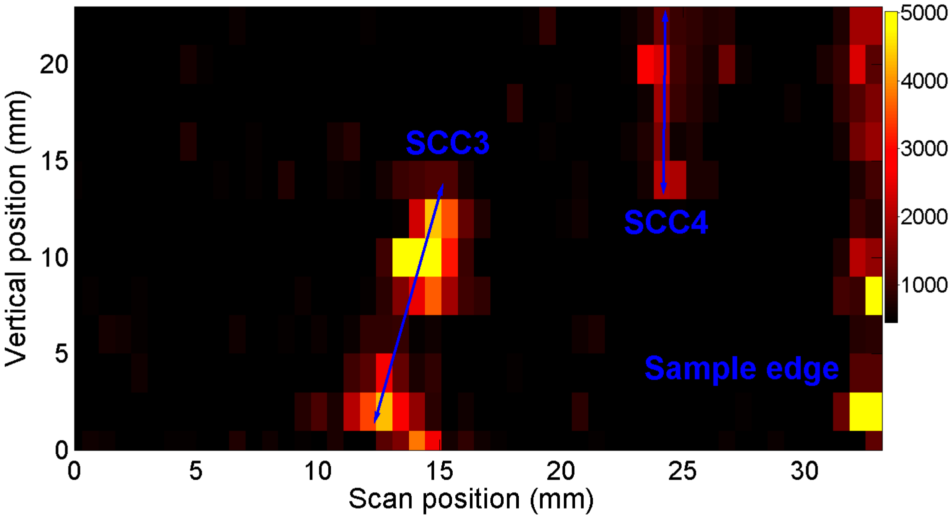

Figure 7.18: Enhancement surface map produced from a raster scan over the damaged region of pipework sample B. The colour scale has been adjusted so that the base level is that of the background noise.

visually, shows the advantage of using the scanning laser source method as the faint SCC4 defect could easily be missed by dye penetrant inspection.

An additional region of enhancement is seen on the right hand side of the surface map that corresponds to the position at which the source is very close to the edge of the sample, which acts like a full-thickness defect perpendicular to the sample surface. The clear defect enhancements illustrates the power of this method for detecting defects that are close together, and in close proximity to large reflectors, such as sample edges.

From visual examination of figure 7.14b it would appear that the SCC3 defect should have a larger spatial extent, extending into the top left region of figure 7.18, than that shown from the enhancement data. However, on closer examination of the sample it was seen that the supposed extra length of the defect was in fact dirt on the sample, with no visually observed defect in the region corresponding to the top left portion once the sample had been cleaned. The fact that there was no enhancement accompanying the phantom defect indicates that the scanning laser source method is not influenced strongly by the surface condition of the sample, which is highly beneficial for industrial application of the technique. The resolution of multiple defects is also important in preventing defects from being missed during inspection.

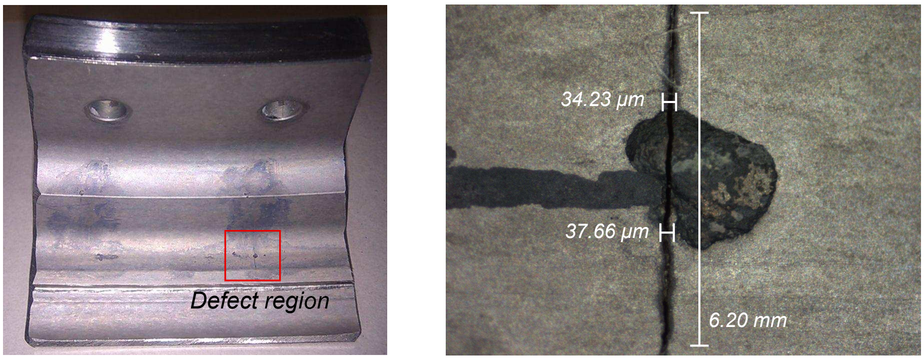

(a) Sample cross-section (b) Defect close-up

Figure 7.19: An image of the irregular test sample highlighting the defective region (a) and a close-up image of the stress corrosion defect showing the defect opening and spatial extent (b).

7.3 Defects in irregularly shaped engine components

Many industrial components do not conform to standard shapes such as bars (chapter 4), plates (chapters 5 and 6) and cylinders (section 7.2), and the real strength of an NDT technique is its ability to be applied to these nonstandard components. To this end an irregularly shaped sample, a titanium disk section with known stress corrosion cracking defects, was investigated using the scanning laser source technique. The sample is a section taken from the mounting for a turbine blade, and an image of the test sample with a close up of the defective region is given in figure 7.19. The turbine blades are mounted on the reverse side of the sample to that shown in the image, and SCC defects can develop on the surface shown in figure 7.19a which has a slight concave curvature along its lateral dimension.

Scans were carried out with the laser source being directed onto the curved sample surface through the use of a right-angled prism held in a two-axis holder, and the laser detector held perpendicular to the sample surface using a retort stand, as shown in figure 3.6. The A-scan data was processed in the same manner as in section 7.1.1 to produce the sonograms shown in figure 7.20. The thickness of the sample at the position of the scan was 6.4 mm. When the source is far away from the defect the signal that is observed is of low frequency, however, when the source directly illuminates the defect an increase in the magnitude at high frequency-thicknesses is observed in figure 7.20b.

The ultrasonic wave produced here is a form of guided wave that is unique to the sample geometry and in order to quantify the enhancement a full understanding of this wave would need to be developed. However, in this section the focus is on the

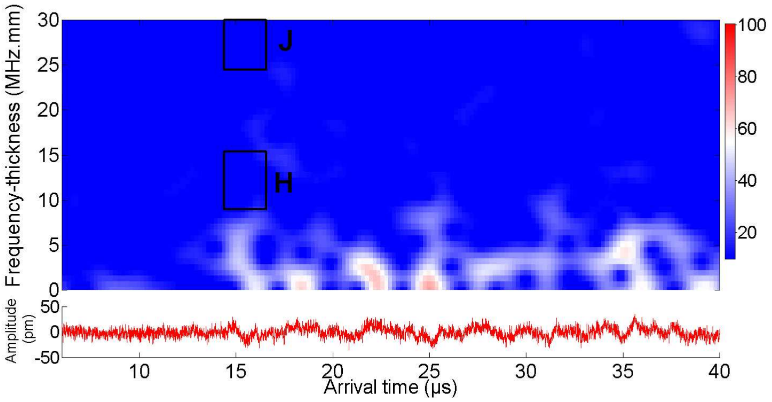

(a) No defect region

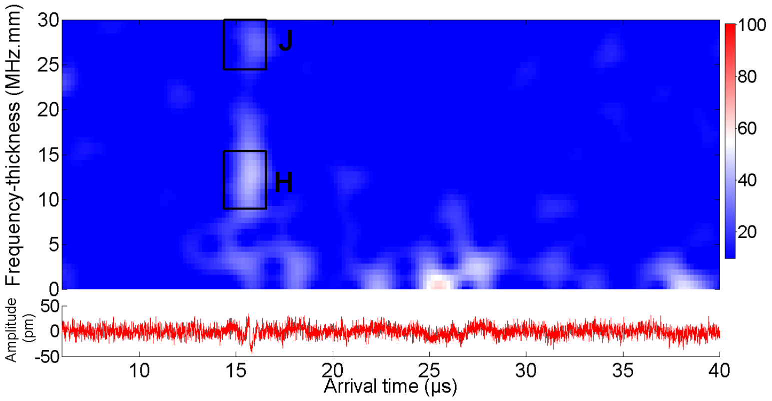

(b) Defect near-field

Figure 7.20: Sonograms produced from A-scans taken with the laser source away from the defect (a) and when the source is close to the defect (b) for a scan across the defect region on the irregularly shaped titanium sample.

ability of the scanning laser source method to detect defects in irregular geometries, and for this purpose the existence of a signal enhancement when the source is over the defect is sufficient to confirm the position and existence of a surface-breaking defect.

To map the defect using this enhancement, the peak magnitude of two tracking regions is studied as a function of the source position. The first of these regions lay between $9.0 \leq fd \leq 15.4$ MHz.mm arriving at $14.37 \leq t \leq 16.57$ μs and the second lay at a higher frequency-thickness of $24.5 \leq fd \leq 30.0$ MHz.mm arriving at $14.37 \leq t \leq 16.57$ μs. These regions are labelled H and J respectively on the sonograms in figure 7.20b. Due to the irregular shape of the component it is no longer possible to highlight specific ultrasonic modes on the sonograms and the regions H and J were chosen as they visually exhibited large enhancements when the source was directly over the defect.

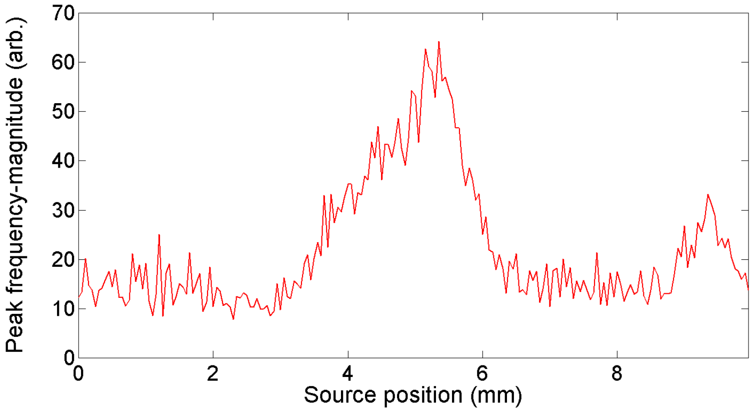

(a) Low frequency-thickness

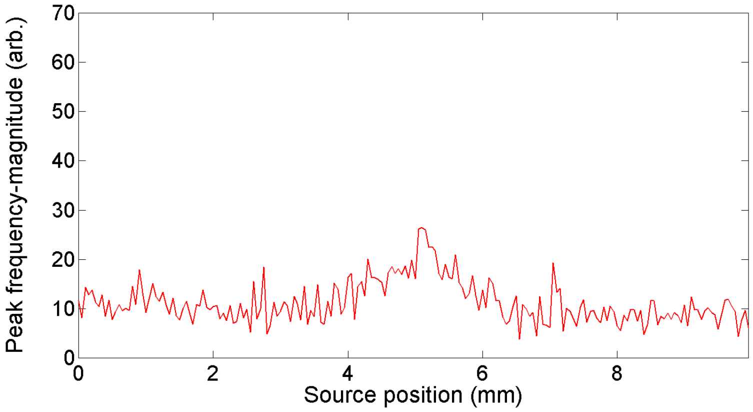

(b) High frequency-thickness

Figure 7.21: Peak frequency magnitudes within the sonogram regions for the lower frequency-thickness region (a), and for the higher frequency-thickness region (b) for the irregularly shaped component.

The peak magnitudes in the regions H and J are plotted as a function of source position in figures 7.21a and 7.21b respectively. Again the product of these two regions is found so that the positions of enhancement that are common to both are emphasised, and this product is plotted as a function of source position in figure 7.22. A single enhancement peak is observed when the source is over the defect in figure 7.22, which indicates that the smaller peak located at 9.35 mm in figure 7.21b is unlikely to be a true enhancement peak and is caused by noise on the signal. This highlights the need to improve the probability of detection by considering more than just one frequency-thickness/time region.

A raster scan using the laser source was performed over the damaged region, and large enhancements were observed at the damage site, giving the position and alignment of the defect (figure 7.23). The curvature of the surface as the raster scan

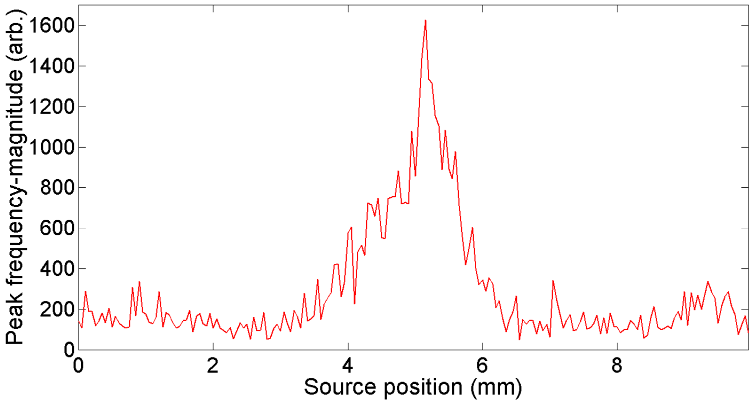

Figure 7.22: Product tracking scan formed from the product of the peak frequency magnitude tracking of the low and high frequency-thickness regions for the irregularly shaped component.

position was increased vertically was small enough that between subsequent scans refocussing of the laser detector and source was not necessary. The enhancement surface map shows the existence of a single defect that is approximately 6 mm long, and the variation in the enhancement factor along the defect length suggests that the defect depth is not constant along its length.

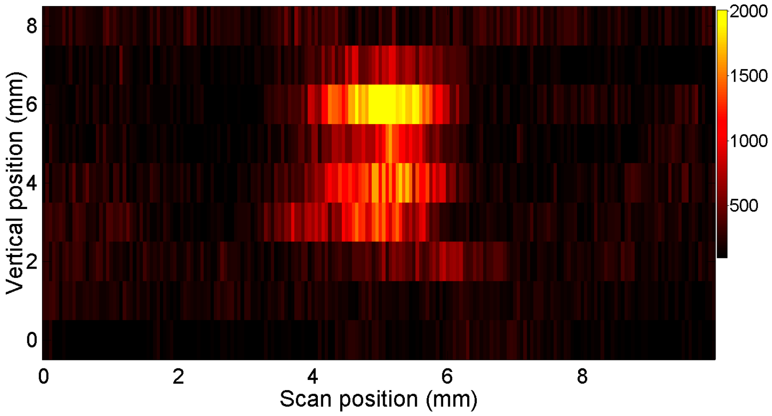

Figure 7.23: Enhancement surface map produced from a raster scan over the damaged region of the irregularly shaped sample. The colour scale has been adjusted so that the base level is that of the background noise.

7.4 Conclusions

In this chapter it has been shown that both scanning laser detection and scanning laser source enhancements can be present when surface waves interact with real defects, and the position and alignment of stress-grown defects have been obtained with a high probability of detection. Raster scanning has been shown to be effective in visualising defects, allowing the resolution of multiple defects and those very close to features such as sample edges. The scanning laser source approach was sucessful in all tests, however the scanning laser detection approach met with less success, due to defects being too tightly closed to provide sufficient reflections from which to produce reflected and mode converted waves of sufficient magnitude to allow an enhancement superposition to be made. However, the sucessful identification of many different defects has shown that the near-field laser scanning approach is a viable method for detection of small, partially-closed defects.

Chapter 8

Conclusions

Early detection and characterisation of defects in industrial components is important for preventing costly economic and environmental failure of critical systems, such as those in the rail transportation[98,99], petrochemical[108] and nuclear industries[109]. Of particular concern is the growth of surface-breaking cracks, such as rolling contact fatigue cracking in railway tracks[96], and stress corrosion cracking[17] which can occur in a multitude of systems. These defects have complicated partially-closed branched structures and can propagate at various angles into a component, which makes detection of them challenging with conventional techniques that rely on the reflection of bulk waves[247]. Ultrasonic inspection with surface waves, such as Rayleigh[90,164,228,248–250] and Lamb waves[21,229–231,259] is becoming a popular inspection strategy. Current techniques rely on the study of changes in ultrasonic propagation far away from the defect, which makes the determination of multiple defects or defects that are close to features such as a sample backwall difficult as the transmission and reflection behaviour is dominated by the deepest defect in a cluster. To this end, a scanning inspection approach has been taken in this thesis that allows the observation of the changes in ultrasonic waves as they occur, and enhancement of the amplitude and frequency content of ultrasound in the near-field of a defect[23,128,235] has been shown to be useful for detecting and characterising multiple defects that are close together or close the sample edge.

Previous work had shown that the enhancement observed for Rayleigh waves incident on artificial perpendicular notches for a scanning laser detector can be explained by a constructive interference between the incident and reflected Rayleigh waves and a mode converted surface skimming longitudinal wave[104,236,237]. The enhancement observed for a scanning laser source experiment can be explained by a combination of wave interference, changes in the boundary conditions of ultrasonic generation and changes in the spatial extent of the area of the laser source[23,235]. However, no consideration had been given to the variation in this enhancement for defect geometries different to slots propagating perpendicular to the surface, such as defects that propagate at an angle with respect to the material surface, as is the case for rolling contact fatigue in rails. It was shown in chapter 4 that the enhancement experienced by a Rayleigh wave varies with the angle of the surface-breaking defect, as do the transmission and reflection coefficients[95,107]. The angle dependence of mode converted waves studied in the defect far-field, that were produced at the defect in scanning laser detection experiments, were shown to be able to be used to position the defect and identify its angle for machined defects (section 4.2.2). The near-field enhancement observed from angled defects for scanning laser detection was attributed to a mode conversion of the Rayleigh wave to Lamb waves in the narrowed material near to the defect (section 4.3). A superposition of many Lamb wave modes at the detector was shown to lead to an increase in the amplitude and frequency content recorded at the defect. An angle dependence in the mechanisms responsible for scanning laser source enhancement in angled defects was also shown to exist and the variation of the enhancement as a function of defect angle for both experimental approaches was used to estimate the defect angle. This is important for the nondestructive detection of defects that propagate at an angle, such as rolling contact fatigue defects[95,107,115,252,271].

The enhancement of Lamb waves had previously been reported to exist for perpendicular defects in thin plates for scanning laser source experiments[64,240], and in this thesis they were observed to also occur for the scanning laser detection approach (chapter 5). Enhancements in the frequency content of individual Lamb modes, which were resolved from broadband signals using time frequency-analysis, were shown to increase as a function of increasing depth for open v-shaped artificial defects in thin sheets. The enhancement of individual Lamb modes was attributed to constructive interference between the incident wave mode, and reflected and mode converted waves from the defect. This enhancement mechanism was validated through the use of theoretically calculated enhancement factors created from two test models, based on a square-based notch and an open mouthed crack (section 5.3), which estimated the enhancement that could be observed for a defect of a given depth. It was shown that the scanning laser detection enhancement of Lamb waves could be used to position a defect and to characterise the defect depth for defects in thin plates, which is useful for the detection of defects in large scale industrial nondestructive testing applications, such as the detection of defects in storage tanks[22,271].

Lamb wave enhancement was also studied for the scanning laser source approach, and was shown to also vary as the defect depth increased (chapter 6). The enhancement was found to arise from contributions from constructive interference between incident and reflected Lamb waves, and variations in the generation conditions of the ultrasound as the source illuminated the defect. The scanning laser source enhancements enabled the defect to be positioned and an estimate to be made of the severity of the defect, proving that the near-field scanning approach can be applied to complicated multimodal ultrasonic signals to identify surface-breaking defects in thin plates[116,271].

Finally, the near-field scanning approach was validated on real partially-closed defects in different sample geometries and it was proven that the approach can be used to position and characterise real defects. Scanning laser source enhancements were observed in artificially grown stress cracks in thin plates (section 7.1.1) and an additional enhancement mechanism that is not present in wide, open machined defects was shown to contribute to the enhancement. This additional mechanism arose from the generation of higher harmonics of the surface wave caused by the clapping together of the opposing faces of the defect when driven by the transient heating of the crack by the laser source. An enhancement at the defect for scanning laser detection of real defects in plates (section 7.1.2) was shown to be caused by the superposition of Lamb wave modes at high frequency-thicknesses, and the enhancement from both scanning approaches were used to estimate the positions and severity of the defects. A raster scanning approach was used that enabled an enhancement surface map of a defect to be constructed, giving a visualisation of the position and severity of the real defects.

The applicability of the scanning laser source method to other sample geometeries that contained real partially-closed defects was shown for sections of pipework (section 7.2) and irregularly shaped engine components (section 7.3). In both cases a raster scan image of the sample provided the location and geometry of the defect, however, scanning laser detection was shown to have difficulties at detecting defects with low reflectivities. The sucessful detection and characterisation of real stress-driven defects in several different defect geometries shown in this thesis highlights the advantages of the near-field scanning method, and the ability to locate multiple defects in close proximity and obtain an estimate of their depth and geometry is very interesting for nondestructive testing applications[180].

8.1 Suggested further work

This thesis has demonstrated the use of near-field enhancements to detect and characterise surface breaking defects, both artificial and real, with a full understanding of the interactions of the ultrasonic surface wave with defects developed for angled defects in bars and for simple v-shaped defects in sheets. Whilst the knowledge of the interactions with defects in sheets is very useful for understanding the interactions present in large storage structures, it cannot be directly transferred to defects in other geometries, such as defects in pipes, which are of interest in non-destructive testing applications.

To fully understand the interactions of ultrasonic waves and calibrate the effects with defect size for defects in cylindrical pipes an investigation into the enhancement behaviour of the various different wave modes that are supported in hollow cylinders with machined artificial defects is proposed. This would require the machining of v-shaped defects that have different known depths, similar to those studied in this work for thin plates, and studying the variation in the enhancement observed for both laser scanning geometries. In turn this would enable the development of an understanding of the mechanisms that cause the enhancement, which would lead to a means of accurately relating the level of enhancement observed to the severity of the defect in pipework. This understanding of the enhancement mechanism in hollow pipes is required before the near-field scanning method could be considered for use in areas such as the petrochemical industry, alongside investigations of reflection and transmission changes.

To understand the nature of the interactions of surface waves with complicated branched SCC defects the knowledge developed from a study of the interactions with v-shaped artificial defects needs to be expanded to study artificial branched defects. Branched surface-breaking defects in plates can be manufactured with a variety of different branching structures, with variations in the position, length and angle of the branches and their influence on the near-field behaviour of the defect all providing interesting avenues for research. Lamb waves that propagate in thin sheets have a varying displacement through the thickness of the sheet, and hence the position and angle of these branches would have an influence on the nature of the near and far-field behaviour of the ultrasonic wave, and a variation in the enhancement observed for these different geometries could be used to identify the character of the defect. To expand the range of defects availiable for this study FEM simulations could be carried out, allowing the study of more complicated defect geometries.

Through building up an ever more complex library of artificial defects the eventual aim is to be able to quantify the enhancement that is observed for real defects. This would be aided by obtaining an expanded selection of artificially grown stress defects such as those studied in chapter 7, with a greater selection of defect depths and geometries. The knowledge gained from the study of the near-field interactions of branched defects would provide a good starting point for quantifying the variations in the real defects with increasing severity. Both the study of branched defects and grown stress defects could also be expanded to other sample geometries, such as that of defects in pipework samples, with the aim of developing an industrial technique that can be used in many different applications. Changes in the near-field behaviour with the changing length of these defects on the top surface of the material would also make for an interesting study as factors such as diffraction around the defect will have more of an influence on the near-field interactions for smaller defects, and would provide a test of the limitations of the near-field inspection method.

Once an understanding of the variation of the near-field behaviour at real stress defects has been achieved the true test of the system would be the implementation of an industrial prototype which would monitor components in situ. This monitoring could be installed such that both laser source and detector would periodically be raster scanned over a set of components and used to detect new defects or to monitor the growth of pre-existing damage, or alternatively the system could be employed statically to look for defects on a moving production line. To this end, smaller generation lasers than the one used in this work, such as a diode pumped Nd:YAG system from CrystaLaser, would make a more compact system which would be easier to implement. With pulse rates of tens of kHz a system could be developed that could achieve faster scanning rates than the one presented in this thesis, allowing swifter inspection of large regions of the test piece. A range of energies and spot sizes are avaliable, with higher energies (up to 3W) and smaller spot sizes of 0.4 mm likely to produce even higher levels of enhancement, allowing defects to be imaged with a high probability of detection. To make the near-field approach more accessible to industry the inclusion of a cheaper non-contact generator or detector, such as an EMAT, could be explored to limit the cost of the method. This has the added advantage that information about the in-plane component of the ultrasound can be obtained, which may exhibit increased enhancement over the out-of-plane component for certain wave modes, again increasing the probability of detection.

References

[1] E. T. Newbrough. *Effective maintenance management.* McGraw-Hill Inc., 1967.

[2] J. Moubray. *Reliability-centred maintenance.* Butterworth Heinemann, 1997.

[3] V. Venkatasubramanian, R. Rengaswamy, K. Yin, and S. N. Kavuri. A review of process fault detection and diagnosis part 1: quantitative model-based methods. *Computers and Chemical Engineering*, **27**:pp. 293–311, 2003.

[4] M. A. Rao and T. S. N. Sankara Narayanan. Failure investigation of a boiler bank tube from a 77 x 2 MW coal based thermal power plant in the northwest region of India. *Engineering Failure Analysis*, **26**:pp. 325–331, 2012.

[5] G. Yang, K. B. Yoon, and Y. C. Moon. Stress corrosion cracking of stainless steel pipes for methyl-methacrylate process plants. *Engineering Failure Analysis*, **29**:pp. 45–55, 2013.

[6] R. Halmshaw. *Non-destructive Testing.* Edward Arnold, 1991.

[7] D. E. Bray and D. McBride. *Nondestructive testing techniques.* John Wiley & Sons Inc, 1992.

[8] C. Garnier, M-L. Pastor, F. Eyma, and B. Lorrain. The detection of aeronautical defects in situ on composite structures using non destructive testing. *Composite Structures*, **93**:pp. 1328–1336, 2011.

[9] J. C. Abry, Y. K. Choi, A. Chateauminois, B. Dalloz, G. Giraud, and M. Salvia. In-situ monitoring of damage in CFRP laminates by means of AC and DC measurements. *Composites Science and Technology*, **61**:pp. 855–864, 2001.

[10] B. Hutchinson, B. Moss, A. Smith, A. Astill, C. Scruby, G. Engberg, and J. Bjorklund. Online characterisation of steel structures in hot strip mill using

laser ultrasonic measurements. *Ironmaking and Steelmaking*, **29**:pp. 77–80, 2002.

[11] Z. Orban and M. Gutermann. Assessment of masonry arch railway bridges using non-destructive in-situ testing methods. *Engineering Structures*, **31**:pp. 2287–2298, 2009.

[12] C Manfredi and J L Otegui. Failure by SCC in buried pipelines. *Engineering Failure Analysis*, **9**:pp. 495–509, 2002.

[13] A Contreras, A Albiter, M. Salazar, and R. Perez. Slow strain rate corrosion and fracture characteristics of X-52 and X-70 pipeline steels. *Materials Science and Engineering A*, **407**:pp. 45–52, 2005.

[14] P. Marcus. *Corrosion Mechanisms in Theory and Practice*. CRC Press, 2011.

[15] H. Cho, H. Nakazawa, and M. Takemoto. Estimation of wall reduction of plate using the fundamental symmetric mode Lamb wave. *Japanese Journal of Applied Phyiscs*, **43**:pp. 3080–3081, 2004.

[16] H. Cho, T. Matsuo, and M. Takemoto. Long range inspection of wall reduction of tank utilizing zero-th order symmetric mode Lamb wave. *Materials Transactions*, **48**:pp. 1179–1183, 2007.

[17] R A Cottis. Stress corrosion cracking. *NPL*, 2000.

[18] W. Zhu and J. L. Rose. Lamb-wave generation and reception with time-delay periodic linear arrays: A BEM simulation and experimental study. *IEEE Transactions on Ultrasonics, Ferroelectrics and Frequency Control*, **46**:pp. 654–664, 1999.

[19] Y. Zhang and G. Yan. Detection of gas pipe wall thickness based on electromagnetic flux leakage. *Russian Journal of Nondestructive Testing*, **43**:pp. 123–132, 2007.

[20] S. Dixon, C. Edwards, and S. B. Palmer. A laser-EMAT system for ultrasonic weld inspection. *Ultrasonics*, **37**:pp. 273–281, 1999.

[21] P. Cawley and D. N. Alleyne. The use of Lamb waves for the long range inspection of large structures. *Ultrasonics*, **34**:pp. 287–290, 1996.

[22] A. R. Clough and R. S. Edwards. Lamb wave near field enhancements for surface-breaking defects in plates. *Journal of Applied Physics*, **111**:p. 104906, 2012.

[23] A. K. Kromine, P. A. Fomitchov, S. Krishnaswamy, and J. D. Achenbach. Laser ultrasonic detection of surface breaking discontinuities: Scanning laser source technique. *Materials Evaluation*, **58**:pp. 173–177, 2000.

[24] A. McNab, K. J. Kirk, and A. Cochran. Ultrasonic transducers for high temperature applications. *IEE Proceedings - Science Measurement and Technology*, **145**:pp. 229–236, 1998.

[25] B. A. Auld. *Acoustic fields and waves in solids.* Krieger Publishing Company, 1990.

[26] J. David and N. Cheeke. *Fundamentals and applications of ultrasonic waves.* CRC Press, 2002.

[27] C.B. Scruby and L.E. Drain. *Laser ultrasonics. Techniques and applications.* Adam Hilger, 1990.

[28] M Hirao and H Ogi. *EMATs for science and industry. Noncontacting ultrasonic measurements.* Kluwer Academic Publishers, 2003.

[29] S. Shepard. Introduction to active thermography for non-destructive evaluation. *Anti-corrosion Methods and Materials.*, **44**:pp. 236, 1997.

[30] A. L. Jones and K. F. Pezdirtz. Nondestructive eddy current testing. *IEEE Transactions on Instrumentation and Measurement.*, **21**:pp. 11–15, 1972.

[31] D. E. Bray and R. K. Stanley. *Nondestructive Evaluation. A tool in design, manufacturing and service.* CRC Press, 1997.

[32] A. J. McEvily. Failures in inspection procedures: case studies. *Engineering Failure Analysis*, **11**:pp. 167–176, 2004.

[33] P. Samsonov. Remote visual inspection for NDE in power plants. *Materials Evaluation*, **51**:pp. 662–663, 1993.

[34] Y. Zhu, G. Tian, R. Lu, and H. Zhang. A review of optical NDT technologies. *Sensors*, **11**:pp. 7773–7798, 2011.

[35] R. C. Tennyson, A. A. Mufti, S. Rizkalla, G. Tadros, and B. Benmokrane. Structural health monitoring of innovative bridges in Canada with fibre optic sensors. *Smart Materials and Structures*, **10**:pp. 560–573, 2001.

[36] W. J. Staszewski, S. G. Pierce, K. Worden, W. R. Philp, G. R. Tomlinson, and B. Culshaw. Wavelet signal processing for enhanced Lamb-wave defect detection in composite plates using optical fiber detection. *Optical Engineering*, **36**:pp. 1877–1888, 1997.

[37] H. Li, D. Li, and G. Song. Recent applications of fibre optic sensors to health monitoring in civil engineering. *Engineering Structures*, **26**:pp. 1647–1657, 2004.

[38] A. de Sterke. A practical introduction to penetrants. *Nondestructive Testing*, **1**:pp. 306–307, 1968.

[39] N. P. Migun, A. B. Gnusin, and I. V. Volovich. Some possibilities of enhancing the efficiency of penetrant inspection. *Russian journal of nondestructive testing*, **41**:pp. 452–455, 2005.

[40] J.R. W. C. Morrey. Penetrant testing in the quality control of nuclear power plant construction. *NDT International*, **10**:pp. 9–12, 1977.

[41] D. C. Jiles. Review of magnetic methods for nondestructive evaluation (Part 2). *NDT International*, **23**:pp. 93–92, 1990.

[42] J. Y. Lee, S. J. Lee, D. C. Jiles, M. Garton, R. Lopez, and L. Brasche. Sensitivity analysis of simulations for magnetic particle inspection using the finite-element method. *IEEE Transactions on Magnetics*, **39**:pp. 3604–3606, 2003.

[43] G. M. Massa. Finding the optimum conditions for weld testing by magnetic particles. *Nondestructive Testing*, **9**:pp. 16–26, 1976.

[44] D. Groves and D. Connell. Offshore structure fabrication experience with magnetic particle inspection. *NDT International*, **18**:pp. 85–88, 1985.

[45] A. Sophian, G. Y. Tian, and S. Zairi. Pulsed magnetic flux leakage techniques for crack detection and characterisation. *Sensors and Actuators A*, **125**:pp. 186–191, 2006.

[46] Y. Li, J. Wilson, and G. Y. Tian. Experiment and simulation study of 3D magnetic field sensing for magnetic flux leakage defect characterisation. *NDT & E International*, **40**:pp. 179–184, 2007.

[47] Y. Zhang, Z. Ye, and C. Wang. A fast method for rectangular crack sizes reconstruction in magnetic flux leakage testing. *NDT & E International*, **42**: 369–375, 2009.

[48] Y. Li, G. Y. Tian, and S. Ward. Numerical simulation on magnetic flux leakage evaluation at high speed. *NDT & E International*, **39**:pp. 367–373, 2006.

[49] F. Caleyo, J. L. Gonzalez, and J. M. Hallen. A study on the reliability assessment methodology for pipelines with active corrosion defects. *International Journal of Pressure Vessels and Piping.*, **79**:pp. 77–86, 2002.

[50] R. Hanke, T. Fuchs, and N. Uhlmann. X-ray based methods for non-destructive testing and material characterisation. *Nuclear Intruments and Methods in Physics Research A*, **591**:pp. 14–18, 2008.

[51] D. Babot, G. Berodias, and G. Peix. Detection and sizing by X-ray Compton scattering of near-surface cracks under weld deposited cladding. *NDT & E International*, **24**:pp. 247–251, 1991.

[52] W. L. Dunn and A. M. Yacout. Corrosion detection in aircraft by X-ray backscatter methods. *Applied Radiation and Isotopes*, **53**:pp. 625–632, 2000.

[53] E. R. Doering, J. P. Basart, and J. N. Gray. Three-dimensional flaw reconstruction and dimensional analysis using a real-time X-ray imaging system. *NDT & E International*, **26**:pp. 7–17, 1993.

[54] A. Maksimenko, M. Ando, H. Sugiyama, and E. Hashimoto. Possibility of computed tomographic reconstruction of cracks from X-ray refraction contrast. *Japanese Journal of Applied Phyiscs*, **44**:pp. 633–635, 2005.

[55] M. S. Rapaport and A. Gayer. Application of gamma ray computed tomography to nondestructive testing. *NDT&E International*, **24**:pp. 141–144, 1991.

[56] N. Chankow, S. Punnachaiya, and S. Wonglee. Neutron radiography using neutron imaging plate. *Applied Radiation and Isotopes*, **68**:pp. 662–664, 2010.

[57] P. J. McMahon, B. E. Allman, K. A. Nugent, D. L. Jacobson, M. Arif, and S. A. Werner. Contrast mechanisms for neutron radiography. *Applied Physics Letters*, **78**:pp. 1011–1013, 2001.

[58] J. S. Brenizer, B. Hosticka, H. Berger, and G. T. Gillies. The use of contrast agents to enhance crack detection via neutron radiography. *NDT&E International*, **32**:pp. 37–42, 1999.

[59] S. Pierret, A. Evans, A. M. Paradowska, A. Kaestner, J. James, T. Etter, and H. Van Swygenhoven. Combining neutron diffraction and imaging for residual

strain measurements in a single crystal turbine blade. *NDT & E International*, **45**:pp. 39–45, 2012.

[60] D J Titman. Applications of thermography in non-destructive testing of structures. *NDT & E International*, **34**:pp. 149–154, 2001.

[61] N. P. Avdelidis, D. P. Almond, A. Dobbinson, B. C. Hawtin, C. Ibarra-Castanedo, and X. Maldague. Aircraft composites assessment by means of transient thermal NDT. *Progress in Aerospace Sciences*, **40**:pp. 143–162, 2004.

[62] T. J. Barden, D. P. Almond, S. G. Pickering, M. Morbidini, and P. Cawley. Detection of impact damage in CFRP composites by thermosonics. *Nondestructive Testing and Evaluation*, **22**:pp. 71–82, 2007.

[63] S. E. Burrows, A. Rashed, D. P. Almond, and S. Dixon. Combined laser spot imaging thermography and ultrasonic measurements for crack detection. *Nondestrutive Testing and Evaluation*, **22**:pp. 217–227, 2007.

[64] S. E. Burrows, S. Dixon, S. G. Pickering, T. Li, and D. P. Almond. Thermographic detection of surface-breaking defects using a scanning laser source. *NDT&E International*, **44**:pp. 589–596, 2011.

[65] T. Zweschper, A. Dillenz, G. Riegert, D. Scherling, and G. Brusse. Ultrasound excited thermography using frequency modulated elastic waves. *Insight*, **45**: pp. 178–182, 2003.

[66] R. J. Ditchburn, S. K. Burke, and C. M. Scala. NDT of welds: state of the art. *NDT & E International*, **29**:pp. 111–117, 1996.

[67] W. D. Dover and C. C. Monahan. The measurement of surface breaking cracks by the electrical systems ACPD/ACFM. *Fatigue Fracture Engineering Material Structure*, **17**:pp. 1485–1492, 1994.

[68] H. Saguy and D. Rittel. Flaw detection in metals by the ACPD technique: Theory and experiments. *NDT & E International*, **40**:pp. 505–509, 2007.

[69] M. Ph. Papaelias, M. C. Lugg, C. Roberts, and C. L. Davis. High-speed inspection of rails using ACFM techniques. *NDT & E International*, **42**:pp. 328–335, 2009.

[70] R. LeTessier, R. W. Coade, and B. Geneve. Sizing of cracks using the alternating current field measurement technique. *International Journal of Pressure Vessels and Piping.*, **79**:pp. 549–554, 2002.

[71] J. Garcia-Martin, J. Gomez-Gil, and E. Vazquez-Sanchez. Non-destructive techniques based on eddy current testing. *Sensors*, **11**:pp. 2525–2565, 2011.

[72] R. J. Ditchburn, S. K. Burke, and M. Posada. Eddy-current nondestructive inspection with thin spiral coils: Long cracks in steel. *Journal of Nondestructive Evaluation*, **22**:pp. 63–77, 2003.

[73] C. V. Dodd and W. E. Deeds. Analytical solutions to eddy-current probe-coil problems. *Journal of Applied Physics*, **39**:pp. 2829–2838, 1968.

[74] H. A. Wheeler. Formulas for the skin effect. *Proceedings of the I.R.E.*, pages pp. 412–424, 1942.

[75] M. P. Blodgett and P. B. Nagy. Eddy current assessment of near-surface residual stress in shot-peened nickle-base superalloys. *Journal of Nondestructive Evaluation*, **23**:pp. 107–123, 2004.

[76] H. Shaikh, N. Sivaibharasi, B. Sasi, T. Anita, R. Amirthalingam, B. P. C. Rao, T. Jayakumar, H. S. Khatak, and B. Raj. Use of eddy current testing method in detection and evaluation of sensitisation and intergranular corrosion in austenitic stainless steels. *Corrosion Science*, **48**:pp. 1462–1482, 2006.

[77] Y. He, F. Luo, M. Pan, F. Weng, X. Hu, J. Gao, and B. Liu. Pulsed eddy current technique for defect detection in aircraft riveted structures. *NDT & E International*, **43**:pp. 176–181, 2010.

[78] A. Sophian, G. Y. Tian, D. Taylor, and J. Rudlin. Design of a pulsed eddy current sensor for detection of defects in aircraft lap-joints. *Sensors and Actuators A*, **101**:pp. 92–98, 2002.

[79] J. Blitz and G. Simpson. *Ultrasonic methods of Non-destructive Testing.* Chapman & Hall, 1996.

[80] B. Masserey and P. Fromme. Surface defect detection in stiffened plate structures using Rayleigh-like waves. *NDT & E International*, **42**:pp. 564–572, 2009.

[81] F. Jenot, M. Ouaftouh, M. Duquennoy, and M. Ourak. Corrosion thickness gauging in plates using Lamb wave group velocity measurements. *Measurement Science and Technology*, **12**:pp. 1287–1293, 2001.

[82] N. Terrien, D. Royer, F. Lepoutre, and A. Deom. Numerical predictions and experiments for optimizing hidden corrosion detection in aircraft structures using Lamb modes. *Ultrasonics*, **46**:pp. 251–265, 2007.

[83] A. S. Murfin and R. J. Dewhurst. Estimation of wall thinning in mild steel using laser ultrasound Lamb waves and a non-steady-state photo-emf detector. *Ultrasonics*, **40**:pp. 777–781, 2002.

[84] X. Zhao, H. Gao, G. Zhang, B. Ayhan, F. Yan, C. Kwan, and J. L. Rose. Active health monitoring of an aircraft wing with embedded piezoelectric sensor/actuator network: I. Defect detection, localization and growth monitoring. *Smart Materials and Structures*, **16**:pp. 1208–1217, 2007.

[85] D. A. Hutchins and A. C. Tam. Pulsed photoacoustic materials characterization. *IEEE Transactions on Ultrasonics, Ferroelectrics and Frequency Control*, **33**:pp. 429–449, 1986.

[86] M. H. Rosli, R. S. Edwards, and Y. Fan. In-plane and out-of-plane measurements of Rayleigh waves using EMATs for characterising surface cracks. *NDT & E International*, **49**:pp. 1–9, 2012.

[87] G. Baskaran, K. Balasubramaniam, and C. L. Rao. Shear-wave time of flight diffraction (S-TOFD) technique. *NDT & E International*, **39**:pp. 458–467, 2006.

[88] K. Kawashima. Quantitative calculation and measurement of longitudinal and transverse ultrasonic wave pulses in solids. *IEEE Transactions on sonics and ultrasonics*, **31**:pp. 83–93, 1984.

[89] J. L. Rose. *Ultrasonic waves in solid media.* Cambridge University Press, 1999.

[90] B. Q. Vu and V. K. Kinra. Diffraction of Rayleigh waves in a half-space. I. Normal edge crack. *Journal of the Acoustical Society of America*, **77**:pp. 1425–1430, 1985.

[91] M. Castaings and P. Cawley. The generation, propagation, and detection of Lamb waves in plates using air-coupled ultrasonic transducers. *Journal of the Acoustical Society of America*, **100**:pp. 3070–3077, 1996.

[92] M. A. Hamstad. A review: Acoustic emission, a tool for composite-materials studies. *Experimental Mechanics*, **26**:pp. 7–13, 1986.

[93] O. Muransky, M. R. Barnett, D. G. Carr, S. C. Vogel, and E. C. Oliver. Investigation of deformation twinning in a fine-grained and coarse-grained ZM20 Mg alloy: Combined in situ neutron diffraction and acoustic emission. *Acta Materialia*, **58**:pp. 1503–1517, 2010.

[94] B. Masserey and P. Fromme. On the reflection of coupled Rayleigh-like waves at surface defects in plates. *Journal of the Acoustical Society of America*, **123**: pp. 88–98, 2008.

[95] B. Dutton, A. R. Clough, and R. S. Edwards. Near field enhancements from angled surface defects: A comparison of scanning laser source and scanning laser detection techniques. *Journal of Nondestructive Evaluation*, **30**:pp. 64–70, 2011.

[96] D. F. Cannon and H. Pradier. Rail rolling contact fatigue. Research by the European rail research institute. *Wear*, **191**:pp. 1–13, 1996.

[97] J. Tani, M. Mayuzumi, T. Arai, and N. Hara. Stress corrosion cracking growth rates of candidate canister materials for spent nuclear fuel storage in chloride-containing atmosphere. *Materials Transactions*, **48**:pp. 1431–1437, 2007.

[98] D. F. Cannon, K. O. Edel, S. L. Grassie, and K. Sawley. Rail defects: an overview. *Fatigue Fracture Engineering Material Structure*, **26**:pp. 685–887, 2003.

[99] T. N. Farris, L. M. Keer, and R. K. Steele. The effect of service loading on shell growth in rails. *Journal of the Mechanics and Physics of Solids.*, **35**:pp. 677–700, 1987.

[100] R. Clark, S. Singh, and C. Haist. Ultrasonic characterisation of defects in rails. *Insight*, **44**:pp. 341–347, 2002.

[101] Y. Fan, S. Dixon, R. S. Edwards, and X. Jian. Ultrasonic surface wave propagation and interaction with surface defects on rail track head. *NDT & E International*, **40**:pp. 471–477, 2007.

[102] J. L. Rose, M. J Avioli, P. Mudge, and R. Sanderson. Guided wave inspection potential of defects in rail. *NDT & E International*, **37**:pp. 153–161, 2004.

[103] S. Dixon, R. S. Edwards, and X. Jian. Inspection of the rail track head surfaces using electromagnetic acoustic transducers (EMATs). *Insight*, **46**:pp. 326–330, 2004.

[104] R. S. Edwards, S. Dixon, and X. Jian. Enhancement of the Rayleigh wave signal at surface defects. *Journal of Physics D: Applied Physics*, **37**:pp. 2291–2297, 2004.

[105] R. S. Edwards, S. Dixon, and X. Jian. Characterisation of defects in the railhead using ultrasonic surface waves. *NDT & E International*, **39**:pp. 468–475, 2006.

[106] V. K. Kinra and B. Q. Vu. Diffraction of Rayleigh waves in a half-space. ii. Inclined edge crack. *Journal of the Acoustical Society of America*, **79**:pp. 1688–1698, 1986.

[107] B. Dutton, A. R. Clough, M. H. Rosli, and R. S. Edwards. Non-contact ultrasonic detection of angled surface defects. *NDT & E International*, **44**:pp. 353–360, 2011.

[108] B. Y. Fang, A. Atrens, J. Q. Wang, E. H. Han, Z. Y. Zhu, and W. Ke. Review of stress corrosion cracking of pipeline steels in low and high ph solutions. *Journal of Materials Science*, **8**:pp. 127–132, 2003.

[109] D. R. Diercks, W. J. Shack, and J. Muscara. Overview of steam generator tube degradation and integrity issues. *Nuclear Engineering and Design*, **194**: pp. 19–30, 1999.

[110] S. Ramadan, L. Gaillet, C. Tessier, and H. Idrissi. Detection of stress corrosion cracking of high-strength steel used in prestressed concrete structures by acoustic emission technique. *Applied Surface Science*, **254**:pp. 2255–2261, 2008.

[111] P. Shull. *Nondestructive evaluation.* CRC Press, 2002.

[112] S. Baby, T. Balasubramanian, R. J. Pardikar, M. Palaniappan, and R. Subbaratnam. Time-of-flight diffraction (TOFD) technique for accurate sizing of surface-breaking cracks. *Insight*, **45**:pp. 426–430, 2003.

[113] B. Kim and Y. Roh. Simple expression of the reflection and transmission coefficients of fundamental Lamb waves by a rectangular notch. *Ultrasonics*, **51**:pp. 734–744, 2011.

[114] M. Castaings, E. Le Clezio, and B. Hosten. Modal decomposition method for modeling the interaction of Lamb waves with cracks. *Journal of the Acoustical Society of America*, **112**:pp. 2567–2582, 2002.

[115] R. S. Edwards, B. Dutton, and A. R. Clough. Interaction of laser generated ultrasonic waves with wedge-shaped samples. *Applied Physics Letters*, **100**:p. 184102, 2012.

[116] A. R. Clough and R. S. Edwards. Scanning laser source Lamb wave enhancements for defect characterisation. *Under review*, 2013.

[117] Grigoryants. *Basics of laser material processing.* CRC Press, 2000.

[118] George Chryssolouris. *Laser machining. Theory and Practice.* Springer-Verlag, 1991.

[119] J. D. Achenbach. Quantitative nondestructive evaluation. *International Journal of Solids and Structures*, **37**:pp. 13–27, 200.

[120] J. H. Cantrell and W. T. Yost. Nonlinear ultrasonic characterization of fatigue microstructures. *International Journal of Fatigue*, **23**:pp. 487–490, 2001.

[121] A Kumar, T Jayakumar, and Baldev Raj. Ultrasonic spectral analysis for microstructural characterisation of austenitic and ferritic steels. *Philosophical Magazine A*, **80**:pp. 2469–2487, 2000.

[122] S. Sharples, M. Clark, and M. G. Somekh. Spatially resolved acoustic spectroscopy for fast noncontact imaging of material microstructure. *Optics Express*, **14**:pp. 10435–10440, 2006.

[123] R. S. Edwards, R. Perry, D. J. Backhouse, I. J. Moore, D. Cleanthous, A. R. Clough, and D. Stone. Non-contact ultrasonic measurements of the elastic constants of magnetic materials. *Condensed Matter and Materials Physics Conference Proceedings*, **286**:p. 012050, 2011.

[124] O. Trushkevych, Y. Fan, R. Perry, and R. S. Edwards. Magnetic phase transitions in GdSc studied using non-contact ultrasonics. *Journal of Physics D: Applied Physics*, **46**:pp. 1–9, 2013.

[125] J B Spicer. In situ, laser-ultrasonic monitoring of stainless steel microstructural evolution during heat treatment. *High Temperature and Materials Science*, **37**:pp. 23–41, 1997.

[126] J. Pei, M. I. Yousuf, F. L. Degertekin, B. V. Honein, and B. T. Khuri-Yakub. Lamb wave tomography and its application to erosion corrosion monitoring. *Research in Nondestructive Evaluation*, **8**:pp. 189–197, 1996.

[127] A. S. Murfin, R. A. J. Soden, D. Hatrick, and R. J. Dewhurst. Laser-ultrasonic detection systems: a comparative study with Rayleigh waves. *Measurement Science and Technology*, **11**:pp. 1208–1219, 2000.

[128] I. Arias and J. D. Achenbach. A model for the ultrasonic detection of surface-breaking cracks by the scanning laser source technique. *Wave Motion*, **39**:pp. 61–75, 2004.

[129] C. Valle, M. Niethammer, J. Qu, and L. J. Jacobs. Crack characterization using guided circumferential waves. *Journal of the Acoustical Society of America*, **110**:pp. 1282–1290, 2001.

[130] X. Jian, S. Dixon, N. Guo, R. S. Edwards, and M. Potter. Pulsed Rayleigh wave scattered at a surface crack. *Ultrasonics*, **44**:pp. 1131–1134, 2006.

[131] T. Wu and I. C. Ume. Prediction and experimental validation of penetration depth of butt welds in thin plates using superimposed laser sources. *NDT & E International*, **50**:pp. 10–19, 2012.

[132] B. Hosten and M. Castaings. Surface impedance matrices to model the propagation in multilayered media. *Ultrasonics*, **41**:pp. 501–507, 2003.

[133] Z. Su, L. Ye, and Y. Lu. Guided lamb waves for identification of damage in composite structures: A review. *Journal of Sound and Vibration*, **295**:pp. 753–780, 2006.

[134] J.D. Achenbach. *Wave propagation in elastic solids.* Series in applied mathematics and mechanics. North-Holland, 1st edition, 1973.

[135] I.A. Viktorov. *Rayleigh and Lamb waves: Physical theory and applications.* Plenum press, 1967.

[136] B. Luthi. *Physical acoustics in the solid state.* Springer, 2007.

[137] R. Truell, C. Elbaum, and B. Chick. *Ultrasonic methods in solid state physics.* Academic Press, 1969.

[138] T. Chen, P. Que, O. Zhang, and Q. Liu. Ultrasonic nondestructive testing accurate sizing and locating technique based on time-of-flight diffraction method. *Russian Journal of Nondestructive Testing*, **41**:pp. 594–601, 2005.

[139] M. K. Kuo, T. R. Lin, and P. L. Liu. Locating the crack tip of a surface-breaking crack part 1. Line crack. *Ultrasonics*, **36**:pp. 803–811, 1998.

[140] B. Masserey and E. Mazza. Ultrasonic sizing of short surface cracks. *Ultrasonics*, **46**:pp. 195–204, 2007.

[141] G.W.C. Kaye and T.H. Laby. *Tables of physical and chemical constants.* Harlow-Longman, 16th edition, 1995.

[142] T. Grahn. Lamb wave scattering from a circular partly through-thickness hole in a plate. *Wave Motion*, **37**:pp. 63–80, 2003.

[143] M. Niethammer, L. J. Jacobs, J. Qu, and J. Jarzynski. Time-frequency representation of Lamb waves using the reassigned spectrogram. *Journal of the Acoustical Society of America*, **107**, 2000.

[144] W. H. Prosser, M. D. Seale, and B. T. Smith. Time-frequency analysis of the dispersion of Lamb modes. *Journal of the Acoustical Society of America*, **105**: pp. 2669–2676, 1999.

[145] M. Niethammer, L. J. Jacobs, J. Qu, and J. Jarzynski. Time-frequency representation of Lamb waves. *Journal of the Acoustical Society of America*, **109**: pp. 1841–1847, 2001.

[146] M. Holschneider, M. S. Diallo, M. Kulesh, M. Ohrnberger, E. Luck, and F. Scherbaum. Characterisation of dispersive surface waves using continous wavelet transforms. *Geophysics Journal International*, **163**:pp. 463–478, 2005.

[147] Leon Cohen. *Time-frequency analysis.* Prentice Hall, 1995.

[148] G. Arfken, H. Weber, and F. Harris. *Mathematical methods for physicists.* Academic Press, 2012.

[149] A. M. Robinson, B. W. Drinkwater, and J. Allin. Dry-coupled low-frequency ultrasonic wheel probes: application to adhesive bond inspection. *NDT & E International*, **36**:pp. 27–36, 2003.

[150] M. Kobayashi and C-K. Jen. Piezoelectric thick bismuth titanate/lead zirconate titanate composite film transducers for smart NDE of metals. *Smart Materials and Structures*, **13**:pp. 951–956, 2004.

[151] S. B. Palmer and S. Dixon. Industrially viable non-contact ultrasound. *Insight*, **45**:pp. 211–217, 2003.

[152] W. A. Grandia and C. M. Fortunko. NDE applications of air-coupled ultrasonic transducers. *IEEE Ultrasonics Symposium*, **1**:pp. 697–709, 1995.

[153] E. Benes, M. Groschl, W. Burger, and M. Schmid. Sensors based on piezoelectric resonators. *Sensors and Actuators A*, **48**:pp. 1–21, 1995.

[154] D. N. Alleyne and P. Cawley. The excitation of Lamb waves in pipes using dry-coupled piezoelectric transducers. *Journal of Nondestructive Evaluation*, **15**:pp. 11–20, 1996.

[155] J. F. Tressler, S. Alkoy, and R. E. Newnham. Piezoelectric sensors and sensor materials. *Journal of Electroceramics*, **2**:pp. 257–272, 1998.

[156] M. Rafiq and C. Wykes. The performance of capacitive ultrasonic transducers using v-grooved backplates. *Measurement Science and Technology*, **2**:pp. 168–174, 1991.

[157] D. W. Schindel, D. A. Hutchins, L. Zou, and M. Sayer. The design and characterisation of micromachined air-coupled capacitance transducers. *IEEE Transactions on Ultrasonics, Ferroelectrics and Frequency Control*, **42**:pp. 42–50, 1995.

[158] D. W. Schindel and D. A. Hutchins. Applications of micromachined capacitance transducers in air-coupled ultrasonics and nondestructive evaluation. *IEEE transactions on Ultrasonics, Ferroelectrics and Frequency Control*, **42**: pp. 51–58, 1995.

[159] T. H. Gan, D. A. Hutchins, D. R. Billson, and D. W. Schindel. The use of broadband acoustic transducers and pulse-compression techniques for air-coupled ultrasonic imaging. *Ultrasonics*, **39**:pp. 181–194, 2001.

[160] I. S. Grant and W. R. Phillps. *Electromagnetism.* John Wiley & Sons, 1991.

[161] S. Dixon, C. Edwards, and S. B. Palmer. High accuracy non-contact ultrasonic thickness gauging of aluminium sheet using electromagnetic acoustic transducers. *Ultrasonics*, **39**:pp. 445–453, 2001.

[162] R Ribichini, P. B. Nagy, and H. Ogi. The impact of magnetostriction on the transduction of normal bias field EMATs. *NDT & E International*, **51**:pp. 8–15, 2012.

[163] R. Ribichini, F. Cegla, P. B. Nagy, and P. Cawley. Experimental and numerical evaluation of electromagnetic acoustic transducer performance on steel materials. *NDT & E International*, **45**:pp. 32–38, 2012.

[164] R. S. Edwards, S. Dixon, and X. Jian. Depth gauging of defects using low frequency wideband Rayleigh waves. *Ultrasonics*, **44**:pp. 93–98, 2006.

[165] M. Hirao and H. Ogi. An SH-wave EMAT technique for gas pipeline inspection. *NDT & E International*, **32**:pp. 127–132, 1999.

[166] S. J. Davies, C. Edwards, G. S. Taylor, and S. B. Palmer. Laser-generated ultrasound: its properties, mechanisms and multifarious applications. *Journal of Physics D: Applied Physics*, **26**:pp. 329–348, 1993.

[167] A. M. Lomonosov, A. P. Mayer, and P. Hess. *Experimental methods in the physical sciences.* Academic Press, 2001.

[168] T. Sanderson, C. Ume, and J. Jarzynski. Laser generated ultrasound: A thermoelastic analysis of the source. *Ultrasonics*, **35**:pp. 115–124, 1997.

[169] J. E. Geusic, H. M. Marcos, and L. G. Van Uitert. Laser oscillations in Nd doped yttrium aluminium, yttrium gallium and gadolinium garnets. *Applied Physics Letters*, **4**:pp. 182–184, 1964.

[170] C. B. Scruby. Some applications of laser ultrasound. *Ultrasonics*, **27**:pp. 195–209, 1989.

[171] Y. Sohn and S. Krishnaswamy. Mass spring lattice modeling of the scanning laser source technique. *Ultrasonics*, **39**:pp. 543–551, 2002.

[172] R. J. Dewhurst, C. Edwards, A. D. W. McKie, and S. B. Palmer. Estimation of the thickness of thin metal sheet using laser generated ultrasound. *Applied Physics Letters*, **61**:pp. 1066–1068, 1987.

[173] S. Dixon, C. Edwards, and S. B. Palmer. Generation of ultrasound by an expanding plasma. *Journal of Physics D: Applied Physics*, **29**:pp. 3039–3044, 1996.

[174] L. R. F. Rose. Point-source representation for laser-generated ultrasound. *Journal of the Acoustical Society of America*, **75**:pp. 723–732, 1984.

[175] A. M. Aindow, R. J. Dewhurst, and S. B. Palmer. Laser-generation of directional surface acoustic wave pulses in metals. *Optics Communications*, **45**:pp. 116–120, 1982.

[176] P. A. Doyle and C. M. Scala. Near-field ultrasonic Rayleigh waves from a laser line source. *Ultrasonics*, **34**:pp. 1–8, 1996.

[177] P. Cielo, F. Nadeau, and M. Lamontagne. Laser generation of convergent acoustic waves for materials inspection. *Ultrasonics*, **23**:pp. 55–62, 1985.

[178] D. Royer and E. Dieulesaint. Analysis of thermal generation of Rayleigh waves. *Journal of Applied Physcs*, **56**:pp. 2507–2511, 1984.

[179] M. Clark, F. Linnane, S. D. Sharples, and M. G. Somekh. Frequency control in laser ultrasound with computer generated holography. *Applied Physics Letters*, **72**:pp. 1963–1965, 1998.

[180] F. Hernandez-Valle, A. R. Clough, and R. S. Edwards. Stress corrosion cracking detection using laser/laser and laser/EMAT techniques. *Under review*, 2013.

[181] S. Dixon, T. Harrison, Y. Fan, and P. A. Petcher. Thermoelastic laser generated ultrasound using a ring source. *Journal of Physics D: Applied Physics*, **45**:pp. 1–7, 2012.

[182] X. Wang, M. G. Littman, J. B. McManus, M. Tadi, Y. S. Kim, A. Askar, and H. Rabitz. Focused bulk ultrasonic waves generated by ring-shaped laser illumination and application to flaw detection. *Journal of Applied Physics*, **80**:pp. 4274–4281, 1996.

[183] M. Noroy, D. Royer, and M. Fink. The laser-generated ultrasonic phased array: analysis and experiments. *Journal of the Acoustical Society of America*, **94**: pp. 1934–1943, 1993.

[184] S. Kenderian and B. Boro Djordjevic. Narrow band laser-generated surface acoustic waves using a formed source in the ablative regime. *Journal of the Acoustical Society of America*, **113**:pp. 261–266, 2003.

[185] Jin Huang, S. Krishnaswamy, and J. D. Achenbach. Laser generation of narrow-band surface waves. *Journal of the Acoustical Society of America*, **92**:pp. 2527–2531, 1992.

[186] S. D. Sharples, M. Clark, and M. Somekh. Efficient and flexible laser ultrasound generation using spatial light modulators. *Electronics Letters*, **37**:pp. 1145–1146, 2001.

[187] M. Clark, S. Sharples, and M. Somekh. Non-contact acoustic microscopy. *Measurement Science and Technology*, **11**:pp. 1792–1801, 2000.

[188] A. Meyer, S. Gspan, S. Bernet, and M. Ritsch-Marte. Tailoring ultrasonic beams with optoacoustic holography. *Laser Resonators and Beam Control IV*, **4969**:pp. 105–114, 2003.

[189] J. D. Hamilton, C. J. Brooks, G. L. Vossler, and M. O'Donnell. High frequency ultrasound imaging using an active optical detector. *IEEE Transactions on Ultrasonics, Ferroelectrics and Frequency Control*, **45**:pp. 719–727, 1998.

[190] B. Culshaw, G. Pierce, and P. Jun. Non-contact measurement of the mechanical properties of materials using an all-optic technique. *IEEE Sensors Journal*, **3**:pp. 62–70, 2003.

[191] G. A. Antonelli, H. J. Maris, S. G. Malhotra, and J. M. E. Harper. Picosecond ultrasonics study of the vibrational modes of a nanostructure. *Journal of Applied Physics*, **91**:pp. 3261–3267, 2002.

[192] L. Noui and R. J. Dewhurst. A laser beam deflection technique for the quantitative detection of ultrasonic Lamb waves. *Ultrasonics*, **31**:pp. 425–432, 1993.

[193] Josef Krautkramer and Herbert Krautkramer. *Ultrasonic testing of materials.* Springer-Verlag, 1990.

[194] G. Wild and S. Hinckley. Acousto-ultrasonic optical fiber sensors: Overview and state-of-the-art. *IEEE Sensors Journal*, **8**:pp. 1184–1193, 2008.

[195] J. P. Monchalin. Optical detection of ultrasound at a distance using a confocal Fabry-Perot interferometer. *Applied Physics Letters*, **47**:pp. 14–16, 1985.

[196] H. S. Park, G. Thursby, and B. Culsham. Detection of laser-generated ultrasound based on phase demodulation technique using a fibre Fabry-Perot interferometer. *Measurement Science and Technology*, **16**:pp. 1261–1266, 2005.

[197] P. Castellini, M. Martarelli, and E. P. Tomasini. Laser Doppler vibrometry: development of advanced solutions answering to technology's needs. *Mechanical Systems and Signal Processing*, **20**:pp. 1265–1286, 2006.

[198] B. J. Halkon and S. J. Rothberg. Vibration measuremetns using continous scanning laser Doppler vibrometry: theoretical velocity sensitivity analysis with applications. *Measurement Science and Technology*, **14**:pp. 382–393, 2003.

[199] M.-H. Nadal, C. Hubert, and R. Oltra. High temperature shear modulus determination using a laser-ultrasonic surface acoustic-wave device. *Journal of Applied Physics*, **106**:pp. 1–6, 2009.

[200] Intelligent Optical Systems. Accessed, November 2012. URL `http://www.intopsys.com/products/laser/laserultrasound08.html`.

[201] M. B. Klein, G. D. Bacher, A. Grunnet-Jepsen, D. Wright, and W. E. Moerner. Homodyne detection of ultrasonic surface displacements using two-wave mixing in photorefractive polymers. *Optics Communications*, **162**:pp. 79–84, 1999.

[202] A. Blouin and J-P. Monchalin. Detection of ultrasonic motion of a scattering surface by two-wave mixing in a photorefractive GaAs crystal. *Applied Physics Letters*, **65**:pp. 932–934, 1994.

[203] R. K. Ing and J. P. Monchalin. Broadband optical detection of ultrasound by two-wave mixing in a photorefractive crystal. *Applied Physics Letters*, **59**:pp. 3233–3235, 1991.

[204] P. Delaye, L. A. de Montmorillon, and G. Roosen. Transmission of time modulated optical signals through an absorbing photorefractive crystal. *Optics Communications*, **118**:pp. 154–164, 1995.

[205] B. F. Pouet, R. K. Ing, S. Krishnaswamy, and D. Royer. Heterodyne interferometer with two-wave mixing in photorefractive crystals for ultrasound detection on rough surfaces. *Applied Physics Letters*, **69**:pp. 3782–3784, 1996.

[206] S. Sathish, R. W. Martin, and T. J. Moran. Local surface skimming longitudinal wave velocity and residual stress mapping. *Journal of the Acoustical Society of America*, **115**:pp. 165–171, 2004.

[207] S. Sathish and R. W. Martin. Quantitative imaging of Rayleigh wave velocity with a scanning acoustic microscope. *IEEE transactions on Ultrasonics, Ferroelectrics and Frequency Control*, **49**:pp. 550–557, 2002.

[208] R. A. Lemons and C. F. Quate. Acoustic microscope - scanning version. *Applied Physics letters*, **24**:pp. 163–165, 1974.

[209] F. B. Cegla, P. Cawley, J. Allin, and J. Davies. High-temperature (>500 °C) wall thickness monitoring using dry-coupled ultrasonic waveguide transducers. *IEEE Transactions on Ultrasonics, Ferroelectrics and Frequency Control*, **58**: pp. 156–167, 2011.

[210] M. Z. Silva, R. Gouyon, and F. Lepoutre. Hidden corrosion detection in aircraft aluminium structures using laser ultrasonics and wavelet transform signal analysis. *Ultrasonics*, **41**:pp. 301–305, 2003.

[211] D. G. Aggelis and T. Shiotani. Repair evaluation of concrete cracks using surface and through-transmission wave measurements. *Cement & Concrete Composites*, **29**:pp. 700–711, 2007.

[212] R. J. Dewhurst and Q. Shan. Through-transmission ultrasonic imaging of sub-surface defects using non-contact laser techniques. *Optics and Lasers in Engineering*, **16**:pp. 163–179, 1992.

[213] M. G. Silk and B. H. Lidington. An evaluation of single probe bulk-wave time-delay techniques in sizing cracks in steel. *NDT International*, **10**:pp. 129–134, 1977.

[214] M. G. Silk and B. H. Lidington. The potential of scattered or diffracted ultrasound in the determination of crack depth. *Nondestructive Testing*, **8**:pp. 146–151, 1975.

[215] J. P. Charlesworth and J. A. G. Temple. *Enginerring applications of ultrasonic time-of-flight diffraction.* Research Studies Press Ltd., 2001.

[216] J. A. Ogilvy and J. A. G. Temple. Diffraction of elastic waves by cracks: application to time-of-flight inspection. *Ultrasonics*, **21**.:pp. 259–269, 1983.

[217] F. A. Ravenscroft, K. Newton, and C. B. Scruby. Diffraction of ultrasound by cracks: comparison of experiment with theory. *Ultrasonics*, **29**:pp. 29–37, 1991.

[218] L. Capineri, H. G. Tattersall, J. A. G. Temple, and M. G. Silk. Time-of-flight diffraction tomography for NDT applications. *Ultrasonics*, **30**:pp. 275–288, 1992.

[219] B. W. Drinkwater and D. Wilcox. Ultrasonic arrays from non-destructive evaluation: A review. *NDT & E International*, **39**:pp. 525–541, 2006.

[220] S. D. Sharples, M. Clark, and M. G. Somekh. All-optical adaptive scanning acoustic microscope. *Ultrasonics*, **41**:pp. 295–299, 2003.

[221] J. Li and J. L. Rose. Implementing guided wave mode control by use of a phased transducer array. *IEEE Transactions on Ultrasonics, Ferroelectrics and Frequency Control.*, **48**:pp. 761–768, 2001.

[222] M. Sutcliffe, M. Weston, B. Dutton, P. Charlton, and K. Donne. Real-time full matrix capture for ultrasonic non-destructive testing with acceleration of post-processing through graphic hardware. *NDT & E International*, **51**:pp. 16–23, 2012.

[223] S. Dixon, S. Hill, Y. Fan, and G. Rowlands. The wave-field from an array of periodic emitters driven simultaneously by a broadband pulse. *Journal of the Acoustical Society of America*, **133**:pp. 3692–3699, 2013.

[224] C. Holmes, B. W. Drinkwater, and P. D. Wilcox. Post-processing of the full matrix of ultrasonic transmit-receive array data for non-destructive evaluation. *NDT & E International*, **38**:pp. 701–711, 2005.

[225] P. Fromme, P. D. Wilcox, M. J. S. Lowe, and P. Cawley. On the development and testing of a guided ultrasonic wave array for structural integrity monitoring. *IEEE Transactions on Ultrasonics, Ferroelectrics and Frequency Control*, **53**:pp. 777–785, 2006.

[226] I. Komura, T. Hirasawa, S. Nagai, J. Takabayashi, and K. Naruse. Crack detection and sizing technique by ultrasonic and electromagnetic methods. *Nuclear Engineering and Design*, **206**:pp. 351–362, 2001.

[227] P. Wilcox, C. Holmes, and B. W. Drinkwater. Advanced reflector characterisation with ultrasonic phased arrays in NDE applications. *IEEE Transactions on Ultrasonics, Ferroelectrics and Frequency Control*, **54**:pp. 1541–1550, 2007.

[228] X. Jian, Y. Fan, R. S. Edwards, and S. Dixon. Surface-breaking crack gauging with the use of laser-generated Rayleigh waves. *Journal of Applied Physics*, **100**:p. 064907, 2006.

[229] M. J. S. Lowe, P. Cawley, J-Y Kao, and O. Diligent. The low frequency reflection characteristics of the fundamental antisymmetric Lamb wave A0 from a rectangular notch in a plate. *Journal of the Acoustical Society of America*, **112**:pp. 2612–2622, 2002.

[230] M. J. S. Lowe and O. Diligent. Low-frequency reflection characteristics of the S0 Lamb wave from a rectangular notch in a plate. *Journal of the Acoustical Society of America*, **111**:pp. 64–74, 2002.

[231] M. J. S. Lowe, D. N. Alleyne, and P. Cawley. Defect detection in pipes using guided waves. *Ultrasonics*, **36**:pp. 147–154, 1998.

[232] T. Hayashi and M. Murase. Defect imaging with guided waves in a pipe. *Journal of the Acoustical Society of America*, **117**:pp. 2134–2140, 2005.

[233] A. Lovstad and P. Cawley. The reflection of the fundamental torsional guided wave from multiple circular holes in pipes. *NDT & E International*, **44**:pp. 553–562, 2011.

[234] Z. Yan and P. Nagy. Enhanced laser generation of surface acoustic waves by discontinuities. *Review of Progress in Quantitative Nondestructive Evaluation*, **20a**:pp. 204–211, 2001.

[235] S. Dixon, B. Cann, D. L. Carroll, Y. Fan, and R. S. Edwards. Non-linear enhancement of laser generated Rayleigh waves by cracks. *Nondestrutive Testing and Evaluation*, **23**:pp. 25–34, 2008.

[236] X. Jian, S. Dixon, N. Guo, and R. Edwards. Rayleigh wave interaction with surface-breaking cracks. *Journal of Applied Physics*, **101**:p. 064906, 2007.

[237] R. S. Edwards, X. Jian, Y. Fan, and S. Dixon. Signal enhancement of the in-plane and out-of-plane Rayleigh wave components. *Applied Physics Letters*, **87**:p. 194104, 2005.

[238] Z. Yan and P. Nagy. Thermo-optical modulation of ultrasonic surface waves for NDE. *Ultrasonics*, **40**:pp. 689–696, 2002.

[239] X. Jian, S. Dixon, and S. B. Palmer. In-plane and out-of-plane particle velocity measurement using electromagnetic acoustical transducers. *IEEE Ultrasonics Symposium*, **1-4**:pp. 1276–1279, 2005.

[240] S. E. Burrows, B. Dutton, and S. Dixon. Laser generation of Lamb waves for defect detection: Experimental methods and finite element modelling. *IEEE Transactions on Ultrasonics, Ferroelectrics and Frequency Control*, **59**:pp. 82–89, 2012.

[241] J. Travis. *LabView for Everyone.* Prentice Hall, 2002.

[242] C. T. F. Ross. *Finite element methods in structural mechanics.* Ellis Horwood Limited, 1985.

[243] C. T. F. Ross. *Advanced applied finite element methods.* Horwood Publishing Limited, 1998.

[244] O. C. Zienkiewicz, R. L. Tayor, and J. Z. Zhu. *The finite element method. Its basis and fundamentals.* Elsevier Ltd., 2000.

[245] J. Robinson. *Integrate theory of finite element methods.* John Wiley & Sons Inc, 1973.

[246] PZFlex. Accessed, November 2012. URL `http://www.pzflex.com/`.

[247] S. K. Nath, Krishnan Balasubramaniam, C. V. Krishnamurthy, and B. H. Narayana. Reliability assessment of manual ultrasonic time of flight diffraction (TOFD) inspection for complex geometry components. *NDT&E International*, **43**:pp. 152–162, 2010.

[248] A. Moura, A. M. Lomonosov, and P. Hess. Depth evaluation of surface-breaking cracks using laser-generated transmitted Rayleigh waves. *Journal of Applied Physics*, **103**, 2008.

[249] R. J. Blake and L. J. Bond. Rayleigh wave scattering from surface features: up-steps and troughs. *Ultrasonics*, **30**:pp. 255–265, 1992.

[250] X. Jian, I. Baillie, and S. Dixon. Steel billet inspection using laser-EMAT system. *Journal of Physics D: Applied Physics*, **40**:pp. 1501–1506, 2007.

[251] D. Hesse and P. Cawley. Surface wave modes in rails. *Journal of the Acoustical Society of America*, **120**:pp. 733–740, 2006.

[252] R. S. Edwards, B. Dutton, A. R. Clough, and M. H. Rosli. Enhancement of ultrasonic surface waves at wedge tips and angled defects. *Applied Physics Letters*, **99**:p. 249901, 2011.

[253] M. Ech-Cherif El-Kettani, F. Luppe, and A. Guillet. Guided waves in a plate with linearly varying thickness: experimental and numerical results. *Ultrasonics*, **42**:pp. 807–812, 2004.

[254] Y. Cho. Estimation of ultrasonic guided wave mode conversion in a plate with thickness variation. *IEEE Transactions on Ultrasonics, Ferroelectrics and Frequency Control*, **47**:pp. 591–603, 2000.

[255] L. De Marchi, A. Marzani, N. Speciale, and E. Viola. Prediction of pulse dispersion in tapered waveguides. *NDT & E International*, **43**:pp. 265–271, 2010.

[256] J. K. Cooper, D. C. Lawton, and G. F. Margrave. The wedge model revisited: A physical modelling experiment. *Geophysics*, **75**:pp. T15–T21, 2010.

[257] D. N. Alleyne and P. Cawley. The interaction of Lamb waves with defects. *IEEE Transactions on Ultrasonics, Ferroelectrics and Frequency Control.*, **39**: pp. 381–397, 1992.

[258] M. A. Flores-López and R. D. Gregory. Scattering of Rayleigh-Lamb waves by a surface breaking crack in an elastic plate. *Journal of the Acoustical Society of America*, **119**:pp. 2041–2049, 2006.

[259] O. Diligent, T. Grahn, A. Boström, P. Cawley, and M. J. S. Lowe. The low-frequency reflection and scattering of the S0 Lamb mode from a circular through-thickness hole in a plate: Finite element, analytical and experimental studies. *Journal of the Acoustical Society of America*, **112**:pp. 2589–2601, 2002.

[260] F. Benmeddour, S. Grondel, J. Assaad, and E. Moulin. Experimental study of the A0 and S0 Lamb waves interaction with symmetrical notches. *Ultrasonics*, **49**:pp. 202–205, 2009.

[261] S. Dixon, S. E. Burrows, B. Dutton, and Y. Fan. Detection of cracks in metal sheets using pulsed laser generated ultrasound and EMAT detection. *Ultrasonics*, **51**:pp. 7–16, 2011.

[262] R. P. Gangloff, R. S. Piascik, D. L. Dicus, and J. C. Newman. Fatigue crack propagation in aerospace alloys. *Journal of Aircraft.*, **31**:pp. 720–729, 1994.

[263] Trueflaw. Accessed, August 2013. URL `http://www.trueflaw.com/`.

[264] M. Kemppainen and I. Virkkunen. Crack characteristics and their importance to NDE. *Journal of Nondestructive Evaluation*, **30**:pp. 143–157, 2011.

[265] H. Xiao and P. B. Nagy. Enhanced ultrasonic detection of fatigue cracks by laser-induced crack closure. *Journal of Applied Physics*, **83**:pp. 7453–7460, 1998.

[266] A. M. Lomonosov, P. V. Grigoriev, and P. Hess. Sizing of partially closed surface-breaking microcracks with broadband Rayleigh waves. *Journal of Applied Physics*, **105**:p. 084906, 2009.

[267] J-Y. Kim, V. A. Yakovlev, and S. I. Rokhlin. Surface acoustic wave modulation on a partially closed fatigue crack. *Journal of the Acoustical Society of America*, **115**:pp. 1961–1972, 2004.

[268] C. Pecorari. Scattering of a Rayleigh wave by a surface-breaking crack with faces in partial contact. *Wave Motion*, **33**:pp. 259–270, 2001.

[269] Y. V. Zhitlukhina, D. V. Perov, and A. B. Rinkevich. A spatiotemporal picture of the acoustic field of elastic-wave diffraction at the edge of a crack. *Russian Journal of Nondestructive Testing*, **44**:pp. 712–718, 2008.

[270] E. J. Moukawsher, A. F. Grandt, and M. A. Neussl. Fatigue life of panels with multiple site damage. *Journal of Aircraft.*, **33**:pp. 1003, 1996.

[271] A. R. Clough and R. S. Edwards. Detection of open and partially closed surface defects in plates using ultrasonic enhancement. In *AIP Conference Proceedings: Reveiw of Progress in Quantitative Nondestructive Evaluation.*, 2013.